

Falko Riechert

Speckle Reduction in Projection Systems



Falko Riechert

Speckle Reduction in Projection Systems

Speckle Reduction in Projection Systems

by
Falko Riechert



universitätsverlag karlsruhe

Dissertation, Universität Karlsruhe (TH)
Fakultät für Elektrotechnik und Informationstechnik, 2009

Impressum

Universitätsverlag Karlsruhe
c/o Universitätsbibliothek
Straße am Forum 2
D-76131 Karlsruhe
www.uvka.de



Dieses Werk ist unter folgender Creative Commons-Lizenz
lizenziert: <http://creativecommons.org/licenses/by-nc-nd/3.0/de/>

Universitätsverlag Karlsruhe 2009
Print on Demand

ISBN: 978-3-86644-418-8

Speckle Reduction in Projection Systems

**zur Erlangung des akademischen Grades eines
DOKTOR-INGENIEURS**

von der Fakultät für

Elektrotechnik und Informationstechnik
der Universität Fridericana Karlsruhe

genehmigte

DISSERTATION

von

Dipl.-Phys., Dipl.-Inform. Falko Riechert

geb. in Heidelberg

Tag der mündlichen Prüfung: 23. Juli 2009
Hauptreferent: Prof. Dr. rer. nat. Uli Lemmer
Korreferent: Prof. Dr. Ir. Hugo Thienpont

Publications

Journal publications

- **F. Riechert**, G. Craggs, Y. Meuret, H. Thienpont, U. Lemmer, and G. Verschaffelt, “Far Field Nonmodal Laser Emission for Low-Speckle Laser Projection,” in press, Photonics Technology Letters (2009).
- **F. Riechert**, G. Bastian, and U. Lemmer, “Laser speckle reduction via colloidal-dispersion-filled projection screens,” Appl. Opt. **48**, Issue 19, 3742-3749 (2009).
- **F. Riechert**, F. Dürr, U. Rohlfing, and U. Lemmer, “Ray-based simulation of the propagation of light with different degrees of coherence through complex optical systems,” Appl. Opt. **48**, Issue 8, 1527-1534 (2009).
- **F. Riechert**, F. Glöckler, and U. Lemmer, “Method to determine the speckle characteristics of front projection screens,” Appl. Opt. **48**, Issue 7, 1316-1321 (2009).
- **F. Riechert**, G. Craggs, Y. Meuret, B. Van Giel, H. Thienpont, U. Lemmer, and G. Verschaffelt, “Low speckle laser projection with a broad-area vertical-cavity surface-emitting laser in the nonmodal emission regime,” Appl. Opt. **48**, Issue 4, 792-798 (2009).
- **F. Riechert**, G. Verschaffelt, M. Peeters, G. Bastian, U. Lemmer, and I. Fischer, “Speckle characteristics of a broad-area VCSEL in the incoherent emission regime,” Opt. Commun. **281**, Issue 17, 4424-4431 (2008).

Conference proceedings, posters and presentations

- G. Craggs, G. Verschaffelt, **F. Riechert**, I. Fischer, “Spatially incoherent laser emission and its applications”, Photonics@be Doctoral School, Oostduinkerke, Belgium, March 16-18 (2009).
- **F. Riechert**, “Ray-based simulation of the propagation of coherent light through complex optical systems,” Autumn Colloquium of the Karlsruhe School of Optics and Photonics, Stuttgart, Germany, November 10-11 (2008).
- **F. Riechert**, F. Dürr, U. Lemmer, “Ray-Based Simulation of the Propagation of Coherent Light Through Complex Optical Systems,” Proc. of the 14th MicroOptics Conference (MOC’08), pp. 123-124, September 25-27, 2008, Brussels, Belgium.

- **F. Riechert**, G. Verschaffelt, G. Craggs, Y. Meuret, B. Van Giel, U. Lemmer, H. Thienpont, “Low-Speckle Laser Projection with a Broad-Area VCSEL in the Incoherent Emission Regime,” Proc. of the 14th MicroOptics Conference (MOC’08), pp. 290-291, September 25-27, 2008, Brussels, Belgium.
- B. Van Giel, Y. Meuret, G. Verschaffelt, G. Craggs, **F. Riechert** and H. Thienpont, “Improvement of the Homogenization by Microlens Arrays in Laser Projection Systems Using a Broad-Area VCSEL,” Proc. of the 14th MicroOptics Conference (MOC’08), pp. 292-293, September 25-27, 2008, Brussels, Belgium.
- **F. Riechert**, “Speckle reduction in laser projection applications,” Summerschool of the Karlsruhe School of Optics and Photonics, Bad Herrenalb, Germany, August 20-21 (2008).
- **F. Riechert**, “Information Displays: An Overview of Technologies, Modern Applications and Market Trends,” 1st Ph.D. seminar of the Karlsruhe School of Optics and Photonics, Karlsruhe, Germany, June 6 (2008).
- **F. Riechert**, G. Verschaffelt, G. Craggs, U. Lemmer, Y. Meuret, B. Van Giel, H. Thienpont, “Low-speckle laser projection with a broad-area VCSEL in the incoherent emission regime,” Display Week 2008: International Symposium, Seminar & Exhibition, Los Angeles, California, USA, May 18-23 (2008), published in Society for Information Display Digest of Technical Papers **39**, 2098-2101 (2008).
- **F. Riechert**, “Speckle Reduction in Laser-Projection Applications,” Karlsruhe Days of Optics and Photonics, Karlsruhe, Germany, November 5-6 (2007).
- **F. Riechert**, “Speckle Reduction in Laser-Projection Applications,” KSOP Autumn Colloquium, Oberkochen, September 20th/21st (2007).
- **F. Riechert**, G. Verschaffelt, I. Fischer, G. Bastian, M. Peeters, U. Lemmer, “Speckle phenomena in pulsed broad-area vertical-cavity surface-emitting laser emission under different driving and illumination conditions,” European Conference on Lasers and Electro-Optics (CLEO) and the International Quantum Electronics Conference (IQEC), CB5-3-TUE, Munich, Germany, June 17-22 (2007).
- **F. Riechert**, “Speckle Reduction in projection systems,” Inauguration of the Karlsruhe School of Optics and Photonics, March 23 (2007).
- **F. Riechert**, G. Bastian, U. Lemmer, “Numerical simulation tool for synthetic speckle pattern images and their intensity-based integration under variable conditions for metrology applications,” Proc. of SPIE **6617**, 661709 (2007).
- M. Peeters, I. Fischer, **F. Riechert**, G. Bastian, G. Verschaffelt, “Speckle characteristics of broad-area vertical-cavity surface-emitting laser emission,” EOS Annual Meeting 2006, Topical Meeting 3, ISBN: 978-3-00-019533-4, Porte de Versailles, Paris, France, October 16-19 (2006).

Contents

Zusammenfassung	vii
Abstract	xi
1 Introduction	1
1.1 Aims and Objectives	1
1.2 Structure	1
2 An Introduction to Speckle	3
2.1 Speckle Emergence	3
2.1.1 Nomenclature and History of Speckle Research	4
2.2 Some Statistical Properties of Speckle	5
2.2.1 Objective and Subjective Speckles, Speckle Size and Speckle Length	7
2.2.2 Speckle Measurement	8
2.3 Applications of Speckles	10
2.4 Problems Associated With Speckles	11
2.5 Chapter Summary	12
3 Lasers in Projection Applications	15
3.1 Segmentation of the Projection Systems Market	15
3.2 Typical Architectures of Projection Systems	15
3.3 Today's Laser Projection Systems Market	18
3.4 Characteristics of Different Light Sources and Their Suitability for Different Applications	19
3.5 Gamut	20
3.6 Polarization	24
3.7 Étendue and Lightguiding	24
3.8 Laser Safety	27
3.9 Laser Price	27
3.10 Laser Speckle and Speckle Disturbance Limit	27
3.11 Chapter Summary	29
4 Methods for Speckle Reduction	31
4.1 Wavelength Decorrelation	34
4.1.1 Instantaneous Wavelength Decorrelation with Multiple Illumination Lines or a Broadband Source	34

4.1.2	Time-Sequential Wavelength Decorrelation by a Chirp of the Source's Emission Wavelength	37
4.2	Angular Decorrelation	37
4.2.1	Instantaneous Angular Decorrelation	38
4.2.2	Time-Sequential Angular Decorrelation	39
4.3	Spatial Decorrelation	39
4.3.1	Visual Acuity	40
4.3.2	Instantaneous Spatial Decorrelation	40
4.3.3	Instantaneous Spatial Decorrelation in Combination With a Volume Scattering Target	40
4.3.4	Time-Sequential Spatial Decorrelation	42
4.4	Scrambling	42
4.4.1	Instantaneous Polarization Scrambling	42
4.4.2	Time-Sequential Polarization Scrambling	43
4.4.3	Time-Sequential Phasefront Scrambling	43
4.5	Combination of Methods for Speckle Reduction	44
4.6	Chapter Summary and Motivation of the Following Chapters	44
5	Simulation Tool for the Ray-Based Investigation of the Propagation of Light With Different Degrees of Coherence	47
5.1	Introduction	47
5.2	Review of Methods to Investigate the Propagation of Coherent Light	48
5.3	Functional Extension of a Standard Raytracer	49
5.4	Simulation of a Spatially Fully Incoherent Source With One Simulation Run .	50
5.5	Simulations Compared to Analytical Theory	53
5.6	Investigation of a Two-Tandemarray Microlens Beam Homogenizer	57
5.7	Future Extensions of the Simulation Tool	63
5.8	Chapter Summary and Conclusion	63
6	Speckle Reduction With Volume Scattering Projection Screens	65
6.1	Introduction	65
6.2	Modeling of Speckle Contrast Reduction	66
6.2.1	Depolarization	66
6.2.2	Broadband Illumination of a Rough Target	66
6.3	Experimental Setups	68
6.4	Experimental Results and Interpretation	70
6.4.1	Depolarization	70
6.4.2	Scattering Path Time Distributions of the Screens	71
6.5	Chapter Conclusion and Outlook	74
7	Speckle Reduction With Colloidal-Dispersion-Filled Projection Screens	77
7.1	Introduction	77
7.2	Experimental Setup	78
7.3	Experimental Results	80
7.4	Modeling and Discussion of Blurring and the Speckle Contrast	83
7.5	Additional Speckle Contrast Reducing Effects	86
7.6	Chapter Conclusion and Outlook	87

8 Speckle Reduction With a Broad-Area Vertical-Cavity Surface-Emitting Laser (BA-VCSEL)	89
8.1 Investigation of the Basic Speckle Characteristics of a BA-VCSEL	90
8.1.1 Introduction	90
8.1.2 Experimental Setups	91
8.1.3 Experimental Results	92
8.1.4 Modeling of the Speckle Contrast	98
8.1.5 Interpretation of Results	101
8.1.6 Conclusion and Outlook	105
8.2 Low-Speckle Laser Projection Using the Nearfield Emission of a Nonmodal BA-VCSEL	107
8.2.1 Introduction	107
8.2.2 Experimental Setup	107
8.2.3 Experimental Results	108
8.2.4 Modeling of the Speckle Contrast	110
8.2.5 Summary and Outlook	115
8.3 Low-Speckle Laser Projection Using the Farfield Emission of a Nonmodal BA-VCSEL	116
8.3.1 Introduction	116
8.3.2 Experimental Setup	116
8.3.3 Experimental Results	116
8.3.4 Modeling of the Speckle Contrast	117
8.3.5 Maximal Image Size for Angular Decorrelation	120
8.3.6 Summary	121
8.4 Chapter Conclusion and Outlook	121
9 Conclusion of the Thesis	123
Bibliography	125
List of Figures	142
List of Tables	143
Symbols and Abbreviations	145
Acknowledgements	149
Index	151

Zusammenfassung

Im Jahr 2008 wurden weltweit mehr als sechs Millionen Front- und Rückprojektionsysteme für private und professionelle Anwendungen verkauft. Es wird erwartet, dass der Gesamtmarkt bis zum Jahr 2013 um etwa 25% wachsen wird. Durch den Einsatz von Lasern und Lichtemittierenden Dioden (LEDs) als Lichtquellen entsteht zusätzlich das Marktsegment der Pico-Projektoren. Da Laser-Lichtquellen in Projektionssystemen beträchtliche Vorteile im Vergleich zu Standard-Projektionslampen bieten können, wird ihr Einsatz in Projektionssystemen bereits seit den sechziger Jahren angestrebt und zahlreiche Firmen betreiben Entwicklungsaktivitäten auf dem Gebiet der Laserprojektion. Mit Laser-Lichtquellen kann beispielsweise ein großer Farbraum mit dem Projektionssystem wiedergegeben werden, Laser haben eine kleine Étendue, emittieren polarisiertes Licht und können sehr große Lebensdauern haben. Beim Einsatz von Lasern in Projektionssystemen ist jedoch das Auftreten einer ungewollten granularen Struktur in projizierten Bildern zu beobachten. Aufgrund der hohen Kohärenz des Laserlichts entsteht ein quasi-zufälliges Interferenzmuster welches als *Specklemuster* bezeichnet wird. Speckles finden in vielen Bereichen Anwendung, allerdings stellen sie in vielen anderen Gebieten unerwünschtes Rauschen dar. Das Specklephänomen wird meist durch den Kontrast des Specklemusters quantifiziert, wobei ein Laser-Specklemuster typischerweise einen Kontrast von 1 bzw. 100% aufweist. Dies resultiert in einer starken Intensitätsvariation in projizierten Bildern, was die Bildqualität in Projektionsanwendungen beträchtlich verschlechtern kann. Um eine Beeinträchtigung der Bildqualität auszuschließen, muss ein Specklekontrast kleiner als ca. 4% erreicht werden. In den meisten Projektionsanwendungen ist eine starke Bildverschlechterung durch Speckles nicht akzeptabel, weshalb Specklereduktion ein Hauptpunkt ist, wenn Laser als Lichtquellen in Projektionsanwendungen in Betracht gezogen werden.

Ziel der vorliegenden Arbeit ist die Untersuchung verschiedener Methoden zur Speckle-reduktion in Projektionsanwendungen. Da die Anwendbarkeit, Praktikabilität und Effektivität der einzelnen Methoden von der Architektur des Projektionssystems abhängen kann, werden diese ebenfalls betrachtet.

In der vorliegenden Arbeit wird zunächst die funktionale Erweiterung einer Standard Raytracing-Software gezeigt, die dazu benutzt werden kann, die Speckleeigenschaften von optischen Systemen zu untersuchen und vorherzusagen. Optische Felder mit verschiedenen zeitlichen und räumlichen Kohärenzeigenschaften werden dazu mittels Kugelwellen modelliert, womit dann die Kohärenzeigenschaften von komplexen, makroskopischen optischen Systemen untersucht werden können. Die Intensitätsverteilung und Kohärenzfunktion kann an jeder beliebigen Stelle eines untersuchten Systems berechnet und dargestellt werden. Dies ist von praktischer Relevanz, da sich die Kohärenzeigenschaften des Lichts bei Propagation durch ein System im Allgemeinen ändern,

und die Kohärenzeigenschaften des Lichts am Bildschirm den von einem Beobachter wahrgenommenen Specklekontrast entscheidend beeinflussen können. Monochromatische Simulationen einer Freiraumpropagation und eines 1-Linsen Aufbaus werden gezeigt, und exzellente Übereinstimmung mit einer theoretischen Beschreibung der Systeme wird erreicht. Außerdem werden die grundlegenden Kohärenzeigenschaften eines Mikrolinsen-Homogenisierers bestehend aus zwei Tandem-Mikrolinsenarrays untersucht. Es handelt sich um einen aktuellen in Projektionsanwendungen benutzten Homogenisierer, der allerdings nicht mit einfachen Mitteln theoretisch modelliert werden kann. Resultate für verschiedene Beleuchtungssituationen werden gezeigt.

Des Weiteren werden die Speckleeigenschaften von verschiedenen volumenstreuernden Frontprojektionsbildschirmen gemessen und modelliert. Die Specklereduktion aufgrund der Depolarisationseigenschaften und aufgrund der Wellenlängendekorrelation bei breitbandiger Beleuchtung der Bildschirme wird untersucht. Dazu werden mittels ultrakurzer Titan:Saphir (Ti:Sa) Laserpulse und einer Streak-Kamera die Photon-Streuzeitverteilungen in den Bildschirmen ermittelt. Diese bestimmen die Volumenrauheiten der Bildschirme und beeinflussen maßgeblich deren Speckleeigenschaften. Mit den ermittelten Rauheitswerten werden die Specklekontrastreduktionen in den Bildschirmen für deren Beleuchtung mit verschiedenen Bandbreiten modelliert. In einer Überprüfung des Modells mittels breitbandiger Ti:Sa-Beleuchtung der Bildschirme wird hervorragende Übereinstimmung zwischen den Messungen und der Modellierung erzielt. Es wird gezeigt, dass vollständig depolarisierende Streuung in den Bildschirmen nicht kritisch für das Erreichen niedriger Specklekontrastwerte ist. Eine Specklekontrastreduktion von annähernd dem maximalen Wert $1/\sqrt{2}$ wurde mit allen Bildschirmen erzielt. Die Selektion eines Bildschirms mit breiter Photon-Streuzeitverteilung, d.h. großer Volumenrauheit, ist jedoch unerlässlich, um eine hohe Specklekontrastreduktion bei breitbandiger Beleuchtung zu erzielen. Es wird gezeigt, dass die Bildschirmauswahl insbesondere bei kleinen Beleuchtungsbandbreiten ausschlaggebend ist, da sich die für die verschiedenen Bildschirme resultierenden Specklekontrastwerte trotz identischer Beleuchtungssituation um bis zu 30% unterscheiden können.

Darüber hinaus wird Specklereduktion mittels Bildschirmen untersucht, die mit einer kolloidalen Dispersion gefüllt werden. Durch Vielfachstreuung an den Streupartikeln der Dispersion, die Brownscher Bewegung unterliegen, wird ein zeitveränderliches Specklemuster erzeugt. Es werden keine weiteren Komponenten, wie beispielsweise bewegliche Diffusoren, benötigt, um die zeitliche Änderung der Specklemuster zu erreichen. Ein menschlicher Beobachter integriert zeitlich das veränderliche Specklemuster und nimmt einen reduzierten Specklekontrast wahr. Der beabsichtigten Specklereduktion wird das Verwischen (Blurring) projizierter Bilder in den Bildschirmen gegenübergestellt, welches nur in gewissen Grenzen akzeptabel ist. Es wird gezeigt, dass eine hochstreuende Dispersion mit großen Streupartikeln gewählt werden muss, um bei kleinem Blurring möglichst viel Specklereduktion zu erzielen. Das verringerte Blurring aufgrund der mit größeren Streupartikeln stärker nach vorne gerichteten Streuung überkompensiert die aufgrund der reduzierten Dynamik der Streuzentren kleinere Specklekontrastreduktion. Specklekontrastwerte von weniger als 4% werden bei akzeptablem Blurring erzielt.

Im darauf folgenden Abschnitt wird specklereduzierte Laserprojektion mit einem im nahen Infraroten oberflächenemittierenden Laser (BA-VCSEL) untersucht. Mittels starker Strompulse kann der Laser in einem Regime nichtmodiger Emission betrieben

werden. In diesem Regime emittiert der Laser keine transversalen Moden mehr, kann jedoch als quasi-homogene Gauß-Schell-Modell Quelle modelliert werden, die mehr als 300 wechselseitig inkohärente Einzelstrahlen emittiert. Zuerst wird eine Untersuchung der grundlegenden Speckleeigenschaften des Lasers im Modenemissionsregime und im nichtmodigen Regime in verschiedenen Beleuchtungs- und Messaufbauten durchgeführt. Drei Effekte, die den Specklekontrast reduzieren, werden quantitativ modelliert. Dies sind depolarisierende Streuung am Bildschirm, eine erwärmungsinduzierte Verschiebung der Emissionswellenlänge des Lasers während der Strompulse und die drastisch reduzierte räumliche Kohärenz der Laserquelle. Gute Übereinstimmung zwischen den modellierten und den gemessenen Specklekontrastwerten wird erzielt. Aufgrund der Kombination der drei Specklekontrast reduzierenden Effekte können niedrige Specklekontrastwerte auf effiziente Weise ohne den Einsatz sich bewegender oder rotierender Bauteile erzielt werden. In einem Aufbau in dem sich der Bildschirm außerhalb des Fokus der Messkamera befindet wird ein Specklekontrastwert von 1,3% erreicht. Aufbauend auf diesen vielversprechenden Resultaten wird das BA-VCSEL dann als Lichtquelle in einem Aufbau verwendet, der besser einer Projektionsapplikation entspricht in der ein menschlicher Beobachter einen Bildschirm betrachtet. Das BA-VCSEL wird dazu in einem realistischen Projektionssystem eingesetzt, und die Apertur des BA-VCSEL wird auf einen Mikrolinsen-Strahlhomogenisierer abgebildet. Auch der Messaufbau wird adaptiert, damit er möglichst getreu der Beobachtung des Bildschirms durch einen menschlichen Beobachters aus drei Metern Entfernung entspricht. Specklekontrastwerte von 3,6% werden in diesem realistischen Aufbau erzielt. Das Modell für die drei kontrastreduzierenden Effekte wird erweitert und exzellente Übereinstimmung zwischen den modellierten und den gemessenen Werten wird erzielt. Es wird gezeigt, dass die emittierten Einzelstrahlen des nichtmodigen BA-VCSELs mindestens so groß wie die Mikrolinsen des Strahlhomogenisierers sein müssen, um das volle Potential des BA-VCSELs für kleine Specklekontrastwerte auszuschöpfen. Der Strahlhomogenisierer sorgt dafür, dass der Bildschirm mit den Einzelstrahlen aus ausreichend unterschiedlichen Winkeln beleuchtet wird, damit alle am Bildschirm überlagerten Specklemuster dekorreliert sind, und eine hohe Specklekontrastreduktion resultiert. Da eine Beleuchtung des Strahlhomogenisierers mit dem Fernfeld des BA-VCSELs einige Vorteile mit sich bringt, wird auch Fernfeldbeleuchtung untersucht. Beispielsweise kann der Strahlhomogenisierer direkt, ohne zusätzliche optische Komponenten beleuchtet werden, und eine akkurate Positionierung des VCSELs ist nicht nötig. Die Modellierung des Specklekontrasts wird auf die Fernfeldbeleuchtung angepasst und es wird gezeigt, dass die Einzelstrahlen des Fernfelds wiederum größer als die Mikrolinsen des Homogenisierers sein müssen, um das volle Potential der kleinen räumlichen Kohärenz des BA-VCSELs auszuschöpfen. Die Größe der Einzelstrahlen am Homogenisierer kann bei Fernfeldbeleuchtung auf einfache Weise über den Abstand zwischen BA-VCSEL und dem Strahlhomogenisierer eingestellt werden. Es werden Specklekontrastwerte von 2,5% in hervorragender Übereinstimmung mit der Modellierung gemessen.

Im letzten Abschnitt der Arbeit wird abschließend diskutiert, dass niedrige Specklekontrastwerte (auch unter der 4% Grenze) effizient durch die Kombination verschiedener Methoden zur Specklereduktion erzielt werden können. Dies sollte auf kosteneffiziente Weise erfolgen, und möglichst viele der Vorteile, die der Einsatz von Laserquellen mit sich bringt, sollten erhalten bleiben. Darüber hinaus wird erläutert, dass Methoden zur

Specklereduktion, die mit dem Bildschirm verknüpft sind, besonders attraktiv sind, da deren Effektivität wenig von einer speziellen Projektiorarchitektur oder einem speziellen Systemaufbau abhängt.

Abstract

The current worldwide market for rear- and front projection systems is a multi billion dollar market. In the year 2008 more than six million projection systems were sold for consumer and professional applications and the total annual sales figures are expected to increase by approximately 25% until the year 2013. Laser or Light Emitting Diode (LED) light sources even create the new market segment of pico-projectors. The use of lasers as light sources in projection applications has been envisaged already since the 1960s. This is because they can provide considerable advantages compared to standard projection lamps. These are, for example, a larger color gamut, a small étendue of the light source, emission of polarized light and a long lifetime. Many companies are known to be active in developing laser projection systems. When using lasers in projection applications, the appearance of an unwanted granular structure in projected images is observable. Because of the high coherence of the laser source, a quasi-random interference pattern (speckle pattern) is formed. Speckle can be useful in several applications, while in other applications speckles act as noise. Speckle disturbance is usually quantified via the speckle contrast. A typical laser speckle pattern has a contrast of 1, i.e. 100% and large intensity fluctuations. Therefore, speckle can severely degrade the image quality in laser projection applications. A speckle contrast lower than approximately 4% has to be achieved to avoid speckle disturbance. Speckle reduction is a major issue when considering lasers as illumination source because in most projection applications large speckle disturbance will not be acceptable.

The objective of this thesis is the investigation of different practical methods for speckle reduction in laser projection applications. As the applicability and effectiveness of the different methods can depend on the projection system architecture, they are considered, too.

First, the functional extension of a standard raytracing software is presented in this thesis, which is a step towards the prediction of speckle phenomena in projection systems. By representing optical fields with different temporal and spatial coherence properties by spherical waves, the coherence properties of macroscopic and complex optical systems can be investigated. The intensity distribution as well as the mutual coherence function or the complex degree of coherence can be calculated and depicted at arbitrary positions in an investigated system. This is of practical importance because the coherence properties of the light typically change during the propagation through the optical system and the coherence properties on the projection screen can crucially influence the speckle contrast perceived by an observer. Monochromatic coherence simulations of a free space optical system and a single lens system are exemplarily shown and excellent agreement with theory is achieved. Furthermore, investigations of the coherence properties of a practical two-tandemarray microlens beam homogenizer system are shown.

This homogenizer cannot be easily modeled analytically. Results for different illumination conditions are presented.

Furthermore, the speckle characteristics of different front projection screens are investigated in this thesis. Speckle reduction because of depolarization and wavelength decorrelation in the screens under broadband illumination, are investigated. Therefore, the scattering path time distributions of the screens are measured with an ultrafast Titanium:Sapphire (Ti:Sa) laser and a streak camera. These determine the screens' volume roughnesses and have a major influence on their speckle characteristics. Using the measured values, the speckle contrast reduction resulting for illumination of the screens with different bandwidths is modeled. The modeling is verified with a reference measurement using broadband Ti:Sa illumination of the screens. Good agreement between measurement and model is achieved. The achieved results show that strongly depolarizing backscattering from the front projection screens is not that critical in order to achieve low speckle contrast values. A depolarization induced speckle contrast reduction close to the maximum value of $1/\sqrt{2}$ is achieved with all investigated screens. However, the proper selection of a screen with a broad scattering path time distribution, i.e. a large volume roughness, is essential to maximize the speckle reduction resulting from broadband illumination. It is shown that a proper selection is especially crucial for small illumination bandwidths as the resulting speckle contrast values can differ more than 30% for the different screens under identical illumination conditions.

Moreover, speckle reduction with colloidal-dispersion-filled rear projection screens is investigated. A time varying speckle pattern is created via multiple scattering of the laser light on the scattering globules of the colloidal dispersion which do Brownian movement. Therefore, there is no necessity for any additional components like moving or rotating diffusers to achieve the time variation. A human observer temporally integrates the time-varying speckle pattern and perceives a reduced speckle contrast. The intended speckle contrast reduction and unwanted blurring of a projected image in the screen are discussed. From the achieved results it is deduced that a highly scattering colloidal dispersion with highly forward peaked scattering has to be chosen in order to achieve a high speckle contrast reduction at comparably low blurring. The reduced blurring because of more forward peaked scattering when larger scattering globules are used overcompensates the reduction of the globule dynamics and the connected decrease of the speckle reduction which also result from the increased globule size. Speckle contrast values below the 4% disturbance limit of a human observer are measured.

Then, low-speckle laser projection with a near infrared broad-area vertical-cavity surface-emitting laser (BA-VCSEL) is investigated. With strong current pulses the BA-VCSEL can be driven in a nonmodal emission regime where it no longer emits transverse modes but can be modeled as quasi-homogeneous Gaussian Schell-model source which emits more than 300 mutually incoherent beamlets. First, an investigation of the basic speckle characteristics of the BA-VCSEL in the modal and nonmodal emission regime in different measurement and illumination setups is presented. Three speckle contrast reducing effects are quantitatively modeled and good agreement between the model and the measurements is achieved. These contrast reducing effects are polarization scrambling of the paper screen, a thermally induced shift in the BA-VCSEL's emission wavelength and the reduced spatial coherence of the source. With the combination of the three contrast reducing effects, low speckle contrast values are achieved in an

efficient way without the use of moving or rotating components. In a setup where the screen is out of focus of the observer, speckle contrast values as low as 1.3% are achieved. Based on these promising results, the VCSEL is then used as illumination source in an experimental setup which is more realistic for projection applications with a human observer looking at a screen. The BA-VCSEL is used as illumination source in a practical full frame projection system and the BA-VCSEL's nearfield is imaged onto a microlens beam homogenizer. Also the camera setup is adapted in order to mimic a human observer imaging the screen from a distance of three meters. Speckle contrast values as low as 3.6% are measured in this realistic projection setup. The quantitative model of the three speckle contrast reducing effects is improved and excellent agreement between the measured and the modeled contrast values is achieved. It is shown that, in order to exploit nonmodal emission to its full potential, the size of the BA-VCSEL's beamlets on the beam homogenizer in comparison to the size of the beam homogenizer's lenses is a crucial parameter. Each beamlet should be equal to or larger than one microlens of the homogenizer. The homogenizer then introduces sufficient angular diversity to decorrelate the resulting speckle patterns that are superimposed on the screen. As farfield instead of nearfield illumination of the beam homogenizer has some important advantages for a practical projection system, also farfield illumination is also investigated. The field emitted by the BA-VCSEL can then be directly projected onto the homogenizer without the need for additional lenses or accurate alignment. The modeling of the speckle contrast is adapted to farfield illumination. Again, each beamlet has to be larger than one microlens of the homogenizer in order to exploit the full potential of the BA-VCSEL's low spatial coherence. The size of the beamlets on the homogenizer can be simply chosen by tuning the distance between BA-VCSEL and homogenizer. Speckle contrast values as low as 2.5% are achieved which are again in excellent agreement with the modeling.

In the last part of the thesis, it is concluded that low speckle contrast values (even below the 4% disturbance limit) can be efficiently achieved by the combination of several methods for speckle reduction. This should be done in a cost-effective way and without loosing the vast advantages connected to the use of laser sources. Furthermore, it is discussed that methods for speckle reduction which are connected to the screen are very attractive because they are less dependent on a particular projection system architecture or a particular system setup.

Chapter 1

Introduction

The current worldwide market for rear- and front projection systems is a multi billion dollar market. In 2008 more than six million projection systems for consumer and professional applications were sold [1]. Although the rear projection TV segment is strongly declining, the total annual sales figures are expected to increase by approximately 25% by 2013 [1]. The use of lasers as light sources in projection applications has long been envisaged [2],[3]. This is because they can provide considerable advantages compared to standard projection lamps. These are for example a larger color gamut, a small étendue, emission of polarized light and a long lifetime of the source. With laser or Light Emitting Diode (LED) light sources also the new market segment of pico-projectors emerges. These are tiny projectors with very small volumes which might be integrated in or sold as companion device for handheld devices such as mobile phones, digital cameras or personal media players. Current standard projection lamps cannot provide the small volumes required for such systems. It is estimated that the annual pico-projector market can reach 30 million units in 2012 [4].

A major problem when using lasers in projection applications is the appearance of an unwanted granular structure in projected images. Because of the high coherence of the laser source a quasi-random interference pattern is formed which severely degrades the image quality. This disturbing interference pattern is named *speckle pattern*. In most projection applications high speckle disturbance is not tolerable. Speckle reduction is therefore a major issue when considering lasers as illumination sources in projection systems.

1.1 Aims and Objectives

The objective of this thesis is the investigation of different methods for speckle reduction in laser projection applications. Also the practicability and the effectiveness of the different methods for different projection system architectures will be considered.

1.2 Structure

In the first chapter, the topic of the thesis is introduced and explained. The aims and objectives of the Ph.D. project are defined and the structure of the thesis is outlined.

In Chapter 2, a short introduction into various aspects of speckle is presented. Speckle emergence is explained, the historical development of speckle research is summarized and relevant statistical properties of speckles are summarized. Furthermore, various applications in which speckles are useful and applications which suffer from speckle are introduced.

In Chapter 3, several aspects of the use of lasers in projection applications are discussed. Today's projection systems market is segmented and typical projection system architectures are discussed. Furthermore, the currently developing laser projection systems market is introduced. Several advantages which laser sources can provide in projection applications are discussed.

In Chapter 4, several methods to achieve speckle reduction are presented. The practical applicability of the different methods in different laser projection systems is considered.

In Chapter 5, the functional extension of a raytracing simulation tool is presented. The coherence properties of the light used in projection applications crucially influences the speckle contrast values an observer perceives. The coherence properties on the screen can differ a lot from those close to the light source. With the extended tool the propagation of light with different degrees of coherence through optical systems can be investigated which helps to understand their speckle properties.

In Chapter 6, the speckle characteristics of volume scattering projection screens are investigated. Therefore, the screens' depolarization characteristics and their volume roughnesses are determined. It is shown that a proper selection of the projection screen can be crucial to achieve low speckle contrast values.

In Chapter 7, speckle reduction using a colloidal-dispersion-filled projection screen will be presented. A time varying speckle pattern is created via multiple scattering of the laser light on the scattering globules in the dispersion which do Brownian movement. The two counteracting effects image blurring and speckle reduction are compared and different colloidal dispersions are investigated.

In Chapter 8, low speckle laser projection with a nonmodal broad-area vertical-cavity surface-emitting laser is measured and modelled. Speckle reduction is efficiently achieved with the combination of the three speckle contrast reducing effects polarization scrambling, a chirp of the laser's emission wavelength and the drastically reduced spatial coherence in the nonmodal regime.

In Chapter 9, the thesis is concluded and a short outlook is given.

Chapter 2

An Introduction to Speckle

In this chapter, an introduction into various aspects of the speckle phenomenon is presented. In Section 2.1, speckle emergence is explained and a review of the development of speckle research is presented. In Section 2.2, important statistical properties of speckles are introduced. In Section 2.3, a number of experimental techniques is presented in which speckles find applications. In Section 2.4, applications are introduced in which speckles act as noise and can lead to serious problems. In Section 2.5, the chapter is summarized. A comprehensive coverage of the topic speckle can be found in the books [5]-[10].

2.1 Speckle Emergence

Speckles emerge when at least partly coherent light is scattered from an optically rough surface, is scattered in a volume or propagates through a material with quasi-random fluctuations of the refractive index. Mathematically, coherence is typically described with the *mutual coherence function* Γ . For a monochromatic and scalar field U , the mutual coherence function between the positions \vec{x}_1 and \vec{x}_2 at times t_1 and $t_2 = t_1 + \tau$ in a stationary optical field is given by

$$\Gamma(\vec{x}_1; \vec{x}_2; \tau) = \langle U(\vec{x}_1, t_1) U^*(\vec{x}_2, t_2) \rangle_e, \quad (2.1)$$

where $*$ denotes complex conjugation, τ denotes a time difference and $\langle \rangle_e$ denotes an ensemble average over different realizations of the field [11].

An intuitive illustration of speckle formation for the case of the illumination of an optically rough surface with fully coherent light is depicted in Fig. 2.1. Each point of the illuminated surface can be seen as a secondary source, emitting a spherical wave into free space (Fig. 2.1(a)). Speckle can then be seen as a quasi-random interference pattern where the interfering spherical waves have quasi-random amplitudes and phases. The term *quasi-random* is used because the phases are determined by the distances between the secondary sources and the observation point and the amplitudes are determined by the same distances, the surface reflectivity and the illuminating light field. Mathematically, each spherical wave can be interpreted as a phasor in the complex plane and speckle formation can therefore be modeled as a quasi-random phasor sum which represents a random walk in the complex plane. The field A_{obs} in the observation point

can then be expressed as

$$A_{obs} = \frac{1}{\sqrt{N}} \sum_{n=1}^N a_n e^{i\varphi_n}, \quad (2.2)$$

where a_n is the length of the n -th out of N contributing complex phasors and φ_n is its phase. A typical image of a laser speckle pattern is shown in Fig. 2.2.

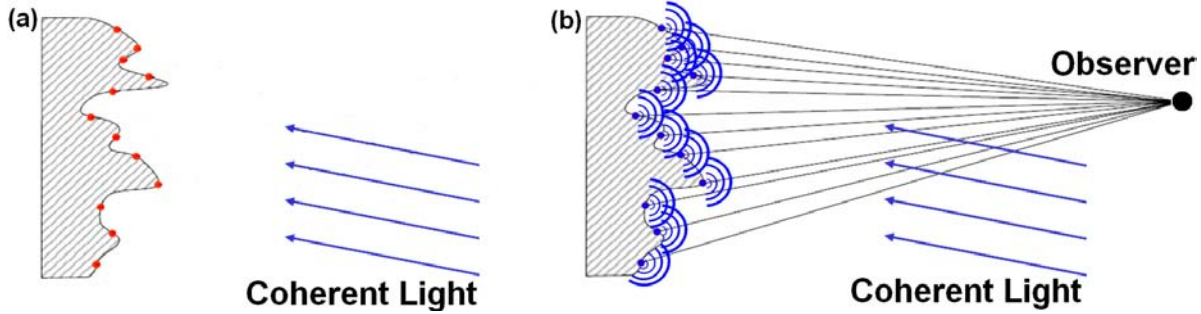


Figure 2.1: Illustration of speckle emergence: (a) each point of the surface can be seen as a secondary source, emitting a spherical wave, (b) the field in the observation point can be modeled as quasi-random phasor sum.

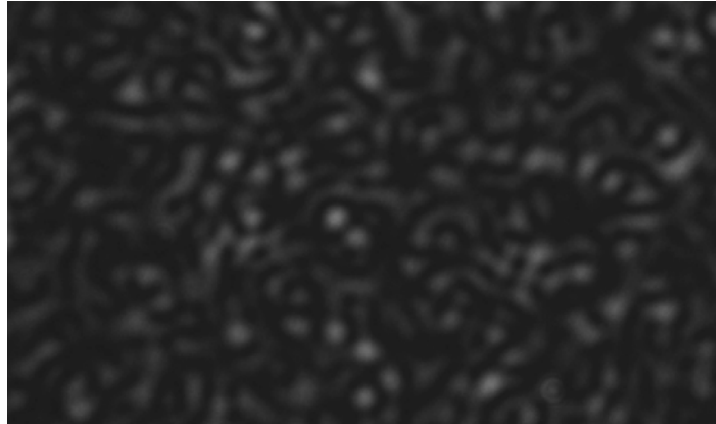


Figure 2.2: Image of a typical laser speckle pattern.

The emergence of speckles is not restricted to optical wavelengths or to the regime of electromagnetic waves. Speckles also play a role in numerous other applications where “coherent” radiation is transmitted through or reflected from objects which are rough on the length scale of the wavelength of the radiation. Speckles appear in radar [12] and x-ray applications [13] but also in medical ultrasound [14] or even in particle beams which can show wave characteristics [15].

2.1.1 Nomenclature and History of Speckle Research

The term *speckle* has been in use since the 1960s. Before the terms *granularity* or *granular structure* had been commonly used. Today, the terms *speckle* and *speckles* are used

to describe the speckle phenomenon. To avoid confusion, the term (single) *speckle spot* is used in this thesis to describe a single bright spot in a speckle pattern.

Following [16] and [17], first descriptions of the appearance of speckle go back to the 19th century when Exner described the appearance of granular structures when he studied the diffraction of a light beam from a point source from a number of randomly distributed particles in 1877 [18]. Later von Laue [19]-[20], de Haas [21]-[22], Raman [23] and Buchwald [24] conducted further studies. First quantitative measurements were performed by Ramachandran in 1943 [25].

However, descriptions of appearing scintillations when stars are observed are much older. Nowadays it is well understood that this phenomenon is closely related to atmospheric speckle. Starlight can reach the Earth with considerable coherence. Different rays can pass through domains of the atmosphere with different refractive indices because of different air density, humidity and temperature. As the atmosphere is in constant motion its optical properties can change across an observer's line of sight. This can produce the irregular changes in intensity known as scintillation. This explanation can already be found in a book from 1855 [26] in which von Humboldt states that he already published extracts from this theory as early as in 1814 in [27].

However, only with the invention of the laser in the early 1960s, the speckle phenomenon became prominent and a lot of research was "re-invented". The first publication on the formation of laser speckle patterns by Ridgen and Gordon appeared in 1962 [28]. In 1963 works on the topic from Langmuir [29], Allen [30], Goodman [31] and Oliver [32] followed.

2.2 Some Statistical Properties of Speckle

In this section, some statistical properties of speckle are summarized which will be relevant throughout this thesis. Detailed and comprehensive descriptions of the theoretical foundations can be found in [5]-[10].

Speckle is usually quantified via the contrast C of the quasi-random interference pattern. The contrast of a speckle pattern is given by $C = \sigma_I/\bar{I}$, where σ_I indicates the standard deviation of the intensity values and \bar{I} the mean intensity [9]. The speckle contrast will be used throughout this work to quantify speckle. The signal to noise ratio S/N is given by the reciprocal of the contrast C .

A speckle pattern which is formed by a large number of statistically independent phasors whose phases are uniformly distributed over the interval $[0..2\pi]$ is typically named a *fully developed* speckle pattern. A fully developed speckle pattern has a contrast $C = 1$ and the quasi-random phasor sum shows circular complex Gaussian statistics [9]. A fully developed speckle pattern is for example created if a surface, which is sufficiently rough and has a Gaussian height distribution, is illuminated with coherent and polarized light. For a large surface roughness, the resulting phase distribution modulo 2π of the phasors is asymptotically uniform over the interval $[0..2\pi]$ [9]. Furthermore, the scattering on the surface has to be polarization preserving, as it is the case for reflection from typical metal surfaces for example.

The probability density function of the intensity distribution in a fully developed

speckle pattern is given by

$$p_I(I) = \frac{1}{\bar{I}} \cdot \exp\left(-\frac{I}{\bar{I}}\right), \quad (2.3)$$

where \bar{I} is again the mean intensity and σ_I is again the standard deviation of the intensity [9]. It can be seen that the intensity distribution has a negative exponential shape.

If a constant phasor contributes to the quasi-random phasor sum forming a speckle pattern, the resulting speckle contrast is given by [9]

$$C = \frac{\sqrt{1+2r}}{1+r}. \quad (2.4)$$

Here, $r = I_0/\bar{I}_n$, where I_0 is the intensity of the constant phasor and \bar{I}_n is the mean intensity of the random phasor sum (without the constant phasor). Such a constant phasor contribution might arise, if part of the light illuminating a surface is specularly reflected.

In the following, two speckle patterns are named *statistically independent*, if they add on an intensity basis. This is for example the case for two speckle patterns, which were produced by two mutually incoherent laser sources. Also a laser which emits more than one transverse mode can produce statistically independent speckle patterns. Each of the emitted transverse modes is individually fully spatially coherent [33] and will produce a speckle pattern which is statistically independent from the others. In Chapter 8, a nonmodal broad-area vertical-cavity surface-emitting laser (BA-VCSEL) with drastically reduced spatial coherence will be used to create statistically independent speckle patterns. The laser can be modeled as a source which does not emit transverse modes but a large number of beamlets which are mutually incoherent. In this case each of the beamlets can produce an independent speckle pattern.

The normalized intensity correlation coefficient $|\rho_{n,m}|$ of two speckle patterns n and m is given by

$$|\rho_{n,m}| = \left| \frac{\overline{I_n \cdot I_m} - \overline{I_n} \cdot \overline{I_m}}{\sqrt{(\overline{I_n} - \bar{I}_n)^2} \cdot \sqrt{(\overline{I_m} - \bar{I}_m)^2}} \right|, \quad (2.5)$$

where $\overline{I_n}$ and $\overline{I_m}$ are the mean intensities of the patterns. The two patterns are named *uncorrelated* or *fully decorrelated* if $\rho_{n,m} = 0$. In case of $0 < |\rho_{n,m}| < 1$ the two patterns are *partly correlated* or *partly decorrelated*. For $|\rho_{n,m}| = 1$, the two patterns are *fully correlated*, i.e. they have the same intensity distribution.

The resulting speckle contrast C for the superposition of several statistically independent and at least partly decorrelated speckle patterns is reduced. The speckle contrast reduction can be intuitively understood, as the outcome of the superposition of quasi-random interference patterns should be a more homogeneous intensity distribution. If the superimposed pattern were fully correlated, i.e. they showed exactly the same intensity distributions, the resulting speckle contrast would not be reduced. The resulting contrast reduction is somehow dependent on the mutual correlation and the mean intensities of the superimposed patterns. Following [9], the resulting contrast for

the superposition of M statistically independent and fully decorrelated speckle patterns is given by

$$C = \frac{\sqrt{\sum_{n=1}^M \bar{I}_n^2}}{\sum_{n=1}^M \bar{I}_n}, \quad (2.6)$$

where \bar{I}_n is the mean intensity of the n -th pattern. It can be seen in Eq. (2.6), that the minimal achievable speckle contrast is given by $1/\sqrt{M}$ which results, if all superimposed speckle patterns have the same mean intensity. As mentioned above, the resulting contrast depends on the mutual correlation and intensity of the superimposed patterns if the superimposed statistically independent speckle patterns are partly correlated [9]. All values between $C = 1$ and $C = 1/\sqrt{M}$ are possible.

The contrast C of a speckle pattern which is partially depolarized is given by [9]

$$C = \sqrt{\frac{1+P}{2}}, \quad (2.7)$$

where P is the degree of polarization. P is defined as $P = |(\bar{I}_1 - \bar{I}_2)/(\bar{I}_1 + \bar{I}_2)|$, where \bar{I}_1 and \bar{I}_2 are the mean intensities in two orthogonal directions. It can be seen that a coherent and polarized source whose polarization is preserved during scattering on a sufficiently rough illuminated target will produce a speckle pattern with $C = 1$. An unpolarized source or a source which lost its polarization during scattering will produce a speckle pattern with $C = 1/\sqrt{2}$. The situation can be seen as if an independent speckle pattern was produced in each of the two orthogonal polarization components which are then superimposed.

2.2.1 Objective and Subjective Speckles, Speckle Size and Speckle Length

Following [9], the area A_{cov} of the normalized covariance function of the intensity distribution in a speckle pattern can be used as a measure for the average size of a single speckle spot in the speckle pattern. It is shown in [9] that under some practical assumptions A_{cov} is given by

$$A_{cov} = \int_{-\infty}^{+\infty} \int_{-\infty}^{+\infty} |\Gamma_A(\Delta x, \Delta y)/\Gamma_A(0, 0)|^2 d\Delta x d\Delta y, \quad (2.8)$$

that is an integral over the squared magnitude of the normalized field autocorrelation function $\Gamma_A(\Delta x, \Delta y)$ of the speckle pattern. $\Gamma_A(\Delta x, \Delta y)$ is given by

$$\Gamma_A(\Delta x, \Delta y) = \overline{A(x_1, y_1) A^*(x_2, y_2)}, \quad (2.9)$$

i.e. the correlation between the amplitudes at the positions (x_1, y_1) and (x_2, y_2) in the speckle field, where $\Delta x = x_1 - x_2$ and $\Delta y = y_1 - y_2$. In the following, the resulting speckle spot size for nonimaging and imaging detection setups will be summarized.

It is common in literature to distinguish between *objective* and *subjective* speckle. A setup with which objective speckle can be measured is sketched in Fig. 2.3. A rough target is illuminated with a laser beam. The speckle field is produced by the scattering object and propagates in free space. If the screen is for example a bare CCD chip, objective speckle can be measured. The term *objective* indicates that no imaging system is used which might somehow influence the speckle pattern. The illumination beam's diameter, i.e., its spot size on the illuminated object can be seen as the limiting aperture in this setup. For illumination of an object with a uniformly bright circular spot of wavelength λ and diameter d_{spot} , the diameter of a single speckle spot $d_{speckle}$ in a distance d from the object is approximately given by [5]

$$d_{speckle} \approx 1.22 \frac{\lambda d}{d_{spot}}. \quad (2.10)$$

It can be seen that the speckle spot size on the detector can be increased either by increasing the distance between object and detector, by increasing the wavelength or by decreasing the illumination spot size on the object. The average length of a single speckle $l_{speckle}$ in the speckle pattern is approximately given by [34]

$$l_{speckle} \approx 8 \left(\frac{\lambda d}{d_{spot}} \right)^2. \quad (2.11)$$

The expressions for the speckle size and the speckle length are valid for $d \gg d_{spot}$. The ratio length/width increases linearly with increasing distance from the scattering object. It can be seen that a speckle progressively elongates with increasing distance from the illuminated surface. Close to the surface they are more bubble shaped, with increasing distance they get more cigar shaped like.

A setup where the object is imaged onto a detector or screen is shown in Fig. 2.4. In an imaging setup, subjective speckles are measured. The speckle pattern is generated by the scattering surface and forms in the image plane of the imaging system. Following [5] again, the resulting diameter of a single speckle spot $d_{speckle}$ in the image is then given by

$$d_{speckle} \approx 0.61 \frac{\lambda}{N.A.}, \quad (2.12)$$

where $N.A.$ is the numerical aperture of the imaging system. This result can be deduced by using an approximation by Zernike [35] in which the aperture of the imaging system itself is considered as effective scattering spot [9]. It can be seen that in an imaging setup the size of a single speckle spot on the detector can be easily increased by placing a pupil in front of the imaging optics. By decreasing the pupil opening, the numerical aperture of the imaging system can be decreased.

2.2.2 Speckle Measurement

Measurements of speckle patterns have to be performed carefully for several reasons. Any movement in the measurement setup has to be suppressed. The camera taking

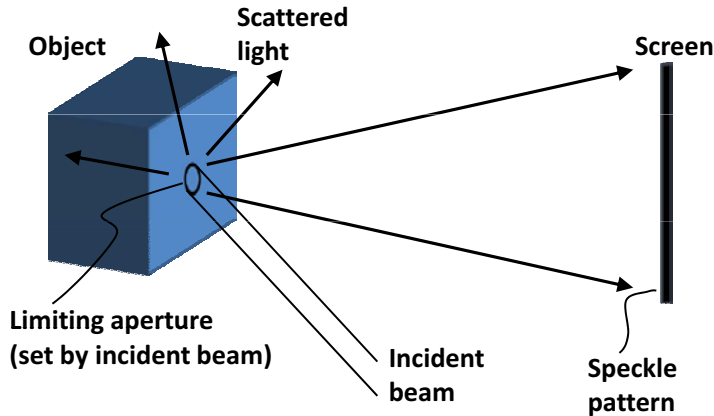


Figure 2.3: Schematic of a setup with which an objective speckle pattern is measured. The limiting aperture is the illumination beam diameter.

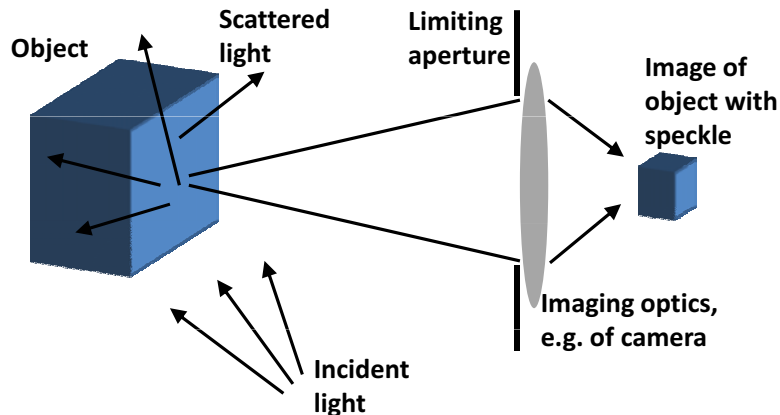


Figure 2.4: Schematic of a setup with which a subjective speckle pattern is measured. The limiting aperture is given by the imaging system.

the speckle picture has a certain integration time. If an illuminated screen or the camera moves or vibrates during the integration time, the speckle-image on the CCD chip changes. The changing pattern is temporally integrated and averaged on the CCD chip. This can especially lead to an incorrect resulting speckle contrast.

Furthermore, the size of the single speckle spots of the speckle pattern has to be sufficiently large in order to avoid any averaging in the CCD pixels. One spot of the speckle pattern has to be larger than approximately ten CCD pixels for proper contrast measurement. It was shown in the previous section how the speckle spot size can be influenced in an imaging and in a nonimaging measurement setup. As mentioned above, a fully developed speckle pattern of contrast $C = 1$ has a negative exponential intensity distribution. Therefore, low intensity values contribute with highest probability to a speckle pattern. If a speckle image is captured, camera noise and ambient light should therefore be reduced as much as possible.

2.3 Applications of Speckles

This section summarizes experimental techniques in which speckles find useful application or the working principle of which is fundamentally based on the speckle phenomenon.

Following [17], a very early application of speckles was described by Raman in 1959 who showed Brownian movement of globules via speckle illumination [36].

As the spatial power spectrum of a speckle pattern is known ([12],[37]) a speckle pattern can be used to determine the modulation transfer function (MTF) of an optical system [38].

In the field of experimental mechanics it was found in the late 1960s that laser speckle photography can be used to investigate rough objects. In speckle photography, rough objects are illuminated with coherent light and two statistically independent speckle patterns (which add on an intensity basis) are superimposed. The first speckle pattern is captured from the object in an initial state and the second one from the same object after it was displaced in some form. The two speckle patterns are then somehow correlated depending on the displacement. The resulting superposition pattern is then analyzed to gain information about the nature of the displacement. A relatively simple example is a small lateral displacement of the illuminated object between the two exposures. This will result in a visible fringe pattern in the Fourier transform of the superposition pattern. The period of the fringe pattern is determined by the distance the object has been translated [9]. Early work in the field of speckle photography can be found in [39], [40] and [41] which used speckle photography to investigate target displacements and target vibrations. [42] used speckle photography to determine the roughness of illuminated surfaces, and the lateral correlation length of rough surfaces is investigated in [43].

The use of speckle interferometry techniques in experimental mechanics also evolved in the late 1960s. Speckle interferometry is based on the superposition of speckle patterns on amplitude basis. Early work on speckle interferometry are [44] in which vibrations are investigated and [45] which deals with displacements. Nowadays laser speckle interferometry is a typically fully electronic technique, i.e. with electronic detection and analysis of speckle patterns, and is therefore often called Electronic Speckle Pattern Interferometry (ESPI). With modern computers also real-time ESPI, e.g. for the detection of stress and strain in objects under investigation can be realized. Further information on speckle interferometry can be found in [46] and [7]. A detailed discussion of many of the mentioned applications and others can be found in [6].

Also well known techniques from other scientific fields like Laser Speckle Imaging (LSI) or Laser Speckle Contrast Analysis (LASCA) are based on the speckle phenomenon. In these techniques, spatially resolved images of time varying speckle patterns are taken with a certain integration time and speckle contrast values are evaluated in different regions of interest. These techniques are widely used to investigate the dynamics of scattering media or of flow fields [47]-[50]. Regions of high contrast in a captured image correspond to low dynamics or slow movement of the scattering centers, whereas low speckle contrasts reveal regions of highly dynamic scatterers. An example taken from work from Dunn [50] is given in Fig. 2.5. It shows a 5 mm x 4 mm section of the surface of an animal brain which is illuminated with a 780 nm wavelength laser and is imaged

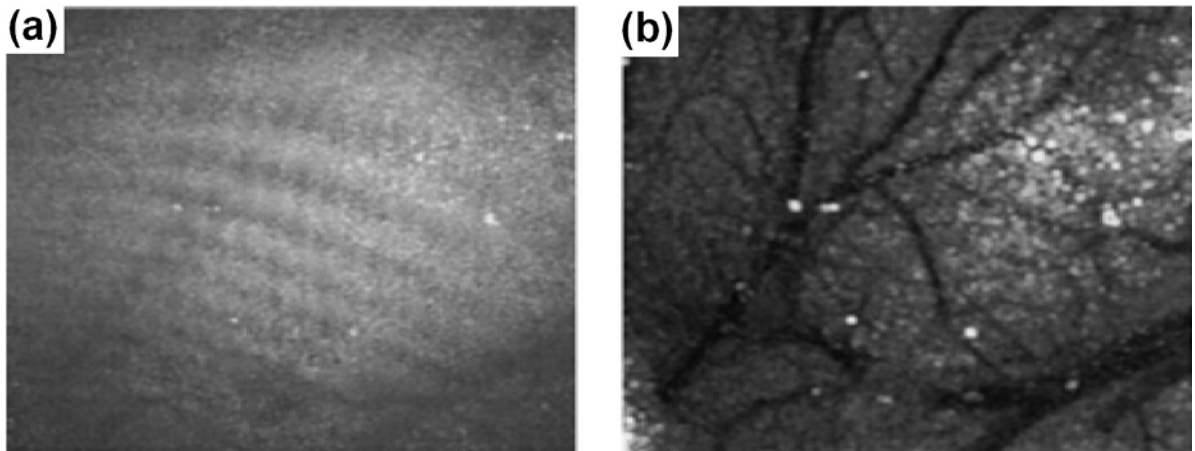


Figure 2.5: (a) raw CCD image of a section of a rat brain (b) the same section. The color in (b) is determined by the speckle contrast in regions of 5x5 pixels of the raw image, taken from [50].

onto a CCD chip. In (a) the raw image is shown. In (b) the same section is presented, however the color is determined by the speckle contrast in regions of 5x5 pixels of the raw image. Low speckle contrast values (dark areas in (b)) correspond to increased speckle averaging and identify regions of high cerebral blood flow. Comprehensive material on dynamic laser speckle can be found in [10].

Speckle can also be used for ophthalmic testing. Some recognized publications are [51], [52], [53] and [54].

An example of an application based on speckle in the nonoptical wavelength range are x-ray speckles. So called fourth generation x-ray sources can produce fully coherent and pulsed x-ray beams [13]. X-ray charge scattering and x-ray magnetic scattering on materials can be used to produce x-ray speckle patterns to investigate the structure of the material samples with atomic resolution [13]. [55] used x-ray speckles to characterize the roughness of semiconductor materials for example.

2.4 Problems Associated With Speckles

The high contrast and the signal to noise ratio of 1 in a typical speckle pattern indicates that speckle can make the extraction of spatial information from images disturbed with speckle difficult. This section summarizes numerous applications and experimental techniques which suffer from speckle.

Texereau observed in 1963 [56] that telescope images of distant stars can exhibit a speckle structure which reduces resolution. However, in [57] diffraction limited imaging of distant double stars is first described which was achieved by Fourier analyzing the captured speckled images.

Standard holography uses coherent light and therefore speckles are typically present in a holographic image and disturb it. Several methods for speckle reduction in holography can be found in literature, for example [58], [59] or [60].

As it is the case in holography, also the working principle of optical coherence tomog-

raphy (OCT) is based on the coherence of the light source. Also in OCT-applications speckles emerge and can severely reduce the image quality. A detailed coverage of the OCT technique and attempts for speckle reduction in OCT can be found in [61].

It is not surprising that speckles also appear in laser microscopy where lasers are used to illuminate investigated samples. Several manuscripts on speckle reduction in laser microscopy can be found in literature, for example [62] and [63].

Also in laser Doppler vibrometry applications speckles typically appear and act as noise. [64] deals with this problem and shows a method to reduce the speckle-caused noise floor.

If coherent light is coupled into a multimode optical fiber, light from different fiber modes propagates with different phase velocities. At the exit surface of the fiber, strong interference effects can be seen if the source is sufficiently coherent and the phase variety of the different modes is large enough. This quasi-random interference pattern was first described in [65]. The topic is covered in detail in [9]. As this modal interference is disturbing in many applications, several attempts for speckle reduction in multimode fibers were proposed, see for example [66] or [67].

An example of speckle emergence with electromagnetic waves in the nonoptical wavelength range is speckles in radar applications which typically use electromagnetic radiation in the GHz frequency range. Early work on radar speckles can be found in [12], a method for speckle reduction in radar applications for example in [68].

[69] and [70] show that the presence of speckles results in an uncertainty limit in distance sensing techniques which use laser triangulation. A small speckle contrast is therefore also in these applications desirable.

Very similar is the unwanted appearance of speckles in bar code scanning systems, which is for example treated in [71].

In medical ultrasound applications speckles also degrade the image quality whereas the radiation is not electromagnetic but sonic with a frequency in the MHz range. Early work on speckle reduction in ultrasound can be found in [14].

Speckle appearance is also a problem in current projection lithography. [72] and [73] discuss the limiting influence of speckle on the line width roughness of the projected structures and the dose control.

Besides all these applications where speckles are disturbing, they are also a major problem in laser projection applications. In addition to the strong degradation in image quality, [74] and [75] report of fatigue an observer experiences when viewing an image full of speckles over longer periods of time. In Section 3.10 several aspects of laser speckle in projection applications will be discussed. As already mentioned, the objective of this thesis is the investigation of different methods for speckle reduction in laser projection applications.

2.5 Chapter Summary

In this chapter it was shown that speckle is a quasi-random interference pattern which has typically a high contrast and therefore large intensity fluctuations. Early speckle research reaches back to the 19th century, however, speckle only became prominent with the invention of the laser in the early 1960s. It was shown that speckle can be useful in several applications (like testing of optical systems, experimental mechanics,

flow field investigation, ...). However, in many applications speckles act as noise and degrade image quality (like OCT, medical ultrasound, radar, laser projection, ...). In the following chapter, it will be shown that the use of lasers in projection applications has long been envisaged because projectors with high color saturation, highly efficient optical engines and long lifetime of the light source can be realized. Also the speckle phenomenon in laser projection application will be discussed in more detail.

Chapter 3

Lasers in Projection Applications

This chapter covers several aspects of the use of lasers in projection applications. Today's projection systems market is segmented in Section 3.1. Typical projection system architectures are introduced in Section 3.2 and the actually developing laser projection systems market is summarized in Section 3.3. In Section 3.4 - 3.10, several advantages which lasers can provide in projection applications are discussed, and aspects which have to be considered are introduced. In Section 3.11, the chapter is summarized.

3.1 Segmentation of the Projection Systems Market

The projection systems market can be reasonably divided into five segments. The segment of pico-projectors is currently developing. Pico-projectors have very small volumes. If the integration into hand held devices such as mobile phones or personal digital assistants (PDAs) is targeted, the volume has to be smaller than circa 10 ccm. If the projector is a small companion module for a hand held device, its volume has to be smaller than about 300 ccm. Pico-projectors typically are aimed to be battery powered. Second, there are so called pocket-projectors. These are still tiny projectors with a volume of circa 300-500 ccm which still fit into a pocket. Battery powered and wall plug systems are possible. The third segment comprises ultra portable projectors. A typical application is the projection of a presentation for a small audience. They are wall plugged and have volumes larger than about 800 ccm. The fourth segment covers consumer front and rear projection systems. Typical fields of applications are in rear projection TVs, home cinema and the like. The last segment are large projectors with a need for high lumen output. These are business projectors for large audiences, projectors for cinemas, projectors for flight simulators or other large venue applications.

3.2 Typical Architectures of Projection Systems

It is common to distinguish between *full frame*, *line scanning* and *raster scanning* projection systems. In the following, a short description of the architectures and functioning of these three types will be given. A more comprehensive coverage can be found in [76] or [77].

In a typical full frame projection system, a small 2D imager which is homogeneously illuminated is used to form the image. This microimage is then magnified and projected onto a screen. The imager can be a transmissive liquid crystal (LC) panel, where in this case polarized illumination of the imager is necessary. For a dark pixel in the image, the corresponding pixel in the LC microdisplay is switched to an absorbing state, for a bright pixel in the image the LC pixel is switched to a transmissive state. Besides such a transmissive light valve, also reflective implementations exist. These are known as Liquid Crystal on Silicon (LCoS) imagers. By transmitting more or less light through a LC-pixel, the pixel brightness in the image can be selected. A reflective imager can achieve higher fill factors, i.e. the part of the imager's surface which is really reflecting as a transmissive light valve. This is because the electrical contacting can be done from the pixel backplane.

Another implementation of a 2D reflective imager is a 2D array of tiltable micromirrors, with one micromirror for each pixel in the image. For a bright pixel in the image, the mirror is electrically switched into a position, at which the incident light is reflected to the projection optics and reaches the screen. If the pixel has to be dark, the mirror is tilted into a position in which it reflects the light to an absorber. By directing more or less light of a pixel to the screen during the frame time, the brightness of the pixel can be selected. This micromirror array technique is used by Texas Instruments [78] under the trademark Digital Micromirror Device (DMD). An image of a DMD-chip is shown in Fig. 3.1. A demonstration of the working principle can be found in [79].

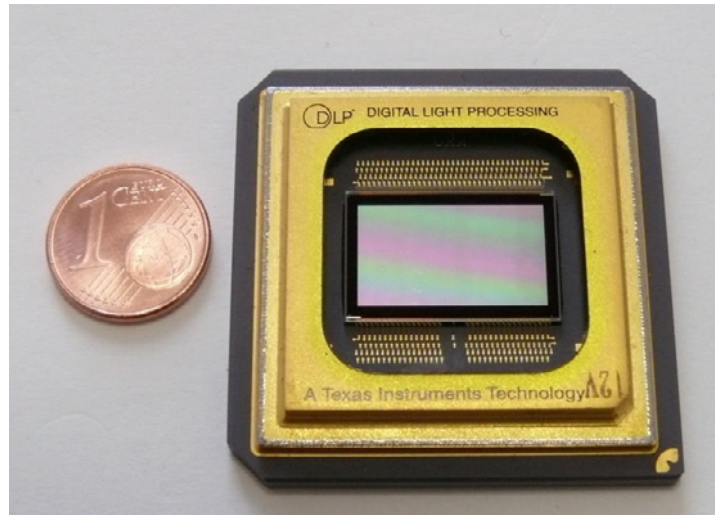


Figure 3.1: Image of a typical DMD micromirror chip.

Different system architectures using 2D imagers can be realized. So called three-panel or three-imager systems use an imager for each primary color. Typically the white light from the illumination source is separated into the primary colors red, green and blue via dichroic mirrors or color filters. All three imagers are illuminated at the same time, an image for each primary color is created, the three images are recombined and projected onto the screen. Single-panel systems typically use a spinning color filter wheel to produce the primary colors sequentially at a high rate. The images for the three primary colors are therefore created with only one imager and are projected onto the

screen time-sequentially. If the color rate is high enough, virtually no color break up is visible for a human observer.

Also small cathode ray tubes (CRT) can be used to create a small 2D image which is then magnified and projected onto a screen. However, CRT projectors nearly vanished from the market in the last years and are therefore not further discussed here. Major drawbacks were their bulkiness and burning-in of static images.

A 2D image on a screen can also be created by using a 1D line imager. Only one line (or column) of the image is produced by the imager which is then scanned across the screen. With the imager changing the line content at a high rate, a 2D image can be created. An implementation of such a 1D line imager is for example the Grating Light Valve (GLV) technology from Silicon Light Machines [80]. There, an individual pixel is formed by several parallel reflective ribbons. By applying a voltage to alternate ribbons they can be moved downwards by approximately a quarter of the illumination wavelength to form a grating structure. If all ribbons are at the same level, the incident light is reflected and does not reach the screen (dark image pixel). If every second ribbon of a pixel is deflected, the incident light is diffracted and reaches the projection optics (bright image pixel). Kodak [81] uses a similar technology named Kodak Grating Electromechanical System (GEMS).

A so called raster scanning display produces one image pixel which is then 2D scanned over the screen to produce an image. It is obvious that raster scanning projection systems can be efficiently realized with scanning laser beams. In full color systems, a laser beam for each primary color is used. The beams are directly modulated in their brightness to form an image on the screen. For the beam deflection two single mirrors can be used, where each mirror deflects the beams in one direction. Also systems using a single small mirror which deflects the beams in two dimensions can be used, an example used by Microvision is shown in Fig. 3.2 [82]. In raster scanning architectures no imager and no projections optics are needed, therefore the system's volume can be very small. This makes raster scanning architectures especially suited for pico-projectors. Furthermore, they provide an infinite depth of focus. This principally allows for the projection at any distance and also on curved surfaces.

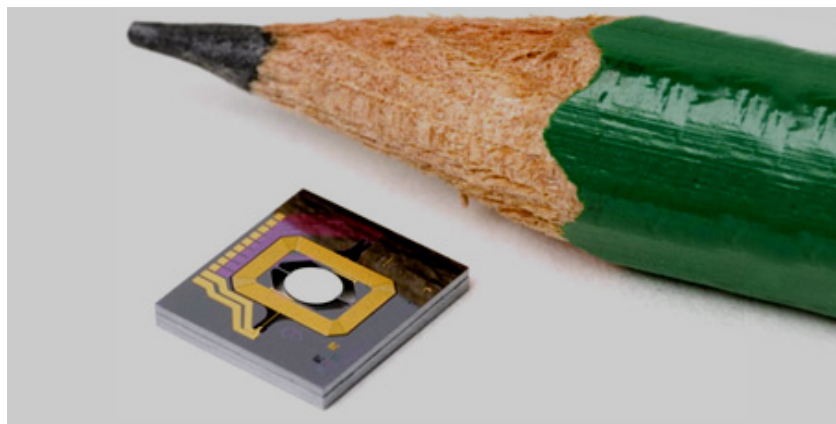


Figure 3.2: 2D scanning mirror used by Microvision, taken from [82].

3.3 Today's Laser Projection Systems Market

The use of lasers in projection applications has been envisioned already since the development of the laser in the early 1960s. A Texas Instruments patent from 1969 [3] related to laser projectors contains a reference to a still earlier company internal report from 1966 [2]. Today, there are numerous companies which are known to be active in the development of laser projection systems. Microvision [82] and the Fraunhofer Institute for Photonic Microsystems [83] have shown prototypes of raster scanning laser pico-projectors. An application scenario for a mobile-phone-embedded pico-projector and a prototype of an accessory pico-projector are shown in Fig. 3.3 and Fig. 3.4 [82].

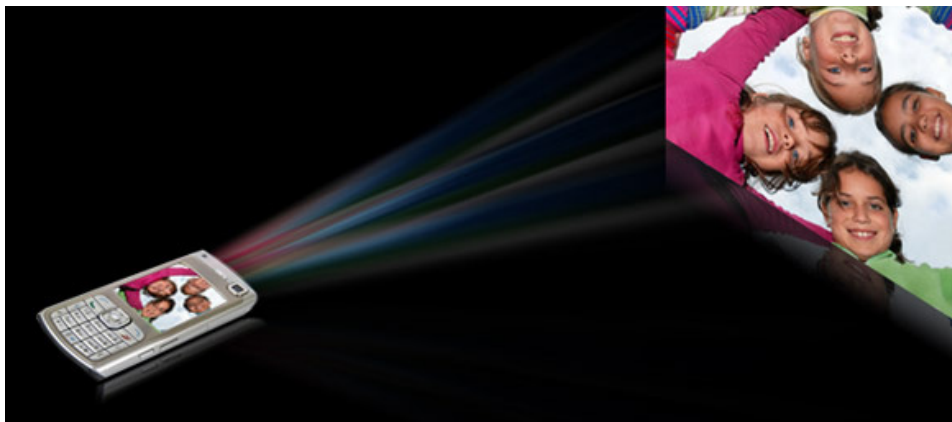


Figure 3.3: Application scenario for a mobile-phone-embedded pico-projector, taken from [82].



Figure 3.4: Prototype of an accessory pico-projector from Microvision, taken from [82].

Kodak [81] has demonstrated a prototype of a digital laser cinema projector. Sony [84] had a large venue laser projection installation at the Expo 2005 in Japan and showed

a prototype of a laser rear projection television. Light Blue Optics [85] demonstrated a prototype of a holographic laser projection system. An LCoS micropanel is used to generate a phase hologram of the image to be projected.

Nevertheless, up till now, only few products are commercially available. Commercially available products are mainly for the professional sector. LDT Laser Display Technology GmbH [86], Evans & Sutherland Computer Corporation [87] and the Corporation for Laser Optics Research [88] sell high end laser projection systems for large venue applications like planetariums and virtual reality environments. The first commercially available laser rear projection TV for the consumer market from Mitsubishi Electric recently went on sale in November 2008 [89].

3.4 Characteristics of Different Light Sources and Their Suitability for Different Applications

Following [90], actually mainly high intensity discharge (HID) lamps are used in lamp based projection systems. HID lamps with a high pressure mercury filling have the largest sales numbers [90]. They have typically 100-350 W. Xenon filled HID lamps provide a better colorimetry than mercury filled lamps. As they are typically higher priced they are normally used in premium products. They are available with more than 5000 W, so they are suitable for large venue and cinema applications. Electrode erosion is the main reason for the limited lifetime of HID lamps. Typical maximal lifetimes are about 8,000 hours (time until the maximal light output drops below 50% of the initial value). Lamp replacement in a consumer product costs about 200-300 US\$. The problem of electrode limited lifetime might be overcome in the future with electrode free lamps [91]. More information on discharge lamps can be found for example in [92].

Typically indicated lifetimes of LEDs are about 20,000 hours until the light output drops to 50% of the initial value. The electrical and optical properties and also the aging of LEDs are very sensitive to temperature [93],[94]. If three different LEDs are used to produce red, green and blue light, the different chips may age at different speeds and there might be a gradual color shift in projected images over time. This has to be considered and corrected. The same issue applies if laser sources are used. Novalux developed the Novalux extended cavity surface emitting laser (NECSEL) [95] which is dedicated to be used in projection systems. On the NECSEL webpage it is stated that the lifetime of a NECSEL source is more than 50,000 hours at 100% light output and that there is no color shift problem. One should be critical about this information, however, this might indicate, that color shift can be managed in practice. It can be seen that lasers and LEDs can have much longer lifetimes as compared to standard lamps. [96] estimates the minimal required lifetimes of the projection system (not the light source) to be about 3,000 hours for pico-projectors, about 5,000 - 10,000 hours for ultra-portable, consumer front projectors and business front projectors, up to 20,000 hours for consumer rear projection systems and even more than 20,000 hours for large professional systems like cinema projectors. Considering the lifetimes of the light sources given above, it can be seen that a replacement of the light source during the lifetime of the projection systems would virtually be no longer necessary when laser or LED sources are used.

The mercury contained in most projection lamps is an environmental issue which can be overcome with the use of lasers or LEDs.

Lasers sources would furthermore be suitable for certain 3D projection techniques because of their narrow bandwidth. The Infitec Technology [97] for example uses passive eyewear with two sets of red, green and blue filters. The left eye filters transmit slightly different wavelengths in the red, green and blue wavelength range as the right eye filters do. Using this, a stereoscopic effect can be created by projecting two images simultaneously, one for the left eye and one for the right eye. The narrow linewidth of typical laser sources can help minimize filter losses to create efficient systems and to improve the color matching of the left and the right eye image.

The demand for the small volume pico- and pocket-projectors practically excludes current lamps from being used as an illumination source. For pico-projectors which are built into handheld devices, lasers might be the only suitable light sources. In companion pico-projectors and pocket-projectors, besides lasers also LEDs might be used. A companion pico-projector with LED illumination was launched by Optoma USA [98]. For ultra portable projectors, lasers, LEDs and standard projection lamps can be suited. For applications with demand for high lumen outputs (business projectors, cinema projectors, ...), lasers and lamps are the preferable light sources. For high lumen output systems, current LEDs are not yet competitive with projection lamps or high power lasers.

The warm-up time of the light source should be as short as possible in consumer projection applications. Following [96], the warm-up time of modern CRT systems is approximately ten seconds. LEDs and xenon lamps have very short warm-up times so that a delay between the switch on of the light source and the image being visible on the screen is related to electronics [96]. Again following [96], modern mercury filled HID lamps have a long warm-up time of about one minute to reach their full brightness. This is still acceptable because there is little color shift during the warm-up of the lamp so that the image is already visible after only about 15 seconds with limited brightness but in nearly correct colors. Especially frequency doubled lasers might need a considerable warm-up time which has to be considered.

3.5 Gamut

All colors which a human observer can detect with his eye are represented as an area in the CIExy chromaticity diagram (French: Commission Internationale de l'Éclairage), which is shown in Fig. 3.5. Monochromatic light is located on the perimeter of the area and is maximally saturated. The higher the bandwidth of a source, the more distant is its location from the perimeter and the lower is its color saturation. The wavelengths corresponding to some positions on the perimeter are indicated in the figure. Comprehensive information on color science can be found for example in [99], on human visual perception for example in [99] or [100].

In typical display or projection systems, three primary colors (red, green and blue) are used. The locations of these colors in the chromaticity diagram can be used as edges to form a triangle. All colors inside the formed *color triangle* can then be displayed with the projection system by mixing the three primary colors. This color triangle is commonly named *color gamut* of the display or projection system. In Fig. 3.6 the color gamut of

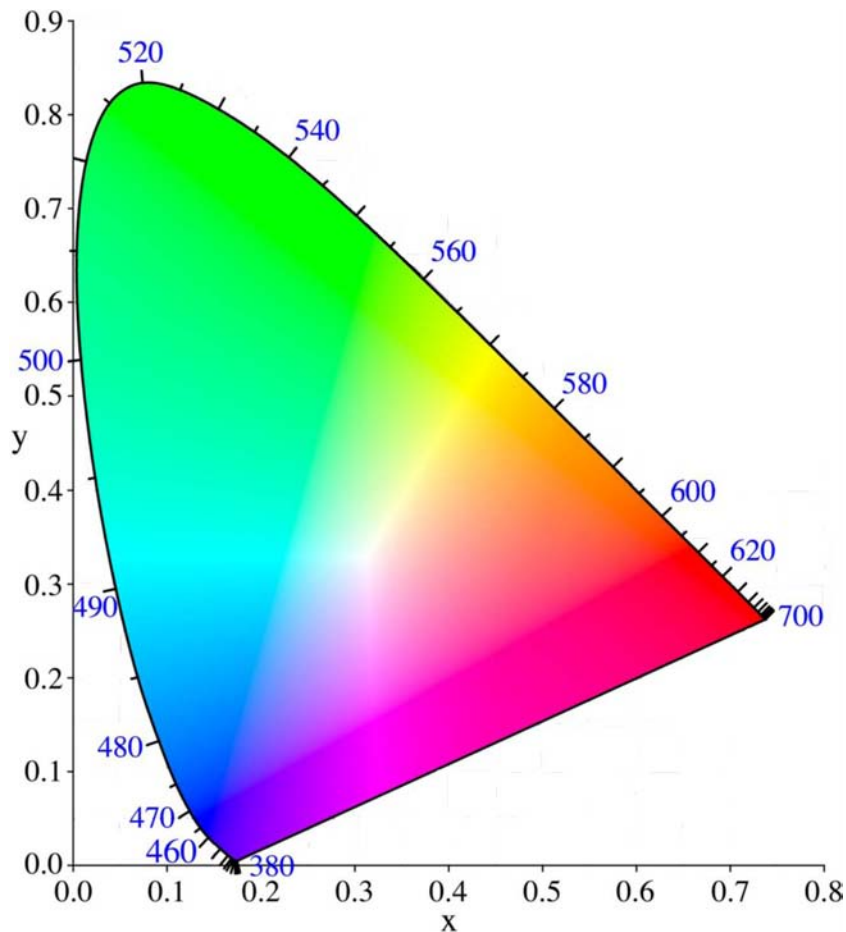


Figure 3.5: CIExy chromaticity diagram. The colored area represents all colors a human observer can see with his eye.

a typical CRT system is shown. It can be seen that the spectral purity of the primary colors is comparably small. The produced colors therefore have a limited saturation and the color triangle is comparably small. Many colors which a human observer would be able to perceive cannot be displayed with such a system. The situation is very similar for standard projection lamps. They produce white light of which red, green and blue light is separated via filters or dichroic mirrors. The characteristics of the filters or mirrors determine the bandwidth and hence the saturation of the primary colors. The higher the saturation which is to be achieved, the more light has to be filtered and the lower is the optical efficiency of the projection system. Figure 3.7 depicts the positions of the emission of several typical LEDs [101]. It can be seen that larger color triangles can be realized as compared to CRT systems. As typical lasers are quasi-monochromatic sources of very narrow bandwidth the achievable color saturation is high. It can be seen in Fig. 3.8 that the color triangle which can be achieved with lasers is large compared to CRT and LED systems and its edges lay close to the perimeter of the gamut.

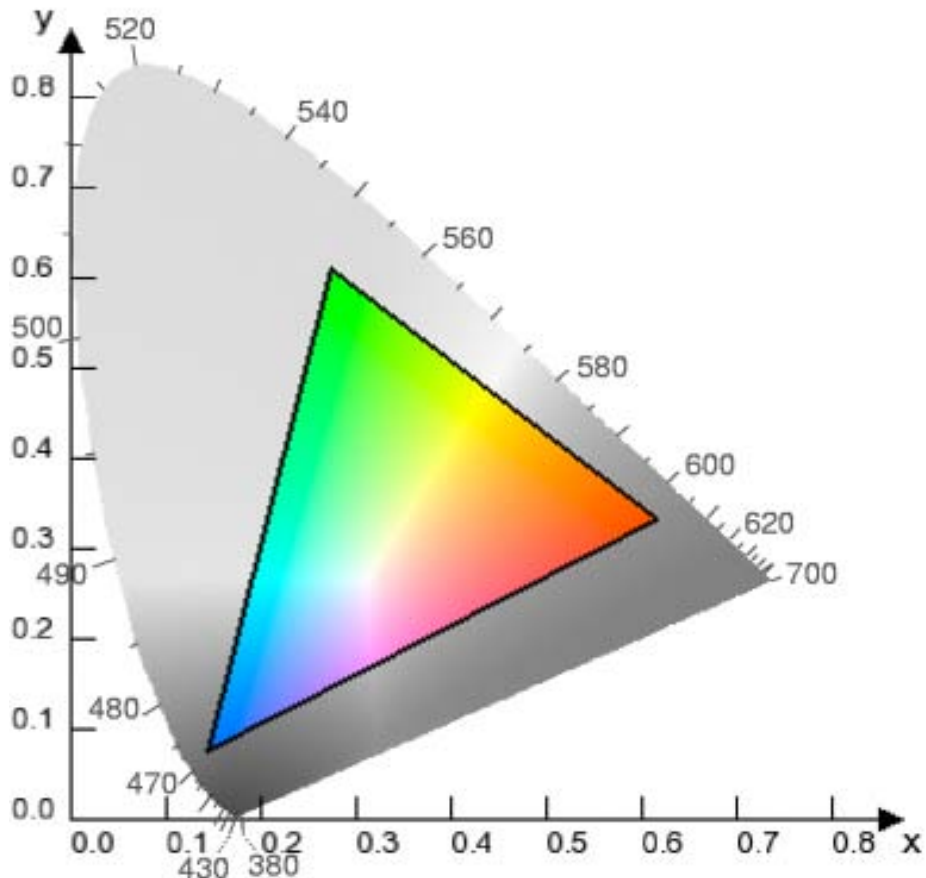


Figure 3.6: Gamut of a typical CRT system

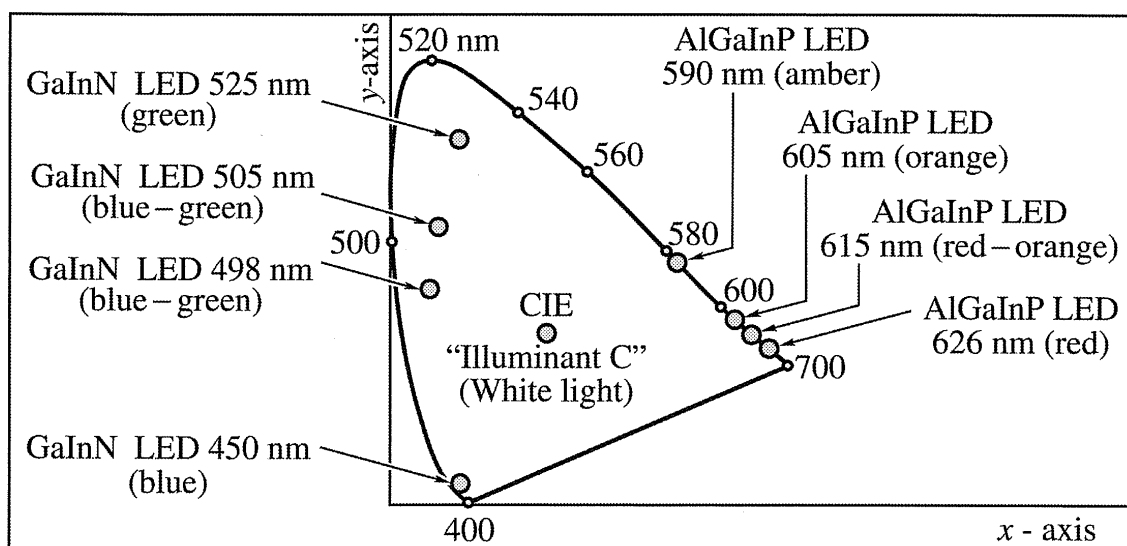


Figure 3.7: Color coordinates of different LEDs, taken from [101].

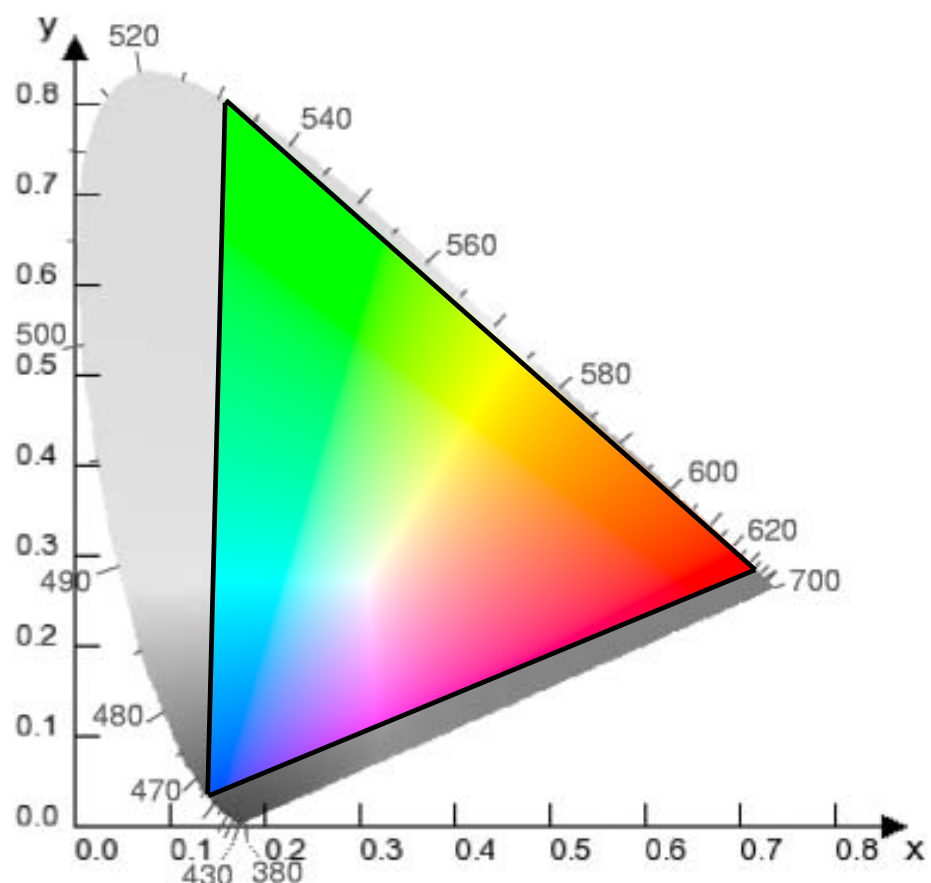


Figure 3.8: Color gamut achievable with a laser projection system.

3.6 Polarization

Projection and display applications using LCoS or LC imagers use the polarization property of light to create an image. The light of standard projection lamps is unpolarized. If simply a polarization filter is used to polarize the light, at least 50% of the light is lost. Different methods for polarization recovery have been proposed (e.g. [102],[103]). One attempt is the use of a polarizing beam splitter. Light with the correct polarization is directly sent to the imager. Light with the wrong polarization direction is sent through a half wave plate to switch its polarization before it is also sent to the imager. Using such techniques, the total light loss can be reduced to approximately 20%. However, their use comes along with the need for additional components which complicate the optical engine and increase costs. Also a standard LED emits unpolarized light. The realization of LEDs which emit at least partly polarized light is a topic of current research and not yet used in projection or display applications. In [104] the output of an LED is enhanced and partially polarized via coupling of the LED's quantum well with surface plasmons on a metal grating on top. The authors in [105] use stretch alignment of an electroluminescent polymer film to produce an intrinsically polarized light emitter. In so called spin-LEDs, polarized light emission can result from the radiative recombination of spin-polarized carriers which are injected into the LED [106]. However, high magnetic fields and typically low temperatures of a few Kelvin are required for efficient production of polarized light. A standard laser already emits polarized light. Therefore, no additional components for polarization or polarization recovery are needed.

3.7 Étendue and Lightguiding

The high étendue of LEDs and projection lamps makes coupling their light into small optics and microdisplays difficult [107]. Typical lasers emit highly directional light with small étendue. Therefore, lightguiding is much easier and smaller optical engines using optics with higher $f/\#$ could be used. This can provide cost and space reduction. Figure 3.9 compares the sizes of the projection lenses used by Mitsubishi in (a) a projection systems with a standard UHP (Ultra High Performance) lamp and (b) laser sources [108]. The diameter of the lens for the laser system could be reduced to 40% compared to the conventional lens.

As mentioned above, additional components (filters or dichroic mirrors) are required to separate red, green and blue light from the white light emitted by a standard projection lamp. Therewith, a large amount of light is produced, which is filtered and therefore unused. With laser and LED light sources, the primary colors can be directly created and only light which is really used for the intended projection is produced. Thus, using lasers and LEDs, projection systems can be created which no longer need color filters or dichroic mirrors [109]. This can reduce cost and allow for much higher color field rates and can therefore virtually eliminate color breakup in color sequential systems [90]. The potential for complexity reduction using laser sources in projection systems can be nicely seen in the schematic Figs. 3.10 - 3.13 which are taken from [110]. The optical engine of a standard projection system using a color wheel and a reflective micromirror imager is depicted in Fig. 3.10. Fig. 3.11 shows a schematic of a corresponding system using



Figure 3.9: Comparison of the sizes of recent projection lenses used by Mitsubishi in systems with (a) standard UHP lamps and (b) lasers, taken from [108].

NECSEL illumination. It can be seen that several components for beam collimation and the color filter wheel are no longer needed. In Fig. 3.12 a schematic of a standard projection system using a lamp, three dichroic mirrors and three transmissive 2D imagers is shown. Figure 3.13 depicts an analog system where the lamp is replaced by a NECSEL module. It can be seen that again several components for beam collimation and the dichroic mirrors are no longer needed.

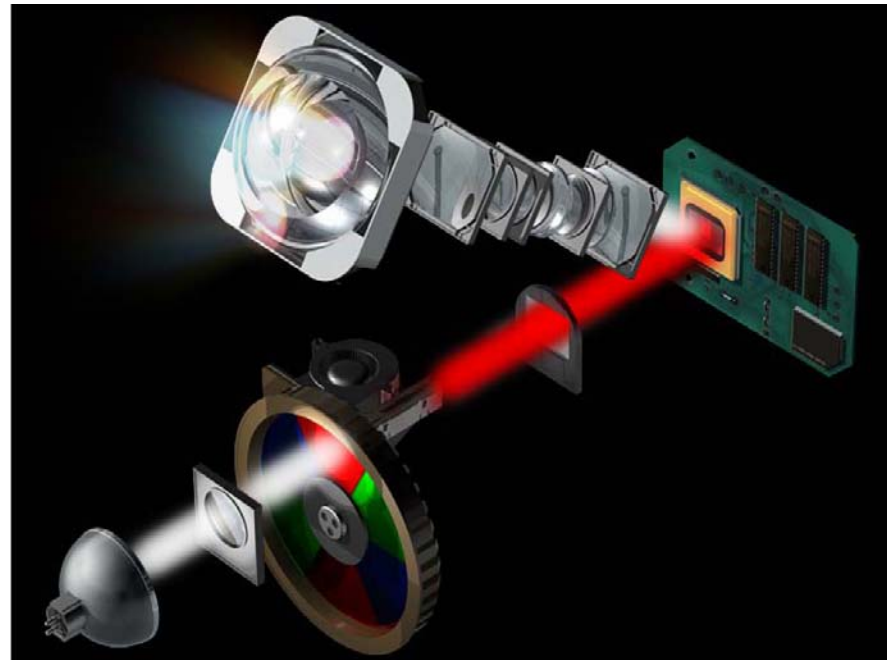


Figure 3.10: Schematic of a color sequential lamp projection system using a color filter wheel, taken from [110].

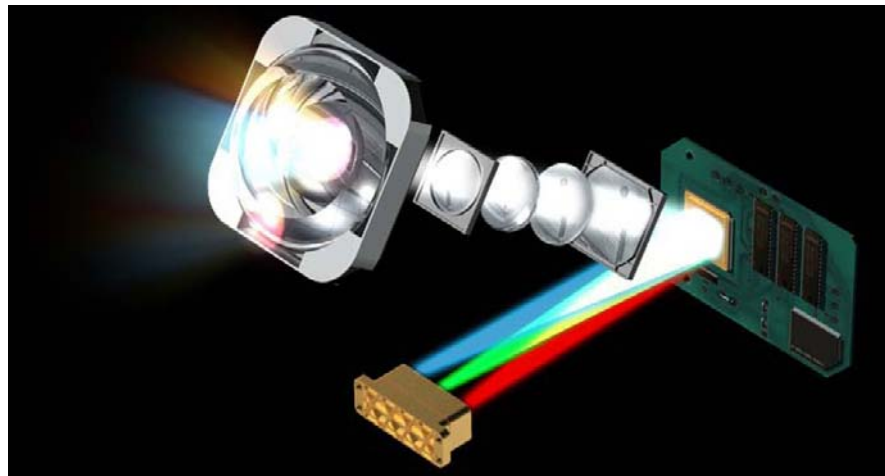


Figure 3.11: Schematic of NECSEL based color sequential projection system, taken from [110].

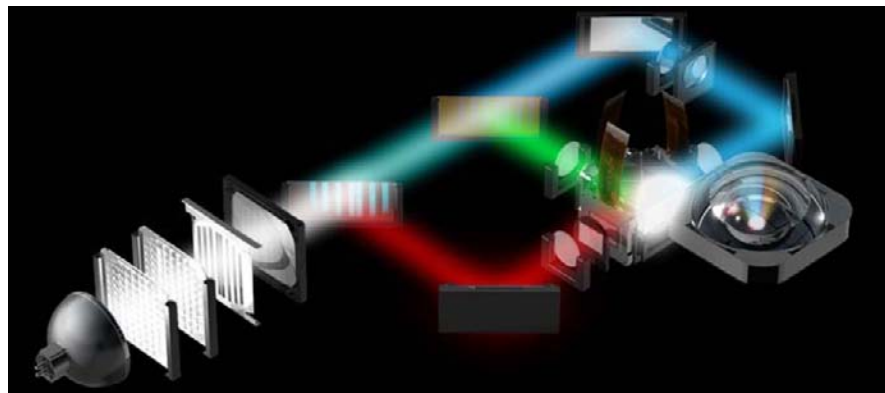


Figure 3.12: Schematic of a three imager projection system using a lamp, taken from [110].

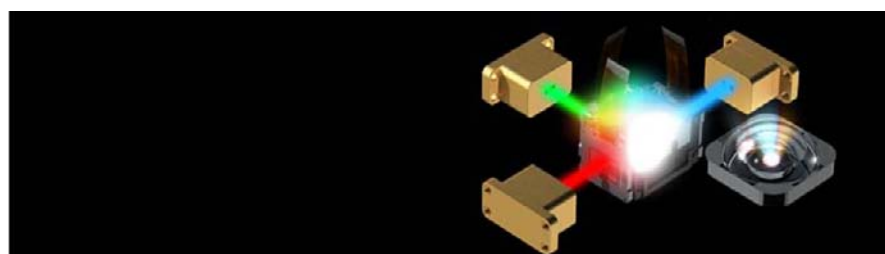


Figure 3.13: Schematic of a three imager system using NECSEL illumination of the imagers, taken from [110].

3.8 Laser Safety

Lasers are typically classified into the classes 1, 1M, 2, 2M, 3R, 3B and 4 with increasing potential hazard. Comprehensive information on laser safety and laser classes can be found in [111]. Laser safety in projection applications has to be considered. In a pico-projector or pocket-projector application, the user will be able to look directly into the projection lens. This sets limits to the maximum output power. It can be expected that pico- and pocket-projectors must not exceed laser class 2 or 2M (eyesafe up to 0.25 seconds direct exposure). This is the laser class of typical commercially available laser pointers. The situation differs for a rear projection application. The lasers themselves might be of class 4 (very dangerous for eye and skin). However, if the laser set is properly sealed in the projection systems chassis, no laser radiation is directly accessible. So, the product can be laser class 1 without any necessary safety precautions as long as the chassis is not opened. This is the situation with the recent Mitsubishi laser rear projection TV [112]. For high power front projection systems, laser safety will be a major issue. If scanning beam architectures are used, the beam scanning mechanics has to be failsafe or the laser has to be switched off if the scanner fails. A product for the consumer market might have a maximum laser class of 2M maybe 3R. If the product would be classified a class 3B or 4 product, the setup of warning signs and a laser safety officer would be required. This might be feasible in dedicated applications such as flight simulators or the like, but not in standard consumer projection applications. Further considerations on laser safety in laser projection applications can be found in [96].

3.9 Laser Price

The price of lasers which are suitable for projection application is a major issue when considering consumer products. The longer lifetime and potentially cheaper optical engine cannot yet compensate the higher source price of lasers as compared to standard lamps [96]. It is estimated in [96] that, based on laser prices in 2007, lasers will not be competitive with lamp technology in any main stream application before 2012 even when high price reductions are considered. However, with technical and manufacturing breakthroughs this date might be reached earlier. Furthermore, for prestige and lifestyle applications, price might not be that critical. Moreover, for certain applications (e.g. embedded pico-projectors) there is simply no alternative to laser sources.

3.10 Laser Speckle and Speckle Disturbance Limit

A major drawback when using lasers in projection applications compared to other light sources is the emergence of speckles. They are typically present in any application producing a real image. In head-up displays for example, the image is reflected into a car's windshield and is virtual. The windshield typically is not rough enough to produce considerable speckle. As already mentioned, a standard laser produces speckle patterns with a contrast and a signal to noise ratio of 1. This results in a strong degradation of the image quality.

The contrast sensitivity of the human visual system has been extensively investigated in the past. Mostly images of printed sinusoidally modulated line patterns of different spatial and temporal frequencies are used to measure the ability to quantify contrast sensitivity. The contrast sensitivity of a human observer is dependent upon several parameters, including the luminance level [113], the color of the observed image [114],[115], the temporal and spatial frequency of the observed patterns [116] and the age of the observer [117]. Following [118], the contrast sensitivity decreases with increasing age of an observer. It can be also influenced with the amount of alcohol in the blood of the observer [119]. For the perception of speckle contrast, the situation is somewhat different as a speckle pattern is not an image of a sinusoidally modulated line pattern. The spatial frequency parameter is connected to the lateral speckle size. Moreover, a speckle pattern moves in the foreground of a static image background when the observer moves his head. Wang states in [120] that under most conditions a human observer will detect speckle down to a contrast of approximately 4%. [74] states a detection limit of speckle with a contrast of only 1%. Self-conducted empirical tests have revealed that an “experienced” human observer still can detect speckle at a contrast value of 4%, but disturbance is very low. Therefore, a contrast value of four percent is referred to as *disturbance limit* in the following. A simulated speckle pattern with a contrast of 4% in comparison to one with a contrast of 100% is given in Fig. 3.14.

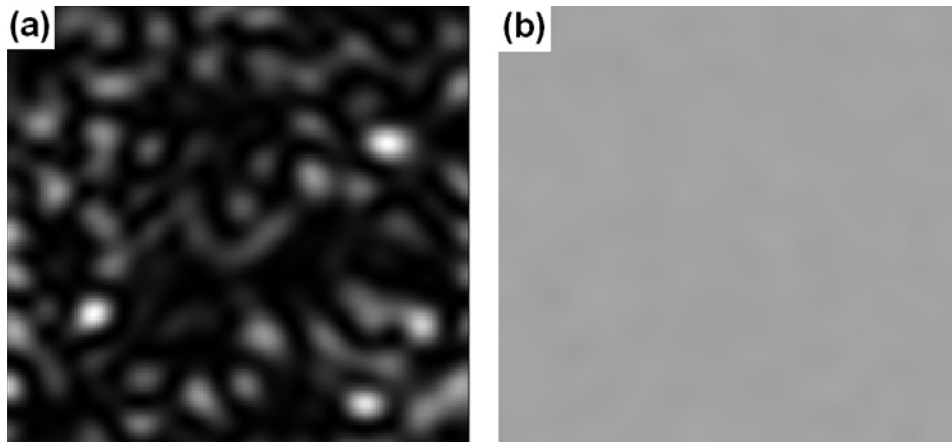


Figure 3.14: Simulated speckle images with (a) $C=100\%$ and (b) $C=4\%$.

Additional to the strong degradation of the image quality, [74] and [75] report of fatigue an observer experiences when viewing speckle disturbed images over longer periods of time.

Depending on the projection application, more or less speckle disturbance might be acceptable. In a low cost application where e.g. a small pico-projector in a mobile phone produces a monochromatic image, some speckle contrast might be acceptable. In professional projection applications or in cinema, speckle disturbance will not be tolerable and speckles will have to be nearly eliminated.

3.11 Chapter Summary

It was shown in this chapter that laser sources can provide numerous advantages in projection applications compared to projection lamps and even LEDs. The main advantages are a large color gamut, emission of polarized light, a long lifetime and their small étendue. However, issues like laser safety and especially the emergence of laser speckle have to be considered. Many companies have activities in the field of laser projection. As in most applications large speckle disturbance will not be acceptable, speckle reduction is a major issue. A general introduction into methods for speckle reduction will be given in the following chapter.

Chapter 4

Methods for Speckle Reduction

In this chapter, several methods to achieve speckle reduction are introduced. The main focus of this work is on speckle reduction in projection applications. The practical applicability and effectiveness of the different methods in different projection system architectures are discussed. Image processing techniques for speckle reduction are not considered in this thesis. An example would be the low pass filtering of a speckled image. These “offline” methods cannot be practically used to reduce speckle for an observer in projection and display applications.

As indicated in Chapter 2, the resulting speckle contrast decreases following Eq. (2.6) if statistically independent, fully developed and mutually uncorrelated speckle patterns are superimposed. Many methods to achieve speckle reduction are based on the principle of superimposing partly decorrelated or fully uncorrelated, statistically independent speckle patterns. In the following, different methods for speckle reduction are therefore classified according to whether the statistically independent speckle patterns are created instantaneously or time-sequentially and according to how these speckle patterns are mutually decorrelated. This classification is depicted in Fig. 4.1.

The chapter is organized as follows: In Section 4.1, wavelength decorrelation will be discussed. Section 4.2 deals with angular decorrelation and in Section 4.3, spatial decorrelation will be treated. In Section 4.4 different scrambling methods will be presented and discussed and combinations of methods for speckle reduction will be treated in Section 4.5. The chapter is summarized in Section 4.6 and the following chapters are motivated.

The following discussion focuses on the illumination of a rough surface which is observed from the illumination side (backscattering geometry = front projection geometry). Other geometries can be similarly treated. If a rough surface is illuminated with coherent light, the intensity distribution in the resulting speckle pattern is determined by surface characteristics, the illumination wavelength, the illumination angle, and the observation angle. If one or more of these parameters is changed also the intensity distribution in the speckle pattern will change. The intensity distribution after the change will be more or less decorrelated from the distribution before the change. If the parameter variation is done during the integration time of the observer, the changing speckle pattern will be

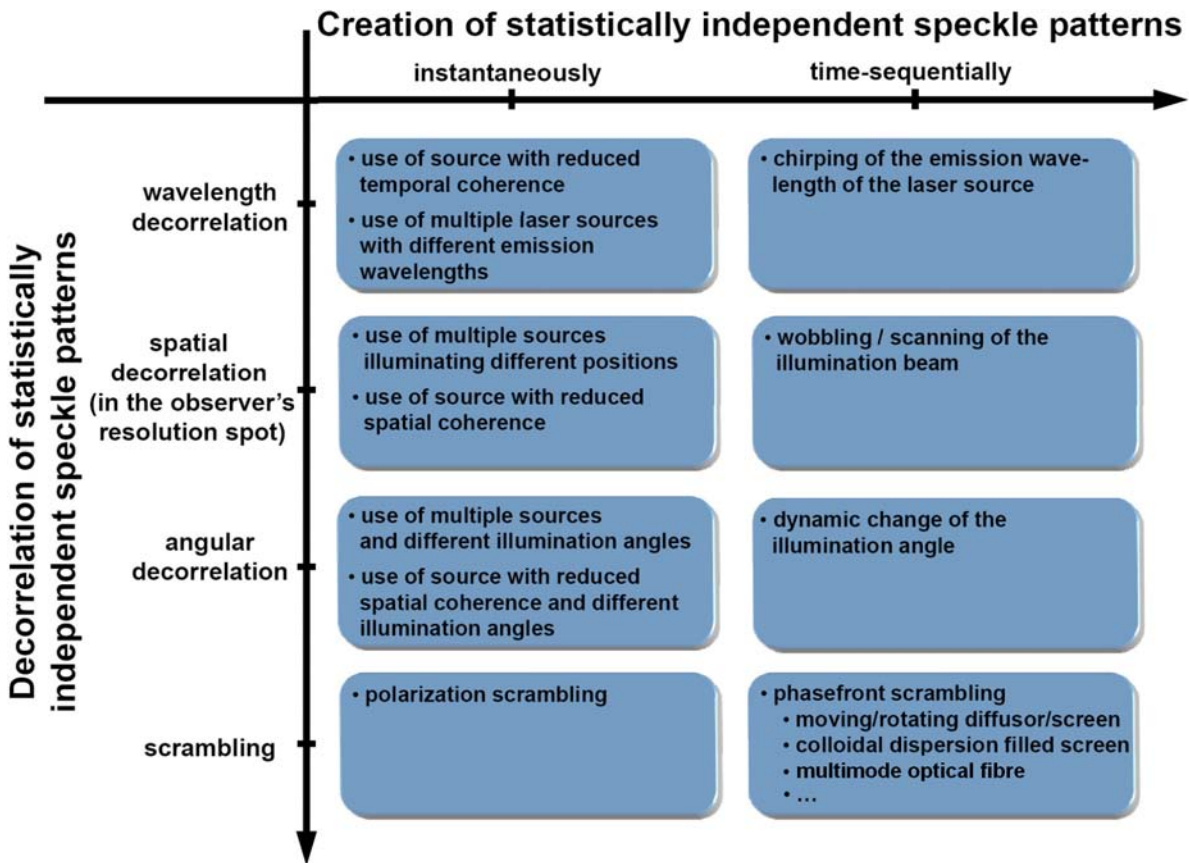


Figure 4.1: Classification of methods for speckle reduction according to whether the statistically independent speckle patterns are created instantaneously or time-sequentially and according to how these speckle patterns are mutually decorrelated.

temporally integrated and the observer may perceive a reduced speckle contrast.

In the following, the scattering surface lays in the xy -plane and the z -direction is the direction normal to the scattering surface. The mean wavevector of the incident light is \vec{k}_i . Its length is given by $2\pi/\lambda$, where λ is the illumination wavelength. The wavevector in the observation direction is named \vec{k}_o . The illumination situation is sketched in Fig. 4.2.

The scattering vector \vec{q} of the scattering process is then given by $\vec{q} = \vec{k}_o - \vec{k}_i$. q_z is the normal component of the scattering vector (normal to the surface) and \vec{q}_t is its transverse component (transverse to the surface). If two speckle patterns are created via illumination of the surface from different angles and/or via illumination with different wavelengths and/or via observation from different angles, the scattering vectors \vec{q}_1 and \vec{q}_2 and the intensity distributions will differ of the two speckle patterns will differ. Now the interest does not lay on the field autocorrelation function $\Gamma_A(\Delta x, \Delta y)$ in one speckle field as it was the case in Chapter 2 when the size of a single speckle spot was determined. Now, the field crosscorrelation of two different speckle fields A_1 and A_2 has to be determined which is given by $\Gamma_A(x_1, y_1; x_2, y_2) = \overline{A_1(x_1, y_1)A_2^*(x_2, y_2)}$. It is deduced in [9] that the normalized field crosscorrelation $\mu_A(\vec{q}_1, \vec{q}_2)$ of two speckle fields for a given

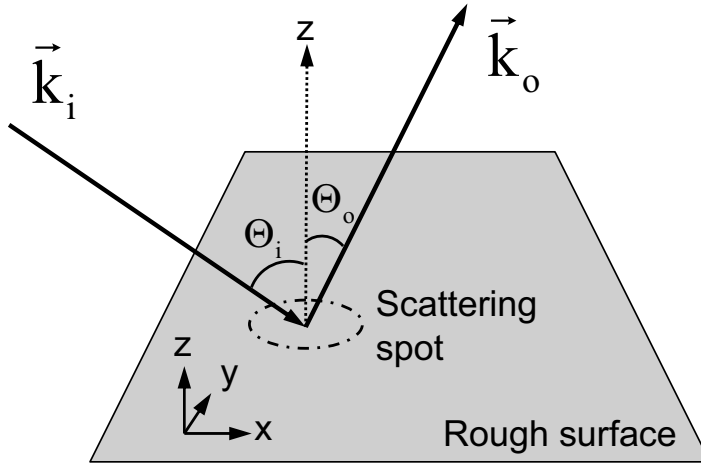


Figure 4.2: Wavevectors for the illumination of a rough surface and observation in reflection.

illuminated surface can be expressed as

$$\mu_A(\vec{q}_1, \vec{q}_2) = M_l(\Delta q_z) \Psi(\Delta \vec{q}_t), \quad (4.1)$$

where \vec{q}_1 and \vec{q}_2 are the scattering vectors of the two speckle fields. The normalization is introduced by dividing the field crosscorrelation function by its value for $\vec{q}_1 = \vec{q}_2$.

In Eq. (4.1), $\Delta \vec{q}_t$ is the component of the scattering vector difference $\vec{q}_1 - \vec{q}_2$ which is transverse to the scattering surface. Δq_z is the magnitude of the component of $\vec{q}_1 - \vec{q}_2$ which is normal to the scattering surface. $M_l(\Delta q_z)$ in Eq. (4.1) is the characteristic function of the surface height fluctuations l . $M_l(\Delta q_z)$ is defined as

$$M_l(\Delta q_z) = E[e^{il\Delta q_z}], \quad (4.2)$$

where $E[\cdot]$ denotes “expected value”. Furthermore, $\Psi(\Delta \vec{q}_t)$ in Eq. (4.1) is given by

$$\Psi(\Delta \vec{q}_t) = \frac{\int_{-\infty}^{+\infty} \int_{-\infty}^{+\infty} |S(x, y)|^2 \exp(-i\Delta \vec{q}_t \cdot \vec{r}) dx dy}{\int_{-\infty}^{+\infty} \int_{-\infty}^{+\infty} |S(x, y)|^2 dx dy}, \quad (4.3)$$

that is a normalized Fourier transform of the intensity distribution across the scattering spot $|S(x, y)|^2$.

If the assumption of sufficient roughness and therefore circular complex Gaussian statistics holds and polarization effects, specular reflections and shadowing are neglected, the normalized *intensity* crosscorrelation of the two speckle patterns is given by $|\mu_A|^2$.

Goodman further shows in [9] that the factor $M_l(\Delta q_z)$ in Eq. (4.1) contains differences of the intensity distributions of the two speckle patterns connected to a difference in their internal structure, i.e. distribution and shape of the single speckle spots. On the other hand, the factor $\Psi(\Delta \vec{q}_t)$ in Eq. (4.1) contains differences of the speckle patterns connected to translations, contraction or expansions without a major change of the internal structure. If the surface is for example illuminated with the same wavelength from two slightly different directions, the main difference between the two speckle patterns is

a slight shift with respect to each other without much difference of their internal structures. If the surface is illuminated from a fixed illumination angle with two independent sources with slightly different wavelengths, the speckle pattern formed with the light of the longer wavelength will be somewhat expanded, the one with the shorter wavelength will be somewhat contracted. As mentioned above, there will be also a change of the internal structure which is dependent on the surface roughness and the wavelength separation.

In the following Section 4.1, fixed angles of incidence and observation but different contributing wavelengths are further investigated. In Section 4.2, a fixed illumination wavelength will be assumed and the effects of a change of the illumination angle will be considered.

4.1 Wavelength Decorrelation

In this section, it will be discussed how speckle contrast reduction can be achieved if statistically independent speckle patterns are decorrelated because of the fact that they are produced with light of different wavelengths. The treatment is oriented on [9] where further information can be found. The statistically independent speckle patterns can be created either instantaneously (by illumination with a broadband source or multiple sources which emit at different wavelengths) or time-sequentially (by chirping of the source's emission wavelength). In practical situations the resulting speckle contrast reduction because of wavelength decorrelation is the same for an imaging or a nonimaging observer.

4.1.1 Instantaneous Wavelength Decorrelation with Multiple Illumination Lines or a Broadband Source

If a rough target is illuminated (at the same position under the same angle) with two independent sources of different wavelengths, the two resulting speckle patterns will be somehow decorrelated. It is obvious that two very similar wavelengths will produce two speckle patterns with relatively high correlation and hence small speckle contrast reduction because of their superposition. If the wavelength difference is increased, the resulting speckle patterns will become more and more decorrelated and full decorrelation might be reached.

In the following, two statistically independent sources emitting at the wavelengths λ_1 and λ_2 (mean wavelength $\bar{\lambda}$) and wavelength separation $\Delta\lambda$ are considered. The speckle patterns are created in reflection from a rough surface with normal illumination and observation. It can be easily shown that $\Delta\vec{q}_t$ is then zero and $\Delta q_z = 4\pi(|1/\lambda_1| - |1/\lambda_2|)$. If the surface height values are Gaussian distributed with surface roughness σ_l the resulting intensity correlation $\rho_{1,2}$ of the two speckle patterns is given by [9]

$$\rho_{1,2} = |\mu_A|^2 = \exp(-\sigma_l^2 |\Delta q_z|^2). \quad (4.4)$$

To achieve a normalized intensity correlation coefficient $\rho_{1,2}$ of the two resulting speckle patterns which is lower or equal $1/e^2$ (nearly decorrelated patterns), the sources' wave-

length separation has to be approximately [9]

$$|\Delta\lambda| \geq \frac{\bar{\lambda}^2}{2\sqrt{2}\pi\sigma_l}. \quad (4.5)$$

It can be seen that the larger the surface roughness, the lower is the wavelength difference which is necessary to decorrelate the resulting speckle patterns. If the light from the two light sources would be transmitted through a transparent diffusor of which one side is rough (surface scattering in a transmission setup), the scattering vector difference would differ from the reflection case above. The treatment of a transmission geometry can be found in [9] and yields qualitatively similar results. Also there, the decorrelation increases with the wavelength separation and the surface roughness.

The situation is very similar, if not two or several separated illumination wavelengths are used but a broadband source. The spectrum can be virtually decomposed into single lines. Again, lines of the spectrum which are very close to each other may produce speckle patterns, which are highly correlated. Lines which are far enough separated might produce speckle patterns that are uncorrelated. Following [9], the speckle contrast C for normal observation and normal illumination of a scattering target with a polarized, spatially fully coherent but broadband source is approximately given by

$$C = \sqrt{\int_{-\infty}^{\infty} K_{\hat{G}}(\Delta\nu) |M_l(\Delta q_z)|^2 d\Delta\nu}, \quad (4.6)$$

where $K_{\hat{G}}(\Delta\nu)$ is the autocorrelation function of the source's normalized power spectrum. In many practical cases, a Gaussian shaped spectrum of the illumination source can be assumed. Such a source can be characterized by the 1/e-width $\delta\nu$ of its spectrum and $K_{\hat{G}}(\Delta\nu)$ is then given by [9]

$$K_{\hat{G}}(\Delta\nu) = \sqrt{\frac{2}{\pi\delta\nu^2}} \exp\left(-\frac{2\Delta\nu^2}{\delta\nu^2}\right), \quad (4.7)$$

where $\Delta\nu$ is a frequency shift. $M_l(\Delta q_z)$ is again the characteristic function corresponding to the path length distribution $p(l)$ of the scattered photons which is connected to the surface height values. Following [9], it is generally given by

$$|M_l(\Delta q_z)|^2 = \left| \int_0^\infty p(l) e^{i\Delta q_z l} dl \right|^2. \quad (4.8)$$

With a change of variables $M_l(\Delta q_z)$ is the Fourier transform of $p(l)$. In many practical cases, $p(l)$ can be well approximated by a Gaussian shaped curve. $|M_l(\Delta q_z)|^2$ can then be written as $\exp(-\sigma_l^2(\Delta q_z)^2)$, where σ_l is the standard deviation of the scattering path length distribution of the scattered photons. Considering a rough surface with Gaussian distributed height values is illuminated, σ_l is the root-mean-square surface roughness.

Δq_z has the same meaning as before and is again dependent on the setup. It has to be taken into account whether the screen is surface or volume scattering and whether the observer is on the illumination side (front projection setup) or behind the screen (rear projection setup). Following [9], Δq_z for normal illumination and normal observation

of a surface scattering object in reflection is given by $\Delta q_z = 4\pi(|1/\lambda_1| - 1/\lambda_2|)$. The resulting speckle contrast for polarization preserving scattering, Gaussian distributed surface height values and a Gaussian illumination spectrum is then given by [9]

$$C = \left[1 + 8\pi^2 \left(\frac{\delta\lambda}{\bar{\lambda}} \right)^2 \left(\frac{\sigma_l}{\bar{\lambda}} \right)^2 \right]^{-\frac{1}{4}}, \quad (4.9)$$

where σ_l is the surface roughness, $\delta\lambda$ is the 1/e-width of the wavelength spectrum of the source, $\bar{\lambda}$ is its mean emission wavelength and the assumption of $\delta\lambda \ll \bar{\lambda}$ has been made.

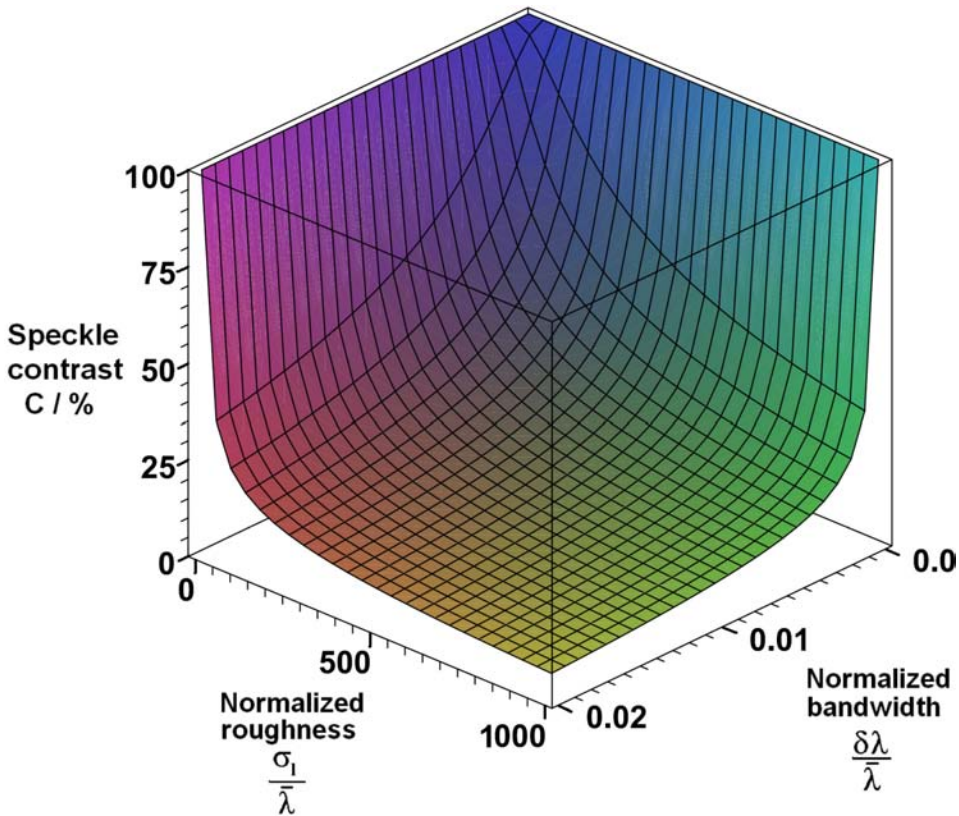


Figure 4.3: Resulting speckle contrast for broadband illumination of a surface with roughness σ_l in reflection where the source has an 1/e-bandwidth $\delta\lambda$ and a mean wavelength $\bar{\lambda}$.

Fig. 4.3 shows a plot of this equation. The resulting speckle contrast values are plotted in dependence of the surface roughness normalized with the mean illumination wavelength $\sigma_l/\bar{\lambda}$ and the normalized illumination bandwidth $\delta\lambda/\bar{\lambda}$. It can be seen that small speckle contrast values can only be achieved if the wavelength spectrum is sufficiently broad *and* the surface roughness is large.

4.1.2 Time-Sequential Wavelength Decorrelation by a Chirp of the Source's Emission Wavelength

In the previous section, the wavelength decorrelation was achieved quasi-instantaneously. Now a source is taken into account which changes its emission wavelength over time. If this change happens within the integration time of an observer, the dynamically changing speckle pattern is temporally integrated and the intensity fluctuations become more and more “smeared out” on the detector. There is no conceptual difference to the findings in the previous subsections. However, the observer’s integration time and the correct autocorrelation function of the sources’ time integrated power spectrum have to be considered.

It was shown in Section 4.1 that the resulting speckle contrast values for wavelength decorrelation of individual patterns are mainly determined by the surface roughness and the diversity of the contributing wavelengths. In Chapter 6, it will be shown that the modeling and dependencies for volume scattering screens are similar.

Speckle reduction via wavelength decorrelation is not restricted to a special projection system architecture and can in principle be effectively used in raster scanning, line scanning and full frame architectures. A practical problem which arises is the method to achieve broadband emission of a laser source. Laser systems emitting ultrashort pulses can have considerable linewidths. However, today’s picosecond and femtosecond pulse laser systems are, by far, too expensive to be used in consumer products. Also actual white-light lasers are typically high priced. A chirping of the laser’s emission wavelength might therefore be more promising as it can be realized at a low cost, e.g. with a modulation of the laser’s driving current. The wavelength chirp which is achievable is dependent on the laser system used. In Chapter 8, the emission wavelength of a BA-VCSEL will be chirped over approximately 2 nm by driving the laser with strong current pulses.

4.2 Angular Decorrelation

In this section, a constant illumination wavelength is assumed. Detection from different *observation* angles results in the detection of somewhat decorrelated speckle patterns both in an imaging and a nonimaging setup. However, considering a human observer in a projection application, it would require a continuous movement of the observer’s head to achieve a continuous reduction of the perceived speckle contrast. This is not practical in projection applications and therefore not further considered here. A treatment of the topic can be found in [9].

In this work, different *illumination* angles in combination with an observer imaging the screen from a constant observation angle are considered. As already mentioned, two resulting speckle patterns will be somehow decorrelated if a screen is illuminated with two statistically independent sources from slightly different directions. For small angular difference the resulting speckle patterns will be mainly shifted with respect to each other. The required angular difference ζ between the two illumination directions to achieve a full decorrelation of the corresponding speckle patterns can be determined relatively easily for pure surface scattering. ζ is approximately given by $\sin(\zeta/2) = N.A_{image}$,

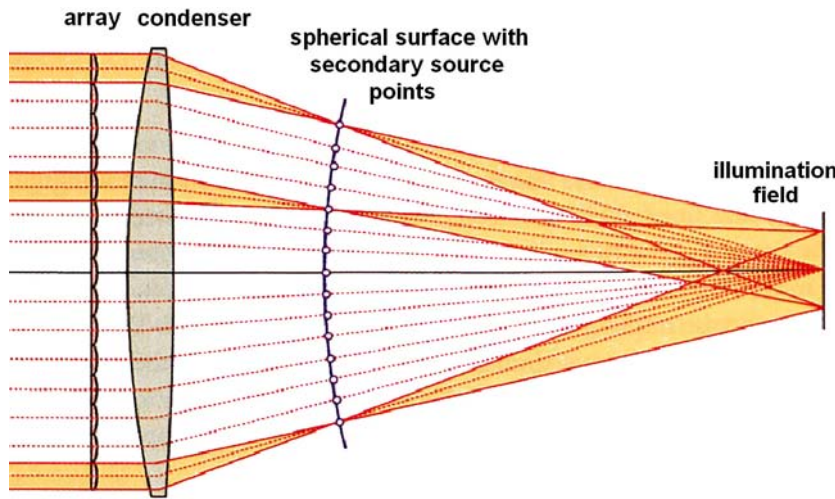


Figure 4.4: Schematic of a single microlens array beam homogenizer, taken from [121].

where $N.A._{image}$ is the numerical aperture of the imaging system [9]. This means that the smaller the numerical aperture of observation, the smaller is the required angular difference to decorrelate the two speckle patterns. A reduction of the numerical aperture with which a human observer images the screen can be easily achieved by increasing the distance between screen and observer.

4.2.1 Instantaneous Angular Decorrelation

Instantaneous angular decorrelation can be practically achieved in full frame projection systems via using a microlens beam homogenizer in the projection system. A microlens beam homogenizer is typically used to achieve a homogeneous illumination of a microimager (e.g. LC panel, LCoS imager, micromirrors) which is then magnified and projected onto the screen. The working principle of a simple microlens beam homogenizer is depicted in Fig. 4.4. The homogenizer consists of a 2D array of microlenses and a condenser lens. The array is illuminated from the left. Light falling in each illuminated microlens produces an illumination spot on the imager. As a large number of such spots is superimposed in the illumination field, the intensity distribution can be very homogeneous. The fact that the light from different microlenses illuminates the illumination field under slightly different angles can be used to achieve speckle reduction. To do so, different microlenses of the homogenizer can be illuminated with mutually incoherent sources, which produce statistically independent speckle patterns. With sufficiently different angles of incidence of the light from different sources on the screen, the produced speckle patterns can be mutually decorrelated.

Instantaneous angular decorrelation will be used to achieve speckle reduction in Chapter 8 of this thesis. There, a state-of-the-art microlens beam homogenizer is illuminated with a nonmodal BA-VCSEL. This laser can be modeled as Gaussian Schell-model source, emitting a large number of mutually incoherent beamlets. The individual beamlets play the same role on the microlens homogenizer as the light spots from individual sources as they are also mutually incoherent. Angular decorrelation will be achieved

by imaging different beamlets through different microlenses of the homogenizer. In Chapter 8, also size constraints will be discussed in detail, which the light spots on the homogenizer have to meet to achieve optimal speckle reduction. It will be also shown in Chapter 8 that volume scattering projection screens can drastically reduce the angular difference which is required to fully decorrelate the resulting speckle patterns.

4.2.2 Time-Sequential Angular Decorrelation

If the angle of illumination is changed during the integration time of the observer, the changing speckle pattern will again be temporally integrated and a reduced speckle contrast will be perceived. Also time-sequential angular decorrelation can practically be achieved with a microlens beam homogenizer. A scheme of the required illumination of the microlens beam homogenizer is sketched in Fig. 4.5 (not to scale). The illuminating light spot can be scanned in circular motion over the microlens beam homogenizer. The screen will then be continuously illuminated from slightly different angles. The scanning can easily be done much faster as the frame time and the integration time of the observer. The required angular difference for full decorrelation is again dependent on the scattering mechanism (surface or volume scattering screen) and the observer's numerical aperture.

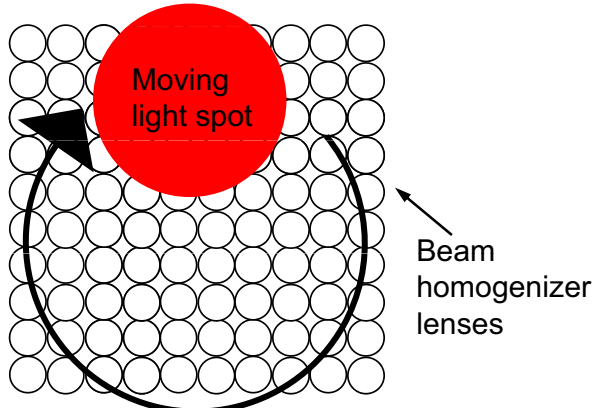


Figure 4.5: The illuminating light spot is scanned in circular motion over the microlens beam homogenizer. This results in a continuous change of the screen illumination angle.

4.3 Spatial Decorrelation

It was mentioned in Chapter 2 that statistically independent speckle patterns can be produced by using several independent laser sources, a laser which emits several statistically independent transverse modes or quasi-homogeneous sources such as a nonmodal BA-VCSEL. It will be shown in the following that the spatial resolution of an observer on the screen in comparison to the size of the spatial coherence area can crucially influence the perceived speckle contrast value. The coherence area indicates the area over which the light in a spot has a considerable coherence. So, light from different coherence areas will produce statistically independent speckle patterns which add on an intensity basis.

For a spatially fully coherent source, the light spot size and the coherence area have the same size. With a quasi-homogeneous source, the coherence area is much smaller than the overall light spot. A precise definition of coherence will follow in Chapter 5 of this thesis. In many projection applications, the observer is a human looking onto a screen from a certain distance. The following subsection will therefore deal with the spatial resolution of the human eye.

4.3.1 Visual Acuity

The spatial resolution of a human observer is determined by the visual acuity of the human eye. The visual acuity has a theoretical lower bound which is set by diffraction on the eye's pupil opening. The pupil opening typically has values between approximately 2 mm for a bright adapted eye of a senior and 8-9 mm for a dark adapted eye of a child. This results in a theoretical limit of the visual acuity of about 0.4 arc minutes for the largest pupil opening. This limit is however not reached in practice because of the imperfection of the human eye [118]. A visual acuity of one arc minute ($1/60^\circ$) is defined as a visus of one and is commonly assumed for a healthy and bright adapted eye [122]. An observer with a visus of one can just resolve two points separated by one arc minute. This corresponds to a resolution element of about 1 mm diameter in a distance of 3 m from a screen.

4.3.2 Instantaneous Spatial Decorrelation

If the spatial resolution of the observer on the screen is much smaller than the coherence area of the light on the screen, the observer (which images the screen plane) virtually sees a fully coherent light spot at each position of the screen. Each coherence area produces locally a speckle pattern of full contrast which the observer will image. A schematic of this situation is shown in part (a) of Fig. 4.6. If the coherence areas are much smaller than the spatial resolution spot of the observer (case (b) in Fig. 4.6), the observer cannot resolve the single coherence areas and spatially integrates their light. Again, each coherence area produces a local speckle pattern of high contrast. As each speckle pattern is created at a different spatial position on the screen, the speckle patterns will be decorrelated, i.e. they show more or less different intensity distributions. For realistic screens, the lateral correlation length of the surface microstructure is extremely small. Therefore, the resulting speckle patterns are most likely fully decorrelated. The observer spatially integrates the speckle patterns inside its spatial resolution spot and will therefore perceive a reduced speckle contrast. A system where this method for speckle reduction can be realized is a full frame display where the imager is illuminated with light of very low spatial coherence.

4.3.3 Instantaneous Spatial Decorrelation in Combination With a Volume Scattering Target

Some speckle contrast reduction might be achieved even if the single coherence areas can be resolved by the observer, when a volume scattering screen is used. This is further illustrated in Fig. 4.7. The coherence areas on the screen do not overlap each other

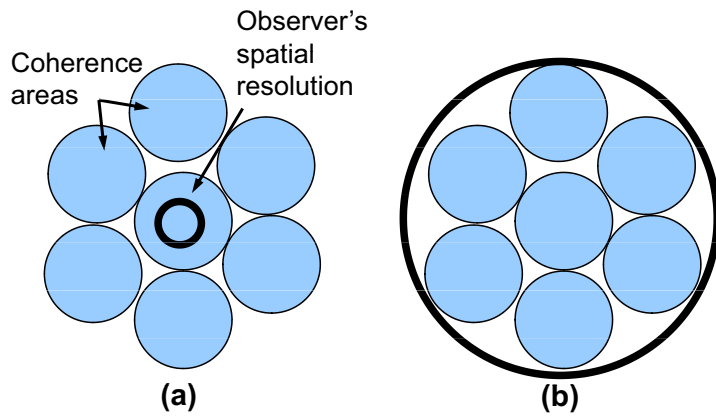


Figure 4.6: An observer resolves the individual coherence areas on the screen and perceives a high speckle contrast in (a). In (b) a reduced speckle contrast will be perceived because of spatial integration.

(part (a) of Fig. 4.7). The volume scattered light spots (backscattered or transmitted) may however partly overlap because of diffuse scattering in the screen. This is depicted in Fig. 4.7(b). The light of the different coherence areas adds on an intensity basis in the regions of overlap. As the photons from the different coherence areas started their quasi-random scattering paths inside the screen at different positions, the resulting speckle patterns will be somewhat decorrelated. Therefore, the resulting speckle contrast in the regions of overlap will be reduced. The speckle contrast value is dependent on the scattering characteristics of the screen, the number and size of regions of overlap and the observer's spatial resolution. Therefore, the exact modeling of the speckle contrast values is complicated.

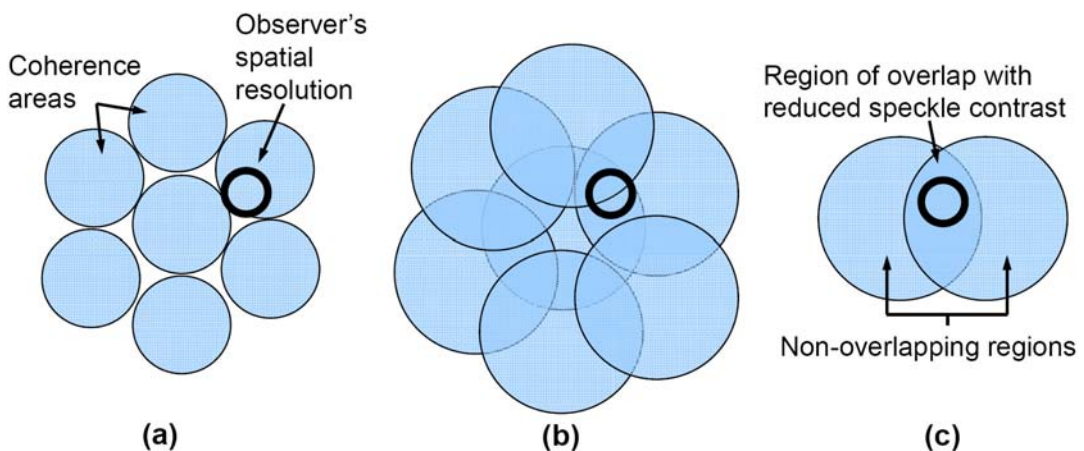


Figure 4.7: Schematic of (a) coherence areas incident onto a volume scattering target, (b) backscattered or transmitted coherence areas with regions of overlap because of diffuse scattering, (c) reduced speckle contrast in the regions of overlap.

4.3.4 Time-Sequential Spatial Decorrelation

In this section, a source of full spatial coherence and therefore only one coherence area is assumed. It is considered that the illuminated spot and hence the coherence area are smaller than the observer's spatial resolution area. If the coherence area moves through the observer's resolution spot during his temporal integration time, the observer will detect a reduced speckle contrast. If the lateral correlation length of the screen is again assumed to be much smaller than the coherence area, a fully decorrelated speckle pattern will be created at least for each non-overlapping position of the illumination spot inside the spatial resolution area. The number of decorrelated speckle patterns which are integrated can be enlarged if the illumination spot passes the spatial resolution area not in a straight line as in Fig. 4.8(a), but in an oscillating manner as indicated in Fig. 4.8(b). This method for speckle contrast reduction is mainly suitable for raster scanning displays as the coherence area has to be scanned and has to be smaller than the observer's spatial resolution area.

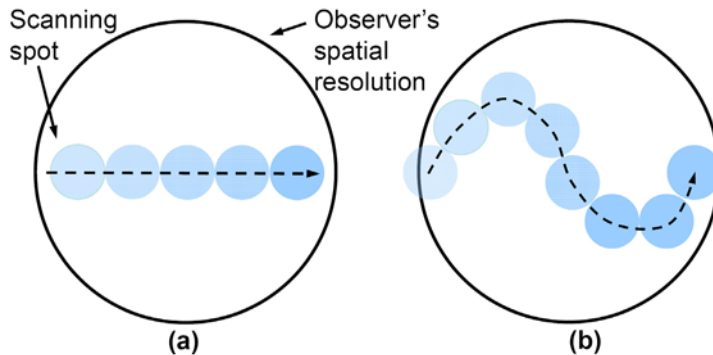


Figure 4.8: Schematic of (a) linearly scanned spot, (b) nonlinearly scanned spot with increased speckle contrast reduction.

4.4 Scrambling

In this section, speckle contrast reduction via scrambling techniques is discussed. Scrambling includes polarization scrambling and wavefront scrambling.

4.4.1 Instantaneous Polarization Scrambling

If polarized light is backscattered from a typical metallic surface, its degree of polarization is preserved. However, many screens which produce speckles do not preserve the polarization of the incident light. It will be shown in Chapter 6 of this thesis that typical volume scattering projection screens nearly fully depolarize incident light because of multiple scattering. As mentioned in Chapter 2, the resulting speckle contrast is reduced by a factor of $1/\sqrt{2}$ for full depolarizing scattering. As the depolarizing screen reduces the speckle contrast, this technique can in principle be used in raster scanning, line scanning and full frame projection systems.

4.4.2 Time-Sequential Polarization Scrambling

Following [9], additional speckle contrast reduction can be achieved via polarization switching. As already mentioned, if a screen is illuminated with horizontally polarized light (without loss of generality) and scattering is fully polarization scrambling, it can be seen as two independent speckle patterns were produced, one in each of two orthogonal polarization components. If the initial state of polarization is switched to the orthogonal state (vertical polarization), the screen again produces two speckle patterns and they can be uncorrelated from the two patterns generated with horizontally polarized illumination. It is now obvious that a speckle contrast reduction of $1/\sqrt{4}$ is perceived if the source is half of the observer's integration time in the horizontal polarization state and the other half in the vertical polarization state. Goodman states that the contrast reduction of $1/\sqrt{4}$ will not be observed if the two incident polarization states are present simultaneously and are mutually coherent [9]. The similarly polarized and reflected speckle patterns would then add on an amplitude basis rather than an intensity basis, and the contrast would only be reduced by a factor $1/\sqrt{2}$. However, many of the projection systems described in the previous chapter use the polarization of the light for image generation (e.g. LCoS or LC systems). Therefore, this method for speckle reduction might be unpractical in many projection systems and is not further considered in this work.

4.4.3 Time-Sequential Phasefront Scrambling

An effective strategy to achieve speckle contrast reduction in laser projection systems is the insertion of moving or rotating diffusors into the laser beam. However, this typically comes along with a degradation of the beam quality and an increase of the beam's étendue. Furthermore, an additional diffusor needs space, produces cost and the use of a moving or rotating component is typically unwanted. A theoretical treatment of speckle reduction with moving diffusors can be found in [9]. As the diffusor is typically located somewhere inside the projection system, the applicability and effectiveness of this method for speckle reduction has to be checked for each projection system architecture. A successful use of a rotating diffusor for speckle reduction can be found in [123]. As a rule of thumb, speckle reduction with diffusors is more promising in full frame systems as in raster scanning systems. This is because the phasefront scrambling has to be achieved during the illumination time of one pixel in a raster scanning system and not during the much longer frame time as in the case of a full frame system.

Another method to achieve speckle reduction by phasefront scrambling is to move the projection screen itself instead of using a moving diffusor. Several configurations based on the moving screen method have been proposed, including a single moving screen [123],[124] or the use of two spatially separated screens which are in relative circular or linear motion to each other [75],[125],[126]. Mechanical movement of the potentially large projection screen is, however, also not a favorable solution.

Another method to achieve time-sequential scrambling is with the use of multimode optical fibers. If laser light is coupled into such a fiber, the different fiber modes propagate along the fiber with a variety of phase velocities. If the fiber is static, the su-

perposition of the field contributions from the different fiber modes at the exit surface resembles a static speckle pattern. By changing the stress and strain conditions in the fiber, this interference pattern can be easily made time varying. This can be done for example by bending or vibrating the fiber. Very often, already little turbulences or slight temperature changes in the air surrounding the fiber are sufficient to make the pattern at the exit surface time varying. Examples for speckle reduction in optical fibers can be found in [66] or [67]. Again, with sufficient variation during the observer's integration time, speckle can efficiently be averaged by the eye.

4.5 Combination of Methods for Speckle Reduction

Many methods for speckle reduction can be effectively combined. If the individual methods are “conceptually different”, the resulting speckle contrast reduction factors multiply. A case in point is a polarization scrambling screen which is illuminated with a broadband source. The polarization scrambling contributes a speckle contrast reduction factor of $1/\sqrt{2}$ which can be multiplied with the speckle contrast reduction factor because of the wavelength decorrelation. Another example would be the illumination of a screen with three sources under sufficiently different angles to produce three fully decorrelated speckle patterns. If the sources additionally have a certain bandwidth, the speckle contrast reduction factors multiply. An example for the combination of two methods for speckle reduction which are not conceptually different would be as follows: Two monochromatic lasers with different emission wavelengths are used to illuminate a screen from different angles. Each of the lasers produces a speckle pattern of full contrast. There are two mechanisms which contribute to the decorrelation of the two patterns. A sufficiently large wavelength separation can decorrelate the resulting patterns, and also a sufficient angular separation can decorrelate them. However, the two patterns cannot be more decorrelated than fully decorrelated, i.e. with a normalized intensity correlation coefficient $\rho_{n,m} = 0$. The maximal achievable speckle contrast reduction is therefore $1/\sqrt{2}$.

4.6 Chapter Summary and Motivation of the Following Chapters

It was shown in this chapter that numerous methods for speckle reduction exist. Many are based on the creation, decorrelation and superposition of statistically independent speckle patterns. The applicability and effectiveness of the different methods can depend on the projection system architecture. Furthermore, the costs connected with the different methods have to be considered when speckle reduction in a consumer product is to be achieved.

The following chapters contain the main part of this thesis. In Chapter 5, a simulation tool is presented, with which the propagation of light with different coherence properties through optical systems can be investigated. The coherence properties of the light are influenced by the propagation through a projection system. The properties on the projection screen can differ a lot from the coherence properties close to the light

source. As mentioned, the coherence properties on the projection screen crucially influence the speckle contrast values an observer perceives. The tool can therefore be used to investigate the coherence and speckle properties of optical systems.

In Chapter 6-8, three strategies for speckle reduction are shown which effectively and efficiently combine different methods for speckle reduction.

It has been shown that a large screen roughness is essential to achieve low speckle contrast values via wavelength decorrelation. This is the case for illumination with several emission lines, illumination with a broadband source or illumination with a source whose wavelength is chirped. In Chapter 6, the speckle characteristics of volume scattering screens are investigated. It will be demonstrated that volume scattering screens can have very large volume roughnesses and can cause a strong depolarization of the scattered light. It will be shown that the proper selection of a volume scattering screen can be essential to achieve low speckle contrast values.

In Chapter 7, speckle reduction with colloidal-dispersion-filled projection screens will be investigated. These screens produce time varying speckle patterns without the need to either move the screen itself or the use of moving or rotating diffusors. The time varying speckle pattern is created via multiple scattering of the laser light on the dispersed scattering globules which do Brownian movement.

In Chapter 8, low speckle laser projection with a nonmodal BA-VCSEL is investigated. Speckle reduction with the BA-VCSEL is particularly practical since three methods for speckle contrast reduction can be efficiently combined. A polarization scrambling screen with large volume roughness will be used, the source's emission wavelength will be chirped and angular decorrelation via a beam homogenizer will be used to benefit from the reduced spatial coherence of the BA-VCSEL and to realize low-speckle laser projection.

Chapter 5

Simulation Tool for the Ray-Based Investigation of the Propagation of Light With Different Degrees of Coherence

It was shown in the previous chapter that the coherence properties of the light on the screen can drastically influence the speckle contrast values which an observer perceives. If more than one spatial coherence area falls into the spatial resolution spot of the observer, a reduced speckle contrast will be perceived. The coherence properties on the screen can differ a lot from the coherence properties close to the light source. This is because the coherence characteristics of a propagating light field are influenced by parameters of the system through which it propagates. This fact can be useful in several applications, e.g. for the determination of the diameter of a distant star by interference experiments. This is possible because the originally incoherent starlight becomes spatially more and more coherent on its way to the earth [127]. On the other hand, this fact can be disturbing, e.g. when speckles arise and degrade image quality on the screen of a projection system, even if an originally spatially incoherent projection lamp is used as a light source. It can be seen that an understanding of the coherence properties of optical systems is of major interest in many applications.¹

5.1 Introduction

As mentioned in Chapter 2, coherence is mostly described by the *mutual coherence function* Γ . It was shown that for a monochromatic and scalar field U , the mutual coherence function between the positions \vec{x}_1 and \vec{x}_2 at times t_1 and $t_2 = t_1 + \tau$ in a stationary optical field is given by

$$\Gamma(\vec{x}_1; \vec{x}_2; \tau) = \langle U(\vec{x}_1, t_1) U^*(\vec{x}_2, t_2) \rangle_e, \quad (5.1)$$

where $*$ denotes complex conjugation, τ denotes a time difference and $\langle \rangle_e$ denotes an ensemble average over different realizations of the field [11]. Furthermore, the *complex*

¹Parts of this chapter are published in: F. Riechert, F. Dürr, U. Rohlfing, and U. Lemmer, “Ray-based simulation of the propagation of light with different degrees of coherence through complex optical systems,” Appl. Opt. **48**, Issue 8, 1527-1534 (2009).

degree of mutual coherence $\gamma(\vec{x}_1; \vec{x}_2; \tau)$ is given by

$$\begin{aligned}\gamma(\vec{x}_1; \vec{x}_2; \tau) &= \frac{\Gamma(\vec{x}_1; \vec{x}_2; \tau)}{\sqrt{\Gamma(\vec{x}_1; \vec{x}_1; 0)\Gamma(\vec{x}_2; \vec{x}_2; 0)}} \\ &= \frac{\Gamma(\vec{x}_1; \vec{x}_2; \tau)}{\sqrt{I(\vec{x}_1)I(\vec{x}_2)}},\end{aligned}\tag{5.2}$$

where $I(\vec{x})$ denotes the intensity at a point \vec{x} [11]. In the following, the absolute value of $\gamma(\vec{x}_1; \vec{x}_2; \tau)$ is named the *degree of coherence*.

The remainder of the chapter is organized as follows: In Section 5.2, methods for the analytical and simulative investigation of the propagation of coherent light through optical systems are reviewed. In Section 5.3, the functional extension of a raytracer is presented which then allows for the ray-based investigation of the propagation of light of different degrees of coherence. The intensity distribution as well as the complex degree of coherence between two points at arbitrary positions in the optical system can be investigated. In Section 5.4 it is shown how a spatially fully incoherent source can be approximately simulated with only one simulation run. In Section 5.5, two basic systems (free space propagation and a single lens setup) are simulated. The simulation results are compared to analytical theory and show excellent agreement. In Section 5.6, the coherence properties of a practical two-tandemarray microlens beam homogenizer system as it is used in projection applications are simulated. In Section 5.7, possible future improvements of the simulation tool are discussed. In Section 5.8, the chapter is summarized and conclusions are drawn.

5.2 Review of Methods to Investigate the Propagation of Coherent Light

A rigorous analytical description of the propagation of coherent light fields by solving Maxwell's equations or of the propagation of the mutual coherence function by using Wolf's equations [128] can typically only be done for simple systems. Usually, the Green's function of the system under consideration has to be known to solve a set of coupled differential equations describing the system. For practical systems this is an almost impossible task. In paraxial approximation, the ABCD-matrix formalism can be used to propagate light fields [129] or their coherence function [130] from an optical system's entrance plane to its exit plane. This formalism was introduced by Kogelnik in the 1960s to describe laser resonator modes [131]. However, the corresponding system matrix has to be known, which can not be found for arbitrary optical systems.

Most simulative methods to investigate the propagation of coherent light have practical restrictions: Finite difference time domain (FDTD) methods have been introduced by Yee in the 1960s [132]. In this formalism the space and time coordinates are discretized and Maxwell's equations are transferred to a set of difference equations which are solved numerically. Finite difference methods are computationally demanding and therefore often limited to nano- or micro scale systems. Beam propagation methods (BPM) are restricted to systems where the beam profile is slowly varying in propagation direction and is typically used for the simulation of waveguides [133].

Standard raytracing works in the regime of geometrical optics and is therefore not capable of simulating wave-optical phenomena or coherence effects [134]. Gaussian beam propagation (GBP) can be seen as an extension of standard raytracing. A Gaussian beam solves the paraxial Helmholtz equation. An optical field can be decomposed into Gaussian beams which can be traced through the considered paraxial system. The characteristic parameters of each Gaussian beam (divergence, beam waist, ...) are therefore build up with geometrical rays [135]-[138]. Effects of diffraction are not covered by this formalism. Some tools offering Gaussian beam decomposition allow for a phenomenological investigation of wave-optical phenomena. However, to the best of the author's knowledge, no commercially available tool supports the calculation and graphical depiction of the coherence function at arbitrary positions.

In the following section, the functional extension of a standard raytracer and the working principles of the extended tool are described.

5.3 Functional Extension of a Standard Raytracer

For the functional extension of the raytracer, an optical field is decomposed into spherical waves which are propagated through a system under investigation. Source modeling, the raytracing routine and the modeling of a detector plane of the Matlab-based standard raytracer *Optical Programming System* (OPS) (developed by Prof. U. Rohlffing and coworkers, Hochschule Darmstadt, Germany) are extended.

Following Douglas in [139], the basic source element is a point source, which emits a fan of equiangular rays of equal start phase. Such a fan represents the normal vectors of the phase front of a spherical wave. A spatially extended source is modeled by an ensemble of point sources in close distance. By adjusting the weights of fans from individual source points of an extended source, different source intensity profiles can be represented. The weight of a fan corresponds to the amplitude of the represented spherical wave. A spatially fully coherent source can be either a single point source or an ensemble of point sources with arbitrary but fixed start phase configuration of the individual point sources. Sources of reduced spatial coherence can be modeled by propagating and superimposing numerous start phase configurations of an ensemble of point sources. This concept is similar to the modeling of a laser which emits transverse modes. If only one transverse mode is emitted, the laser emission is fully coherent. If several transverse modes are emitted, each mode for itself is fully spatially coherent, however the overall laser emission has a reduced spatial coherence. The more transverse modes contribute to the emission, the lower is the spatial coherence of the laser emission [33].

A spatially fully incoherent source could therefore be simulated by the superposition of the results of an infinite number of simulation runs, each of which has a different start phase configuration of the ensemble of point sources. However, a spatially fully incoherent source can be simulated with only one simulation run. This is because the complex degree of coherence in a detector plane is no longer dependent on the start phase configurations in the infinite limit (see Section 5.4).

Another source type of practical interest are quasi-homogeneous sources [140]. If light of a quasi-monochromatic, uniform, spatially fully incoherent circular source of

wavelength λ and radius r propagates in free space, the van Cittert-Zernike theorem can be used to calculate the resulting spatial coherence radius r_{coh} in a given distance d in the farfield of the source. This theorem is based on the seminal work of van Cittert and Zernike in the 1930s [35],[141]. Following [140], r_{coh} is the radius of the area, where the degree of coherence $|\gamma|$ exceeds 0.88 and is approximately given by $0.16\lambda d/(2r)$.

This behavior can be exploited to simulate spatially partially coherent, quasi-homogeneous sources: By adjusting the size of a spatially fully incoherent source and its distance to the entrance plane of the optical system under investigation or an object to be illuminated, the light field's spatial coherence radius and its divergence angle can be adjusted.

The raytracing routine is extended to calculate the optical path of each ray and therewith its resulting phase in a given position. A reduced temporal coherence can be easily simulated by doing a simulation run for each contributing wavelength of a spectrum and subsequent “incoherent” superposition of the individual simulation results.

Again based on Douglas in [139], the detector is modeled as a two-dimensional (2D) array of pixels. Following [139], the mean value of the optical path lengths of all rays from a point source which fall into a given detector pixel, is calculated in the given pixel. So, a “mean ray” or “mean contribution” of each spherical wave is determined in each detector pixel. Local continuity of the optical field within the area of a pixel is implicitly assumed. Knowing the amplitudes and phases of all mean rays in the detector pixels the intensity in the pixel can be calculated. After this was done for all detector pixels, the mutual coherence function and also the complex degree of coherence can be calculated at each detector position. If the number of rays per spherical wave is large enough, this methodology is not restricted to paraxial systems. The size of the detector pixels has to be chosen small enough to resolve any fluctuations of the calculated coherence function at a chosen detector position. The necessary detector resolution is therefore dependent on the optical system under consideration. Also the number of rays per spherical wave has to be large enough to achieve sufficient statistical averaging in each detector pixel. For the interferometer simulated in [139] about ten rays per pixel have been sufficient. In the current state a “good” simulation result is identified visually by showing smooth, detailed curves. A more quantitative approach is shortly discussed in the Conclusion section.

5.4 Simulation of a Spatially Fully Incoherent Source With One Simulation Run

In this section it is shown how an extended, spatially fully incoherent source can be approximately simulated with only one simulation run. It will be shown that it is not necessary to superimpose the simulation results of an infinite number of start phase and amplitude configurations of the ensemble of point sources. In the following, a lower index indicates a point source, an upper index indicates a pixel of the detector. The optical field U_j of a point source j is given by

$$U_j = A_j e^{i\phi_j} \quad (5.3)$$

with arbitrary start phase ϕ_j and arbitrary amplitude A_j . As mentioned above, the spherical wave is represented by a large number of rays emerging from the point source, where the amplitude of the point source is assigned to each of its rays. In analogy to the propagation of a spherical wave, the amplitude assigned to each ray decreases by a factor of $1/opl$, where opl is the optical path lengths the ray propagated.

After the propagation of the fields of all point sources, the field U^l in a detector pixel l can be expressed as

$$U^l = \sum_j A_j^l e^{i(\frac{2\pi}{\lambda} opl_j^l + \phi_j)}, \quad (5.4)$$

which is a superposition of all point source contributions. A_j^l is the mean value of the amplitudes of the rays from point source j which contribute to detector pixel l . λ is the wavelength assigned to the point source and opl_j^l indicates the mean value of the optical path lengths of all rays from the point source j in the detector pixel l .

To calculate the mutual coherence between two detector pixels l and m for a single start phase and amplitude configuration of the ensemble of point sources, the product

$$U^l U^{m*} = \sum_j \sum_k A_j^l A_k^{m*} e^{i\frac{2\pi}{\lambda}(opl_j^l - opl_k^m)} e^{i(\phi_j - \phi_k)} \quad (5.5)$$

has to be evaluated. Of physical interest is only the ensemble average, i.e., the superposition of N start phase and amplitude configurations. Following Eq. (6) in [35], mean values are therefore introduced and the superposition of N start phase and amplitude configurations can be expressed as

$$\langle U^l U^{m*} \rangle = \frac{1}{N} \sum_{n=1}^N \sum_j \sum_k \underbrace{\overline{A_j^n A_k^{m*}} e^{i\frac{2\pi}{\lambda}(opl_j^n - opl_k^m)}}_{\text{independent of } n} \cdot e^{i(\phi_{jn} - \phi_{kn})}. \quad (5.6)$$

It is now shown that this expression can be further simplified for the superposition of an infinite number of start phase configurations. The n -dependent sum

$$\sum_{n=1}^N e^{i(\phi_{jn} - \phi_{kn})} \quad (5.7)$$

corresponds to a mathematical representation of a two-dimensional random walk in the complex plane [142]. Under the assumption of equally distributed and statistically independent random variables ϕ_{jn} and ϕ_{kn} it follows for Eq. (5.7)

$$\sum_{n=1}^N e^{i(\phi_{jn} - \phi_{kn})} = N + \sum_{n=1, j \neq k}^N e^{i(\phi_{jn} - \phi_{kn})}. \quad (5.8)$$

For $N \rightarrow \infty$, the n -dependency of Eq. (5.8) reduces to

$$\lim_{N \rightarrow \infty} \frac{1}{N} \sum_{n=1}^N e^{i(\phi_{jn} - \phi_{kn})} = \delta_{jk}, \quad (5.9)$$

where δ_{jk} is the Kronecker delta [142]. For $N \rightarrow \infty$, which corresponds to a spatially fully incoherent source, Eq. (5.6) can therefore be written as

$$\lim_{N \rightarrow \infty} \langle U^l U^{m*} \rangle = \sum_j \overline{A_j^l A_j^{m*}} e^{i \frac{2\pi}{\lambda} (opl_j^l - opl_j^m)}. \quad (5.10)$$

The complex degree of mutual coherence between the detector pixels l and m can therefore be expressed as

$$\gamma_{lm} = \frac{\langle U^l U^{m*} \rangle}{\sqrt{\langle U^l U^{l*} \rangle \cdot \langle U^m U^{m*} \rangle}} = \frac{\sum_j \overline{A_j^l A_j^{m*}} e^{i \frac{2\pi}{\lambda} (opl_j^l - opl_j^m)}}{\sqrt{\sum_j |A_j^l|^2 \cdot \sum_j |A_j^m|^2}}. \quad (5.11)$$

It can be seen that Eq. (5.10) and Eq. (5.11) are no longer dependent on the start phase configurations of the ensemble of point sources. The difference $opl_j^l - opl_j^m$ of the mean optical path lengths from a point source j in the detector pixels l and m can be determined with only one simulation run. However, this is not generally possible for the ensemble mean value $\overline{A_j^l A_j^{m*}}$ because it is determined by the source statistics. Therefore, the approximation

$$\gamma_{lm} \approx \frac{\sum_j \overline{A_j^l A_j^{m*}} e^{i \frac{2\pi}{\lambda} (opl_j^l - opl_j^m)}}{\sqrt{\sum_j |A_j^l|^2 \cdot \sum_j |A_j^m|^2}} \quad (5.12)$$

is introduced. It can be seen that the expression $\overline{A_j^l A_j^{m*}}$ is approximated by $\overline{A_j^l \overline{A_j^{m*}}}$. This approximation is exact, if $A_j^l = A_j^m$, i.e., if the amplitude contribution from point source j is identical in the detector pixels l and m . In many practical cases the differences of the mean optical path lengths from a point source to the different detector pixels is very small compared to the absolute value of the optical path lengths. This is typically the case for comparably small sources and detectors and comparably large distances from the source to the detector plane. In such cases the amplitude contribution of a point source j is very similar in different detector pixels and the shown approximation will be well fulfilled. It is emphasized that the aim is to simplify the simulation of spatially fully incoherent sources with the method presented here. Therefore, the “non-zero” part of the degree of coherence in the detector plane is typically only of small lateral extent and the detector can be chosen small, too.

As mentioned earlier a mean amplitude value is directly assigned to each point source in the software tool. Therefore, the ensemble average $\overline{A_j^l} = A_j^l$. Applying this to Eq. (5.12) leads to

$$\gamma_{lm} \approx \frac{\sum_j A_j^l A_j^{m*} e^{i \frac{2\pi}{\lambda} (opl_j^l - opl_j^m)}}{\sqrt{\sum_j |A_j^l|^2 \cdot \sum_j |A_j^m|^2}}. \quad (5.13)$$

Using the presented method optical systems with a spatially fully incoherent source can be investigated with only one simulation run, provided that the approximation in Eq. (5.12) is well fulfilled. With the use of this method simulation runtimes can be drastically reduced.

5.5 Simulations Compared to Analytical Theory

In this section simulations of basic optical systems which can be described analytically are shown and the simulation results are compared to theory. Figure 5.1 shows the setup of an optical system consisting of a uniform, quadratic source with a side length a of 0.43 mm. The source is monochromatic, spatially fully incoherent, linearly polarized. This source is formed by an array of 100×100 point sources. Each point source emits a fan consisting of 40,000 equiangular rays. Light from this source propagates through free space to a detector placed at a distance of 1 m from the source. The degree of coherence in the detector plane can be analytically calculated using the van Cittert-Zernike theorem.

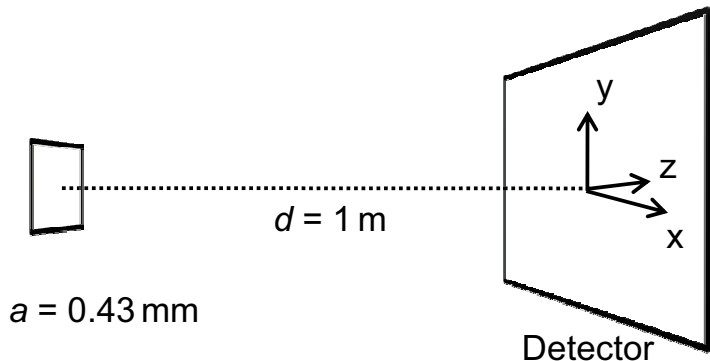


Figure 5.1: Schematic of the investigated free space propagation setup.

Figure 5.2(a) depicts a 3D plot of the resulting simulated degree of coherence $|\gamma|$ regarding the central point (0/0) of the detector plane which is located on the optical axis. The detector has a size of $8 \text{ mm} \times 8 \text{ mm}$ and consists of 49×49 pixels. Figure 5.2(b) depicts a cut along the x-axis of Fig. 5.2(a) with the indicated theoretical curve of $|\gamma|$ (solid line), which is determined using the van Cittert-Zernike theorem. It can be seen that excellent agreement between simulation and theory is achieved. A number of approximately ten rays from each point source per detector pixel have been sufficient to achieve the shown results. The calculation time has been about 3.5 minutes on a personal computer system².

²Quadcore personal computer with a 2.67 GHz processor and eight GBytes of random access memory.

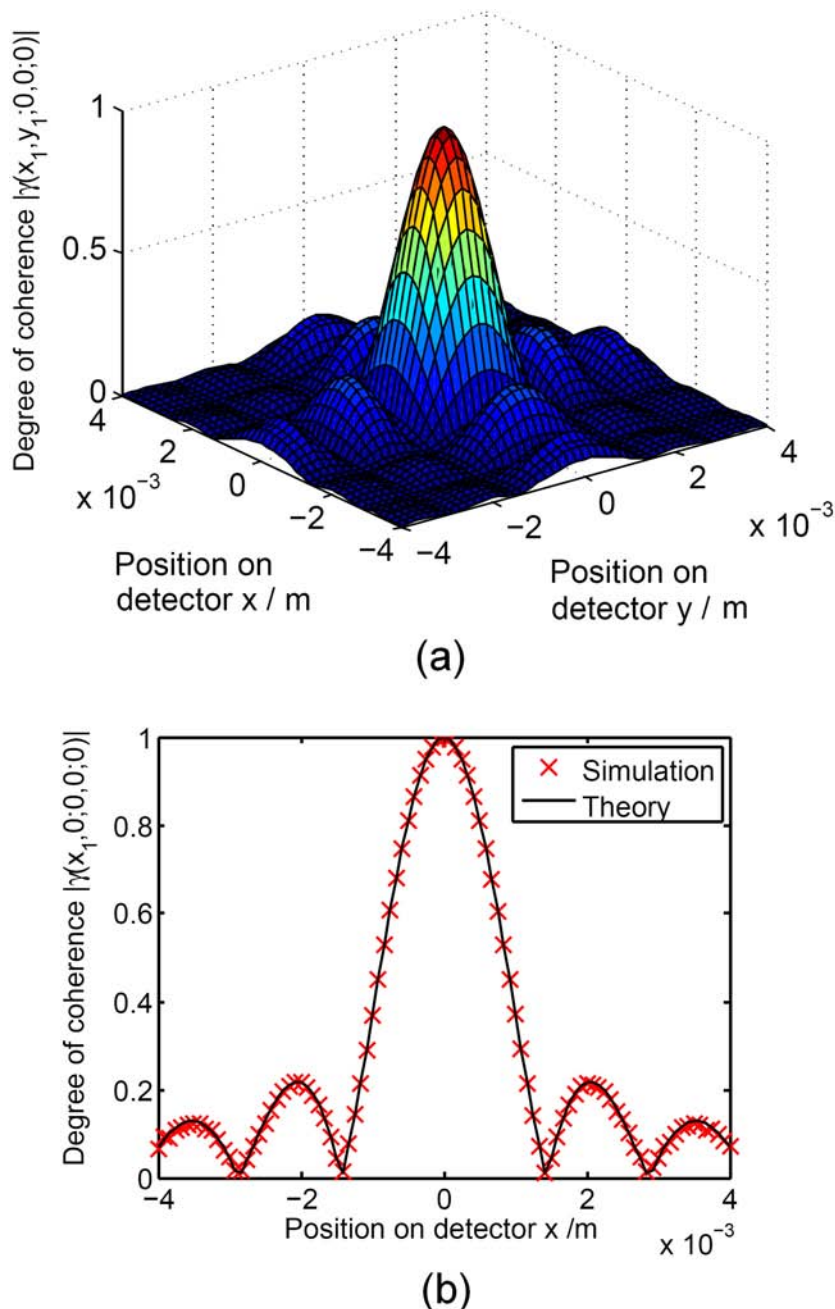


Figure 5.2: (a) 3D plot of the simulated degree of coherence regarding the centre of the detector plane for the free space propagation setup. (b) Cut along the x-axis of the plot in (a). The solid line indicates the theoretical description using the van Cittert-Zernike theorem.

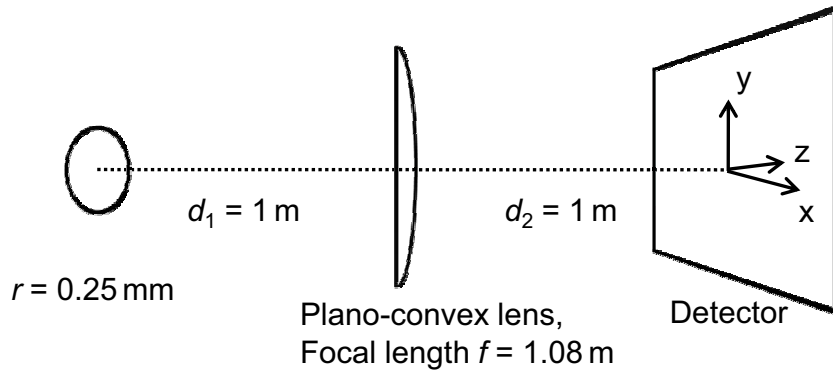


Figure 5.3: Schematic of the investigated single lens system setup.

As a second optical system a single lens system is discussed, which is shown in Fig. 5.3. The source is uniform, monochromatic, spatially fully incoherent, linearly polarized and circular in shape with a radius r of 0.25 mm. This source is formed by approximately 10,200 point sources which are uniformly arranged. Each source point emits a fan of 82,000 rays. The thin lens is plano-convex and has a focal length of 1.08 m. The detector has again a size of 8 mm \times 8 mm and consists of 49×49 pixels. Figure 5.4(a) shows a 3D plot of the simulated resulting degree of coherence regarding the centre of the detector. Figure 5.4(b) depicts a cut along the x-axis of the plot in Fig. 5.1(a) and the theoretical curve of $|\gamma|$ determined with ABCD-matrix formalism (solid line). Again excellent agreement between simulation and theory is obtained. Approximately eight rays per point source in each detector pixel were sufficient to achieve the shown results. For this task the simulation time was approximately 20 minutes.

Based on the promising results of this section, a complex beam homogenizer system is investigated in the following section.

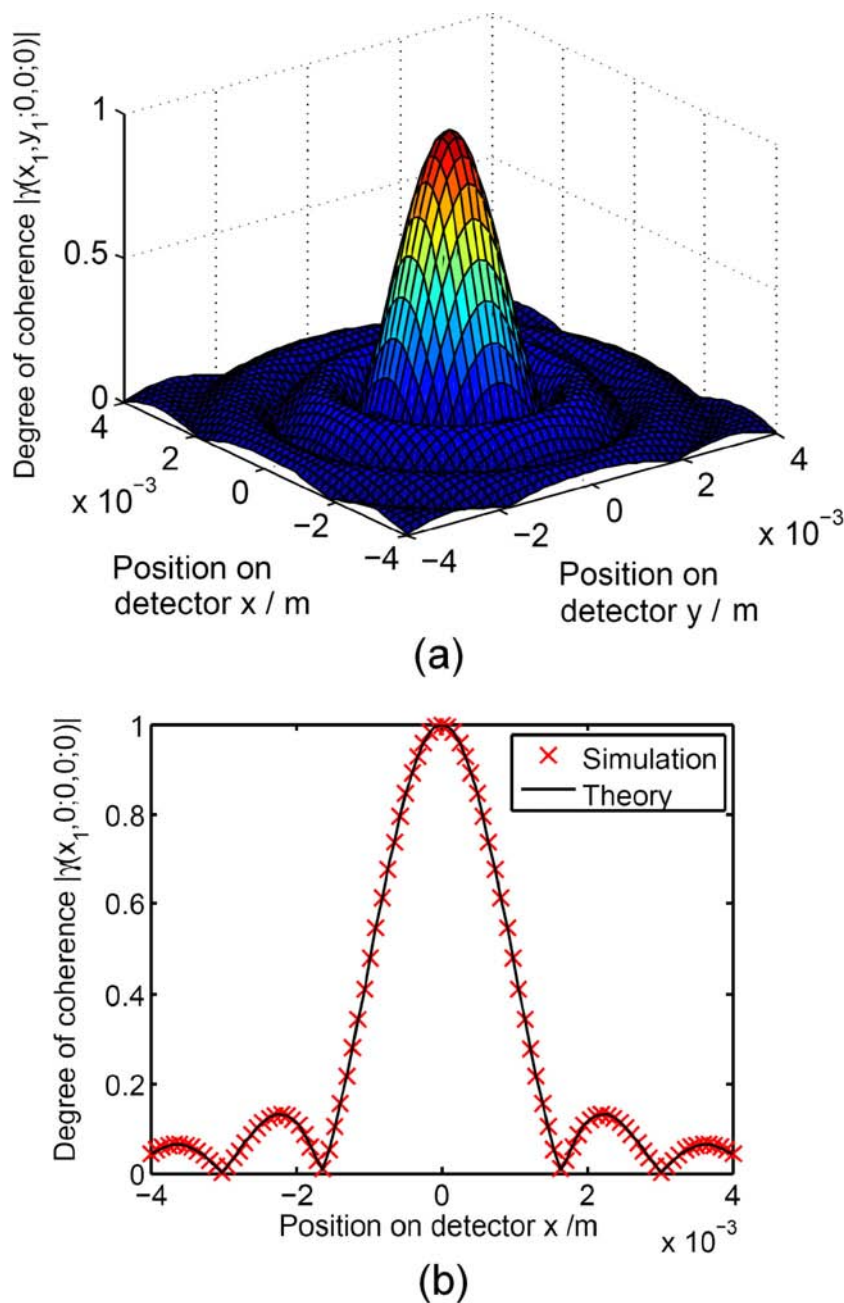


Figure 5.4: (a) 3D plot of the simulated degree of coherence regarding the centre of the detector plane for the single lens setup. (b) Cut along the x-axis of the plot in (a). The solid line indicates the theoretical description using ABCD-matrix formalism.

5.6 Investigation of a Two-Tandemarray Microlens Beam Homogenizer

Figure 5.5 shows a practical beam homogenizer system which is typically used in projection applications. This system cannot be easily modeled with analytical approaches. In the following, its coherence properties are investigated using the simulation tool. The homogenizer setup consists of two microlens-stripe arrays which are rotated by 90 degrees with respect to each other which is depicted in Fig. 5.6, a condenser lens and a field lens.

Each microlens-stripe array has parallel lens stripes on its front and backside. The rectangular area which is homogeneously illuminated is indicated. Its size is about 15 mm x 8 mm. This corresponds to the position where a transmissive light valve (LCD panel) would be placed to be imaged onto the screen. In the simulations a detector of

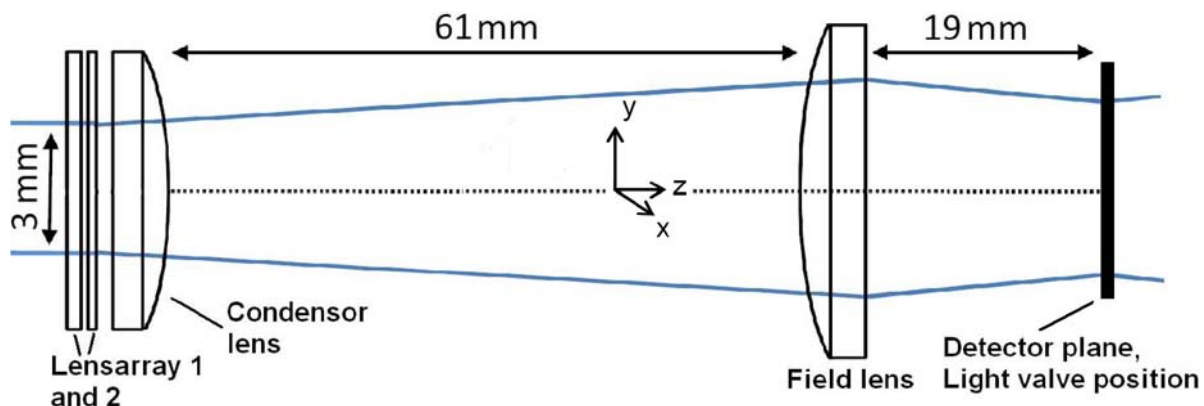


Figure 5.5: Schematic of the investigated two-tandemarray microlens beam homogenizer setup.

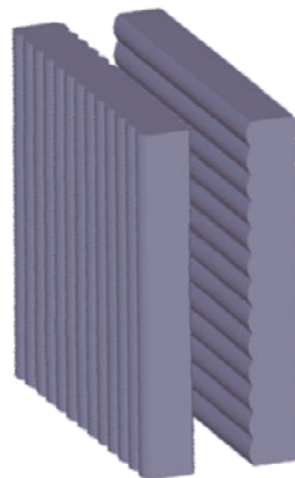


Figure 5.6: Schematic of the two-tandemarray microlens beam homogenizer.

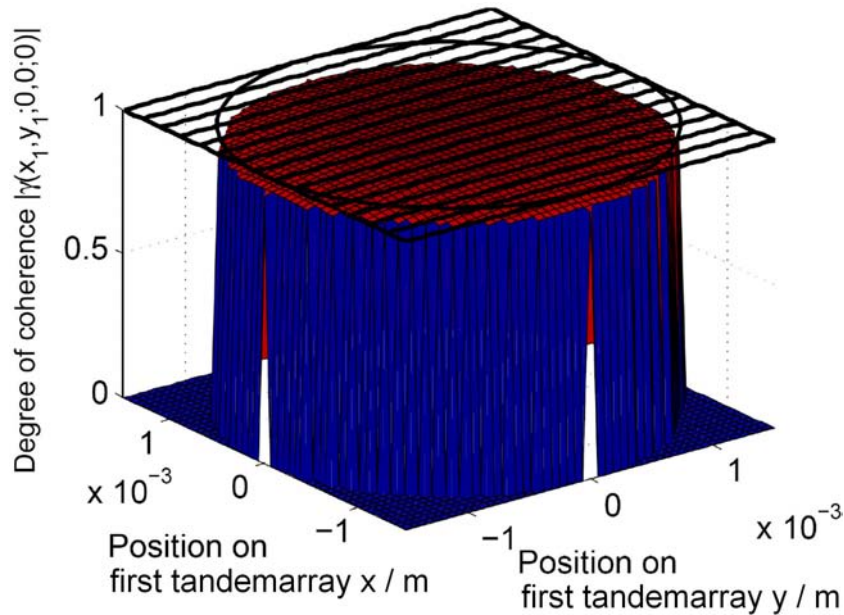


Figure 5.7: 3D plot of the degree of coherence regarding the centre of the fully coherent illumination spot on the first tandemarray of the beam homogenizer.

2 mm \times 2 mm size is chosen which consists of 49×49 pixels and which is placed at this position. The first illumination situation of the beam homogenizer is depicted in Fig. 5.7.

The stripes on top of the figure indicate the size of the microlens stripes of the first tandemarray, the black circle indicates the size of the 3 mm illumination spot on the first tandemarray. It is illuminated quasi-parallel with monochromatic, spatially fully coherent light, i.e., the degree of coherence is practically 1 over the whole illumination spot. This was achieved by placing a spatially fully incoherent, monochromatic, uniform, circular source with a diameter of 2 mm and a full opening angle of 0.0086 degrees for each source fan in a distance of 20 m from the first tandemarray. This illumination situation is comparable to monochromatic illumination with a fully coherent, single mode laser beam. The source is circular and consists of approximately 7,200 uniformly arranged, equally weighted point sources, each of which emits 700,000 equiangular rays. Approximately 15 rays per source fan fall into each detector pixel. The simulated degree of coherence $|\gamma|$ regarding the centre point of the detector is depicted in Fig. 5.8.

It can be seen that besides the central peak numerous side maxima of considerable height occur and a comb like structure is visible. The resulting intensity distribution in the detector plane is depicted in Fig. 5.9. A grid like intensity modulation is clearly visible which comes from the coherent superposition of the light from different lens stripes. Obviously, this counteracts the typically intended function of a beam homogenizer which is to achieve a homogeneously illuminated area.

As mentioned above, the two-tandemarray microlens beam homogenizer system cannot easily be quantitatively modeled. However, the results are in qualitative agreement with findings in [121], where the fully coherent illumination of a simple single monoarray microlens beam homogenizer is modeled. A schematic of the modeled homogenizer was already shown in Fig. 4.4 in Chapter 4.2. For this simple homogenizer system the authors

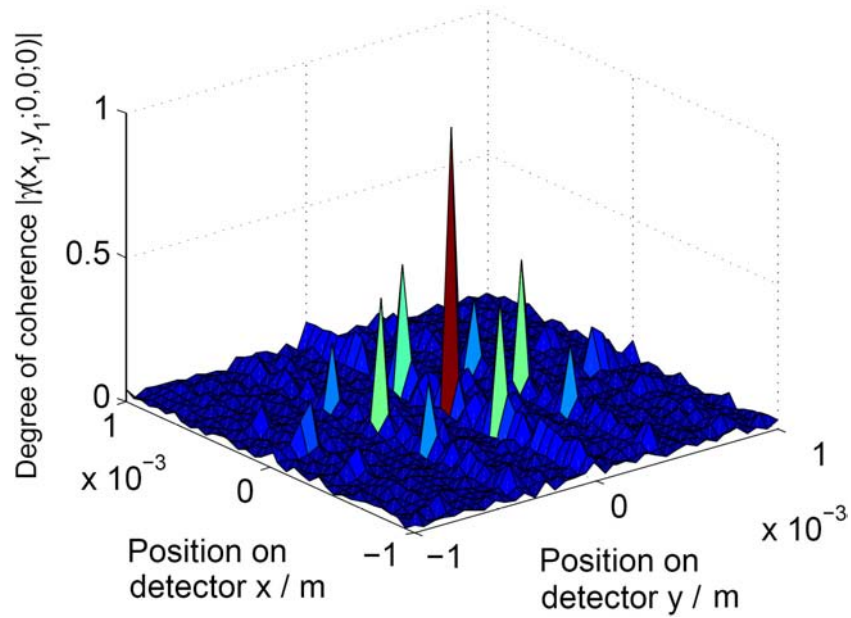


Figure 5.8: 3D plot of the simulated degree of coherence regarding the centre of the detector plane for the two-tandemarray microlens beam homogenizer for fully coherent, quasi-parallel illumination.

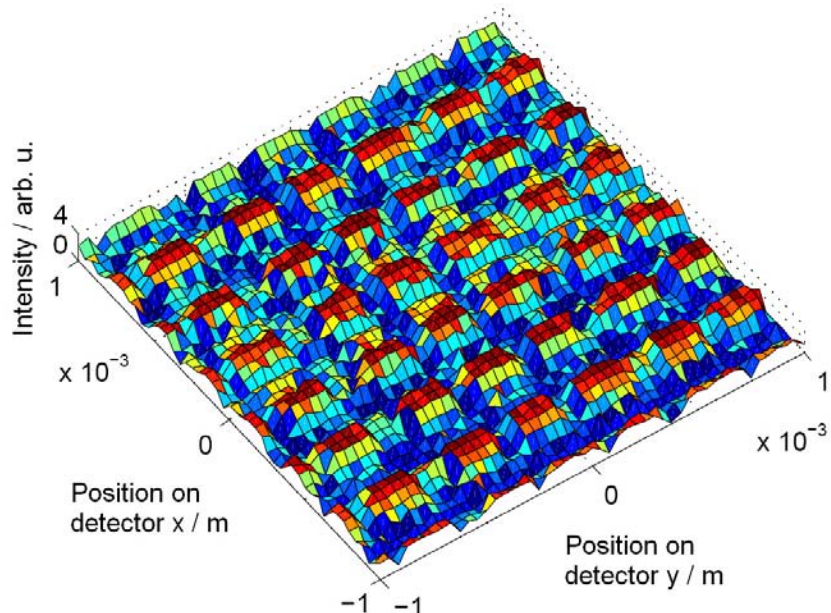


Figure 5.9: 3D plot of the intensity distribution for fully coherent illumination of the beam homogenizer. A grid like interference pattern is clearly visible.

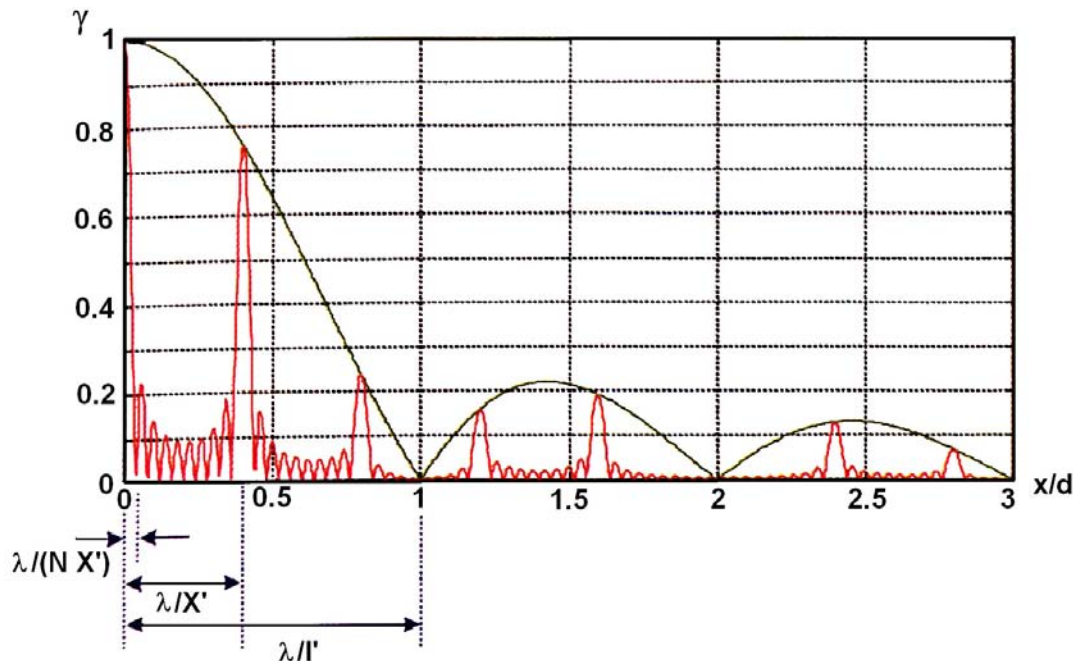


Figure 5.10: Degree of coherence (red line) in the homogenized plane of a single monoarray microlens beam homogenizer as depicted in Fig. 4.4 under fully coherent illumination, taken from [121].

in [121] analytically model the resulting degree of coherence in the homogenized plane which is depicted as a red line in Fig. 5.10. It is influenced by two terms: First, a fast oscillating interference term which is determined by the coherent superposition of light from the different homogenizer array lenses. Second, a slowly varying envelope function coming from the physical lens profiles (black line in Fig. 5.10). The resulting intensity distribution also corresponds to a grating diffraction and shows a grid like modulation. A detailed discussion can be found in [121].

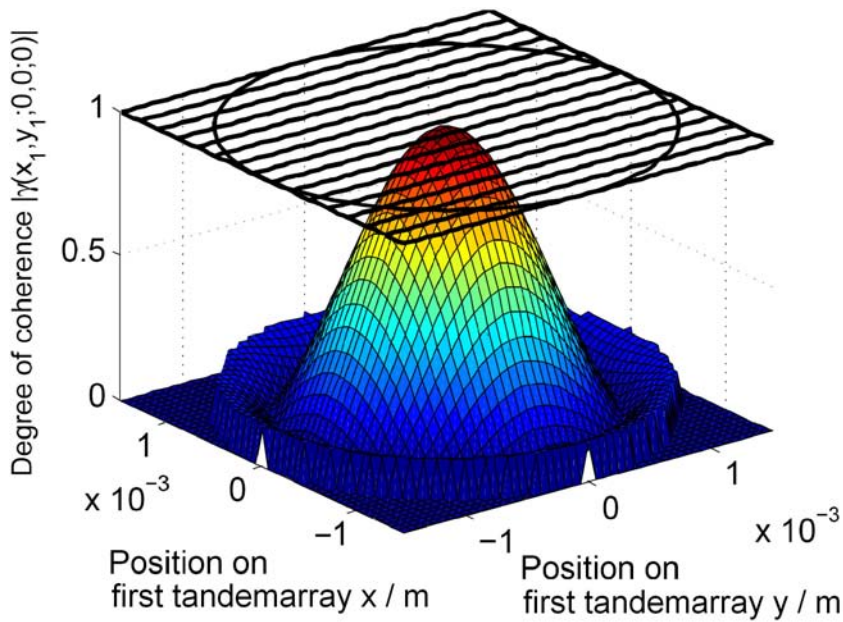


Figure 5.11: 3D plot of the degree of coherence regarding the centre of the spatially partially coherent illumination spot on the first tandemarray of the beam homogenizer.

Now a partially coherent illumination of the two-tandem beam homogenizer is investigated. The illumination situation is depicted in Fig. 5.11, where the stripes again indicate the size of the microlens stripes of the first tandemarray and the black circle indicates again the size of the illumination spot. It is illuminated quasi-parallel with monochromatic light of reduced spatial coherence. The coherence radius is comparable to the diameter of one microlens stripe. This was achieved by placing a spatially fully incoherent, monochromatic, uniform, circular source with a diameter of 2 mm in a distance of 3 m from the first tandemarray. By choosing an opening angle of 0.1 degrees for each source fan, again an illumination spot diameter of 3 mm is realized. This illumination situation is comparable to the experiments described in [143] and Chapter 8 of this thesis, where a quasi-homogeneous broad-area vertical-cavity surface-emitting laser is used to illuminate a similar beam homogenizer. The simulated source again consists of approximately 7,200 uniformly arranged, equally weighted point sources each of which emits a fan consisting of 700,000 equiangular rays. This results in about 15 rays per source fan in each detector pixel.

The simulated degree of coherence $|\gamma|$ regarding the centre point of the detector is depicted in Fig. 5.12. It can be seen that the number and height of the side maxima is drastically reduced. This reduction can be accounted to the partially coherent superposition of light from microlens stripes which are illuminated partially coherent. In [144] this effect is called “coherence scrambling effect”. There, it is shown experimentally that this reduces the typically unwanted intensity modulation in the detector plane. The simulated intensity distribution in the detector plane is depicted in Fig. 5.13. It can be clearly seen that the intensity distribution is much more homogeneous and no grid like intensity distribution is visible. The resolution of the shown simulations of the homogenizer system are not high enough to extract the finest details of the oscillation of $|\gamma|$. The simulation time of the two illumination situations was 71 hours each.

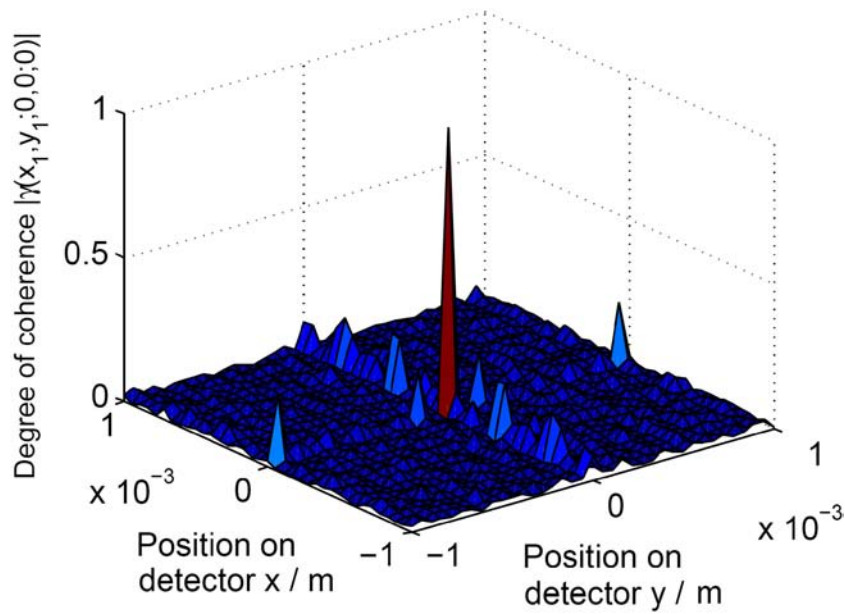


Figure 5.12: 3D plot of the simulated degree of coherence regarding the centre of the detector plane for the two-tandemarray microlens beam homogenizer for spatially partially coherent, quasi-parallel illumination.

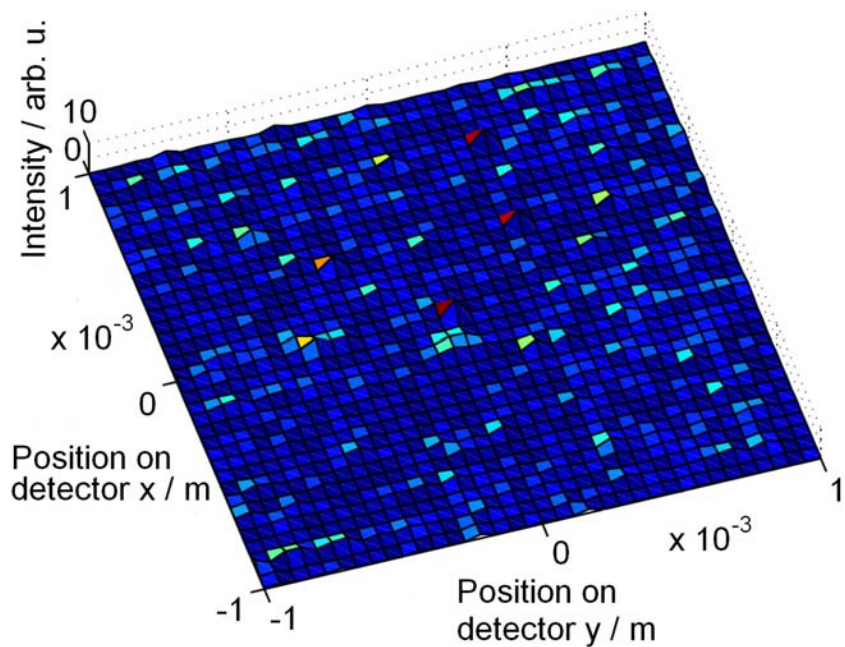


Figure 5.13: 3D plot of the intensity distribution for partially coherent illumination of the beam homogenizer. The interference pattern is no longer visible.

5.7 Future Extensions of the Simulation Tool

The tool does not yet cover any effects of diffraction in its current form. However, methods exist which extend geometrical optics to include diffraction [145]. These methods can possibly be adapted to further improve the tool. Furthermore, an extension to account for polarization can be considered. The most important future task is to find a method to quantify the accuracy of simulation results. The number of point sources and their distance, the number of rays per point source, the detector's pixel size and pixel number and the number of rays from each point source falling into each detector pixel are parameters which influence the simulation results. The standard deviation of the optical path lengths σ_{opl} of the rays from a point source in a detector pixel is a promising starting point. It is obvious that a larger standard deviation of the optical path lengths of the rays in a pixel requires more rays per pixel to give sufficient statistical averaging and smooth results. For a simulated setup $\bar{\sigma}_{opl}$ is therefore calculated, which is the mean value of the standard deviations of the optical path lengths of the rays per point source in each detector pixel. The corresponding maximum value of these standard deviations is $\sigma_{opl,max}$. For the free space propagation setup shown above, $\bar{\sigma}_{opl}$ was approximately 396 nm and $\sigma_{opl,max}$ was approximately 975 nm. For the single lens setup, the corresponding values were $\bar{\sigma}_{opl} \approx 13.5$ nm and $\sigma_{opl,max} \approx 31.6$ nm. These values led to simulation results which showed excellent agreement to theory. In case of the simulated beam homogenizer, the corresponding values were $\bar{\sigma}_{opl} \approx 37.4$ μm and $\sigma_{opl,max} \approx 104.9$ μm . These values are about a factor of 100 larger than those from the free space setup simulation and about a factor of 3,000 larger than those of the single lens setup simulation. This can explain the coarse simulation results of the beam homogenizer setup. Simulations with higher resolution of this system are currently performed. Therefore, the size of the detector pixels has to be decreased in order to increase image resolution, and the number of rays per point source has to be increased by a larger factor in order to improve the statistical averaging per pixel.

5.8 Chapter Summary and Conclusion

The functional extension of a standard raytracing software was presented. Optical fields with different temporal and spatial coherence properties are represented by spherical waves. The extended tool still contains the original standard raytracing capabilities. The intensity distribution as well as the mutual coherence function or the complex degree of coherence can be calculated at arbitrary positions in an investigated system. So, standard raytracing simulations can be combined with simulations to investigate the coherence properties of optical systems. It was shown in Chapter 4 that these can influence the speckle contrast perceived by an observer looking onto a screen. Monochromatic coherence simulations of a free space optical system and a single lens system which are in excellent agreement with theory were exemplarily shown. Furthermore, investigations of the coherence properties of a practical two-tandemarray microlens beam homogenizer system under different illumination conditions were presented. The tool can therefore be used to simulate and investigate the coherence and speckle properties of optical systems.

Chapter 6

Speckle Reduction With Volume Scattering Projection Screens

In this chapter, a method to determine the speckle properties of volume scattering front projection screens is presented. Various practical front projection screens will be investigated and modeled. It will be shown that the proper selection of a screen with large volume roughness is important to achieve low speckle contrast values already with moderate illumination bandwidths.¹

6.1 Introduction

As already mentioned, speckle contrast reduction can be achieved with the use of an illumination source with reduced spatial or temporal coherence to produce (at least partly) decorrelated speckle patterns which superimpose on intensity basis. The modeling and calculation of the resulting speckle contrast reduction can be demanding if an illumination source with reduced spatial coherence is used. The speckle contrast value perceived by an observer is dependent on the coherence properties of the light on the screen and the spatial resolution of the observer on the screen (see Section 4.3). It was shown in Chapter 5 that the spatial coherence properties of the light are influenced by its propagation through the projection system. So, all system components (lenses, beam homogenizer, ...) have to be considered to model the coherence properties and the resulting speckle contrast.

In this chapter, illumination sources of full spatial coherence are assumed and it is focused on speckle reduction caused by a reduced temporal coherence of the illumination source (broadband source). In this case the resulting speckle contrast values are then independent of the spatial resolution of the observer on the screen. Furthermore, the projection system does not influence the temporal coherence properties of laser light in practical systems (if no additional color filters are used to decrease the bandwidth of the source and higher order optical processes are negligible). Therefore, the effectiveness of this method to reduce speckle disturbance is less dependent on a specific system

¹Parts of this chapter are published in: F. Riechert, F. Glöckler, and U. Lemmer, "Method to determine the speckle characteristics of front projection screens," Appl. Opt. **48**, Issue 7, 1316-1321 (2009).

setup. However, the resulting speckle contrast values are dependent on the depolarization characteristic and volume scattering path length distribution of the photons in the used projection screen. In the following, seven different typical volume scattering projection screens are investigated in a backscattering geometry. These are: A sheet of standard 80 g/m² copypaper of approximately 100 µm thickness glued on a cardboard, a white block of Teflon of 10 mm thickness, an approximately 210 µm thick foil of white OP.DI.MA (optical diffusive material) on a black beam block, a double layer of the OP.DI.MA foil on a black beam block and three samples from commercially available projection screens, which were fixed on a beam block. These are named “Sample 1, 2 and 3” in the following.

The remainder of the chapter is organized as follows: In Section 6.2, the speckle contrast reduction resulting from depolarizing scattering and from the reduced temporal coherence of the illumination source is modeled for volume scattering screens. Seven different screens are investigated in a backscattering geometry for illumination with 808 nm light. In Section 6.3, the experimental setups used to measure the depolarization and the scattering path time distributions of the light in the different screens are shown and described. For the determination of the latter, a streak camera setup is used to measure the temporal broadening of ultrashort 50 fs light pulses scattered in the screens. In Section 6.4, the experimental results are presented and interpreted in order to determine the speckle contrast reducing capabilities of the screens. In Section 6.5, an outlook on future work and possible adaptations of the presented method is given.

6.2 Modeling of Speckle Contrast Reduction

6.2.1 Depolarization

A laser source is typically fully linearly polarized, i.e. its degree of polarization P has a value of 1. When polarized light is multiply scattered, the degree of polarization can drop and hence speckle contrast reduction can result. As mentioned in Chapter 2 (Eq. (2.7)), the resulting speckle contrast $C_{Pol.}$ of a speckle pattern produced for partly depolarizing scattering of a fully coherent light source on or in a rough target is given by

$$C_{Pol.} = \sqrt{\frac{1 + P^2}{2}}. \quad (6.1)$$

In case of fully depolarizing scattering, P has a value of zero and the resulting speckle contrast is reduced by a factor of $1/\sqrt{2}$. In the following, the degrees of polarization of originally linearly polarized light after backscattering from the investigated screens is measured and the resulting speckle contrast reduction factors are determined.

6.2.2 Broadband Illumination of a Rough Target

Following [9] and Chapter 4, the speckle contrast $C_{broad.}$ for normal illumination and normal observation of a scattering target with a polarized, spatially fully coherent but broadband source is approximately given by

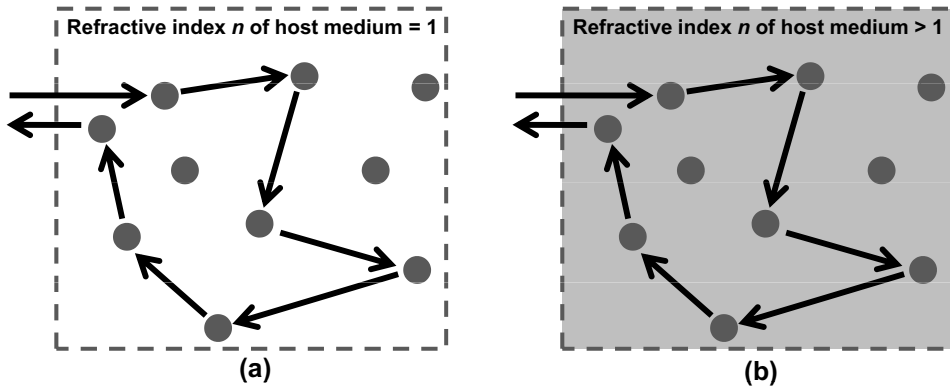


Figure 6.1: Schematic of a typical volume scattering path of a backscattered photon which was incident under normal direction. In case (a) it propagates mainly in air, in case (b) it propagates in a screen material with refractive index $n > 1$.

$$C_{broad.} = \sqrt{\int_{-\infty}^{\infty} K_{\hat{G}}(\Delta\nu) |M_l(\Delta q_z)|^2 d\Delta\nu}, \quad (6.2)$$

It was already mentioned that, for a Gaussian shaped spectrum of the illumination source with $1/e$ -width $\delta\nu$, the autocorrelation function of the source's normalized power spectrum $K_{\hat{G}}(\Delta\nu)$ is given by [9]

$$K_{\hat{G}}(\Delta\nu) = \sqrt{\frac{2}{\pi\delta\nu^2}} \exp\left(-\frac{2\Delta\nu^2}{\delta\nu^2}\right), \quad (6.3)$$

where $\Delta\nu$ is a frequency shift. Following [9] and Chapter 4, the characteristic function corresponding to the path length distribution $p(l)$ of the scattered photons $M_l(\Delta q_z)$ is the Fourier transform of $p(l)$. In many practical cases, $p(l)$ can be well approximated by a Gaussian shaped curve and $|M_l(\Delta q_z)|^2$ can then be written as $\exp(-\sigma_l^2 \Delta q_z^2)$, where σ_l is the standard deviation of the scattering path length distribution of the scattered photons. For scattering on a surface with Gaussian distribution of its height values, σ_l corresponds to the root-mean-square *surface roughness*. For the case of volume scattering σ_l is referred to with *volume roughness* in the following.

$\Delta q_z = |q_{1,z} - q_{2,z}|$, where $q_{1,z}$ and $q_{2,z}$ are again the z-components of the scattering vectors of two light waves of different frequencies, which are normal to the scattering target. Figure 6.1(a) shows a sketch of a material which consists of scattering centers with air in between. This can be some porous material for example. In this case light propagates mainly in air and is scattered or reflected from scattering centers or material boundaries. The scattering centers need not to be of spherical shape but can also be of different shape. Figure 6.1(b) sketches a situation, where light mainly propagates in a host material with (effective) refractive index $n > 1$. For the investigated backscattering geometry $\Delta q_z \approx 2\pi n \Delta\nu / c$. For both situations a typical propagation path of a backscattered photon which was incident under normal direction is indicated in Fig. 6.1. It can be seen that the second case reduces to the first case for $n \rightarrow 1$.

Inserting all this in Eq. (6.2) yields a resulting speckle contrast $C_{broad.}$ for normal illumination and observation of a volume scattering target in a backscattering geometry of

$$C_{broad.} = \left[1 + 2\pi^2 n^2 \left(\frac{\delta\lambda}{\bar{\lambda}} \right)^2 \left(\frac{\sigma_l}{\bar{\lambda}} \right)^2 \right]^{-\frac{1}{4}}, \quad (6.4)$$

where $\delta\lambda$ is the 1/e-width of the wavelength spectrum of the source and $\bar{\lambda}$ is its mean emission wavelength and $\delta\lambda \ll \bar{\lambda}$ has to hold.

The overall expected speckle contrast C when depolarization and broadband illumination of the rough screen are taken into account is given by the product of the two corresponding speckle contrast reduction factors:

$$C = C_{Pol.} C_{broad.} \quad (6.5)$$

6.3 Experimental Setups

The determination of the surface roughness of a material can be done at low expense, e.g. via stylus techniques or light scattering at the material's surface [146]. In contrast, the determination of the volume roughness is more complex. One method to determine the scattering path length distribution $p(l)$ of volume scattering materials is described in [147],[148]. Here, the material is illuminated with three different wavelengths and $p(l)$ can be extracted from third order correlations of the three created speckle patterns.

Another method is to send a short light pulse into the volume scattering material and to measure the scattered light signal. Some photons will have a short scattering path, i.e., they exhibit only a few scattering events before they leave the material and are detected, others will travel longer paths. This technique is widely used to study the scattering characteristics of turbid media like clouds [149], biological tissue [150] or suspensions containing dispersed scattering particles [151]. If the light pulse sent into the material was temporally infinitely short, the measured signal of scattered photons would exactly match the distribution of the times the photons need to travel the scattering paths $p(\tau)$. If a temporally expanded light pulse is used, the scattered light signal is the temporal convolution of the pulse's temporal intensity distribution and $p(\tau)$.

$p(\tau)$ is expected to have widths of several picoseconds for projection screens illuminated in a backscattering geometry (see for example Section 6.4). To measure such short light signals, correlation methods can be used [152]. A possible experimental setup is sketched in Fig. 6.2.

An ultrashort laser pulse is split via a beam splitter. The reference pulse propagates through a delay section and is sent into a second harmonic generation (SHG) crystal under a given angle. The other part of the pulse (probe pulse) illuminates the screen. It is volume scattered and temporally broadened. As mentioned above, the scattered probe pulse corresponds to the temporal convolution of the reference pulse with the path length distribution of the scattered photons. In a reflection setup, backscattered light

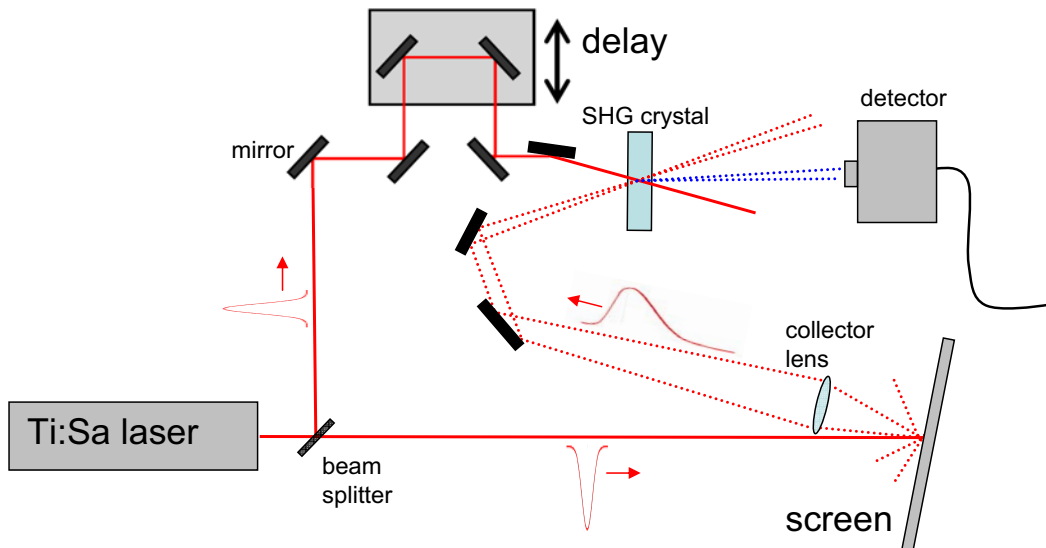


Figure 6.2: Schematic setup for measurement of the path length distribution via intensity crosscorrelation.

has to be collected via a lens and has to be focused into the second harmonic generation crystal. The angle of incidence has to match to the angle of incidence of the reference pulse. In the crossing region of the two pulses, an amount of frequency doubled light will be created in forward direction. The measurable signal of frequency doubled light is proportional to the intensity crosscorrelation between the reference and the probe beam. If the frequency doubled light signal is measured for different delays of the reference beam, the temporally broadened pulse can be “sampled” with the reference pulse. If the shape and length of the reference pulse are known (mostly sech^2 or Gaussian profile for mode-locked lasers) the probe beam and the path length distribution could be determined. There might arise numerous practical and experimental difficulties which can make correlation methods experimentally demanding: The light which is backscattered from the screen is no longer a collimated beam, but highly diffuse for volume scattering screens. It will be difficult to collect sufficient backscattered light and focus it highly directional into the SHG crystal. For efficient second harmonic generation, high intensities have to be achieved inside the crystal. Therefore, only few frequency doubled photons might be produced. To measure these potentially small signals, a lock-in amplifier would have to be used.

A more straightforward approach is a setup with a streak camera (Hamamatsu C 5680) equipped with a sweep unit (M5675 Synchroscan). It is used to measure the backscattered light pulses. The setup is depicted in Fig. 6.3.

The titanium-sapphire laser (Ti:Sa) (Spectra-Physics, type Tsunami) produces sech -shaped pulses with a full width at half maximum (FWHM) duration of approximately 50 fs. The beam has a spatial width of approximately 0.5 mm on the screen. If a laser pulse is measured directly (without temporal broadening because of volume scattering) with the streak camera, the pulse cannot be resolved with the camera and signals as depicted in Fig. 6.4 are measured.

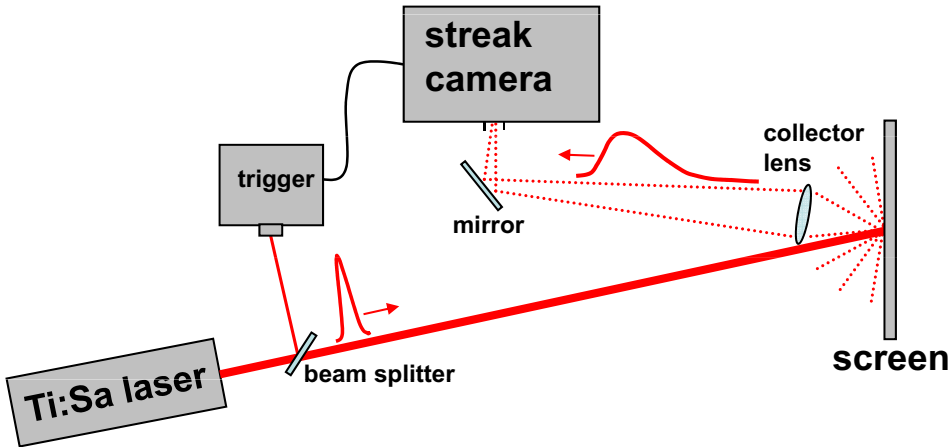


Figure 6.3: Schematic of the streak camera setup.

It can be seen that the measured signal can be well approximated by a Gaussian shaped curve. This is because the measured signals are the convolution of the *sech*-shaped laser pulses and the camera's temporal impulse response, which can be both well approximated by Gaussian shaped curves. Ten reference measurements of unscattered pulses were performed and a standard deviation σ_τ of the Gaussian approximation of 1.062 ± 0.069 ps was determined.

The screen's distributions of the scattering path length $p(l)$ could be determined from the distribution of the measured scattering path times $p(\tau)$. To do so, the scattering path times have to be multiplied by the speed of light in air c in case of a screen, where light propagates mainly in air. For a screen in which light propagates in a screen material with (effective) refractive index $n > 1$, the reduced speed of light has to be considered and $p(l) = p(\frac{c}{n}\tau)$. The standard deviation of the path length distribution σ_l (= volume roughness) can be simply calculated by a multiplication of the standard deviation of the scattering path time distribution σ_τ with the factor c/n , i.e. $\sigma_l = \frac{c}{n}\sigma_\tau$. This shows that it is not necessary to determine the (effective) refractive index n of a screen host material in which the scattered light potentially propagates in order to model the speckle contrast reduction because the factors n^2 and $1/n^2$ in Eq. (6.4) cancel each other.

The Ti:Sa laser used in the streak camera measurements is fully linearly polarized. Therefore, the resulting degrees of polarization P after backscattering from the investigated screens could be simply measured by introducing a linear polarizer followed by a powermeter behind the collector lens. The intensities in the original Ti:Sa polarization direction and in a orthogonal direction in order to calculate P were determined.

6.4 Experimental Results and Interpretation

6.4.1 Depolarization

In Tab. 6.1 the measured coefficients of polarization P after backscattering of the fully linearly polarized Ti:Sa pulses from the screens are given. Furthermore, the resulting speckle contrast reduction factors are indicated which were calculated using Eq. (6.1).

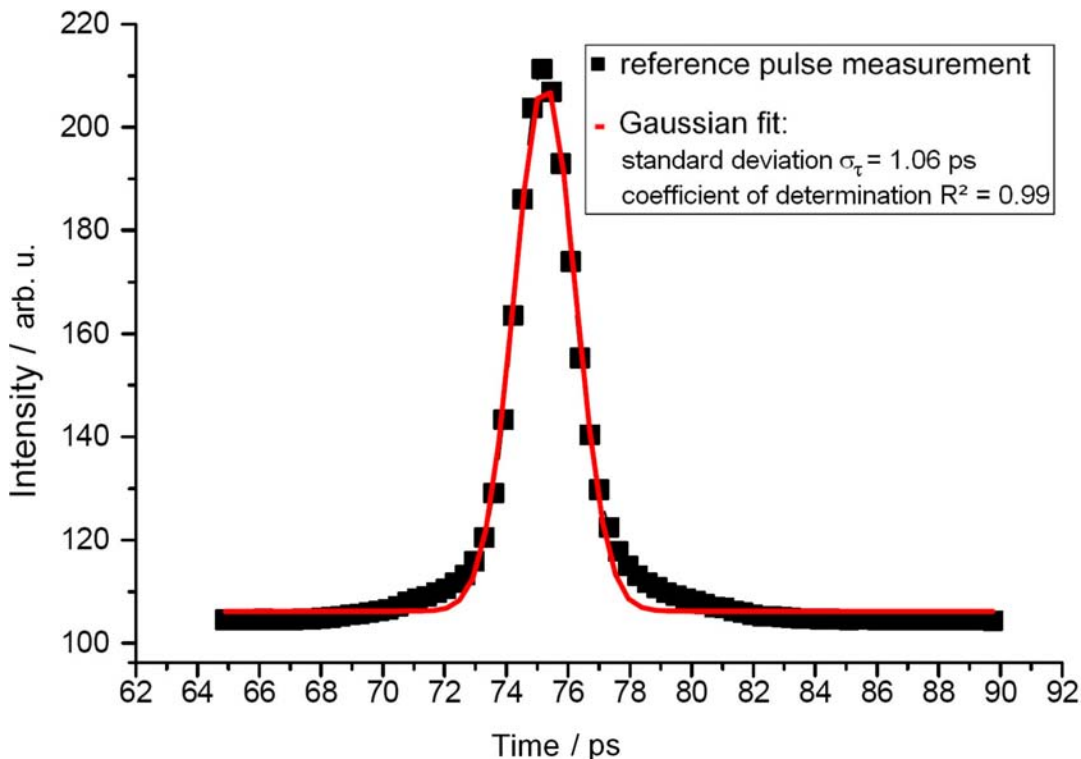


Figure 6.4: Plot of a typical measurement of unscattered Ti:Sa pulses and its approximation by a Gaussian fit.

It can be seen that the highest degree of polarization of $P = 0.224$ remains for illumination of the Sample 2 screen. In this case the intensity in the original polarization direction is still about 1.7 times higher than in the orthogonal direction. Nevertheless, the speckle contrast reduction factor does not deviate more than 4% from the value $1/\sqrt{2}$ for full depolarization. Therefore, achievement of full depolarization is not that critical in order to achieve speckle contrast reduction close to the value of $1/\sqrt{2}$.

6.4.2 Scattering Path Time Distributions of the Screens

The signals backscattered from the screens vary in their width, however their shapes are similar. This agrees well with different simulated scattering path length distributions for example in [153] or measured distributions for light scattering in paper in [154]. The signals backscattered from the screens are the convolution of the reference signal for the unscattered pulses and the screen's scattering path time distributions $p(\tau)$. As an example a typical measurement of the investigated OP.DI.MA screen is shown in Fig. 6.5. It can be seen that the measured curves can again be well approximated by Gaussian distributions even though the distributions shows a tail to longer times. In order to determine the screen's $p(\tau)$, the Gaussian fits of the measured signals are deconvolved with the Gaussian fit of the mean reference pulse of 1.062 ps standard deviation.

For each of the seven investigated screens several measurements were taken and Gaussian error propagation was performed. The mean values of the screen's standard deviations of the scattering path time distributions and the corresponding one sigma

Table 6.1: Determined coefficients of polarization P after scattering in the screens and resulting speckle contrast reduction factors as calculated according to Eq. (6.1).

Screen	P after scattering	Resulting speckle contrast reduction factor
Copypaper	0.076	0.7091
Teflon	0.022	0.7073
OP.DI.MA	0.041	0.7077
OP.DI.MA double	0.024	0.7073
Sample 1	0.175	0.7179
Sample 2	0.262	0.7309
Sample 3	0.224	0.7246

Table 6.2: Determined standard deviations σ_τ of the scattering path time distributions $p(\tau)$ of the investigated screens

Screen	Standard deviation σ_τ of $p(\tau)$ / ps
Copypaper	1.681 ± 0.033
Teflon	1.873 ± 0.056
OP.DI.MA	1.945 ± 0.080
OP.DI.MA double	2.962 ± 0.127
Sample 1	1.578 ± 0.011
Sample 2	1.409 ± 0.023
Sample 3	1.541 ± 0.091

error ranges are given in Tab. 6.2.

By multiplying the two speckle contrast reduction factors for depolarization and broadband illumination, the expected speckle contrast values for illumination of the screens with the Ti:Sa pulses can be calculated. The expected values are given in the third column of Tab. 6.3.

Again Gaussian error propagation of the uncertainties of the screen's scattering path time distributions was performed.

To check the model, the screens were illuminated with a pulsed, fully linearly polarized Ti:Sa laser source which emits in the TEM_{00} mode. Its center wavelength $\bar{\lambda}$ was 808 nm and its 1/e-bandwidth $\delta\lambda$ was 20 nm. The produced speckle patterns were captured via a CCD camera (TechnoTeam, type LMK 98-3). The speckle contrasts for the different screens were extracted and it was accounted for CCD camera noise. The measured contrast values are given in the second column of Tab. 6.3.

It can be seen that good agreement between the measured and the expected speckle contrast values is achieved. For the copypaper screen, the OP.DI.MA foil, the Teflon block and Sample 1 the measured speckle contrast values are somewhat smaller than the modeled values. For Sample 2 and Sample 3, the measured values are marginally larger than the expected ones. The best coincidence between model and measurement is

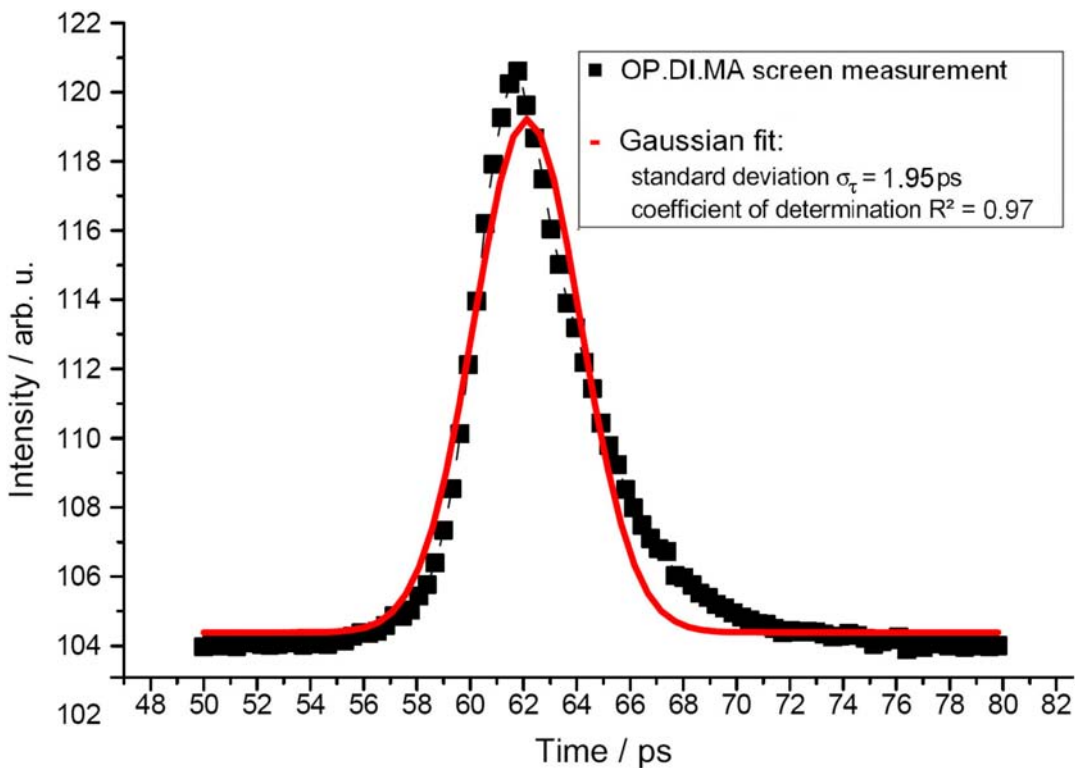


Figure 6.5: Plot of a typical measurement of Ti:Sa pulses backscattered from the OP.DI.MA screen and its approximation by a Gaussian fit.

achieved for the screen which consists of two layers of the OP.DI.MA foil. The deviations between measurement and model might arise from the approximation of the scattering path time distributions by Gaussian distributions. In Fig. 6.5 it can be seen that this approximation does only partially account for the distribution's tails at longer scattering path times, which were observable for most of the screens. This can also be the reason why a slightly higher speckle contrast for the OP.DI.MA screen was measured compared to the Teflon block, even though the OP.DI.MA screen's scattering path time distribution has a slightly larger standard deviation.

If the determined models are now applied to the investigated screens, the resulting speckle contrast values for spatially fully coherent illumination of the screens with a light source of 808 nm mean wavelength and different bandwidths can be deduced. Figure 6.6 shows a plot of this for the mean values of the determined standard deviations of the scattering path time distributions of the screens. Furthermore, the additional speckle contrast reduction factor because of depolarization is taken into account. It can be seen that the resulting speckle contrast values can differ more than 30% for the different screens under identical illumination conditions. Especially for small illumination bandwidth a proper selection of a projection screen is essential to achieve low speckle contrast values.

Table 6.3: Measured and expected speckle contrast values (as calculated according to Eq. (6.5) for illumination of the screens with 20 nm bandwidth Ti:Sa pulses with 808 nm mean wavelength.

Screen	Measured speckle contrast / %	Expected speckle contrast / %
Copypaper	7.8	9.7 ± 0.3
Teflon	5.9	8.9 ± 0.2
OP.DI.MA	7.3	8.7 ± 0.3
OP.DI.MA double	6.6	6.7 ± 0.2
Sample 1	8.0	10.4 ± 0.3
Sample 2	13.4	11.9 ± 0.6
Sample 3	12.4	10.5 ± 0.6

6.5 Chapter Conclusion and Outlook

A method to determine the speckle characteristics of front projection screens in a backscattering geometry was presented. With this method seven different screens were investigated, their depolarization characteristics were measured and the resulting speckle contrast reduction for 808 nm light was determined. Furthermore, the scattering path time distributions of the screens for 808 nm light were measured and the resulting speckle contrast reduction for illumination of these screens with different bandwidths was modeled. The modeling of the speckle contrast reduction was verified with a reference measurement using broadband Ti:Sa illumination of the screens. The modeled speckle contrast values and those from the reference measurement show good agreement.

For two layers of OP.DI.MA foil used as screen, a standard deviation of the scattering path time distribution of about 2.962 ± 0.127 ps was determined, which is the largest value of all investigated screens. Therefore, its volume roughness would exceed the screen thickness by more than a factor of two, even if the screen would have a high refractive index of about two. The measured standard deviation of $p(\tau)$ could consequently be even larger if even more layers of OP.DI.MA foil would be used. This also holds for the copypaper and the Sample 3 screen because also their volume roughness exceeds the screen thickness.

It could be shown in this chapter that strongly depolarizing backscattering from the front projection screens is not that critical in order to achieve low speckle contrast values. A speckle contrast reduction close to the maximum value of $1/\sqrt{2}$ was achieved with all investigated screens. However, the proper selection of a screen with a broad scattering path time distribution, i.e., a large volume roughness, is essential to maximize the speckle reduction resulting from the illumination with light of reduced temporal coherence. In Chapter 8, a volume scattering screen will be combined with other methods for speckle reduction. It will be furthermore shown that volume scattering screens can also facilitate the angular decorrelation of statistically independent speckle patterns.

The investigation in this chapter was done at an illumination wavelength of 808 nm.

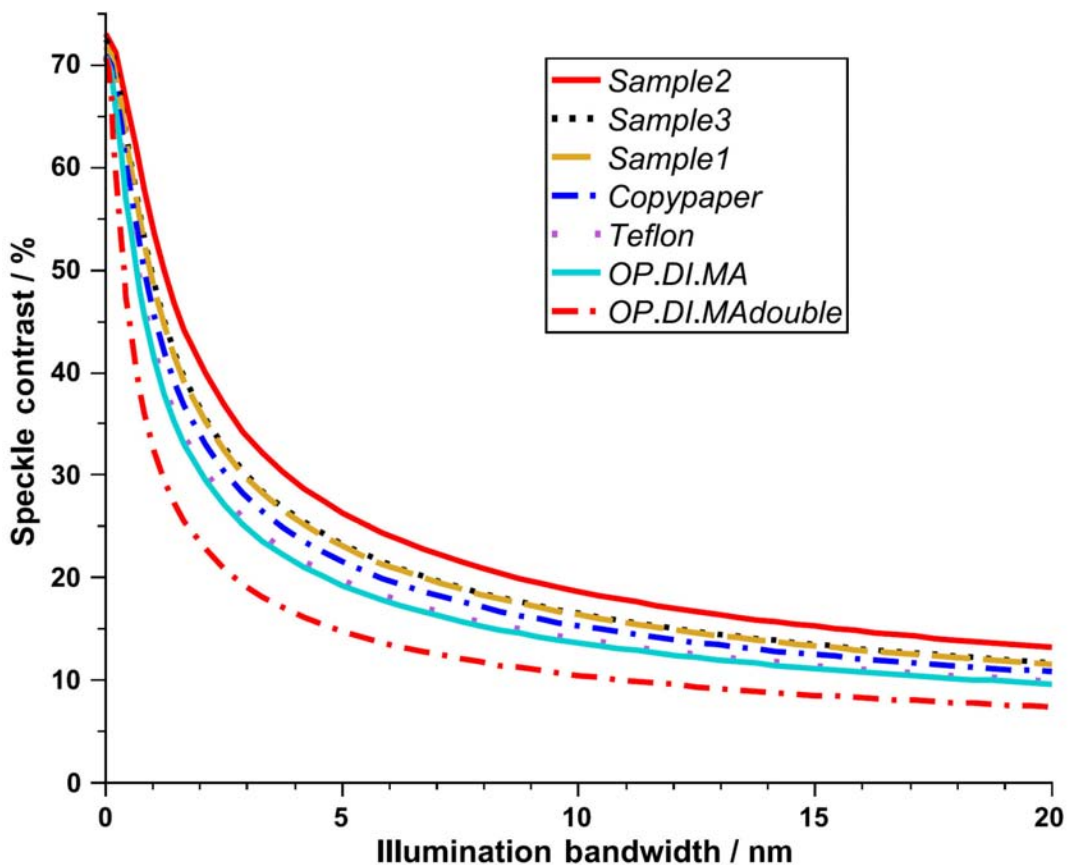


Figure 6.6: Plot of the modeled speckle contrast which results for illumination of the investigated screens with spatially fully coherent 808 nm light of different bandwidths.

In this case, the resulting speckle contrast reductions were not large enough to achieve speckle contrasts lower than the human observer disturbance limit of about 4% with illumination bandwidths which are reasonably small to be used in projection applications. The models and measurements presented in this chapter can be directly transferred to visible wavelength ranges. It has to be emphasized that for a constant volume roughness, the resulting speckle contrast values are smaller for a shorter mean illumination wavelength (see Eq. (6.4)). Furthermore, the volume roughnesses of the screens could be larger for shorter illumination wavelengths leading to further reduced speckle contrast values. Section 7.1 of this thesis and [143] indicate that the volume roughness of a paper screen can be more than a factor of 1.5 larger for 400 nm light as compared to 800 nm light.

The presented method to determine the speckle properties of front projection screens can also be used for transmissive projection screens with some changes. To do so, the modeling presented in Section 6.2 and the measurement setups presented in Section 6.3 have to be adapted. Furthermore, a numerical solution of the modeling presented in Section 6.2 could be considered in the future. This could help to avoid the systematic error which is done if the scattering path time distributions of the screens are approximated with Gaussian curves.

Chapter 7

Speckle Reduction With Colloidal-Dispersion-Filled Projection Screens

In this chapter, projection screens filled with colloidal dispersions are used to reduce the speckle contrast in laser projection applications. It will be shown that speckle contrast values below 3% can be achieved in an efficient way without the use of any additional components by multiple scattering in the colloidal dispersion.¹

7.1 Introduction

The insertion of moving or rotating diffusers into the laser beam is an effective strategy to achieve laser speckle contrast reduction. This is done for example in [123]. Another method is to move the projection screen itself in order to produce a time varying speckle pattern. Because of the integration time of the human eye, an observer will then perceive a reduced speckle contrast. As already mentioned, several configurations based on the moving screen method have been proposed [75],[123]-[126]. Mechanical movement of the potentially large projection screen is, however, not a favorable solution although motion amplitudes of only a few hundred microns can be sufficient to eliminate speckle [75]. A moving screen method might be used to reduce speckle in the first commercially available laser rear projection TV from Mitsubishi (see Chapter 3). In a personal communication one of the engineers from Mitsubishi stated that “the speckle problem was solved, however, it was solved costly” [155]. It was not further specified whether “costly” has to be understood in the sense of dollars or of light loss, power or the like. The TV uses four transportation screws to protect the internal screen from damage when the TV is shipped or moved [112]. This gives a strong indication that a moving screen method is used to eliminate speckle.

Here, rear projection screens filled with colloidal dispersions are used to achieve laser speckle reduction. In the dispersions, particles or droplets of the inner (dispersed) phase do Brownian movement [156] in a liquid outer phase. Laser light is multiply scattered from these moving scattering centers. In analogy to a moving screen, a time varying speckle pattern is created, which is temporally integrated by the eye of a human observer.

¹Parts of this chapter are published in: F. Riechert, G. Bastian, and U. Lemmer, “Laser speckle reduction via colloidal-dispersion-filled projection screens,” Appl. Opt. **48**, Issue 19, 3742-3749 (2009).

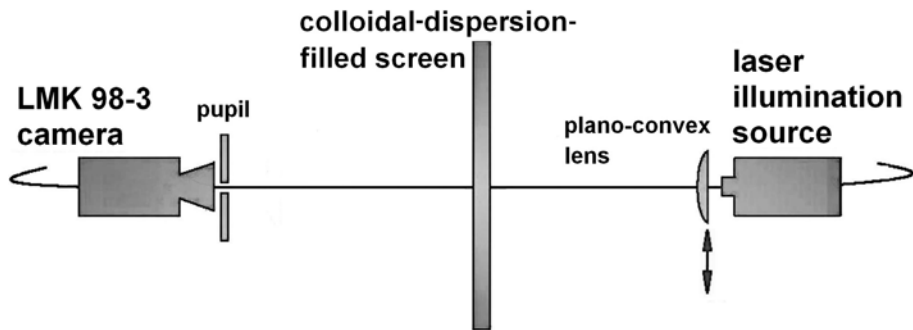


Figure 7.1: Setup to measure the speckle contrast (lens inserted) and the $1/e^2$ -radius of the laser beam after passage through the screen (lens removed). The camera images the screen which is filled with the colloidal dispersions. The thickness of the screen can be varied from approximately 0.1 to 5 mm.

Using colloidal dispersions, speckle contrast reduction is achieved via the intrinsic movement of the scattering globules, no mechanical movement of any component is required. The scattering of the laser light in a colloidal-dispersion-filled projection screen does, however, not only lead to intended speckle contrast reduction but also to unwanted blurring of an image which is projected onto the screen. Blurring can severely reduce image sharpness and image contrast. For these reasons blurring of projected images in a colloidal-dispersion-filled screen should be as low as possible. In the following, the two counteracting effects speckle contrast reduction and image blurring are measured and weighted against each other. Three different colloidal dispersions filled into rear projection (transmission) screens with variable screen thicknesses are investigated.

The remainder of the chapter is organized as follows: In Section 7.2, the experimental setup is described. The intended speckle reduction and the unwanted blurring are measured and compared for three different colloidal dispersions filled into transmission screens of different thicknesses in Section 7.3. In Section 7.4 and 7.5, blurring in the screens is simulated with Monte Carlo techniques. Furthermore, parameters of the colloidal-dispersion-filled screens which influence the resulting speckle contrast values are discussed. In Section 7.6, it is concluded that a high speckle contrast reduction at simultaneously low blurring can be achieved with a thin screen filled with a highly scattering colloidal dispersion with forward peaked scattering and a short outlook on future work is given.

7.2 Experimental Setup

Experiments were performed using the transmission setup sketched in Fig. 7.1. The laser source is a standard polarized diode pumped solid state laser which emits at 532 nm wavelength. The screen is built of two parallel glass side walls of 2.5 mm thickness with sealed sides. The distance between the glass side walls can be varied from about 0.1 mm to 5 mm, so the passage through different thicknesses of colloidal dispersion can be investigated. The screen used in the experiments has a size of about 20 cm x 20 cm. To do the speckle contrast measurements, a plano-convex lens is inserted into the beam path in order to expand the beam and to achieve a large illuminated area on the screen.

The speckle contrast is then evaluated in several regions of interest. A 12-bit linear CCD-camera (TechnoTeam, type LMK 98-3) is used which is properly aligned to image the screen plane. A pupil with an opening diameter of approximately 1 mm is placed in front of the camera to sufficiently enlarge the speckle size on the CCD chip. The size of a single speckle spot is approximately 6 x 6 CCD pixels in all measurements. This is large enough to properly extract speckle contrast values from the measured speckle images. To quantify the blurring in the screen the lens is removed and the $1/e^2$ -radii of the laser beam after passage through the screen with and without colloidal-dispersion filling are compared. By comparing these radii, blurring factors of the dispersion fillings can be determined. As mentioned above, blurring degrades image quality. However, also typical commercially available projection screens cause some intended beam blurring for reasons of light distribution. To quantify at least roughly the blurring which is acceptable in a colloidal-dispersion-filled screen, the blurring caused by a commercially available rear projection screen (Lumin Visual Technologies AG, type 360°) is measured. An increase of the $1/e^2$ -radius of the illumination beam by a factor of 1.7 (70%) was determined. This value is assumed to be the acceptable blurring of the dispersion filled screens in the following.

For the speckle measurements, the camera integration time has to be comparable to the integration time of the human eye. Many different values for the integration time of the human eye are reported in literature: 50 ms are reported in [75],[123] and [157], approximately 40 ms for practical illumination and projection situations are reported in [122] and only 10-15 ms for cone vision are reported in [158]. Therefore, measurements with 20 and 40 ms camera integration time are performed. The laser power incident onto the screen is tuned via neutral density filters to achieve the desired camera integration time. Ambient light was reduced as far as possible during the measurements.

For practical applicability of the presented speckle reduction method, there are some constraints the colloidal dispersions have to meet. The colloidal dispersion has to be stable, i.e., the dispersed globules must not swim up or sedimentate in the continuous phase and agglomeration has to be prevented. Furthermore, light absorption in the dispersion should be as low as possible to achieve high optical efficiency. In the experiments homogenized (and therefore stable) cow milk was used. Milk is an emulsion at room temperature. Liquid fat and protein globules are dispersed in a water based host medium in which a large number of different components are dissolved. Three different colloidal dispersions with different optical properties and dynamics of the internal phase are investigated in the following. Colloidal dispersion 1 is homogenized skimmed milk which contains approximately 0.3 wt-% of fat and approximately 3.4 wt-% of protein (wt-% indicates weight percents). 50 ml of the skimmed milk are diluted with 280 ml of deionized water. Colloidal dispersion 2 is homogenized whole milk again diluted with deionized water. 30 ml of milk were mixed with 500 ml of water. The whole milk contained approximately 3.5 wt-% of fat and approximately 3.4 wt-% of protein. Colloidal dispersion 3 is the same whole milk without any dilution.

The scattering and absorption properties of milk are mainly influenced by the dispersed fat and protein globules [159]. Relevant parameters are the scattering coefficient μ_s , the absorption coefficient μ_a and the average cosine of the scattering angle g for the used laser wavelength of 532 nm [160]. g is also known as scattering anisotropy or asymmetry parameter. A value of $g = 0$ corresponds to isotropic Rayleigh scattering. Forward

Table 7.1: Optical properties of the investigated colloidal dispersions.

	Colloidal dispersion 1	Colloidal dispersion 2	Colloidal dispersion 3
Mean fat globule radius / nm	76	117	351
Mean protein globule radius / nm	43	43	43
Asymmetry parameter g	0.228	0.619	0.889
Scattering coefficient μ_s / cm ⁻¹	3.066	8.182	447.8
Absorption coefficient μ_a / cm ⁻¹	0.003	0.004	0.063
Transport mean free path l^* / cm	0.422	0.317	0.020

peaked scattering as observed in Mie scattering, corresponds to values $0 < g \leq 1$. The larger g the more pronounced is the scattering anisotropy. The asymmetry parameter is mainly influenced by the size of the scattering globules as compared to the illumination wavelength. The transport mean free path l^* is defined as $l^* = [\mu_a + (1 - g)\mu_s]^{-1}$ [160]. Physically, l^* corresponds to the distance over which a photon loses its initial direction [160]. It is seen that the value of l^* can be decreased either by increasing μ_s or μ_a or by decreasing g . The fat and the protein globules both have log-normal size distributions, where the size distribution of the fat globules is influenced by dilution [159]. The single fat and protein globules can be assumed to be noninteracting. With the method shown in [159] and [161], values for μ_s , μ_a , g and l^* of the three colloidal dispersions have been determined for 525 nm light [162]. These values are summarized in Tab. 7.1 and are assumed to be also valid for the 532 nm light used in the experiments. It can be seen in Tab. 7.1 that the absorption coefficients are very small compared to the scattering coefficients. The fat globules of dispersion 1 and 2 are smaller compared to those in dispersion 3. The corresponding mean radius of dispersion 1 is approximately a factor of 4.6 smaller as in dispersion 3. The corresponding value of dispersion 2 is a factor of three smaller as in dispersion 3. Therefore, the fat globules in dispersion 1 and 2 do more Brownian movement as those in dispersion 3 [156]. Colloidal dispersion 1 has an asymmetry parameter g of only 0.228 compared to a value of 0.619 and 0.889 in colloidal dispersion 2 and 3. Therefore, the scattering in dispersion 1 is less forward peaked as compared to dispersions 2 and 3. The scattering coefficient μ_s of dispersion 1 and 2 are comparable and relatively small. In dispersion 3, μ_s exceeds the corresponding values of dispersions 1 and 2 by more than a factor of 50. The resulting transport mean free paths are therefore relatively large in dispersions 1 and 2. However, the corresponding value in dispersion 3 is more than a factor of ten smaller.

7.3 Experimental Results

It can be seen in Tab. 7.1 that dispersion 1 is comparably low scattering, scattering is relatively isotropic and its globules are small and therefore have high dynamics. Figure 7.2 depicts the measured speckle contrast values and the $1/e^2$ -radii of the laser beam after passage through the screen filled with colloidal dispersion 1. The speckle contrast

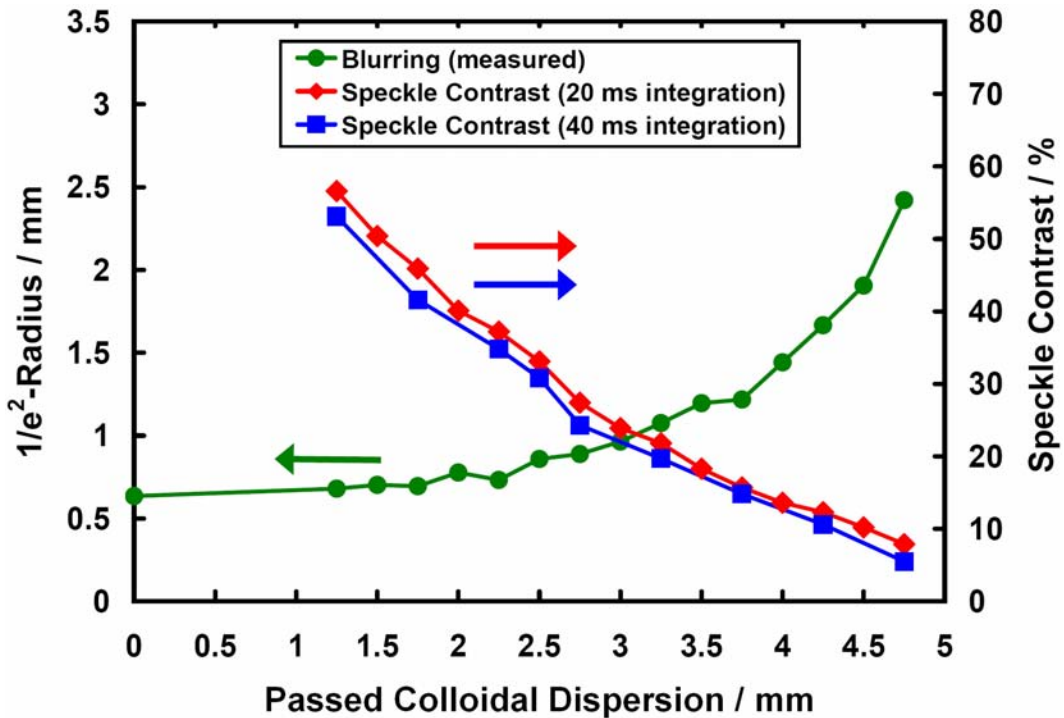


Figure 7.2: Measured speckle contrasts and $1/e^2$ -radii of the laser beam after passage through the screen filled with colloidal dispersion 1 (diluted skimmed milk). The speckle contrast measurements were done for 20 and 40 ms camera integration time. The lines are to guide the eye.

measurements were done for a camera integration time of 20 and 40 ms. It can be seen that the measured speckle contrast values are somewhat smaller for the larger integration time, however the difference is only approximately 2%. This indicates that the main drop of the field autocorrelation already occurred after 20 ms and a doubling of the integration time to 40 ms does not result in much additional speckle reduction. Therefore, the following measurements are restricted to a camera integration time of 40 ms. For screen thicknesses smaller than approximately 1 mm the screen was too transparent to be used in practical projection applications. The resulting speckle contrast values decrease with an increase of the screen thickness. Beam blurring, and hence the resulting $1/e^2$ -radius of the laser beam also increase with the screen thickness. When the laser beam passes the screen without dispersion filling it has a $1/e^2$ -radius of 0.64 mm after the screen. With the constraint of 70% of acceptable blurring it can be easily calculated that the maximal acceptable $1/e^2$ -radius of the laser beam after screen passage is $0.64 \text{ mm} \times 1.7 \approx 1.09 \text{ mm}$. With colloidal-dispersion filling this value is reached for a screen thickness of approximately 3.25 mm. The corresponding speckle contrast values are approximately 22% for 20 ms of camera integration time and approximately 20% for 40 ms camera integration time. So, speckle noise can be reduced with a dispersion 1 screen filling, however, for practical blurring the resulting speckle contrast values are still far above the disturbance limit of about 4%. A highly diluted colloidal dispersion with relatively isotropic scattering seems to be not optimal in order to achieve a high speckle contrast reduction at low blurring. Colloidal dispersion 2 is also comparably low

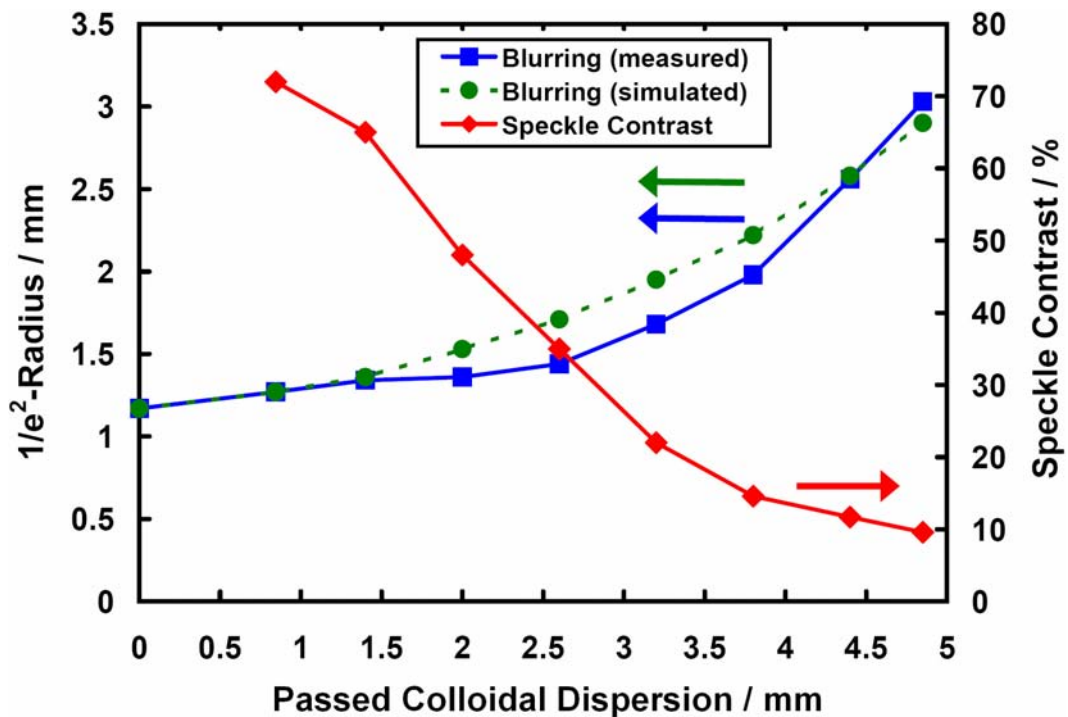


Figure 7.3: Measured speckle contrasts and simulated and measured $1/e^2$ -radii of the laser beam after passage through the screen filled with colloidal dispersion 2 (diluted whole milk). The camera integration time was 40 ms. The lines are to guide the eye.

scattering with small scattering globules and hence high dynamics, however scattering is more forward peaked as in dispersion 1.

In Fig. 7.3 the measured speckle contrast values and the $1/e^2$ -radii of the laser beam after passage through the screen filled with dispersion 2 are depicted. For screen thicknesses smaller than approximately 0.8 mm the screen was again too transparent to be used as projection screen. The $1/e^2$ -radius of the beam was measured to be 1.17 mm after passage of the unfilled screen. The slightly increased value compared to Fig. 7.2 might come from another modal composition of the emission or a larger distance between laser and screen. If an acceptable blurring of 70% is assumed, the acceptable screen thickness for filling with colloidal dispersion 2 can be easily calculated to be approximately 3.8 mm. The corresponding speckle contrast for 40 ms camera integration time was measured to be approximately 15%. This value is still above the 4% disturbance limit. As mentioned above, the dynamics of the globules in dispersion 1 and 2 are similar. Scattering in dispersion 2 is somewhat more forward peaked which results in less blurring. The speckle contrast achieved for acceptable blurring is however only about 5% lower than compared to colloidal dispersion 1. Colloidal dispersion 3 has a much higher scattering coefficient as dispersions 1 and 2 and scattering is peaked into forward direction, however, the globules are comparably large and will therefore show somewhat reduced dynamics. Figure 7.4 depicts the results for passage through the screen filled with dispersion 3. The $1/e^2$ -radius of the laser beam after passage through the unfilled screen is approximately 0.92 mm. By adding the assumed 70% of blurring again it can be calculated that the maximal acceptable $1/e^2$ -beam radius is approximately 1.56 mm.

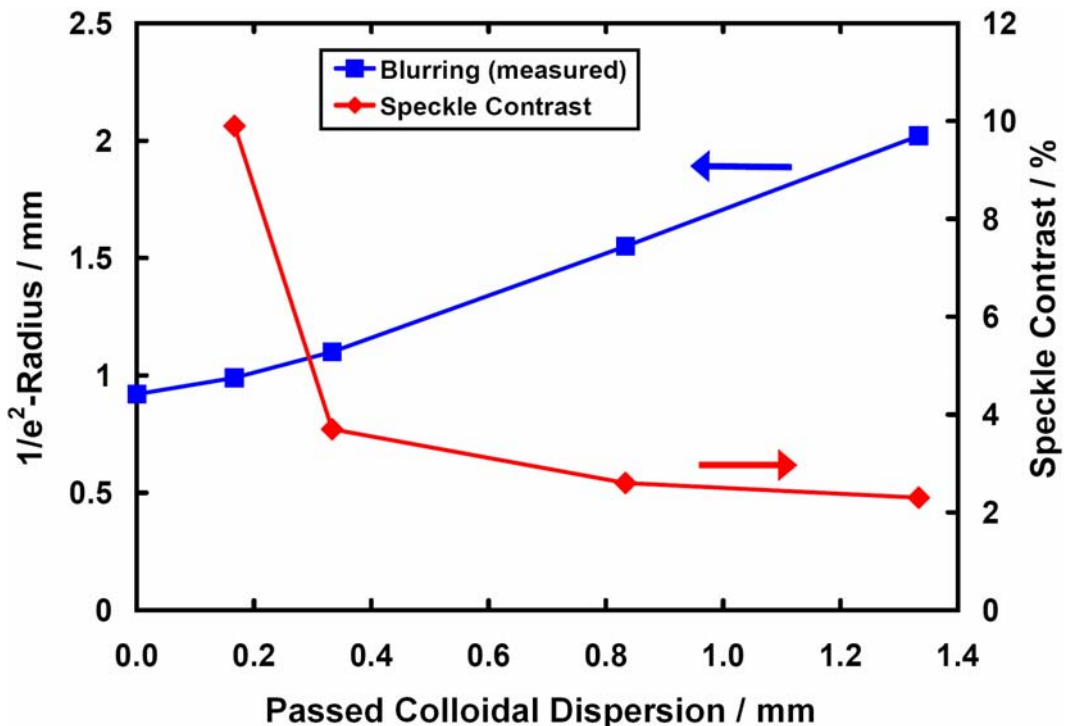


Figure 7.4: Measured speckle contrasts and $1/e^2$ -radii of the laser beam after passage through the screen filled with colloidal dispersion 3 (whole milk). The lines are to guide the eye.

This corresponds to a screen thickness of approximately 0.8 mm and the corresponding speckle contrast value has been measured to be approximately 2.6%. This is below the human disturbance limit, i.e. speckle was no longer visible.

7.4 Modeling and Discussion of Blurring and the Speckle Contrast

In this section it is shown how blurring in the dispersion filled screens can be simulated. Furthermore, parameters of the colloidal-dispersion-filled screens which influence the resulting speckle contrast values are discussed.

The dynamic behavior of the globules in the colloidal dispersions has no relevant influence on its blurring properties. Phenomenologically it is plain that, the larger μ_s (i.e. the more scattering events per propagation length occur when a photon passes the screen) and the smaller g (i.e. the more isotropic the scattering), the more blurring will occur in the screen. Beam blurring can be quantitatively investigated with standard Monte Carlo simulation techniques. The Monte Carlo simulation tool MCML [163] in combination with the convolution tool CONV [164] is used to simulate blurring in the screens. With these tools the resulting light intensity distribution on the observer side of a screen is determined. The screen is illuminated with a Gaussian beam from the illumination side. The screens are modeled with three layers. The glass side walls are

assumed to have $\mu_s = \mu_a = 0$, i.e. any scattering and absorption in the glass side walls is neglected. Their refractive index is assumed to be 1.5. The optical properties of the glass side walls are assigned to the two outer layers in the simulation, those of the investigated dispersions are assigned to the inner layer. In the simulation tool the screen is modeled as being of infinite extent. This assumption is justified as the screen is illuminated with a narrow beam of only about 2 mm diameter to measure blurring. The Monte Carlo simulated values of the $1/e^2$ -radius of the beam after passage through the screen filled with colloidal dispersion 2 are exemplarily shown in Fig. 7.3. It can be seen that good agreement between measured and simulated blurring is achieved. This indicates that the determined values for μ_s , μ_a and g of dispersion 2 are reliable. It can be clearly seen in simulations that, for a constant screen thickness L , a decrease of the asymmetry parameter g leads to increased blurring in the screen. This is because of the more isotropic scattering.

The resulting speckle contrast values are influenced by the scattering and absorption characteristics of the illuminated materials, their structural and dynamic properties and the integration time with which the time varying speckle patterns are captured. Following [165], the perceived contrast $C(T)$ for temporal integration of a time varying speckle pattern is given by

$$C(T) = \sqrt{\frac{2}{T} \int_0^T \beta |g_1(\tau)|^2 (1 - \tau/T) d\tau}. \quad (7.1)$$

In this equation T is the integration time, β is a parameter determined by the ratio of detector size to the size of a single speckle spot and $g_1(\tau)$ is the field autocorrelation function of the scattered light. $g_1(\tau)$ can be analytically determined for several practical experimental setups in the two regimes of single scattering and diffusive light transport. The regime of single scattering is characterized by $L \ll l^*$, where L is the thickness of a scattering material and l^* is the transport mean free path of the photons in the material. In the single scattering regime techniques commonly known as Dynamic Light Scattering (DLS) or Quasi-Elastic Light Scattering (QELS) are widely used to characterize the structural and dynamic properties of materials that scatter light very weakly [166].

The regime of diffusive light transport is characterized by $L \gg l^*$ and techniques like Diffusing-Wave Spectroscopy (DWS) are widely applied [167]. The measurement results in Figs. 7.2 - 7.4 reveal that l^* is comparable to practically relevant screen thicknesses L for all three investigated colloidal dispersions. Therefore, neither the single scattering approximation nor the diffusion approximation can be employed to model the speckle contrast reduction in the experiments. A transition from the single scattering regime to the diffusive regime is clearly visible experimentally [168]. The modeling of this intermediate regime of multiple but not diffusive scattering is however much less developed as the modeling of single scattering and the diffusive regime and is a topic of current research. Extensions of DWS to the nondiffusive regime of few scattering events are presented in [169] and [170]. However, the presented extensions require the determination of the probability density function $p(s|n)$. $p(s|n)$ describes the probability density of a photon traveling a path of length s inside the scattering medium and participating on n scattering events along this path. In general, this probability density function cannot be

easily determined. Therefore, a quantitative modeling of the resulting speckle contrast values cannot be done.

In the following, some qualitative dependencies and general trends are deduced from the regime of diffusive transport whose validity can also be reasonably assumed in the few-scattering regime in the experiments. Therefore, some results from DWS theory are shortly reviewed. Following [167], $g_1(\tau)$ for diffusive light transport in a system of noninteracting moving scattering globules is given by

$$g_1(\tau) = \int_0^{\infty} p(s) \exp[-2(\tau/\tau_0)(s/l^*)] ds, \quad (7.2)$$

with some assumptions. $p(s)$ is the path length distribution of the photons scattered in the considered material and l^* is again the transport mean free path length of the photons. The characteristic diffusion time τ_0 of the scattering globules in the medium is given by $\tau_0 = 1/(Dk_0^2)$, where D is the diffusion coefficient of the moving scattering globules in the medium. Following [171], D is given by $D = (k_B T_{abs})/(N_A 6\pi r \eta)$, where k_B is the Boltzmann constant, T_{abs} is the absolute temperature in Kelvin, N_A is the Avogadro constant, r is the particle radius and η is the viscosity of the surrounding continuous phase. k_0 is given by $k_0 = 2\pi/\lambda$, where λ is the wavelength of the light in the material.

If the scattering material is furthermore modeled as infinite slab of thickness L which is illuminated from one side with an extended plane wave, $g_1(\tau)$ of the light collected in one point on the opposite (detection) side is given by [167]

$$g_1(\tau) = \frac{L}{\gamma l^*} \frac{\sinh[\gamma(6\tau/\tau_0)^{1/2}]}{\sinh[(L/l^*)(6\tau/\tau_0)^{1/2}]}, \quad (7.3)$$

where γ is a constant of order 1-2 which is related to boundary conditions [167],[172]. Inserting Eq. (7.3) into Eq. (7.1) it can be seen that, in order to achieve low speckle contrast values, L/l^* should be as large as possible to achieve a low field autocorrelation of the light and hence a low speckle contrast after passage through the screen. An increase of L/l^* can be either realized by increasing the screen thickness L or by decreasing the transport mean free path l^* . It is plain that an increase of L/l^* will again result in increasing blurring in the screen. The increasing blurring for constant l^* but increasing L can be clearly seen in Figs. 7.2 - 7.4. In Eq. (7.3) it can be furthermore seen that a colloidal dispersion with small viscosity of the continuous phase should be used, the size of the scattering globules should be small and the temperature of the dispersion should be as high as possible. These parameters increase the Brownian movement of the scattering globules and hence the temporal fluctuation of the speckle pattern. However, a decrease of the globule size typically comes along with a decrease of the asymmetry factor g which again results in increased blurring because of less forward peaked scattering. The temperature of the dispersions can be assumed to be relatively fixed at room temperature of approximately 300 K for projection applications. With decreasing viscosity of the continuous phase the Brownian movement of the scattering globules can be increased without increasing blurring at the same time.

7.5 Additional Speckle Contrast Reducing Effects

There are more effects not covered in Eq. (7.2) and Eq. (7.3) which also would have to be included in a quantitative modeling of the resulting speckle contrasts. First, this is a contribution of photons which pass the screen without being scattered. Such an unscattered ballistic component can be modeled as a constant phasor which contributes to the random phasor sum forming a speckle pattern. The resulting speckle contrast in case of a static speckle pattern is then given by $C = \sqrt{1 + 2r}/(1 + r)$ [9]. Here r is the mean intensity of the constant component divided by the mean intensity of the scattered component. It can be seen that the resulting contrast decreases with an increase of the contributing static intensity component. For very small screen thicknesses the ballistic component plays a major role and the resulting speckle contrast values would therefore be small. However, the experiments were not performed in a regime where the ballistic component plays a major role. The screens would cause only very little scattering of the laser light and would therefore not be suited for projection applications as they are nearly transparent. It is shown in [173] that ballistic transmission typically decreases exponentially with increasing screen thickness L . So, there are again two counteracting effects: If the thickness of a colloidal-dispersion-filled screen is decreased, this results on one hand in a decrease of the resulting speckle contrast because of an increasing contribution of ballistic light. On the other hand it was shown above that a decrease of L for constant l^* results in higher contrasts because of less temporal averaging. Because of the missing closed description of the speckle contrast reduction because of temporal averaging in the regime of few-scattering it is difficult to determine an optimum thickness.

As a further effect depolarization can contribute to speckle contrast reduction and is not covered in Eq. (7.2) and Eq. (7.3). A typical laser emits polarized light and hence produces speckle of contrast $C = 1$. The use of a depolarizing screen results in a reduction of the speckle contrast to $C = \sqrt{(1 + P^2)/2}$ [9]. Here, P is the degree of polarization of the light after scattering in or on the screen. The more depolarization the screen causes the lower is the resulting speckle contrast. For full depolarization ($P = 0$) the resulting contrast is therefore reduced by a factor of $1/\sqrt{2}$. In case of a colloidal-dispersion-filled screen the resulting depolarization is dependent on the scattering characteristics of the dispersion. Any scattering or absorption in the glass side walls of the screen is again neglected, therefore these do not contribute to depolarization. Light depolarization by scattering on globules like in the used dispersions is sensitive on the size of the scatterers and their refractive index in a complex way. Models to describe depolarization characteristics are typically again restricted to the regime of diffusive light transport and single scattering [174]-[176]. The resulting depolarization of light after passage through screens filled with different practical suspensions of latex spheres in water are investigated in [174]. It is shown, that the degree of polarization after passage through the suspension decreases exponentially with increasing L/l^* over a wide range of values for $L/l^* > 10$. Expressions which describe the depolarization of light in the diffusive regime for scattering on particles of modest size and refractive index are also given in [175] and [176]. Following [175], the so called depolarization length l_p is given by $l_p = (2.8 - 2.5g)l^*$, where l^* and g are again the transport mean free path of the photons and the anisotropy factor. The shown equation yields that the depolarization length l_p shows the same dependencies as the transport mean free path length

l^* , i.e. it decreases for increasing values of μ_s and μ_a and decreasing values of g . In the few scattering regime of the experiments, the decrease of polarization is expected to be somewhat smaller than in the models described in [174]-[176], as all ballistic light does not contribute to depolarization. It is however reasonable to assume a trend of decreasing polarization with increasing L/l^* for the few scattering regime. It can be deduced from this that an intended decrease of the polarization by decreasing g or increasing μ_s , μ_a or L comes again along with an increase of the blurring in the colloidal dispersion. It is again complicated to find an optimum between maximal depolarization and at the same time small blurring.

7.6 Chapter Conclusion and Outlook

Colloidal-dispersion-filled rear projection screens were used to achieve speckle contrast reduction. The counteracting effects speckle contrast reduction and blurring of a projected image in the screen were discussed. From the achieved results it can be deduced that (within practical limits) a highly scattering colloidal dispersion with highly forward peaked scattering has to be chosen in order to achieve a high speckle contrast reduction at comparably low blurring. The reduced blurring because of more forward peaked scattering with larger scattering globules overcompensates the concurrent decrease of the speckle reduction because of the increased globule size. Speckle contrast values lower than 3% were measured which is below the 4% disturbance limit of a human observer. This was achieved without the necessity of any additional components like moving or rotating diffusers in the setup to destroy the laser's coherence. A future goal is to find an optimal colloidal dispersion for a given experimental setup. This would be a dispersion that causes little blurring but provides as much speckle reduction as possible at the same time. Furthermore, the optical efficiency of the dispersion filled screens should be investigated quantitatively. The best results regarding speckle reduction were achieved with dispersion 3, the absorption coefficient of which is about a factor of 7,000 smaller as its scattering coefficient. In addition to the low light absorption, the scattering is strongly forward peaked into the direction of the observer which results in comparably low light loss. Therefore, the optical efficiency is expected to be reasonably high for a properly selected dispersion filling. In the future it should also be investigated which speckle contrast values are achievable with colloidal-dispersion-filled front projection screens. The optical properties of the dispersions have to be chosen very differently from the case of transmission screens. For a front projection screen the amount of backscattered light has to be increased which had to be small for a transmission screen. Furthermore, it has to be investigated in the future, whether blurring of more than 70% would still be acceptable for projection applications. If so, even further decreased speckle contrast values can be realized. Lower speckle contrast values can also be achieved, if the dispersion filled screen is combined with other practical speckle reduction methods. An efficient method would be the use of an illumination source with reduced temporal coherence, i.e., a source with increased bandwidth. In doing so, there would still be no need for additional components. Because the light is volume scattered inside the colloidal-dispersion-filled screen, the screen can have a large volume roughness [177]. It has been shown in [177], [178] and Chapter 6 that this can result in considerable speckle contrast reduction already for moderate illumination bandwidths.

Chapter 8

Speckle Reduction With a Broad-Area Vertical-Cavity Surface-Emitting Laser (BA-VCSEL)

In this chapter, a broad-area vertical-cavity surface-emitting laser (BA-VCSEL) in a nonmodal emission regime is used to realize low speckle laser projection.

In Section 8.1, an investigation of the basic speckle characteristics of the BA-VCSEL emitting at 840 nm wavelength in different measurement and illumination setups is presented. Depending on the experimental setup, the nonmodal emission regime can lead to a strongly reduced speckle contrast down to 1.3%. This is achieved without using any additional mechanically moving components to destroy the coherence of the laser beam. It will be shown that there are three main contributing speckle contrast reducing effects. These effects are polarization scrambling scattering in the screen, a thermally induced chirp of the VCSEL's emission wavelength, and the VCSEL's strongly reduced spatial coherence. The speckle contrast reduction is quantitatively modeled and good agreement between measurements and the model is achieved.

In Section 8.2, the speckle contrast values achievable in a realistic full frame projection setup are investigated. Therefore, the VCSEL's nearfield is imaged onto a microlens beam homogenizer. The camera to measure the speckles is set up in a way that it corresponds to a human observer looking at the screen from a distance of three meters. It will be shown that the beam homogenizer is essential to exploit the low-speckle capabilities of the VCSEL. Speckle contrast values as low as 3.6% are achieved in the realistic projection setup. Additionally, the model of the speckle contrast values is refined and the agreement between measured and modeled contrast values is improved.

In Section 8.3, the beam homogenizer is illuminated with the VCSEL's farfield instead of its nearfield. Using farfield instead of nearfield illumination has some important advantages for a practical projection system: the field emitted by the VCSEL can be directly projected onto the homogenizer without the need for additional lenses or accurate alignment. Speckle contrast values as low as 2.5% are measured. The model from Section 8.2 is adapted to farfield illumination and again good agreement between model and the measurements is achieved.

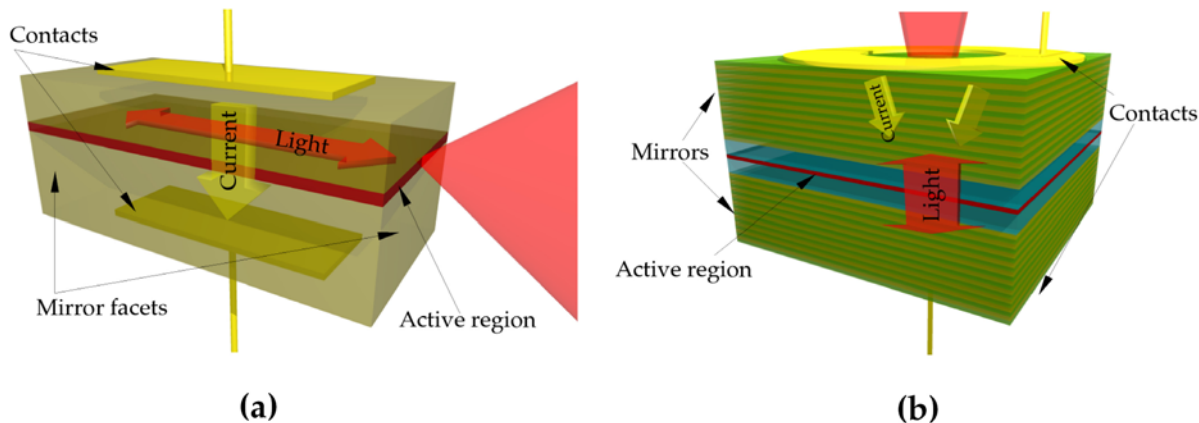


Figure 8.1: Schematic of an edge emitter (a) and a VCSEL (b), taken from [180].

In Section 8.4, the chapter is concluded and an outlook on future work is presented.¹

8.1 Investigation of the Basic Speckle Characteristics of a BA-VCSEL

8.1.1 Introduction

As laser speckle directly result from the coherence of the laser source, a reduction of the source's temporal and/or spatial coherence is a promising strategy to obtain speckle reduction. It has already been shown that the illumination of a rough surface or volume with light of reduced temporal coherence leads to speckle contrast reduction via wavelength decorrelation (see Chapter 4 and Chapter 6). If the mutually incoherent coherence areas of a source with reduced spatial coherence illuminate sufficiently uncorrelated regions on a surface, statistically independent and partially or fully uncorrelated speckle patterns will result. A laser which emits multiple transverse modes has a reduced spatial coherence. Even more promising is the recent finding that VCSELs can be driven into a regime of nonmodal emission [179]. VCSELs are standard semiconductor laser sources that emit perpendicular to the growth direction of the cavity. A schematic of a VCSEL in comparison to a edge emitting laser is shown in Fig. 8.1 [180].

Because of the short cavity length of VCSELs which is of the order of one wavelength, only one longitudinal mode can be lasing. Single-transverse mode operation is achievable with apertures of about $5 \mu\text{m}$. For broader apertures and higher cw driving

¹Parts of this chapter are or will be published in: (a) F. Riechert, G. Verschaffelt, M. Peeters, G. Bastian, U. Lemmer, and I. Fischer, "Speckle characteristics of a broad-area VCSEL in the incoherent emission regime," *Opt. Commun.* **281**, Issue 17, 4424-4431 (2008),
 (b) F. Riechert, G. Craggs, Y. Meuret, B. Van Giel, H. Thienpont, U. Lemmer, and G. Verschaffelt, "Low speckle laser projection with a broad-area vertical-cavity surface-emitting laser in the nonmodal emission regime," *Appl. Opt.* **48**, Issue 4, 792-798 (2009),
 (c) F. Riechert, G. Craggs, Y. Meuret, H. Thienpont, U. Lemmer, and G. Verschaffelt, "Far Field Nonmodal Laser Emission for Low-Speckle Laser Projection," in press, *Photonics Technology Letters* (2009).

currents, the emission of the VCSEL typically consists of a large number of transverse modes. Besides emission in multiple transverse modes, such devices can behave as quasi-homogeneous Gaussian Schell-model sources with reduced spatial coherence [179] when driven by microsecond current pulses. The device then no longer shows modal emission. In a Schell-model source the degree of coherence between two points only depends on the distance between the two points. In a Gaussian Schell-model source, the intensity distribution and the degree of coherence additionally have the shape of a Gaussian distribution [140].

In [179] the transition to this nonmodal emission regime is attributed to the interplay between the thermal chirp and the build-up of a spatially distributed thermal lens. This leads to the break-up of the global cavity modes. The farfield of the total nonmodal beam is then Gaussian shaped with a full opening angle of 22 degrees [179]. The VCSEL's aperture can then be modeled as being filled with mutually independent Gaussian beamlets each having a coherence radius of approximately 1.4 μm . This value has been calculated from the farfield divergence angle of the VCSEL [179]. It has been independently confirmed by nearfield measurements [181]. The coherence radius corresponds to a drop of the magnitude of the degree of coherence to $1/e^2$ throughout this chapter. Experiments with different pulse amplitudes and lengths have shown that the farfield divergence angle (and thus also the nearfield coherence radius) is only weakly dependent on the pulse parameters once the pulse amplitude and length are large enough to establish the nonmodal emission regime [179]. Such a source shows the benefits of a laser source (e.g. the emission of several 100 mW peak output power) while having a Gaussian farfield (opposed to the multi-lobed farfield in modal emission) together with a low degree of spatial coherence. The speckle reduction capabilities in the incoherent emission regime and under cw multimode operation are compared in the following.

The remainder of Section 8.1 is organized as follows: In Subsection 8.1.2, the experimental setups used for the basic investigation of the VCSEL's speckle properties are described. In Section 8.1.3, the experimental results for the different setups and driving conditions are presented. In Section 8.1.4 and Section 8.1.5, the different effects that reduce the speckle contrast are modeled and then compared to the experimental findings. In Section 8.1.6, conclusions are drawn concerning how the spatially incoherent emission from broad area VCSELs can effectively be used to reduce speckle in several nonimaging applications and how high speckle contrast reduction in a projection system might be achieved.

8.1.2 Experimental Setups

A native oxide confined VCSEL, which emits light at an approximate wavelength of 840 nm and has an aperture diameter of 50 μm is used in the experiments. The characterization and detailed parameters of the device can be found in [179]. The VCSEL is mounted on a heat sink to stabilize the mount temperature to room temperature. For cw operation a current source with an accuracy of +/- 0.1% of the driving current is used to drive the VCSEL. In case of pulsed operation of the VCSEL, an arbitrary waveform generator with a 50 Ω output impedance and a 50 MHz bandwidth is used.

The CCD-camera used in the speckle measurements is a 12-bit linear camera (TechnoTeam, type LMK 98-3) with variable integration time. It is used with a “Tamron TT18” objective which has a focal length of 18 mm and a working distance of 9.7 cm. In focus, the full field of view corresponds to about 1 cm^2 . The camera supports automatic correction of systematic errors, e.g. a reduced sensitivity at the edges of the optical elements. All measurements were performed in reflection from a paper screen (standard 80 g/m^2 office paper). Ambient light has been reduced as far as possible. Images - the VCSEL being switched off - with different integration times of the camera were taken to determine the background intensity values caused by camera noise and ambient light. The background intensity was typically between 0.1% and 0.5% of the mean intensity measured in the experiments (see Section 8.1.3) when the VCSEL is switched on. This is sufficiently small to be neglected. The accuracy with which the speckle contrast can be determined is mainly restricted by the (large scale) homogeneity of the captured images. To minimize errors in the determination of the speckle contrast, diverse regions of interest are taken into account in order to determine a medium speckle contrast.

To check the stability of the setup and to show that there is no relevant influence of camera noise and ambient light, a first measurement was performed with an argon ion laser emitting approximately 3.5 mW into a polarized TEM_{00} beam. The laser was mounted at a distance of 1 m from the screen and illuminated the screen directly with only a small angular offset. The camera was placed in the farfield of the screen at a distance of 1.2 m (again with only a small angular offset). A speckle contrast of 70.8% was measured which is in excellent agreement with the theoretical value (see Section 2.2) of $1/\sqrt{2}$ that is expected for the used fully depolarizing paper screen and polarization scrambling being the only speckle contrast reducing effect.

VCSEL Driving Conditions

The VCSEL was operated under different cw and pulsed driving conditions summarized in Tab. 8.1. In cw operation, the VCSEL was driven with three different currents: 20 mA (just above the threshold current), 60 mA (halfway to the maximum driving current) and 100 mA (close to the thermal roll over point of the VCSEL’s PI characteristic). In pulsed operation, three pulse heights and durations were investigated. Using a pulse with an amplitude of 32 mA, the VCSEL emits in multiple transverse modes irrespective of the pulse duration. For pulses with larger amplitude (124 mA and 274 mA), the emission depends on the pulse duration [179]. For a pulse length of 100 ns, which is much shorter than the thermal time-scale of the VCSEL which is determined by an interplay of heating and heat conduction, modal emission can be still observed. When the pulse length is increased to 1 μs and 2 μs (while keeping the amplitude at 124 mA or 274 mA), the VCSEL emits a spatially incoherent beam. The maximum pulse length was limited to 2 μs as this is the longest pulse duration which can be used before modal effects reappear in the VCSEL emission. For all of the pulsed driving conditions, the duty cycle is set to 1% to avoid any average heating of the VCSEL.

8.1.3 Experimental Results

In Figs. 8.2(a) - 8.5(a) the different setups used to characterize the speckle behavior of the VCSEL are shown. Either the nearfield of the VCSEL is projected onto the screen via

Table 8.1: Driving parameters of the VCSEL in cw and pulsed operation.

Cw operating conditions	Pulsed operating conditions
Driving current	Pulse lengths, pulse height
20 mA (just above threshold)	100 ns, 1000 ns and 2000 ns, 32 mA
60 mA (intermediate)	100 ns, 1000 ns and 2000 ns, 124 mA
100 mA (nearby maximum)	100 ns, 1000 ns and 2000 ns, 274 mA

a doublet lens (Fig. 8.2(a) and Fig. 8.3(a)) or the farfield of the VCSEL is directly shone onto the screen (Fig. 8.4(a) and Fig. 8.5(a)). Also for the CCD camera two different positions are used. The camera is either imaging the screen (Fig. 8.2(a) and Fig. 8.4(a)) or the camera is placed in the farfield of the screen (Fig. 8.3(a) and Fig. 8.5(a)). In case of the nonmodal emission, the VCSEL's beam only has to propagate further than 20 μm before the farfield regime is entered [179],[182]. In case of modal emission, the farfield regime is reached at a distance somewhat greater than 1 cm. To ensure that the screen is in the farfield region for all driving conditions, the screen is placed at 3.5 cm (setup in Fig. 8.4(a)) or 4.2 cm (setup in Fig. 8.5(a)) from the VCSEL. When the CCD-camera is imaging the screen, the camera is placed at a distance of 9.7 cm from the screen. For measurements in the farfield of the screen, the camera is placed at a distance larger than 1 m from the screen. In Fig. 8.2(a) and Fig. 8.4(a) a pupil is placed in front of the CCD-camera to enlarge the speckle size in order to ensure that one speckle spot covers at least ten pixels on the CCD chip. The opening diameter of the pupil is approximately 1.5 mm. In Figs. 8.2(b) - 8.5(b) the measured speckle contrast corresponding to the setups given in Figs. 8.2(a) - 8.5(a) are shown.

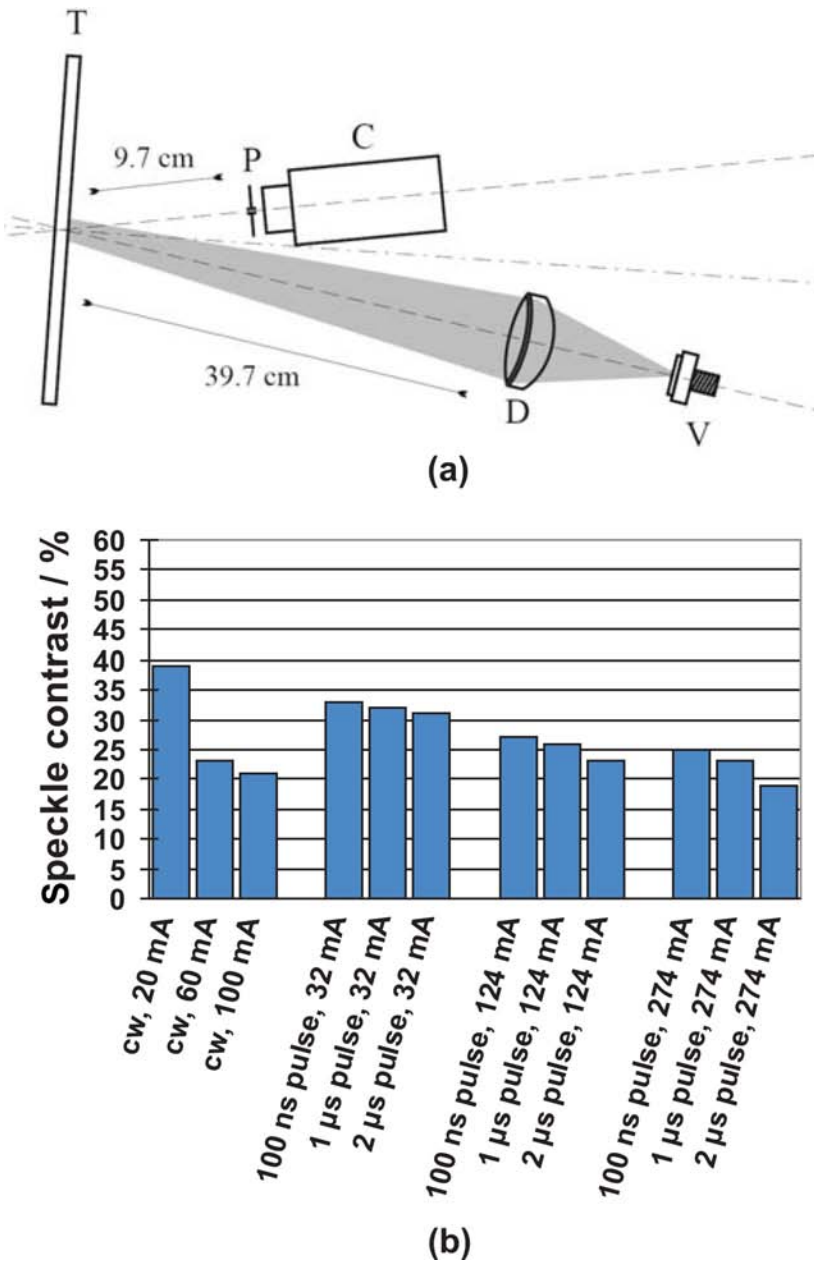


Figure 8.2: (a) Projection with a lens (D) of the VCSEL's (V) nearfield onto the screen (T), CCD-camera (C) imaging the paper screen. (b) Measured speckle contrasts.

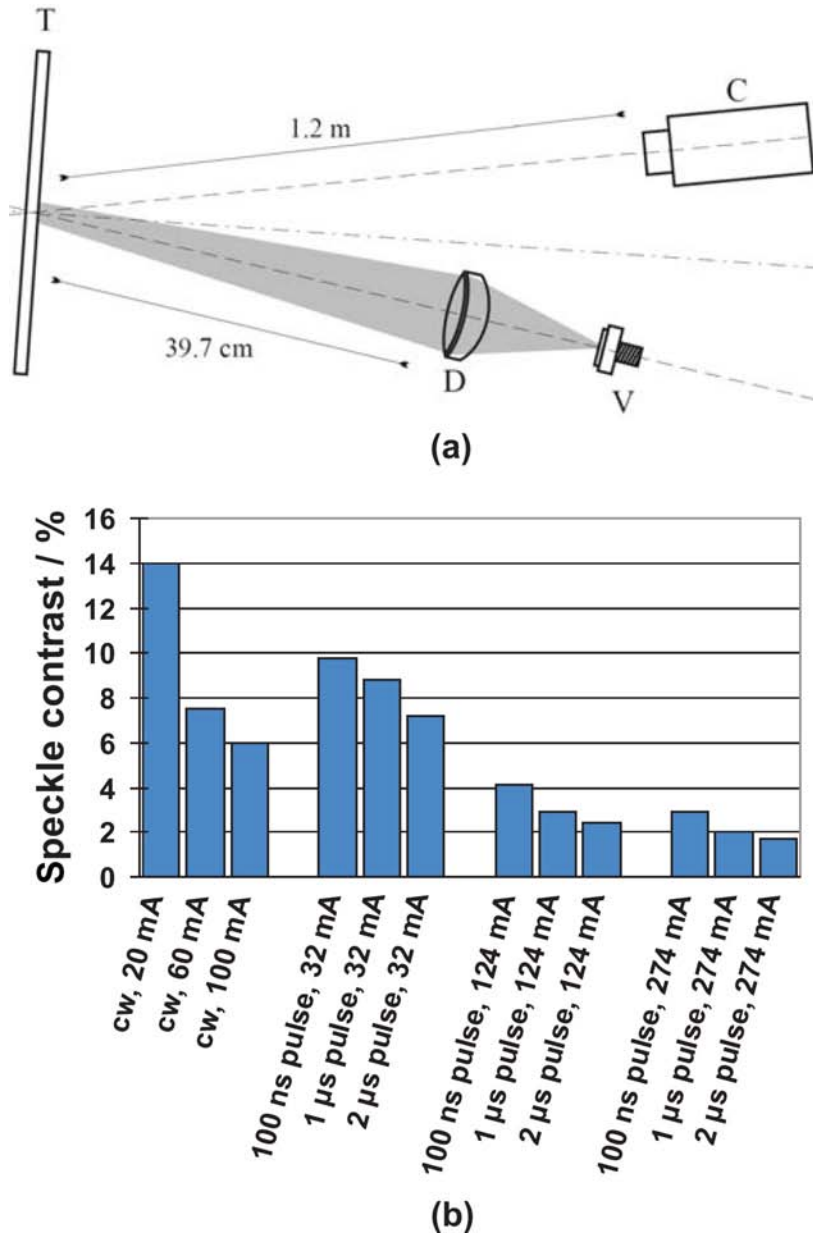


Figure 8.3: (a) Projection with a lens (D) of the VCSEL's (V) nearfield onto the screen (T), CCD-camera (C) placed in the farfield of the paper screen. (b) Measured speckle contrasts.

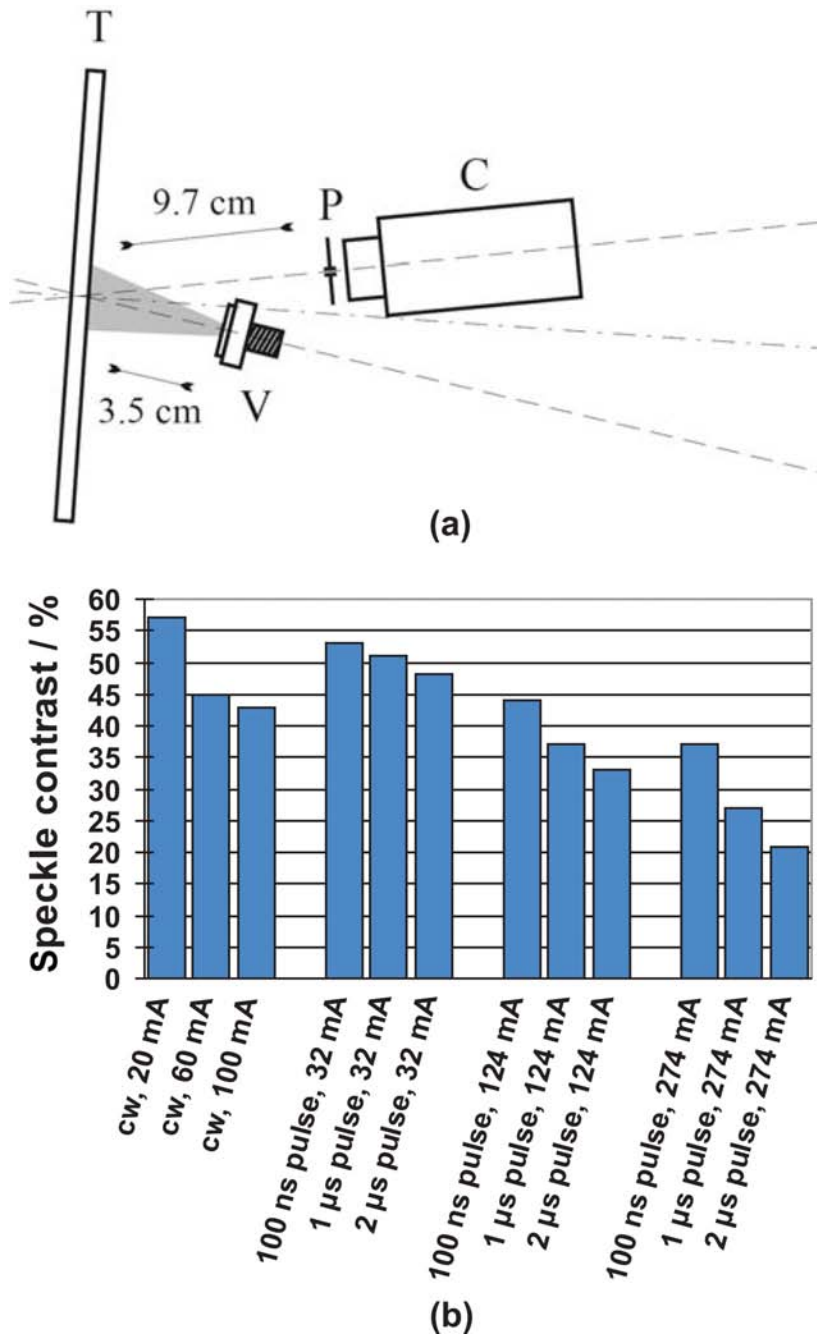


Figure 8.4: (a) Projection of VCSEL's (V) farfield onto the screen (T), CCD-camera (C) imaging the paper screen. (b) Measured speckle contrasts.

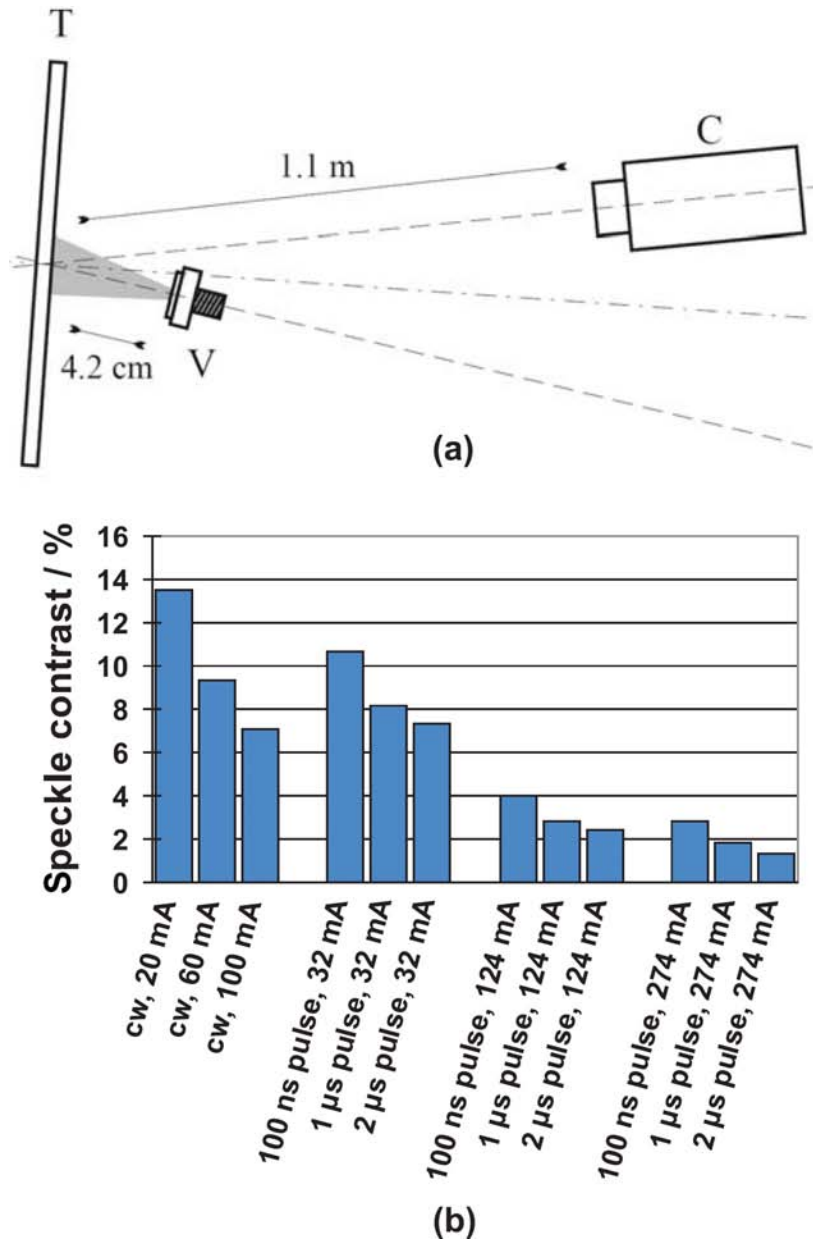


Figure 8.5: (a) Projection of VCSEL's (V) farfield onto the screen (T), CCD-camera (C) placed in the farfield of the paper screen. (b) Measured speckle contrasts.

General Observations

If Fig. 8.2(b) is compared with Fig. 8.4(b) and Fig. 8.3(b) is compared with Fig. 8.5(b), it can be observed that the speckle contrast is almost the same whether the nearfield or the farfield of the VCSEL is projected onto the screen. The speckle contrast is much more dependent on the camera's placement. A clearly much lower speckle contrast is measured when the camera is in the farfield of the screen as compared to the setups when the camera images the screen.

In all four setups, the speckle contrast is decreasing with increasing cw driving current. The lowest speckle contrast in cw operation is achieved in the setup given in Fig. 8.3(a), where the VCSEL's nearfield is projected onto the screen and the CCD-camera is placed in the screen's farfield. The resulting speckle contrast is approximately 6% for a 100 mA driving current.

In pulsed operation, a further substantial speckle contrast reduction can be achieved compared to cw operation. The speckle contrast decreases with increasing pulse amplitude and length in all investigated setups. The relative decrease with increasing pulse amplitude is significantly more pronounced when the camera is placed in the farfield of the screen (see Fig. 8.3 and Fig. 8.5). In that case a speckle contrast as low as 1.7% in Fig. 8.3 and 1.3% in Fig. 8.5 is obtained. If the camera images the screen, the measured speckle contrast is much higher and the contrast is not below 19% in case of Fig. 8.2 and not below 21% in case of Fig. 8.4.

8.1.4 Modeling of the Speckle Contrast

To interpret the measured contrast values, the different effects that may contribute to the reduction of the speckle contrast are described and estimated. If several of these effects play a role at the same time, the speckle contrast is obtained by multiplying the individual contrast reduction factors.

Polarization Scrambling Paper Screen

The backscattering from the used paper screen is nearly fully polarization scrambling (see Chapter 6). Therefore, two mutually uncorrelated and orthogonally polarized speckle images are produced which superimpose and result in a speckle contrast reduction by a factor of $1/\sqrt{2} \approx 0.7071$. In Section 8.1.2 it has already been mentioned that a value of 0.708 was measured in excellent agreement with theory.

Shift of the Emission Wavelength

In [183] it is shown that the emission wavelength of the VCSEL in pulsed operation can shift several nanometers during a current pulse. This shift depends on the pulse duration and amplitude and leads to a dynamically changing speckle pattern during the pulse. If the camera integration time is longer than the pulse duration, this results in a reduced speckle contrast. In the measurements the maximum pulse duration is 2 μ s, which is much smaller than the camera integration time (the lowest integration time used was 90 μ s). Therefore, the same effect is obtained as illuminating the screen with a broadband source. The resulting decrease of the speckle contrast is dependent on source

and screen parameters. Following Chapter 6, the speckle contrast C for broadband illumination of the paper screen in a backscattering geometry is given by

$$C = \left[1 + 2\pi^2 \left(\frac{\delta\lambda}{\bar{\lambda}} \right)^2 \left(\frac{c\sigma_\tau}{\bar{\lambda}} \right)^2 \right]^{-\frac{1}{4}}. \quad (8.1)$$

Here, c is the speed of light in vacuum, $\delta\lambda$ is the 1/e-width of the wavelength spectrum of the source, $\bar{\lambda}$ is its mean emission wavelength and σ_τ is the standard deviation of the scattering path time distribution of the photons in the paper screen.

Before Eq. (8.1) can be applied, $c\sigma_\tau$ needs to be estimated for the VCSEL's wavelength of 840 nm². Therefore, σ_τ is approximately determined with a calibration measurement. The paper screen is illuminated under normal incidence with a pulsed Titanium:Sapphire (Ti:Sa) laser. This laser has a 1/e-bandwidth of 5.31 nm when emitting 150 fs pulses and 0.42 nm when emitting 1 ps pulses. The Ti:Sa laser's emission is in the fundamental TEM₀₀ mode with a central wavelength of 800 nm. The speckle contrast measured in the screen's farfield (and in the direction normal to the screen) is 20.8% when 150 fs pulses are used and 57.4% when 1 ps pulses are used. This knowledge of the speckle contrast and the 1/e-bandwidth of the Ti:Sa laser allows us to use Eq. (8.1) to calculate $c\sigma_\tau$ of the used paper screen. Therewith, $c\sigma_\tau = 0.805$ mm can be calculated for an illumination wavelength of 800 nm. After inserting an external second harmonic generation crystal into the Ti:Sa beam, $c\sigma_\tau = 1.37$ mm has been analogously determined for frequency doubled (400 nm wavelength) photons. If σ_τ is assumed to decay linearly with increasing wavelength, $c\sigma_\tau$ can be linearly extrapolated to be approximately 0.74 mm at the VCSEL's wavelength of 840 nm³.

To complete the characterization of the VCSEL source, the heat induced shift in the VCSEL's emission wavelength during a pulse is estimated by calibrating the wavelength shift with temperature and by calculating the temperature rise during a pulse [184]. The estimated wavelength shift for the investigated driving pulses can be found in the second column of Tab. 8.2.

These values of the emission wavelength shift are used as the 1/e-bandwidth $\delta\nu$ in Eq. (8.1). The approximate assumption of a Gaussian shaped autocorrelation function of the VCSEL's normalized power spectrum $K_{\hat{G}}(\Delta\nu)$ is justified. The assumption of $\delta\nu$ being much smaller than the medium emission frequency $\bar{\nu}$ is clearly fulfilled. The estimated reduction of the speckle contrast because of the shift in the VCSEL's emission wavelength for the used paper screen is shown in the third column of Tab. 8.2.

Reduced Spatial Coherence

In cw operation a multitude of transverse modes contribute to the emission of the VCSEL. In modal operation, each transverse mode in the cavity is individually fully spatially

²The streak camera used in Chapter 6 to measure scattering path time distributions has not yet been available when the experiments in this section were performed.

³It can be seen that the value for the standard deviation of the scattering path time distribution used in this Section is about a factor of two larger as the value which has been directly measured later with the streak camera in Chapter 6. The discrepancy might come from some uncertainties in the speckle measurements or the used linear extrapolation which might be not justified.

Table 8.2: Shift of the emission wavelength of the VCSEL induced by Joule heating for different pulses. Furthermore, the estimated speckle contrast reduction factor as calculated according to Eq. (8.1) is given taking into account quasi-broadband illumination of the paper screen.

Pulse parameters	Estimated shift in emission wavelength / nm	Estimated speckle contrast reduction factor
100 ns, 32 mA	0.008	0.9997
1 μ s, 32 mA	0.048	0.9884
2 μ s, 32 mA	0.096	0.9574
100 ns, 124 mA	0.045	0.9898
1 μ s, 124 mA	0.270	0.7945
2 μ s, 124 mA	0.540	0.6140
100 ns, 274 mA	0.168	0.8913
1 μ s, 274 mA	1.010	0.4611
2 μ s, 274 mA	2.018	0.3290

coherent (if there is no frequency degeneracy of the modes), but the degree of coherence of the superposition of all transverse modes in the cavity is reduced. This behavior is described theoretically in [33] and measured in [185]. The number of transverse modes emitted by the VCSEL increases with increasing driving current (until the thermal roll-over point is reached). For a driving current of 70 mA (close to the cw roll-off point) the number of transverse modes is of the order of 100. As the number of contributing transverse modes increases, the spatial coherence of the laser beam decreases [33]. If each of the modes produces a speckle pattern which is at least partly decorrelated from the others, the resulting speckle contrast of the superposition of the patterns will decrease. Such decorrelation can be achieved if the different modes have slightly different emission wavelengths or illuminate different positions on the screen. The exact number of modes and the coherence function of the emission are difficult to estimate. Therefore, it is difficult to estimate the exact speckle contrast reduction in the modal regime.

As the source behaves as quasi-homogeneous Gaussian Schell-model source in the nonmodal emission regime, the modeling can be done more properly. The source's aperture is assumed to be filled with independent coherence islands. The size of these islands, relative to the total beam's size, will be different in the VCSEL's nearfield and farfield. In the nearfield, the coherence radius is 1.4 μ m whereas the VCSEL aperture radius is 25 μ m. The number of independent coherence islands can be estimated by dividing the total VCSEL aperture area by the coherence area. This results in 318 different islands. When the VCSEL's nearfield is imaged onto the screen, both the VCSEL aperture and the coherence radius will be imaged with the same magnification. Therefore, the number of coherence islands stays the same as in the nearfield of the VCSEL. If all coherence islands are assumed to have the same intensity and that they produce speckle patterns which are all mutually fully uncorrelated, this results in a

maximum speckle contrast reduction by a factor of $1/\sqrt{318} = 0.056$.

For nonmodal emission in the VCSEL's farfield, the situation is slightly different. In that case a coherence radius can be defined based on the farfield angular coherence. The farfield coherence angle can be calculated starting from the nearfield intensity distribution [179] and is approximately 1.2 degrees at full-width. This has been confirmed by direct measurements of the farfield coherence angle [179]. After a propagation distance Z , the total beam's radius is equal to $(Z \times \tan(\Theta_{ff}))$ where Θ_{ff} is the half-width divergence angle. Equivalently, the coherence radius is given by $(Z \times \tan(\Theta_{coh}))$ where Θ_{coh} is the half-width coherence angle. The number of coherence islands is then given by the ratio of the total beam's area and the coherence area, which yields 344 coherence islands in the farfield of the VCSEL. The maximum speckle contrast reduction is thus $1/\sqrt{344} = 0.054$ if all statistically independent coherence islands are again assumed to have the same intensity and produce uncorrelated speckle patterns.

8.1.5 Interpretation of Results

General Considerations

The theoretically expected decrease of the speckle contrast with increasing cw driving current is observed for each setup. In pulsed operation, a decrease of the speckle contrast with increasing pulse duration and amplitude is observed because of the increasing thermally induced shift of the VCSEL's emission wavelength. In all four setups, the speckle contrasts measured for a pulse amplitude of 32 mA are significantly higher than those for stronger pulses. This is because the induced thermal dynamics are not strong enough to induce nonmodal emission when the pulse amplitude is only 32 mA. Therefore, the behavior for a 32 mA pulse is similar to the transverse multimode emission in cw operation with in addition a small thermally induced shift in the emission wavelength. The relative decrease in the measured speckle contrasts for the three investigated pulse lengths fits well with the estimated decrease resulting from the shift in emission wavelength. In the case of a 32 mA pulse of 100 ns pulse length, the influence of the wavelength shift on the speckle contrast is very small (expected decrease by a factor 0.9997). Therefore, the measured speckle contrast should be between the contrast values for cw operation with 20 mA and 60 mA driving current. This is fulfilled for each setup.

The uncertainty in determining the speckle contrast in modal emission is relatively high (a few percent absolute) because of the non-homogeneously distributed intensity in the captured images, which itself is a result of the modal structure. The extraction of the speckle contrast is much more precise in the nonmodal emission regime. No modal structures are visible and the captured images are much more homogeneously illuminated on a large scale (not the small scale speckle intensity fluctuations).

In the next two sections the speckle characteristics under driving conditions where the VCSEL emits in the nonmodal regime are scrutinized. The analysis is restricted to pulse lengths of 1000 ns and 2000 ns, because the nonmodal emission regime is not yet fully reached with 100 ns pulses.

Table 8.3: Comparison between the measured and estimated speckle contrast for the setup in Fig. 8.2(a).

Pulse parameters	Measured speckle contrast / %	Estimated speckle contrast / %
1 μ s pulse, 124 mA	26	56.2
2 μ s pulse, 124 mA	23	43.4
1 μ s pulse, 274 mA	23	32.6
2 μ s pulse, 274 mA	19	23.3

Nonmodal Emission - Projection of VCSEL's Nearfield

In case the VCSEL's nearfield is magnified and imaged onto the screen, a large number of coherence islands (one for each beamlet) is projected as indicated in Fig. 8.6(a). Each beamlet illuminates a different position on the screen. Therefore, each beamlet locally produces a speckle pattern that is uncorrelated from the speckle patterns produced by the other beamlets.

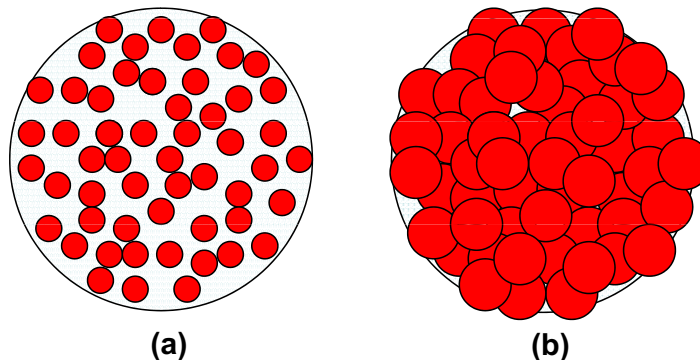


Figure 8.6: Schematics of (a) the VCSEL's nearfield incident onto the screen for the nonmodal emission regime. The nearfield consists of about 318 coherence islands (red spots). (b) the VCSEL's nearfield backscattered from the volume scattering screen. Light from the beamlets is diffusely scattered and the backscattered beamlets overlap.

However, each incident beamlet has an approximate diameter of 106 μ m on the screen which is sufficiently large to be resolved with the CCD-camera which images the screen onto the CCD-chip (setup described in Fig. 8.2(a)). Therefore, many local speckle patterns of high contrast are measured and it can be expected that only two speckle reducing effects play a role: polarization scrambling (which results in a contrast reduction by $1/\sqrt{2}$) and the shift in the emission wavelength (given in Tab. 8.2). A comparison of the measured and the calculated speckle contrast values is given in Tab. 8.3.

The measured speckle contrasts are significantly smaller than the estimated values, which is surprising at a first glance. The additional speckle contrast reduction can be explained by taking into account the scattering characteristics of the volume scattering paper screen. The photons enter the screen material and are then diffusely scattered.

Table 8.4: Comparison between the measured and estimated speckle contrast for the setup in Fig. 8.3(a).

Pulse parameters	Measured speckle contrast / %	Estimated speckle contrast / %
1 μ s pulse, 124 mA	2.9	3.0
2 μ s pulse, 124 mA	2.4	2.3
1 μ s pulse, 274 mA	2.0	1.8
2 μ s pulse, 274 mA	1.7	1.3

Therefore, the backscattered nearfield looks like the schematic given in Fig. 8.6(b). Light from the backscattered beamlets can overlap. The influence of this lateral scattering effect was neglected in the derivation of Eq. (8.1). Although photons of different beamlets can leave the screen at the same position, they did a somewhat different random walk, since they entered the screen at different positions. This can result in a speckle contrast reduction in the region of overlap because partially uncorrelated speckle patterns are superimposed in that region. With these considerations it is reasonable to measure a smaller speckle contrast than expected from the estimates. It is difficult to determine the exact size of the overlapping regions and the mutual correlation of the superimposed speckle patterns. Therefore, it is not possible to estimate the absolute speckle contrast values here. What can be checked is the relative decrease of the measured speckle contrast with increasing pulse length and height, as is given in Tab. 8.2. The relative decrease corresponds reasonably well with the estimates. Further discrepancies might be related to the assumptions made to derive Eq. (8.1) (Gaussian shaped power spectrum of the VCSEL, model for the thermally induced shift of the VCSEL's emission wavelength and Gaussian shaped path length probability density function of the photons).

If the CCD-camera is moved away from the screen (setup described in Fig. 8.3(a)) the interpretation of the measurements becomes simpler. The screen is no longer imaged onto the CCD chip. Instead a plane parallel to the screen at a distance of approximately 1.1 m is imaged onto the CCD chip. Therefore, the superposition of all mutually uncorrelated speckle patterns, each of which is produced by a single beamlet is measured. The lateral scattering effects of the screen are now not influencing the measured farfield contrast values. The speckle contrast is thus further decreased by $1/\sqrt{318}$ compared to the estimation given in Tab. 8.3. In Tab. 8.4 a comparison between the measured and the estimated speckle contrast is presented. There is a good agreement in Tab. 8.4 between measurements and estimates in most cases. A minimal contrast of 1.7% was measured which is only slightly higher than the estimated value of 1.3%. This discrepancy might arise from the fact that not all beamlets contribute with the same intensity which was neglected in the model.

Nonmodal Emission - Projection of VCSEL's Farfield

As already mentioned, the VCSEL's farfield in the nonmodal emission regime is made up of different coherence islands, the size of which is determined by the farfield coherence

Table 8.5: Comparison between the measured and estimated speckle contrast for the setup in Fig. 8.4(a).

Pulse parameters	Measured speckle contrast / %	Estimated speckle contrast / %
1 μ s pulse, 124 mA	37	56.2
2 μ s pulse, 124 mA	33	43.4
1 μ s pulse, 274 mA	27	32.6
2 μ s pulse, 274 mA	21	23.3

angle and the propagation distance to the screen. Analogously as in the previous section, the screen is illuminated by coherence islands or beamlets and each beamlet locally produces a speckle pattern that is uncorrelated from the speckle patterns produced by the other beamlets. The difference with the previous section is the size of the total beam and of each beamlet on the screen. For the setups shown in Fig. 8.4(a) and Fig. 8.5(a), the diameter on the screen of the total beam is 13 mm and 16 mm, respectively and the coherence radius is 0.37 mm and 0.44 mm, respectively. In case the CCD camera images the screen (as in the setup shown in Fig. 8.4(a)), each coherence island is large enough to be resolved by the camera. Therefore, the number of beamlets on the screen will again not influence the speckle contrast and only two speckle reducing effects play a role: polarization scrambling and the shift in the emission wavelength. The speckle contrast estimated based on these two effects is given in Tab. 8.5 together with the measured speckle contrast values from Fig. 8.4(b).

The measured values are smaller than estimated. The additional effect reducing the speckle contrast might again be lateral scattering of the photons similar to what was suggested when the VCSEL's nearfield is projected onto the screen. For the investigated setups, the coherence area in the VCSEL's farfield is larger than the coherence area in the projected VCSEL's nearfield. On the other hand, the lateral scattering length of the screen is not expected to depend on the beam size. Therefore, the additional contrast reduction because of lateral scattering is expected to be smaller in the case where the VCSEL's farfield is projected onto the screen compared to the case where the VCSEL's nearfield is projected. This is confirmed by the experiments: the measured speckle contrasts in Tab. 8.5 are clearly higher than those in Tab. 8.3. Estimation of the absolute contrast value is again difficult, since the scattering dynamics are not known in detail. As in the nearfield case, the relative decrease of the measured speckle contrast for the different pulse parameters given in Tab. 8.2 can be compared. The relative decrease fits well with the estimation.

If the camera is placed in the farfield of the screen (setup shown in Fig. 8.5(a)), the screen is no longer imaged and the superposition of all the uncorrelated speckle patterns produced by the different coherence islands on the screen is measured. Therefore, it is expected that all three contrast reducing effects discussed in Section 8.1.4 contribute: polarization scrambling, shift in the emission wavelength of the VCSEL and the superposition of 344 uncorrelated speckle patterns. A comparison of the measured and

Table 8.6: Comparison between the measured and estimated speckle contrast for the setup in Fig. 8.5(a).

Pulse parameters	Measured speckle contrast / %	Estimated speckle contrast / %
1 μ s pulse, 124 mA	2.8	3.0
2 μ s pulse, 124 mA	2.4	2.3
1 μ s pulse, 274 mA	1.8	1.8
2 μ s pulse, 274 mA	1.3	1.3

the estimated speckle contrast values is given in Tab. 8.6. Good agreement between measured and estimated contrast values is achieved with only small deviations. The minimally obtained contrast is 1.3%.

8.1.6 Conclusion and Outlook

The speckle characteristics of a near-infrared broad-area vertical-cavity surface-emitting laser in multimode and in the spatially incoherent, nonmodal emission regime were investigated. The incoherent emission can help to reduce speckle contrast, but its full potential to do so was only obtained when the camera is not imaging the screen. In that case speckle contrast values as low as 1.3% were achieved in good agreement with theoretical estimates. In the model three speckle contrast reducing effects are taken into account. These are polarization scrambling scattering in the paper screen, a thermally induced shift in the VCSEL's emission wavelength and the reduced spatial coherence of the source. The findings are promising for applications which do not image the laser illuminated target and that suffer from speckle noise. An example of such an application is Doppler vibrometry [64].

Of course, for many applications it is required that the screen is imaged onto a detector. When the screen was imaged with full camera resolution onto the CCD chip, the lowest measured speckle contrast was 19% in the incoherent emission regime. The reason for this albeit limited speckle contrast reduction is that the beamlets illuminate spatially separated regions on the screen together with the fact that these regions can be resolved by the imaging system. Therefore, not much profit from the spatially incoherent emission of the VCSEL could be obtained.

The large potential of the incoherent emission regime to reduce the speckle contrast might however be unlocked. Two approaches can be considered to achieve this goal. First, if the imaging system is not able to resolve the individual beamlets on the screen, the contrast reduction factor will be proportional to the number of beamlets that fall within the resolution spot of the imaging system. This condition can be reached by reducing the size of the VCSEL's beam on the screen for example. This approach can be used in laser active triangulation applications [70]. Second, if the different beamlets

can be made to overlap and their speckle patterns to decorrelate, a contrast reduction can be expected. This can be achieved by using a microlens beam homogenizer. Such a beam homogenizer is commonly used in projection applications in order to shape and homogenize the illumination beam. Light passing through different lenses of the homogenizer illuminates the same area on the screen, but does so under slightly different angles. Assuming each of the mutually incoherent VCSEL beamlets falls into a different lens of the homogenizer, this would result in many speckle patterns which are (at least partly) decorrelated because of the different illumination angles ([9] and Chapter 4). The achievable speckle contrast reduction in a realistic full frame projection setup using a microlens beam homogenizer is investigated in the following sections of this chapter.

8.2 Low-Speckle Laser Projection Using the Nearfield Emission of a Nonmodal BA-VCSEL

8.2.1 Introduction

In the previous section it was shown that the achievable speckle contrast reduction is strongly dependent on the illumination and measurement setup. Speckle contrasts lower than 2% were reached, however so far this was merely possible in a setup where the projection screen was out of focus of the measurement camera. This is somewhat unrealistic for projection applications where a human observer looks at a screen and images it with his eyes. In this section the focus lays on the achievable speckle contrast in a realistic and practical full frame projection setup. It will be shown that a low speckle contrast can be achieved even when the camera images the screen if a microlens beam homogenizer is used.

The remainder of Section 8.2 is organized as follows: In Section 8.2.2, the experimental setup is described. In Section 8.2.3, the measured speckle contrast values for different illumination and VCSEL driving conditions are shown. In Section 8.2.4, the expected contrast values are again quantitatively modeled and compared to the measured values. In Section 8.2.5, conclusions are drawn and an outlook on low-speckle laser projection using the VCSEL's farfield is given.

8.2.2 Experimental Setup

The used projection system is based on a compact microlens beam homogenizer setup described in [186], in which the BA-VCSEL is used as illumination source. The beam

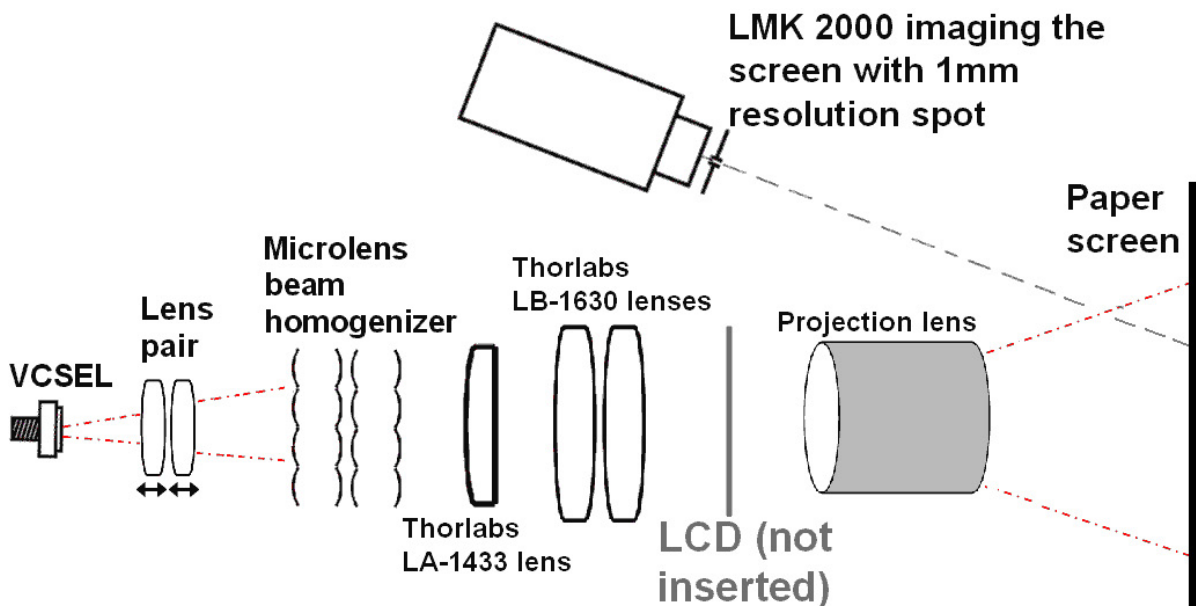


Figure 8.7: Schematic of the illumination and measurement setup.

homogenizer consists of two cylindrical lens tandem arrays of different thickness which are rotated by 90 degrees with respect to each other [187]. The beam homogenizer is sketched in Fig. 5.6 in Chapter 5. The crossed cylindrical lenses of each tandem array have approximately the same functionality as a two dimensional array of rectangular 570 μm x 570 μm lens pairs. Each lens pair creates a rectangular illumination at the position of the LCD. The overlapping light spots formed by all lens pairs guarantee a homogeneous rectangular illumination beam. A schematic illustration of the complete experimental setup is given in Fig. 8.7. An LCD imager was not inserted into the setup because it is not necessary to create real images for speckle measurements. The homogenized light beam is projected onto a screen of standard copy paper using an objective. Speckle contrast could be measured for an image size up to about 7.5 cm x 5.5 cm. For larger images, the intensity in the image plane was too low to measure the speckle contrast accurately. The illuminated area of the screen is measured with a CCD camera (TechnoTeam, type LMK 98-3, objective type TT25). This camera images the screen with a spatial resolution of approximately 1 mm in diameter. This resolution is comparable to the resolution of a human observer looking at the screen from a distance of approximately 3 m with a visual acuity of 1. The imaging resolution is set by placing a pupil with an opening diameter of 0.5 mm in front of the camera objective. The resulting numerical aperture of the camera setup is $0.6 \cdot 10^{-3}$.

Again the speckle characteristics in the nonmodal emission regime are compared with the ones in modal emission. Three different cw driving currents (16 mA, 40 mA and 70 mA) are investigated. These values are just above the cw laser threshold, halfway to and close to the maximum driving current of the VCSEL. In pulsed, nonmodal operation a duty cycle of 4% is used and two different pulse lengths (1 μs and 2 μs) and two pulse heights (157 mA and 240 mA) are investigated. Each of these pulsed driving conditions will coerce the VCSEL in the incoherent emission regime with a corresponding nearfield coherence radius of 1.4 μm . The VCSEL is again mounted onto a heat sink and temperature controlled in order to stabilize its temperature at 25 °C. The beam homogenizer is illuminated by imaging the VCSEL's nearfield onto it. This is done with a pair of lenses with which the nearfield spot size on the homogenizer can be tuned. Speckle measurements are performed for a nearfield spot on the beam homogenizer of either 5.2 mm in diameter, 9 mm in diameter or 18 mm in diameter.

8.2.3 Experimental Results

The light grey bars in Figs. 8.8 - 8.10 depict the measured speckle contrasts for a nearfield spot on the homogenizer of respectively 5.2 mm, 9 mm and 18 mm in diameter for the different driving conditions. These values are corrected for CCD-camera noise, remaining ambient light and for the surface structure of the used paper screen that showed up under white light illumination. It can be observed in these figures that the speckle contrast decreases with increasing injection current in cw operation and decreases with increasing pulse amplitude and duration in pulsed operation. For all three illumination conditions, the speckle contrast is lower in pulsed operation as compared to cw operation. There is not much difference whether a 9 mm or 18 mm nearfield spot is projected onto the homogenizer, but the contrast is clearly larger for the 5.2 mm spot.

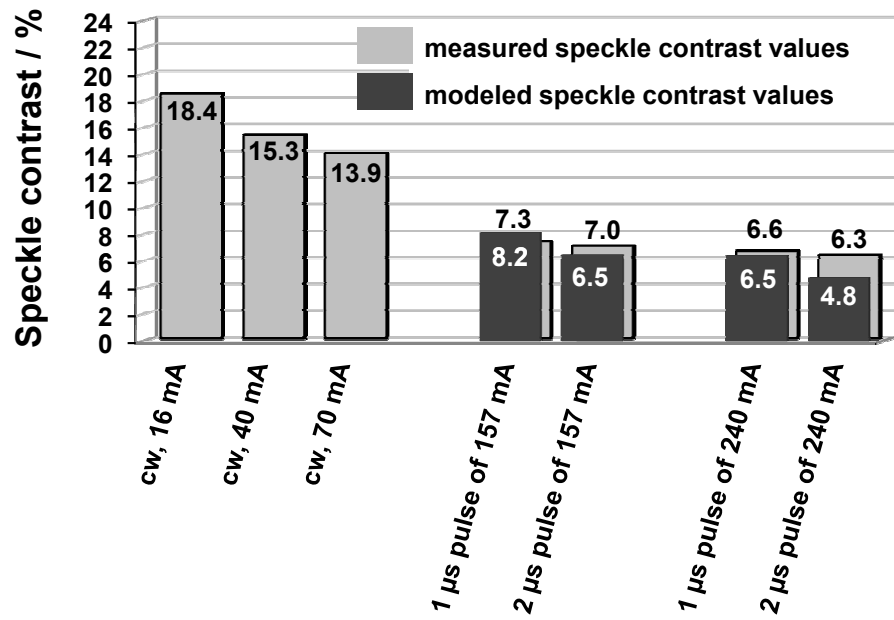


Figure 8.8: Measured and modeled speckle contrast values for illumination of the beam homogenizer with a 5.2 mm diameter nearfield spot.

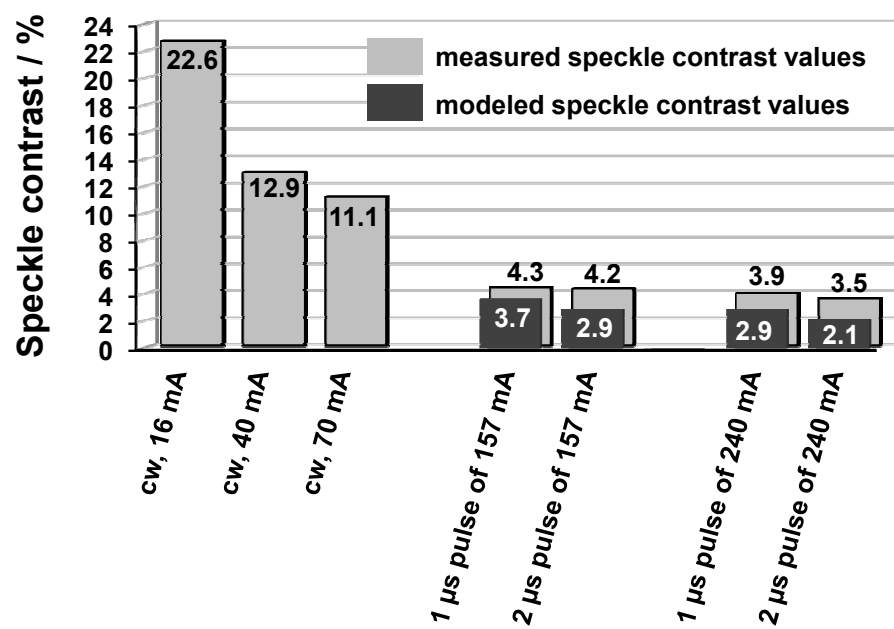


Figure 8.9: Measured and modeled speckle contrast values for illumination of the beam homogenizer with a 9 mm diameter nearfield spot.

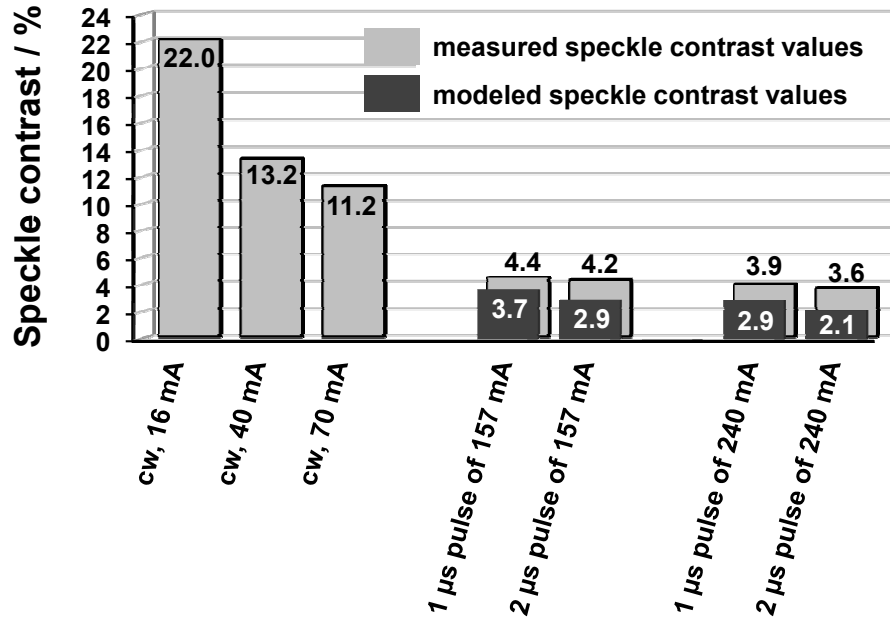


Figure 8.10: Measured and modeled speckle contrast values for illumination of the beam homogenizer with an 18 mm diameter nearfield spot.

8.2.4 Modeling of the Speckle Contrast

To model the speckle contrast values the model presented in Section 8.1 is expanded.

As the paper screen is known to fully depolarize backscattered light, speckle contrast reduction by a factor of $1/\sqrt{2}$ directly results.

The second speckle contrast reducing effect is again the shift of the VCSEL's emission wavelength during the camera's integration time. In cw operation the emission wavelength does not change over time, but in pulsed operation a shift occurs due to Joule heating and expansion of the cavity. As the camera integration time is again much higher than the pulse duration, the situation is again comparable to illumination of the screen with a source that has a bandwidth equal to the shift of the emission wavelength. The connected speckle contrast reduction factor for the used paper screen can again be calculated with Eq. (8.1). In Chapter 6, $c\sigma_\tau$ of approximately 380 μm has been determined for the used paper screen for 808 nm light. This value is assumed to still be valid at 840 nm. The heat induced shift in the VCSEL's emission wavelength during a pulse is again estimated by calibrating the wavelength shift with temperature and calculate the temperature rise during a pulse [184]. The shifts of the emission wavelength and the calculated speckle contrast reduction factors are given in Tab. 8.7.

The main focus is on the third speckle contrast reducing effect that plays a role: the speckle contrast will be reduced due to the reduced spatial coherence of the VCSEL source. In cw operation, the exact number of transverse modes, their intensity and the connected spatial coherence can again not be easily determined. However, the trend of decreasing speckle contrast with increasing driving current which is expected because of the decreasing coherence [33] can be clearly seen in Fig. 8.8, Fig. 8.9 and Fig. 8.10 for all three illumination conditions. The minimal measured speckle contrast in cw operation

Table 8.7: Shift of the emission wavelength of the VCSEL for different pulse parameters and resulting speckle contrast reduction factor for the used paper screen

Pulse parameters	Shift of the emission wavelength / nm	Speckle contrast reduction factor
1 μ s pulse, 157 mA	0.40	0.850
1 μ s pulse, 240 mA	0.81	0.677
2 μ s pulse, 157 mA	0.80	0.681
2 μ s pulse, 240 mA	1.63	0.498

is approximately 11%.

A further reduction can be achieved in pulsed operation. If - as an example - the effect of the emission wavelength shift (factor 0.85) is excluded from the measurement in Fig. 8.9 for a 1 μ s, 157 mA pulse (with a speckle contrast of 4.3%), the speckle contrast would be 5.1%. This is more than a factor of two better than under cw operation and shows that the spatial coherence in the nonmodal emission regime is smaller than in cw operation. In order to estimate the speckle contrast reduction due to the VCSEL's nonmodal emission, the beam's spatial coherence area at the position of the homogenizer has to be known. This spatial coherence area is dependent on the magnification with which the VCSEL's 50 μ m diameter aperture is imaged onto the beam homogenizer. The VCSEL's 50 μ m diameter aperture is again modeled as being filled up with about 318 independent coherence islands each of which has a radius of 1.4 μ m. In case of the 5.2 mm nearfield spot on the homogenizer, the magnification is given by (5.2 mm / 50 μ m) = 104. The coherence radius can be assumed to scale by the same factor, therefore having a value of approximately 145 μ m on the homogenizer. Analogous treatment in case of the 9 mm and the 18 mm diameter nearfield spots leads to coherence radii of approximately 250 μ m and 500 μ m on the homogenizer. The size of the homogenizer's lenses and the coherence islands are sketched in Fig. 8.11 for the three spot sizes.

In order to profit from the reduced spatial coherence in the nonmodal emission regime, two conditions have to be fulfilled: It has to be ensured that the speckle patterns produced by different coherence islands are (at least partly) decorrelated *and* the decorrelated speckle patterns have to superimpose on the screen. If only the first condition is reached, the camera that images the screen will be able to spatially resolve the different decorrelated speckle patterns and thus no averaging of these patterns will occur. As a result, the speckle contrast will not be reduced. This is actually the reason why no satisfactory speckle contrast reduction was achieved in Section 8.1 when the camera imaged the screen.

In the projection system proposed here, the overlapping of the speckle patterns is accomplished by using the beam homogenizer as it images different segments of the illumination beam onto the same position of the screen. In order to fulfill the first condition in nonmodal operation, there are two main effects that may cause a decorrelation between the speckle patterns produced by different coherence islands. First, decorrelation will occur if different coherence islands illuminate the same area on the screen under

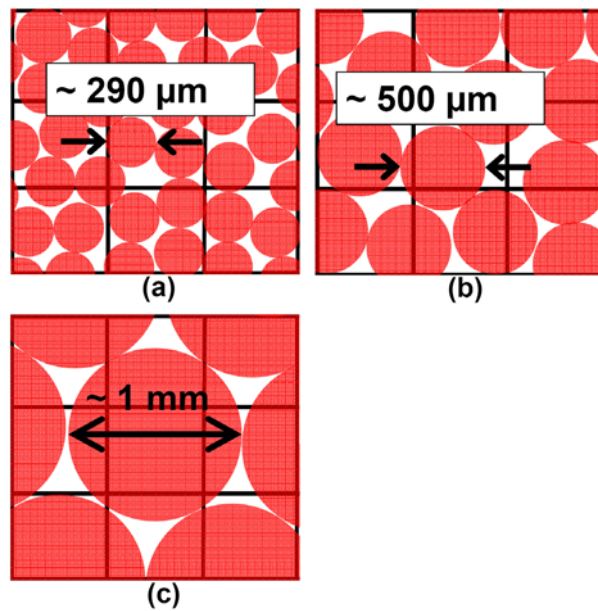


Figure 8.11: Schematic of a section of the illuminated beam homogenizer. The microlenses of the beam homogenizer are indicated by the rectangular grid: (a) for a 5.2 mm nearfield spot with coherence islands of 145 μm radius, (b) for a 9 mm nearfield spot the coherence islands have a radius of approximately 250 μm and their size is comparable to the size of a homogenizer lens, (c) for an 18 mm nearfield spot with coherence islands of 500 μm radius.

sufficiently different illumination angles. Each fully illuminated lens of the homogenizer produces one rectangular spot on the screen with a slightly different angle of incidence for each rectangular spot. On the contrary, light from different non-overlapping regions of *one* lens will be non-overlapping on the screen. Therefore, different coherence islands will illuminate the *same* area of the screen under *different* angles - and thus speckle reduction may be achieved - only if they illuminate different lenses of the homogenizer. Secondly, decorrelation may be caused by a wavelength difference between different coherence islands. The emission wavelength of the coherence islands is dependent on their radial position in the aperture. It is about 1 nm larger in the outer regions of the aperture [183]. But coherence islands at the same radial position have almost the same wavelength. As the emission is mostly concentrated at the outer rim of the VCSEL because of current crowding, the coherence islands carrying most of the intensity have only a small wavelength difference. It is thus expected that wavelength diversity between the coherence islands is the minor effect in causing decorrelation between the corresponding speckle patterns.

The angle at the screen between rays travelling through adjacent lenses should be large enough to fully decorrelate the corresponding speckle patterns. This minimum angular difference ζ is now estimated. As already shown in Chapter 2, ζ can be determined relatively easy for a purely surface scattering screen [9]. In case of a slight change in illumination angle, the resulting speckle pattern is then mainly translated without changing its internal structure. ζ is then approximately given by $\sin(\zeta/2) = N.A._{image}$,

where $N.A._{image}$ is the numerical aperture of the imaging system ($0.6 \cdot 10^{-3}$ in the setup). This results in $\zeta \approx 0.0688^\circ$. The angle between two rays that are transmitted through adjacent lenses of the homogenizer and that illuminate the same area of the screen is 0.158° in the measurement setup. This angle is dependent on the magnification of the projection optics. It is clearly larger than the minimally required angle ζ . Therefore, speckle patterns formed by beamlets transmitted through adjacent homogenizer lenses will be fully decorrelated for pure surface scattering. For beamlets transmitted through lenses that are not adjacent, the angular difference is obviously larger and their speckle patterns will also be fully decorrelated. However, in the experiments not a surface scattering but a volume scattering screen is used and the situation is more complex. The photons perform a random walk inside the screen. In order to determine the correlation between the speckle patterns for different illumination angles, it would be necessary to model these random walks in detail. This has not been investigated and is beyond the scope of this section. However, it is reasonable to assume that this random walk process leads to an even smaller value for ζ .

In the estimate of the speckle contrast it also has to be taken into account that not all beamlets emitted by the VCSEL have the same intensity. Therefore, the speckle reduction due to superposition of the M resulting decorrelated speckle patterns is smaller than $1/\sqrt{M}$. Following [9], the resulting speckle contrast C for the superposition of M uncorrelated speckle patterns of different mean intensities \bar{I}_n is given by

$$C = \frac{\sqrt{\sum_{n=1}^M \bar{I}_n^2}}{\sum_{n=1}^M \bar{I}_n}. \quad (8.2)$$

The intensity of the coherence islands depends on their radial position in the VCSEL aperture. The radial dependence of the emitted relative intensity I_{rel} has been measured and is depicted in Fig. 8.12. Using this measurement it can be determined how many beamlets contribute with which mean intensity and Eq. (8.2) can then be used to calculate the expected speckle contrast.

It can be more clearly explained after the shown considerations why the different illumination spot sizes on the homogenizer were used. The 5.2 mm spot size on the homogenizer was chosen to investigate the situation when the coherence radius on the homogenizer is considerably smaller than the size of the homogenizer's lenses. In case a 9 mm spot is projected onto the homogenizer, the coherence radius is roughly equal to the lens size whereas for the 18 mm spot the coherence radius is approximately twice as large as the lens size. For the three homogenizer illumination conditions sketched in Fig. 8.11, this has the following implications: In case of a 5.2 mm light spot on the homogenizer, on average about five coherence islands illuminate one microlens. Because the light from these non-overlapping coherence islands is non-overlapping on the screen, they do not contribute to speckle contrast reduction. Therefore, only $318/5 \approx 65$ speckle patterns are superimposed on the screen. However, this does not result in a speckle contrast reduction factor of $1/\sqrt{65} \approx 0.125$ as if they had equal intensities. The correct factor can be calculated using Eq. (8.2) and has a somewhat larger value of 0.136. In case of a 9 mm nearfield spot on the beam homogenizer, the coherence radius at the homogenizer is approximately 250 μm . Each of the 318 beamlets thus illuminates an area

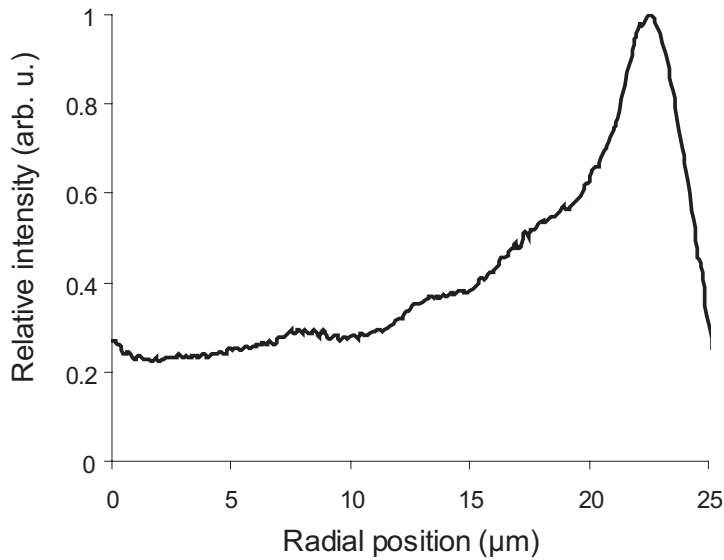


Figure 8.12: Radially resolved measurement of the intensity distribution in the VCSEL's aperture in the nonmodal emission regime.

on the homogenizer comparable to the size of one microlens. Therefore, each coherence island produces a speckle pattern that can be assumed to be fully decorrelated from all the others. This results in an additional speckle contrast reduction factor of 0.061 when the intensity diversity of the beamlets is again taken into account. In case of an 18 mm nearfield spot on the beam homogenizer, the coherence radius at the homogenizer is approximately 500 μm and each of the 318 beamlets thus illuminates an area on the homogenizer which is substantially larger than one microlens. However, light beams that are travelling through different lenses of the homogenizer but which originate from one coherence island are spatially correlated and not statistically independent. Therefore, the number of independent speckle patterns will be the same as for a 9 mm nearfield spot on the beam homogenizer, and the speckle contrast reduction factor will again be 0.061.

The overall estimated speckle contrast is again given by multiplying the reduction factors due to polarization scrambling ($1/\sqrt{2}$), the wavelength shift in pulsed operation (see Tab. 8.7) and the superposition of beamlets/coherence areas. All estimated speckle contrast values are given by the grey bars in Fig. 8.8, Fig. 8.9 and Fig. 8.10. It can be seen that excellent agreement between modeling and measurement is achieved. The speckle contrast values for a 9 mm and an 18 mm nearfield spot on the beam homogenizer are similar and, as expected, lower than the speckle contrast for a 5.2 mm nearfield spot. These observations prove that the speckle contrast is not determined by the size of the spot on the homogenizer as such, but rather by the relative size of the homogenizer's lenses compared to the size of the coherence islands on the homogenizer.

The estimated speckle contrast values in Fig. 8.8, Fig. 8.9 and Fig. 8.10 are however slightly smaller than the measured values. This might be due to the fact that the volume roughness of the paper screen (380 μm) as used during the modeling was determined for 800 nm light. If it would be somewhat smaller for the 840 nm VCSEL, this will indeed

result in larger estimated speckle contrast values. A closer look at Fig. 8.8, Fig. 8.9 and Fig. 8.10 shows that the difference between estimated and measured values is slightly larger for longer pulse durations and higher pulse amplitudes. As the VCSEL's nearfield coherence radius is the same for each of the pulsed driving conditions ([179],[181]), the speckle contrast reduction due to nonmodal emission is equal for each of the pulsed driving conditions. The VCSEL's emission wavelength shift is thus the only speckle contrast reducing effect that is influenced by the pulse height and duration. The effect of the wavelength shift might have been slightly overestimated. This can be due to the fact that the shift has been approximated by a Gaussian spectrum and the wavelength shifts given in Tab. 8.7 are not spatially resolved. However, it has been shown in [183] that the heating of the cavity is spatially non-uniform. This might explain the slight deviations between measurements and modeling.

8.2.5 Summary and Outlook

Speckle contrast values as low as 3.5% were measured in a realistic and practical projection setup. Again, specific driving conditions of the broad-area VCSEL source were used to obtain nonmodal, spatially incoherent emission. The speckle contrast was modeled by taking polarization scrambling of the paper screen and the shift of the VCSEL's emission wavelength in pulsed operation in combination with the volume scattering screen into account. In third instance, the reduced spatial coherence of the VCSEL was modeled and the fact that not all beamlets contribute with the same intensity has been considered. Excellent agreement between measured and modeled speckle contrast values is achieved.

It was shown that, in order to exploit nonmodal emission to its full potential, the size of the coherence islands on the beam homogenizer in comparison to the size of the beam homogenizer's lenses is a crucial parameter. Each coherence island has to be equal to or larger than one microlens of the homogenizer. The homogenizer then introduces sufficient angular diversity to decorrelate the resulting speckle patterns that are superimposed on the screen.

In Chapter 5, the illumination of a two-tandemarray microlens beam homogenizer with fully and partially coherent light was simulated. For fully coherent illumination of the homogenizer, a grid like interference pattern was visible in the homogenized plane, which results from the interference of light from different microlenses. As the individual BA-VCSEL beamlets are mutually incoherent they cannot interfere. The large number of mutually incoherent beamlets therefore assures that no disturbance because of a interference of light from different microlenses occurs in projected images.

In order to fulfill the discussed conditions for maximum speckle contrast reduction, it is not mandatory to project the VCSEL's nearfield onto the homogenizer. Similar results can also be obtained by illuminating the homogenizer with the VCSEL's farfield. This way, several disadvantages can be overcome. In such a setup, the speckle contrast reduction is again determined by the number of coherence islands and their size at the position of the homogenizer. These quantities are determined by the VCSEL's farfield coherence angle [143]. Low-speckle laser projection with the nonmodal BA-VCSEL's farfield illuminating the beam homogenizer is investigated in the following section.

8.3 Low-Speckle Laser Projection Using the Farfield Emission of a Nonmodal BA-VCSEL

8.3.1 Introduction

In the previous section, speckle contrast values as low as 3.5% have been realized by projecting the VCSEL's nearfield onto the microlens beam homogenizer. Using nearfield illumination of the homogenizer introduces several practical disadvantages. Additional lenses have to be introduced into the system in order to image the nearfield onto the homogenizer and the homogenizer needs to be accurately aligned at the position of the imaged nearfield. Furthermore, a relatively large distance is required between the VCSEL and the homogenizer in order to obtain a sufficiently large magnification of the imaged nearfield. In this section it is shown that these disadvantages can be avoided and low speckle contrast values can also be achieved by directly illuminating the homogenizer with the VCSEL's farfield.

The remainder of Section 8.3 is organized as follows: In Section 8.3.2, the experimental setup is explained and in Section 8.3.3 the measurement results are presented. As the modeling of the spatial coherence and intensity distribution of the farfield beam differ from the nearfield case, the nearfield model from the previous section is properly adapted in Section 8.3.4. The measured and modeled speckle contrast values are compared. In Section 8.3.5, the maximal size of an image projected with the used full frame projection setup to be still free of speckle disturbance is estimated. In Section 8.3.6, the section is summarized.

8.3.2 Experimental Setup

The experimental setup is shown in Fig. 8.13. It is similar to the one used in Section 8.2, however the beam homogenizer is now directly illuminated with the VCSEL's farfield. The VCSEL is again mounted onto a heat sink and temperature controlled in order to stabilize its temperature at 25 °C. Speckle is measured for a varying distance z_{ff} between the VCSEL and the homogenizer. In cw (modal) operation, again driving currents of 16 mA (close to lasing threshold) and 70 mA (close to thermal roll-over) are investigated. In pulsed (nonmodal) operation of the VCSEL a pulse length of 2 µs, two different pulse amplitudes of 157 mA and 240 mA are investigated. The duty cycle is again 4% in order to avoid any average heating of the VCSEL. The speckle contrast values are again measured with a CCD camera that has a spatial resolution on the screen of about 1 mm, which is comparable to the spatial resolution of a human observer at a distance of approximately 3 m. The captured speckle images are again corrected for CCD-noise, remaining ambient light and for the small contrast that shows up on the paper screen under room light illumination. The size of the illuminated area on the screen is again about 7.5 cm x 5.5 cm.

8.3.3 Experimental Results

In Fig. 8.14 speckle patterns measured for a short distance of 9 mm between VCSEL and homogenizer is shown in the upper row. At a cw current of 16 mA (see Fig. 8.14(a))

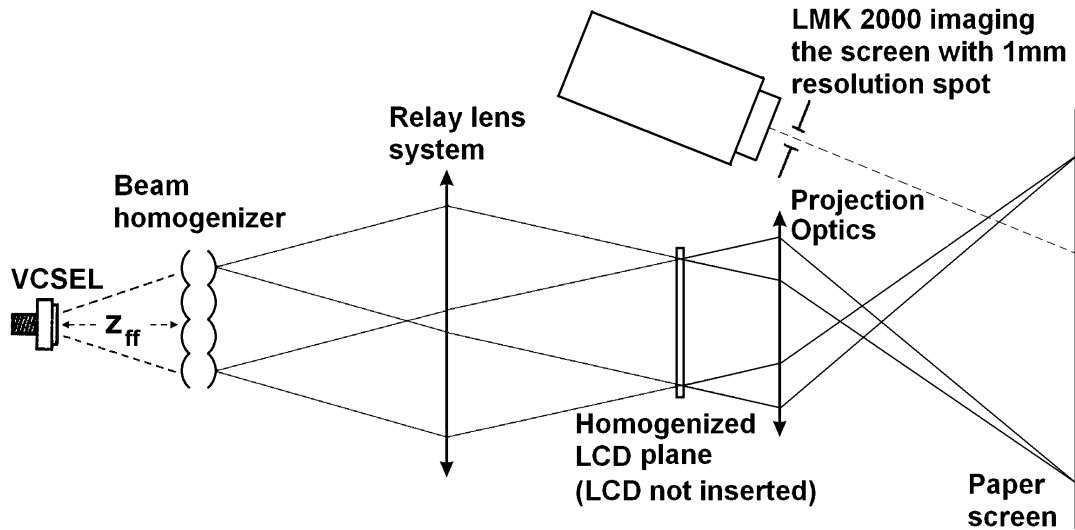


Figure 8.13: Schematic of the illumination and measurement setup.

speckle is clearly visible along with a strong non-uniformity of the intensity distribution. The speckle contrast corresponding to this situation is 36% and is highly disturbing for any observer. In pulsed operation (see Fig. 8.14(b)), both the speckle contrast and the illumination uniformity have strongly improved. The resulting speckle contrast is 8% and is not yet optimal. A further large reduction in speckle contrast can be achieved by increasing the distance between VCSEL and homogenizer.

The lower row of Fig. 8.14 depicts the speckle pattern for the same driving conditions as in the upper row, but now for a distance z_{ff} of 59 mm. In cw operation on the one hand, the illumination homogeneity drastically improves, but speckle remains very visible and the speckle contrast is only reduced to 25%. In pulsed operation on the other hand, the speckle contrast reduces to a mere 2.5% in combination with an excellent illumination homogeneity. The distance between VCSEL and homogenizer thus plays an important role for both the speckle contrast and the illumination uniformity. When this distance is increased, the number of illuminated microlenses of the homogenizer obviously increases and hence an improvement of the illumination uniformity can be expected. The improvement of the speckle contrast is less obvious. This effect is further investigated by plotting the measured speckle contrast versus the distance between VCSEL and homogenizer for the different driving conditions in Fig. 8.15. It can be seen that the speckle contrast again decreases with increasing cw driving current and with increasing current pulse amplitude in pulsed operation. The speckle contrast values in nonmodal operation are again lower than the values achieved in cw operation. For all driving conditions, the speckle contrast first decreases with increasing distance between VCSEL and homogenizer, to then saturate for large distances.

8.3.4 Modeling of the Speckle Contrast

The model again covers the three speckle contrast reducing effects. Depolarization of the light backscattered from the paper screen again results in a speckle contrast reduction by a factor of $1/\sqrt{2}$ in all setups, independent from the specific driving and illumination

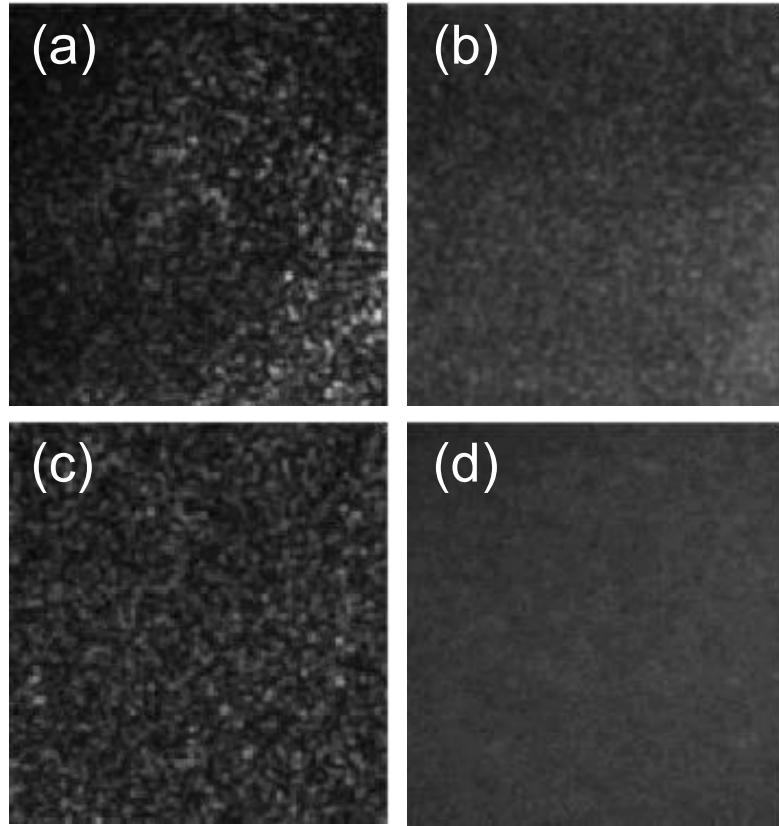


Figure 8.14: Speckle pattern for a distance of 9 mm (upper row) and 59 mm (lower row) between VCSEL and homogenizer: (a) and (c) in cw operation at 16 mA, (b) and (d) in pulsed operation at 240 mA.

conditions. The second effect is again the thermal chirp of the VCSEL's emission wavelength in pulsed operation. The contrast reduction factors resulting from the wavelength chirp were determined in the previous section to be 0.68 for the 157 mA pulses and 0.50 for the 240 mA pulses. The reduced spatial coherence again cannot easily be modeled for cw operation because the VCSEL emits a large number of transverse modes and it is difficult to accurately measure the intensity distribution of these modes. The number of lasing transverse modes again increases (up until the thermal roll-over at 70 mA) with increasing driving current and hence the coherence decreases [33]. The exact speckle contrast values in cw operation can again not be modeled, but the expected trend of a decreasing speckle contrast with increasing driving current is clearly visible in Fig. 8.15. The model of the speckle contrast reduction because of the reduced spatial coherence of the VCSEL in nonmodal operation has to be adapted from nearfield illumination (presented in the previous section) to farfield illumination of the homogenizer. The non-modal VCSEL has a Gaussian farfield intensity distribution and its half-width farfield divergence angle Θ_{ff} is 11° [179]. The half-width farfield coherence angle Θ_{coh} is 0.6° as has been determined from the nearfield intensity distribution [179]. Therefore, the farfield beam can be modeled as consisting of approximately 340 beamlets that are all mutually incoherent. Each beamlet produces a speckle pattern and these patterns add on intensity basis because of the incoherence of the beamlets.

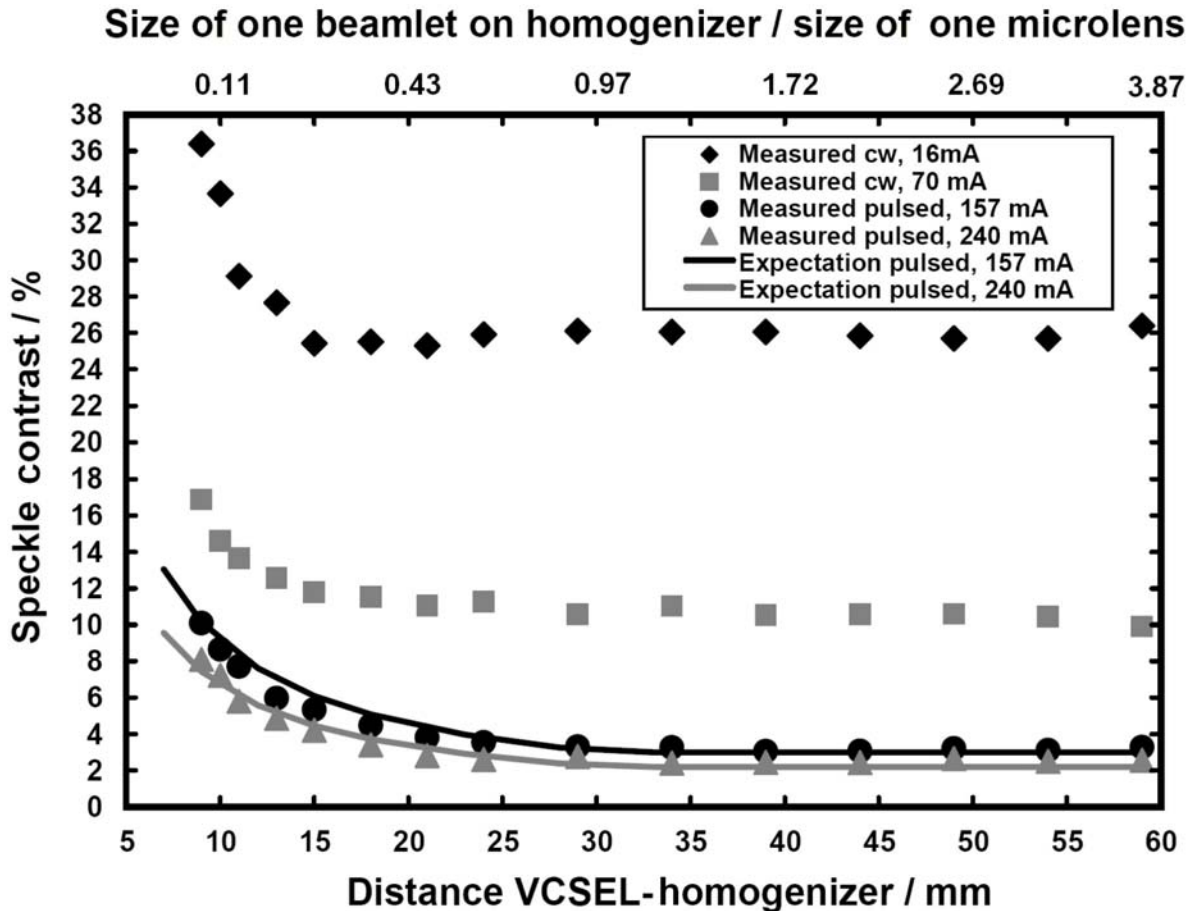


Figure 8.15: Evolution of the speckle contrast as a function of the distance VCSEL - homogenizer for the cw currents of 16 mA (black diamonds) and 70 mA (gray squares), and pulses of 157 mA amplitude (black circles) and 240 mA amplitude (gray triangles). Also shown is the modeled speckle contrast for 157 mA pulses (black line) and 240 mA pulses (gray line).

In case of a farfield beam, the intensity of the individual beamlets depends on their radial position in the farfield beam, which can easily be determined from the Gaussian shape of the farfield intensity distribution. Again the fact is used that beamlets which pass through different microlenses of the homogenizer are superimposed on the screen under slightly different angles and that their speckle patterns are therefore at least partly decorrelated. This angular difference is inversely proportional to the magnification of the projection lens in Fig. 8.13. In the setup used, the magnification is again such that the angle between beamlets originating from adjacent microlenses is 0.16° . The minimally required angular difference ζ to decorrelate beamlets from adjacent lenses for pure surface scattering can again be calculated to be $\zeta = 0.069^\circ$. So, beamlets from adjacent lenses are fully decorrelated (as in the previous section).

The speckle contrast reduction resulting in the experiments is therefore again determined by the amount of microlenses of the homogenizer that are illuminated by different beamlets. Thus the size of the beamlets, i.e. their coherence radius r_{coh} , at the position of the homogenizer is critical in determining the resulting speckle contrast. This farfield

coherence radius is given by $r_{coh} = z_{ff} \tan \Theta_{coh}$. Using this size, the Gaussian intensity profile in the farfield and Eq. (8.2), the expected speckle contrast resulting from the reduced spatial coherence can be calculated. As mentioned above, the three individual contrast reduction factors need to be multiplied in order to determine the overall speckle contrast reduction. The total calculated speckle contrast is plotted in Fig. 8.15 for the two investigated pulse amplitudes. The calculated speckle contrasts correspond excellently with the measured values, and the modeling allows to explain the experimentally observed trends: The size of a single rectangular microlens of the beam homogenizer is approximately 570 $\mu\text{m} \times 570 \mu\text{m}$. For a small distance between VCSEL and homogenizer, the size of a beamlet on the homogenizer is smaller than the size of a single microlens and thus several beamlets fall into each microlens. If the distance z_{ff} is increased, the coherence radius r_{coh} increases such that more lenses in the homogenizer are illuminated by uncorrelated coherence islands and the resulting speckle contrast decreases. The size of one beamlet divided by the size of one microlens of the beam homogenizer is given in Fig. 8.15 on the secondary x-axis. When the size of the beamlets becomes larger than the size of the microlenses, no further speckle reduction can be achieved. The maximum speckle contrast reduction is then determined by the number of beamlets and not by the number of illuminated lenses. Therefore, the speckle contrast remains constant for distances larger than 30.5 mm.

8.3.5 Maximal Image Size for Angular Decorrelation

The calculation of the minimally required angular difference ζ (to decorrelate beamlets from adjacent lenses for pure surface scattering on the paper screen) yielded a value of 0.069° in the used setup. If ζ is measured for the volume scattering paper screen, it is found to be only approximately 0.017° . This value is smaller than expected for pure surface scattering. For volume scattering the random walk of the photons inside the screen leads to a much faster decorrelation of the speckle patterns when the illumination angle is changed. Therefore, the minimally required angle for full decorrelation decreases and is much smaller than the angular difference provided in the used setup, where an image of approximately 7.5 cm \times 5.5 cm was projected onto the screen. However, the difference of the angles of incidence onto the screen between rays travelling through adjacent lenses is dependent on the magnification of the projection system.

With the value of $\zeta = 0.017^\circ$ it can be calculated that image sizes of about 65 cm \times 50 cm can be realized under the constraint that speckle patterns from beamlets from adjacent microlenses are still fully decorrelated because of their angular diversity. For a further increase of the projected images, the speckle patterns will be more and more correlated as the difference of the illumination angles gets smaller. The speckle contrast will therefore increase. However, most microlenses are not mutually adjacent (no direct neighbors). So, the speckle contrast will increase only gradually. As already mentioned, the speckle contrast has to be smaller than approximately 4% to avoid disturbance of a human observer [120]. As the minimally achieved speckle contrast with fully decorrelated patterns was only 2.5%, an increase of the speckle contrast by approximately 1.5% is tolerable. To counteract the increase of the correlation of the resulting speckle patterns with increasing image size, the distance of the observer to the screen can be increased. This will reduce the numerical aperture with which the observer images the screen. It

has been shown in Section 8.2 that this will result in a smaller required decorrelation angle. Another countermeasure would be the selection of a volume scattering screen in which the resulting speckle patterns are already decorrelated for smaller changes of the illumination angle as in the paper screen used in the experiments. This might be a screen with larger volume roughness and therefore more complex random walks as the paper screen. It has been shown in Chapter 6 that such screens exist. Also a combination of the projection setup with a colloidal-dispersion-filled screen as investigated in Chapter 7 can be considered.

8.3.6 Summary

In this section, low-speckle laser projection with a broad area VCSEL in the nonmodal emission regime was shown and modeled, where the VCSEL's farfield was directly projected onto a microlens beam homogenizer. Speckle contrast values as low as 2.5% were achieved. Also for farfield illumination of the homogenizer each beamlet has to be larger than one microlens of the homogenizer in order to exploit the full potential of the VCSEL's low spatial coherence. For farfield illumination the size of the beamlets on the homogenizer can be simply chosen by tuning the distance between VCSEL and homogenizer. The optimum speckle contrast is reached without any critical alignment. The large number of contributing mutually incoherent beamlets again assures that no disturbance because of a grid like interference structure from light from different microlenses is observable. The model of polarization scrambling, the thermal chirp of the VCSEL's wavelength and the reduced spatial coherence has been adapted to farfield illumination of the homogenizer. Again, excellent agreement between the model and the measured speckle contrast values is achieved.

8.4 Chapter Conclusion and Outlook

This chapter demonstrated that BA-VCSEL light sources have large potential to be used in low-speckle laser projection applications. After a basic investigation of the speckle properties of the nonmodal BA-VCSEL, it has been successfully used as illumination source in realistic and practical full frame projection setups. Quasi-speckle-free laser projection could be realized by exploiting and combining the three speckle contrast reducing effects polarization scrambling, and a reduced temporal and spatial coherence of the VCSEL.

The low divergence angle of the VCSEL as compared to HID lamps or LEDs also results in a high efficiency, which cancels the need to introduce additional optics. The shown method is therefore an efficient way to achieve low speckle contrasts.

Laser projection applications generating full color images for human observers need laser sources which emit in the visible wavelength range. The VCSEL used in the experiments emits at a wavelength of 840 nm. One of the main future challenges will be to transfer the nonmodal emission regime to the visible wavelength range using either VCSELs or other laser sources. It is currently under investigation whether the nonmodal BA-VCSELs can be frequency doubled in order to realize a nonmodal source emitting in the blue wavelength range [188].

The results of this chapter are also useful for speckle reduction in projection systems based on laser arrays. Similar to solutions with external cavity laser diodes [189], VCSELs may be arranged in an array configuration in order to scale up the optical output power and to reduce the speckle contrast even further [190]. For an array of single mode lasers each of which is fully spatially coherent, the individual lasers of the array play a similar role as the coherence islands in the BA-VCSEL. Decorrelation between the speckle patterns can again be achieved either by introducing a large enough wavelength shift between the different lasers of the array and/or by introducing sufficient angular diversity.

Chapter 9

Conclusion of the Thesis

It was shown that the use of lasers as illumination sources in projection systems can provide numerous advantages compared to the use of standard projection lamps. The unwanted emergence of laser speckle and the resulting degradation of the image quality are, however, major problems when lasers are used as illumination sources.

Several methods for speckle reduction with different practicability and effectiveness were developed and characterized. Low speckle contrast values (even below the 4% contrast disturbance limit) can be efficiently achieved, if several of the different methods for speckle contrast reduction are combined. Optimally, this combination is done in a cost-effective way without loosing the discussed vast advantages connected to the use of laser sources.

The effectiveness and practicability of the different methods can be dependent on the projection system architecture and the system setup. For example, the resulting speckle contrast for spatial and angular decorrelation is strongly connected to the image size on the screen and the distance of the observer from the screen. These dependencies require a detailed analysis of a projection system and a treatment of the speckle problem on a case to case basis which can be demanding.

Methods for speckle reduction which are connected to the screen are typically less dependent on a particular projection system architecture and the system setup. Speckle reduction by depolarizing scattering and by the use of a colloidal-dispersion-filled projection screen can be simply achieved by a proper selection of the projection screen. The projection system itself does not need to be adapted. This also partly applies to speckle reduction by broadband illumination. It was shown that large speckle contrast reduction can be achieved at low expense by the illumination of a volume scattering screen already with a moderate illumination bandwidth of only several nanometers. The single relevant parameter of the projection system which influences the speckle contrast resulting for a particular projection screen is the illumination bandwidth which can be easily determined. The illumination bandwidth must not be too large in order not to decrease the system's color gamut too much. An illumination bandwidth of about 10 nm still leads to colors which are highly saturated compared to the colors in projection systems which use standard projection lamps or even LEDs as illumination sources. Although speckle contrast values below the 4% disturbance limit could not be achieved with reasonably small illumination bandwidths, speckle reduction by broadband illumination and wavelength decorrelation is a highly attractive method. This is because the resulting speckle

contrast for a given illumination bandwidth will be the same no matter if the system was a full-frame or a raster-scanning projection system and will not be dependent on the image size, the observer's spatial resolution and the like. The promising results found for broad-area VCSELs in the nonmodal emission regime are encouraging for future work. Low-cost methods for the chirping of the emission wavelength of lasers and low-cost broadband-emitting lasers are highly interesting to be used in the upcoming laser projection systems consumer market.

Bibliography

- [1] Information provided by Insight Media, 3 Morgan Avenue, Norwalk, CT 06851, USA (2009).
- [2] Texas Instrument Bulletin No. DLA 1324, “Experimental Laser Display for Large Screen Presentation,” (1966).
- [3] G. Derderian, S. Seaford, and R. J. Klaiber, “Laser beam deflector,” U.S. Patent No. 3,436,546, issued April 1, 1969.
- [4] M. Brennesholtz, C. Chinnock, “2008 Pico-Projector Market Segment Analysis,” Insight Media, 3 Morgan Avenue, Norwalk, CT 06851, USA (2008).
- [5] J. C. Dainty, editor, 2nd ed., *Laser Speckle and Related Phenomena* (Springer, 1984).
- [6] M. Francon, *Laser speckle and applications in optics* (Academic Press, 1979).
- [7] P. K. Rastogi, editor, *Digital Speckle Pattern Interferometry and Related Techniques* (John Wiley & Sons, 2001).
- [8] B. Y. Zel'dovich, A. V. Mamaev, and V. V. Shkunov, *Speckle-Wave Interactions in Application to Holography and Nonlinear Optics* (CRC Press, 1995).
- [9] J. W. Goodman, *Speckle Phenomena in Optics: Theory and Applications* (Roberts & Company, 2006).
- [10] H. J. Rabal, ed., R. A. Braga Jr., ed., *Dynamic Laser Speckle and Applications (Optical Science and Engineering)* (CRC, 2008).
- [11] M. Born and E. Wolf, *Principles of Optics* (Cambridge University Press, 1997).
- [12] J. W. Goodman, “Some effects of target-induced scintillation on optical radar performance,” Proc. IEEE **53**, 1688-1700 (1965).
- [13] M. S. Pierce, R. G. Moore, L. B. Sorensen, S. D. Kevan, O. Hellwig, E. E. Fullerton, and J. B. Kortright, “Quasistatic X-Ray Speckle Metrology of Microscopic Magnetic Return-Point Memory,” Phys. Rev. Lett. **70**, 175502 (2003).
- [14] C. B. Burckhardt, “Speckle in Ultrasound B-Mode Scans,” IEEE Trans. on Sonics and Ultrasonics **25**, 1-6 (1978).

- [15] F. S. Patton, D. P. Deponte, G. S. Elliott, and S. D. Kevan, “Speckle Patterns with Atomic and Molecular de Broglie Waves,” *Phys. Rev. Lett.* **97**, 013202 (2006).
- [16] P. Hariharan, “Speckle patterns : a historical retrospect,” *Optica Acta* **19**, 791-793 (1972).
- [17] P. Hariharan, “Holography and Speckle: The Beginnings,” *J. of Holography and Speckle* **1**, 3-5 (2004).
- [18] K. Exner, *Sitzungsberichte der kaiserl. Akad. d. Wiss. (Wien) Abt. 2* **76**, 522 (1877).
- [19] M. von Laue, “Beugungerscheinungen an vielen unregelmäßig verteilten Teilchen”, *Sitzungsberichte der Kgl. Preuss. Akad. Wiss. (Berlin)* **47**, 11441-1163 (1914).
- [20] M. von Laue, “Mathematische Betrachtungen über die Beugungerscheinungen an vielen unregelmäßig verstreuten Teilchen,” *Mitteilungen der Phys. Gesellschaft Zürich* **18**, 90 (1916).
- [21] W. J. de Haas, *Proc. Sect. Sci. K. ned. Akad. Wet.* **20**, 1278 (1918).
- [22] W. J. de Haas, “Die Beugungerscheinungen, welche an einer großen Anzahl unregelmäßig verstreuter Öffnungen oder undurchlässiger Teilchen auftreten,” *Ann. Phys.* **362**, 568-580 (1918).
- [23] C. V. Raman, “The scattering of light in the refractive media of the eye,” *Philos. Mag.* **38**, 568-572 (1919).
- [24] E. Buchwald, *Berichte der Deutsch. Phys. Gesellschaft* **21**, 492 (1919).
- [25] G. N. Ramachandran, *Proc. Indian Acad. Sci. A* **18**, 190 (1943).
- [26] F. Arago, *Meteorological Essays* (Longman, Brown, Green, and Longmans, 1855).
- [27] A. von Humboldt, “Voyage aux Régions Équinoxiales du Nouveau Continent,” 4th book, (1814).
- [28] J. D. Rigden, E. I. Gordon, “The granularity of scattered optical maser light,” *Proc. IRE* **50**, 2367-2368 (1962).
- [29] R. V. Langmuir, “Scattering of Laser Light,” *Appl. Phys. Lett.* **2**, 29-30 (1963).
- [30] L. Allen and D. G. C. Jones, “An Analysis of the Granularity of Optical Maser Light,” *Phys. Lett.* **7**, 321-323 (1963).
- [31] J. W. Goodman, “Statistical properties of laser speckle patterns,” *Stanford Electronics Lab. Tech. Rep.*, No. 2303-1, (1963).
- [32] B. M. Oliver, “Sparkling Spots and Random Diffraction,” *Proc. of IEEE* **51**, 220-221 (1963).

- [33] E. Wolf and G. Agarwal, "Coherence theory of laser resonator modes," *J. Opt. Soc. Am. A* **1**, 541-546 (1984).
- [34] L. Bruno, A. Poggialini, "Back to the future: From speckle to holography," *Optics and Lasers in Engineering* **45**, 538-549 (2007).
- [35] F. Zernike, "The concept of degree of coherence and its application to optical problems," *Physica* **5**, 785-795 (1938).
- [36] C. V. Raman, *Lectures on Physical Optics*, Part 1, Indian Academy of Sciences, Bangalore, 160 (1959).
- [37] L. I. Goldfischer, "Autocorrelation function and power spectral density of laser-produced speckle patterns," *J. Opt. Soc. Am.* **55**, 247-252 (1965).
- [38] P. Hariharan, "Evaluation of the modulation transfer function of photographic materials using a laser speckle pattern," *Appl. Opt.* **9**, 1482-1494 (1970).
- [39] E. Archibald, J. M. Burch, A. E. Ennos, "Recording of in-plane displacement by double-exposure speckle photography," *Optica Acta* **17**, 883-898, (1970).
- [40] G. Groh, "Engineering use of laser-produced speckle pattern," in: E. R. Robertson and J. M. Harvey, editors, *Engineering uses of holography* (Cambridge University Press, 1970), 483-494 (1970).
- [41] N. Fernelius C. Tome, "Vibration-Analysis Studies Using Changes of Laser Speckle," *J. Opt. Soc. Am.* **61**, 566-572 (1971).
- [42] R. B. Crane, "Use of a laser-produced speckle pattern to determine surface roughness," *J. Opt. Soc. Am.* **60**, 1658-1663 (1970).
- [43] C. Cheng, C. Liu, N. Zhang, T. Jia, R. Li, Z. Xu, "Absolute measurement of roughness and lateral-correlation length of random surfaces by use of the simplified model of image-speckle contrast," *Appl. Opt.* **41**, 4148-4156 (2002).
- [44] E. Archbold, J. M. Burch, A. E. Ennos, and P. A. Taylor, "Visual Observation of Surface Vibration Nodal Patterns," *Nature* **222**, 263-265 (1969).
- [45] J. A. Leendertz, "Interferometric displacement measurement," *J. Phys. E: Scientific Instruments* **3**, 214-218 (1970).
- [46] R. Jones and C. Wykes, *Holographic and Speckle Interferometry* (Cambridge University Press, 1989).
- [47] A. F. Fercher, J. D. Briers, "Flow Visualization by Means of Single-Exposure Speckle Photography," *Opt. Comm.* **37**, 326-330 (1981).
- [48] L. W. Winchester, Jr., N. Y. Chou, "Blood Velocity Measurements Using Laser Speckle Imaging," in Proceedings of the 26th Annual International Conference of the IEEE EMBS, 1252-1255 (2004).

- [49] J. D. Briers, S. Webster, "Laser Speckle contrast analysis (LASCA): a nonscanning, full-field technique for monitoring capillary blood flow," *J. Biomed. Opt.* **1**, 174-179 (1996).
- [50] A. K. Dunn, H. Bolay, M. A. Moskowitz, and D. A. Boas, "Dynamic Imaging of Cerebral Blood Flow Using Laser Speckle," *J. of Cerebral Blood Flow and Metabolism* **21**, 195-201 (2001).
- [51] E. Ingelstam and S. Ragnarsson, "Eye refraction examined by aid of speckle pattern produced by coherent light," *Vision Res.* **12**, 411-420 (1972).
- [52] R. D. Bahaguna and D. Malacara, "Stationarity of speckle in laser refraction," *J. Opt. Soc. Am.* **73**, 1213-1215 (1983).
- [53] W. N. Charman, "Speckle movement in laser refraction. I. Theory," *Am. J. Optom. Physiol. Opt.* **56**, 219-227 (1979).
- [54] W. N. Charman and H. Whitefoot, "Speckle motion in laser refraction. II. Experimental," *Am. J. Optom. Physiol. Opt.* **56**, 295-304 (1979).
- [55] D. L. Abernathy, J. Als-Nielsen, S. B. Dierker, R. M. Fleming, G. Grüberla, R. Pindakc, K. Ploogd and I. K. Robinsone, "1D X-ray speckle patterns: A novel probe of interfacial disorder in semiconductor superlattices," *Solid-State Electronics* **40**, 531-535 (1996).
- [56] J. Texereau, "Limitations à la Qualité des Images d'un Grand Télescope," *Appl. Opt.* **2**, 23-30 (1963).
- [57] A. Labeyrie, Attainment of diffraction limited resolution in large telescopes by Fourier analyzing speckle patterns in star images," *Astron. Astrophys.* **6**, 85-87 (1970).
- [58] F. T. S. Yu and E. Y. Wang, "Speckle Reduction in Holography by Means of Random Spatial Sampling," *Appl. Opt.* **12**, 1656-1659 (1973).
- [59] M. Kato and Y. Okino, "Speckle Reduction by Double Recorded Holograms, " *Appl. Opt.* **12**, 1199-1201 (1973).
- [60] M. Kato, Y. Nakayama, and T. Suzuki, "Speckle Reduction in Holography with a Spatially Incoherent Source," *Appl. Opt.* **14**, 1093-1099 (1975).
- [61] B. E. Bouma and G. J. Tearney, editors, *Handbook of Optical Coherence Tomography* (Marcel Dekker, Inc., New York, 2002).
- [62] H. Ambar, Y. Aoki, N. Takai, T. Asakura, "Mechanism of speckle reduction in laser-microscope images using a rotating optical fiber," *Appl. Phys. B* **38**, 71-78 (1985).
- [63] C. Saloma, S. Kawata, and S. Minami, "Laser-diode microscope that generates weakly speckled images," *Opt. Lett.* **15**, 203-205 (1990).

- [64] M. Denman, N. Halliwell, S. Rothberg, "Speckle noise reduction in Laser Vibrometry: experimental and numerical optimisation," Proc. SPIE **2868**, 12-21 (1996).
- [65] R. E. Epworth, "The phenomenon of modal noise in analog and digital optical fiber systems," Proc. 4th Conf. on Opt. Comm., 492-501 Genoa, Italy (1978).
- [66] W. Ha, S. Lee, Y. Jung, J. Kim, K. Oh, "Speckle reduction in multimode fiber with a piezoelectric transducer in radial vibration for fiber laser marking and display applications," Proc. SPIE **6873**, 68731V (2008).
- [67] V. Kotov, G. Shkerdin, D. Shkerdin, J. Stiens, R. Vounckx, "The speckle reduction of optical fields in multi-mode fibers by means of acousto-optic Bragg diffraction," Proc. IEEE-LEOS Benelux, 249-252 (2001).
- [68] A. Jain, "Radar speckle reduction in synthetic aperture radar processors by a moving diffuser," Opt. Comm. **20**, 239-242 (1977).
- [69] R. Baribeau and Marc Rioux, "Influence of speckle on laser range finders," Appl. Opt. **30**, 2873-2878 (1991).
- [70] R. Dorsch, J. Herrmann, G. Häusler, "Laser Triangulation: Fundamental uncertainty of distance measurement," Applied Optics **33**, 1306-1314 (1994).
- [71] E. Marom, S. Kresic-Juric and L. Bergstein, "Analysis of speckle noise in bar-code scanning systems," J. Opt. Soc. Am. A **18**, 888-901 (2001).
- [72] C. Rydberg, J. Bengtsson, T. Sandström, "Dynamic laser speckle as a detrimental phenomenon in optical projection lithography," J. Microlith., Microfab., Microsyst. **5**, 033004 (2006).
- [73] O. Noordman, A. Tychkov, J. Baselmans, J. Tsacoyeanes, G. Politi, M. Patra, V. Blahnik, M. Maul, "Speckle in optical lithography and the influence on line width roughness," Proc. SPIE **7274**, 72741R (2009).
- [74] R. Martinsen, K. Kennedy, A. Radl, "Speckle in laser imagery: Efficient methods of quantification and minimization," Proc. IEEE-LEOS, San Francisco, USA, 354-355 (1999).
- [75] E. G. Rawson, A. B. Nafarrate, R. E. Norton, J. W. Goodman, "Speckle-free rear-projection screen using two close screens in slow relative motion," J. Opt. Soc. Am. **66**, 1290-1294 (1976).
- [76] M. S. Brennesholtz, E. H. Stupp, *Projection Displays*, 2nd ed., (John Wiley, 2008).
- [77] D. Armitage, I. Underwood, S.-T. Wu, *Introduction to Microdisplays* (John Wiley, 2006).
- [78] Texas Instruments Incorporated, <http://www.ti.com> (2009).
- [79] Demonstration of Texas Instruments' DLP technology, http://www.dlp.com/includes/demo_flash.aspx (2009).

- [80] Silicon Light Machines, 820 Kifer Road, Sunnyvale, CA 94086, USA, <http://www.siliconlight.com> (2009).
- [81] Eastman Kodak Corporation, Rochester, NY, USA, <http://www.kodak.com> (2009).
- [82] Microvision, Inc., 6222 185th Ave NE Redmond WA, 98052, USA, <http://www.microvision.com> (2009).
- [83] Fraunhofer Institute for Photonic Microsystems (IPMS), Maria-Reiche-Str. 2, 01109 Dresden, Germany, <http://www.ipms.fraunhofer.de> (2009).
- [84] Sony Corporation, 1-7-1 Konan, Minato-ku, Tokyo 108-0075, Japan, <http://www.sony.net> (2009).
- [85] Light Blue Optics Ltd., Platinum Building, St John's Innovation Park, Cowley Road, Cambridge, UK, <http://www.lightblueoptics.com> (2009).
- [86] LDT Laser Display Technology GmbH, Göschwitzer Straße 25, 07745 Jena, Germany, <http://www.ldt-jena.de> (2009).
- [87] Evans & Sutherland Computer Corporation, 770 Komas Drive, Salt Lake City, UT 84108, USA, <http://www.es.com> (2009).
- [88] Corporation for Laser Optics Research, 47 Durham Street, Portsmouth, NH 03801, USA, <http://www.colorvision-lasers.com> (2009).
- [89] Webpage of Mitsubishi's LaserVue TV, <http://www.laservuetv.com> (2009).
- [90] M. S. Brennesholtz, "Invited Paper: New-Technology Light Sources for Projection Displays," Society for Information Display Digest of Technical Papers **39**, 858-861 (2008).
- [91] C. J. Joshi, "Development of Long Life, Full Spectrum Light Source for Projection Display," Society for Information Display Digest of Technical Papers, paper 14.4, (2007).
- [92] J. F. Waymouth, *Electric Discharge Lamps* (MIT Press, 1971).
- [93] O. Kückmann, "High power LED arrays: Special requirements on packaging technology", Proc. SPIE **6134**, 613404 (2006).
- [94] S. Bierhuizen, M. Krames, G. Harbers and G. Weijers, "Performance and trends of high power Light Emitting Diodes," Proc. SPIE **6669**, 66690B (2007).
- [95] Webpage <http://necsel.com>, (2009).
- [96] M. Brennesholtz, "Laser Projection Systems 2007," Insight Media, 3 Morgan Avenue, Norwalk, CT 06851, USA (2007).
- [97] INFITEC GmbH, Science Park II, Lise-Meitner-Str. 9, 89081 Ulm, Germany, <http://www.infitec.net> (2009).

- [98] Optoma USA, 715 Sycamore Drive, Milpitas, CA 95035, USA, <http://www.optomausa.com> (2009).
- [99] A. Valberg, *Light Vision Color* (John Wiley & Sons Ltd, 2005).
- [100] T. N. Cornsweet, *Visual Perception* (Academic Press, 1974).
- [101] E. F. Schubert, *Light Emitting Diodes* (Cambridge University Press, 2006).
- [102] M. Duelli, T. D. McGettigan, C. A. Pentico, “Polarization recovery system based on light pipes,” Proc. SPIE **4657**, 9-16 (2002).
- [103] K. K. Li, “Polarization recovery system for projection displays,” US Patent 6587269 (2003).
- [104] K.-C. Shen, C.-Y. Chen, H.-L. Chen, C.-F. Huang, Y.-W. Kiang, C. C. Yang, and Y.-J. Yang, “Enhanced and partially polarized output of a light-emitting diode with its InGaN/GaN quantum well coupled with surface plasmons on a metal grating,” Appl. Phys. Lett. **93**, 231111 (2008).
- [105] P. Dyreklev, M. Berggren, O. Inganäs, M. R. Andersson, T. Hjertberg and O. Wennerström, “Polarized Electroluminescence from an Oriented Substituted Poly-thiophene in a Light Emitting Diode,” Adv. Mater. **7**, 43-45 (1995).
- [106] R. Fiederling, M. Keim, G. Reuscher, W. Ossau, G. Schmidt, A. Waag and L. W. Molenkamp, “Injection and detection of a spin-polarized current in a light-emitting diode,” Nature **402**, 787-790 (1999).
- [107] R. Joachim and W. Alexander, “Requirements on LEDs for Advanced Optical Systems,” Proc. SPIE **6486**, 64860Z (2007).
- [108] H. Sugiura, T. Sasagawa, A. Michimori, E. Toide, T. Yanagisawa, S. Yamamoto, Y. Hirano, M. Usui, S. Teramatsu, and J. Someya1, “65-inch, Super Slim, Laser TV with Newly Developed Laser Light Sources,” Society for Information Display Digest of Technical Papers **39**, 854-857 (2008).
- [109] G. Harbers, M. Keuper and S. Paolini, “Performance of High Power LED Illuminators in Color Sequential Projection Displays”, Proc. of the 10th International Display Workshops, Paper LAD3-4, (2003).
- [110] G. Niven and A. Mooradian, “Trends in Laser Light Sources for Projection Display,” available at www.novalux.com, (2008).
- [111] International Electrotechnical Commission 60825-1:2007, “Safety of laser products - Part 1: Equipment classification and requirements”, 2nd ed., (2007).
- [112] Mitsubishi Electric, owner’s manual to LaserVue TV model L65-A90, http://www.laservuetv.com/pdf/LaserVue_OG.pdf (2009).
- [113] P. G. J. Barten, “Physical model for the contrast sensitivity of the human eye”, Proc. SPIE **1666**, Human Vision, Visual Processing, and Digital Display III, 57-72 (1992).

- [114] C. R. Cavonius, O. Estivez, "Contrast sensitivity of individual colour mechanisms of human vision", *J Physiol.* **248**, 649-662 (1975).
- [115] D. H. Kelly, "Spatio-temporal frequency characteristics of color-vision mechanisms", *J. Opt. Soc. Am.* **64**, 983-990 (1974).
- [116] J. G. Robson, "Spatial and temporal contrast sensitivity functions of the human eye", *J. Opt. Soc. Am.* **56**, 1141 (1966).
- [117] F. Schieber, "The Relationship Between Contrast Sensitivity and the Visual Problems of Older Drivers", *SAE Transactions* **101**, 797-803 (1992).
- [118] D. Methling, *Bestimmen von Sehhilfen* (Ferdinand Enke Verlag, 1996).
- [119] B. Timney, P. Pearson, "Spatiotemporal contrast sensitivity after acute alcohol ingestion", Proc. of the 13th Int. Conf. on Alcohol, Drugs and Traffic Safety, Adelaide, South Australia, (1995).
- [120] L. Wang, T. Tschudi, T. Halldórsson, P. R. Pétursson, "Speckle reduction in laser projection systems by diffractive optical elements," *Appl. Opt.* **37**, 1770-1775 (1998).
- [121] W. Singer, M. Totzeck, and H. Gross, *Handbook of Optical Systems* (Wiley-VCH, 2005).
- [122] J. Trotter, *Das Auge* (DOZ-Verlag, 1985).
- [123] S. C. Shin, S. S. Yooa, S. Y. Leea, C.-Y. Parka, S.-Y. Parka, J. W. Kwon and S.-G. Leea, "Removal of hot spot speckle on laser projection screen using both the running screen and the rotating diffuser," *Displays* **27**, 91-96 (2006).
- [124] C. E. Hauber, R. E. Kittredge, U. S. Patent No. 3,473,862 (Oct. 21, 1969).
- [125] I. Leifer, C. J. D. Spencer, and W. T. Welford, "Grainless Screens for Projection Microscopy," *J. Opt. Soc. Am.* **51**, 1422-1423 (1961).
- [126] F.S. MacAdam, Taylor, Taylor & Hobson Ltd, British Patent No. 592,815, (1947).
- [127] A. A. Michelson, "On the Application of Interference Methods to Astronomical Measurements," *PNAS* **6**, 474-475 (1920).
- [128] E. Wolf, "Optics in terms of observable quantities," *Il Nuovo Cimento* **12**, 884-888 (1954).
- [129] S. A. Collins, "Lens-System Diffraction Integral Written in Terms of Matrix Optics," *J. Opt. Soc. Am.* **60**, 1168-1177 (1970).
- [130] H. T. Yura, "Optical beam wave propagation through complex optical systems," *J. Opt. Soc. Am. A* **4**, 1931-1948 (1987).
- [131] H. Kogelnik and T. Li, "Laser Beams and Resonators," *Appl. Opt.* **5**, 1550-1567 (1966).

- [132] K. Yee, "Numerical solution of initial boundary value problems involving Maxwell's equations in isotropic media," IEEE Trans. Antennas Propag. **14**, 302-307 (1966).
- [133] K. Okamoto, *Fundamentals of Optical Waveguides* (Academic Press, 2005).
- [134] A. S. Glassner, *An Introduction to Ray Tracing* (Morgan Kaufmann, 1989).
- [135] W. H. Steier, "The Ray Packet Equivalent of a Gaussian Light Beam," Appl. Opt. **5**, 1229-1233 (1966).
- [136] J. D. Zook and T. C. Lee, "Geometrical interpretation of Gaussian beam optics," Appl. Opt. **11**, 2140-2145 (1972).
- [137] R. Herloski, S. Marshall, and R. Antos, "Gaussian beam ray-equivalent modeling and optical design," Appl. Opt. **22**, 1168-1174 (1983).
- [138] J. Arnaud, "Representation of Gaussian beams by complex rays," Appl. Opt. **24**, 538-543 (1985).
- [139] N. G. Douglas, A. R. Jones, and F. J. van Hoesel, "Ray-based simulation of an optical interferometer," J. Opt. Soc. Am. A **12**, 124-131 (1995).
- [140] L. Mandel and E. Wolf, *Optical Coherence and Quantum Optics* (Cambridge University Press, 1995).
- [141] P. H. van Cittert, "Die Wahrscheinliche Schwingungsverteilung in Einer von Einer Lichtquelle Direkt Oder Mittels Einer Linse Beleuchteten Ebene," Physica **1**, 201-210 (1934).
- [142] W. H. McCrea and F. J. W. Whipple, "Random Paths in Two and Three Dimensions," Proc. Roy. Soc. Edinburgh **60**, 281-298 (1940).
- [143] F. Riechert, G. Verschaffelt, M. Peeters, G. Bastian, U. Lemmer, and I. Fischer, "Speckle characteristics of a broad-area VCSEL in the incoherent emission regime," Opt. Commun. **281**, Issue 17, 4424-4431 (2008).
- [144] M. Burkhardt, R. Brunner, "Functional integrated optical elements for beam shaping with coherence scrambling property, realized by interference lithography," Appl. Opt. **46**, 7061-7067 (2007).
- [145] J. B. Keller, "Geometrical Theory of Diffraction," J. Opt. Soc. Am. **52**, 116-130 (1962).
- [146] D. J. Whitehouse, *Handbook of Surface Metrology* (Inst. of Physics Pub., 1994).
- [147] M. A. Webster, K. J. Webb, A. M. Weiner, J. Xu, and H. Cao, "Temporal response of a random medium from speckle intensity frequency correlations," J. Opt. Soc. Am. A **20**, 2057-2070 (2003).
- [148] M. A. Webster, K. J. Webb, and A. M. Weiner, "Temporal Response of a Random Medium from Third-Order Laser Speckle Frequency Correlations," Phys. Rev. Lett. **88**, 033901 (2002).

- [149] G. C. Mooradian, M. Geller, "Temporal and angular spreading of blue-green pulses in clouds," *Appl. Opt.* **21**, 1572-1577 (1982).
- [150] M. S. Patterson, B. Chance, and B. C. Wilson, "Time resolved reflectance and transmittance for the non-invasive measurement of tissue optical properties," *Appl. Opt.* **28**, 2331-2336 (1989).
- [151] G. Zaccanti, P. Brusaglioli, A. Ismaelli, L. Carraresi, M. Gurioli, and Q. Wei, "Transmission of a pulsed thin light beam through thick turbid media: experimental results," *Appl. Opt.* **31**, 2141-2147 (1992).
- [152] R. Trebino, *Frequency-Resolved Optical Gating: The Measurement of Ultrashort Laser Pulses* (Springer, 2002).
- [153] C. A. Thompson, K. J. Webb, A. M. Weiner, "Imaging in scattering media by use of laser speckle," *J. Opt. Soc. Am. A* **14**, 2269-2277 (1997).
- [154] J. Carlsson, P. Hellentin, L. Malmqvist, A. Persson, W. Persson and C-G. Wahlström, "Time-resolved studies of light propagation in paper," *Appl. Opt.* **34**, 1528-1535 (1995).
- [155] Y. Hirano, Information Technology R&D Center, Mitsubishi Electric Corporation, 5-1-1 Ofuna, Kamakura, Kanagawa 247-8501, Japan (personal communication, 2008).
- [156] R. Brown, "A brief account of microscopical observations made in the months of June, July and August, 1827, on the particles contained in the pollen of plants; and on the general existence of active molecules in organic and inorganic bodies," *Phil. Mag.* **4**, 161-173 (1828).
- [157] V. Yurlov, A. Lapchuk, S. Yun, J. G. Song, H. Yang, "Speckle suppression in scanning laser display," *Appl. Opt.* **47**, Issue 2, 179-187 (2008).
- [158] H. Kolb, E. Fernandez, R. Nelson, B. W. Jones, "Webvision - The Organization of the Retina and Visual System," <http://webvision.med.utah.edu> (2009).
- [159] J. R. Frisvad, N. J. Christensen, H. W. Jensen, "Computing the scattering properties of participating media using Lorenz-Mie theory," *ACM Trans. Graph.* **26**, article 60 (2007).
- [160] V. V. Tuchin, *Tissue Optics: Light Scattering Methods and Instruments for Medical Diagnosis*, 2nd ed. (Society of Photo-Optical Instrumentation Engineers, 2007).
- [161] J. R. Frisvad, *Light, Matter, and Geometry: The Cornerstones of Appearance Modelling* (VDM Verlag Dr. Müller, 2008).
- [162] J. R. Frisvad, Department of Informatics and Mathematical Modeling, Technical University of Denmark, Richard Petersens Plads, 2800 Lyngby, Denmark (personal communication, 2009).

- [163] L. Wang, S. L. Jacques, L. Zheng, "MCML - Monte Carlo modelling of light transport in multi-layered tissues," *Computer Methods and Programs in Biomedicine* **47**, 131-146 (1995).
- [164] L. Wang, S. L. Jacques, L. Zheng, "CONV - convolution for responses to a finite diameter photon beam incident on multi-layered tissues," *Computer Methods and Programs in Biomedicine* **54**, 141-150 (1997).
- [165] R. Bandyopadhyay, A. S. Gittings, S. S. Suh, P. K. Dixon, and D. J. Durian, "Speckle-visibility spectroscopy: A tool to study time-varying dynamics," *Rev. Sci. Instrum.* **76**, 093110 (2005).
- [166] P. J. Berne and R. Pecora, *Dynamic Light Scattering* (Wiley, New York, 1976).
- [167] D. J. Pine, D. A. Weitz, P. M. Chaikin, and E. Herbolzheimer, "Diffusing-Wave Spectroscopy," *Phys. Rev. Lett.* **60**, 1134-1137 (1988).
- [168] K. K. Bizheva, A. M. Siegel, and D. A. Boas, "Path-length-resolved dynamic light scattering in highly scattering random media: The transition to diffusing wave spectroscopy," *Phys. Rev. E* **58**, 7664-7667 (1998).
- [169] R. Carminati, R. Elaloufi, and J.-J. Greffet, "Beyond the Diffusing-Wave Spectroscopy Model for the Temporal Fluctuations of Scattered Light," *Phys. Rev. Lett.* **92**, 213903 (2004).
- [170] S. Ulyanov, "Diffusing wave spectroscopy with a small number of scattering events: An implication to microflow diagnostics," *Phys. Rev. E* **72**, 052902 (2005).
- [171] A. Einstein, "Über die von der molekularkinetischen Theorie der Wärme geforderte Bewegung von in ruhenden Flüssigkeiten suspendierten Teilchen", *Ann. Phys.* **322**, 549-560 (1905).
- [172] M. Heckmeier and G. Maret, "Visualization of flow in multiple-scattering liquids," *Europhys. Lett.* **34**, 257-262 (1996).
- [173] P.-A. Lemieux, M. U. Vera, and D. J. Durian, "Diffusing-light spectroscopies beyond the diffusion limit: The role of ballistic transport and anisotropic scattering," *Phys. Rev. E* **57**, 4498-4515 (1998).
- [174] D. A. Zimnyakov and Y. P. Sinichkin, "A study of polarization decay as applied to improved imaging in scattering media," *J. Opt. A: Pure Appl. Opt.* **2**, 200-208 (2000).
- [175] M. Xu and R. R. Alfano, "Random Walk of Polarized Light in Turbid Media," *Phys. Rev. Lett.* **95**, 213901 (2005).
- [176] L. F. Rojas-Ochoa, D. Lacoste, R. Lenke, P. Schurtenberger, F. Scheffold, "Depolarization of backscattered linearly polarized light," *J. Opt. Soc. Am. A* **21**, 1799-1804 (2004).

- [177] F. Riechert, F. Glöckler, and U. Lemmer, "Method to determine the speckle characteristics of front projection screens," *Appl. Opt.* **48**, Issue 7, 1316-1321 (2009).
- [178] F. Riechert, G. Craggs, Y. Meuret, B. Van Giel, H. Thienpont, U. Lemmer, and G. Verschaffelt, "Low speckle laser projection with a broad-area vertical-cavity surface-emitting laser in the nonmodal emission regime," *Appl. Opt.* **48**, 792-798 (2009).
- [179] M. Peeters, G. Verschaffelt, H. Thienpont, S. K. Mandre, I. Fischer, and M. Grabherr, "Spatial decoherence of pulsed broad-area vertical-cavity surface-emitting lasers," *Opt. Express* **13**, 9337-9345 (2005).
- [180] M. Peeters, "Polarisation Switching in Vertical-Cavity Surface-Emitting Lasers - A Modeling Perspective," Ph-D.-thesis, Vrije Universiteit Brussel, Faculteit Toegepaste Wetenschappen, (2003).
- [181] G. Verschaffelt, G. Craggs, M. Peeters, S. K. Mandre, H. Thienpont, I. Fischer, "Spatially resolved characterization of the coherence area in the incoherent emission regime of a broad-area Vertical-Cavity Surface-Emitting Laser," *IEEE J. Quantum Electron.* **45**, 249-255 (2008).
- [182] F. Gori, "Far-zone approximation for partially coherent sources," *Opt. Lett.* **30**, 2840-2842 (2005).
- [183] S. K. Mandre, W. Elsässer, I. Fischer, M. Peeters, G. Verschaffelt, "Determining the temporally and radially resolved temperature distribution inside a pulsed broad-area vertical-cavity surface-emitting laser cavity," *Appl. Phys. Lett.* **89**, 151106 (2006).
- [184] H. Li, K. Iga, *Vertical-Cavity Surface-Emitting Laser Devices* (Springer, 2003).
- [185] M. Bertolotti, B. Daino, F. Gori, D. Sette, "Coherence Properties of a Laser Beam," *Nuovo Cimento* **38**, 1505-1514 (1965).
- [186] B. Van Giel, Y. Meuret, L. Bogaert, H. Murat, H. De Smet, and H. Thienpont, "Compact and efficient illumination in LED projection displays," Society for Information Display Symposium Digest **38**, 947-950 (2007).
- [187] P. Schreiber, S. Kudaev, P. Dannberg, and U. D. Zeitner, "Homogeneous LED-illumination using microlens arrays," *Proc. SPIE* **5942**, 59420K (2005).
- [188] G. Craggs, part of the Ph.D. project "Spatial coherence properties after frequency doubling using non-linear optical materials", Department of Applied Physics and Photonics, Vrije Universiteit Brussel, Pleinlaan 2, 1050 Brussels, Belgium (2009).
- [189] A. Mooradian, S. Antikichev, B. Cantos, G. Carey, M. Jansen, S. Hallstein, W. Hitchens, D. Lee, J.-M. Pelaprat, R. Nabiev, G. Niven, A. Shchegrov, A. Umbrasas, and J. Watson, "High Power Extended Vertical Cavity Surface Emitting Diode Lasers and Arrays and their Applications," Micro-Optics Conference, Tokyo, Japan, (2005).

- [190] M. Miller, M. Grabherr, R. Jäger, and K. J. Ebeling, “High-Power VCSEL Arrays for Emission in the Watt Regime at Room Temperature,” *IEEE Photonics Technology Letters* **13**, 173-175 (2001).

List of Figures

2.1	Illustration of speckle emergence: (a) each point of the surface can be seen as a secondary source, emitting a spherical wave, (b) the field in the observation point can be modeled as quasi-random phasor sum.	4
2.2	Image of a typical laser speckle pattern.	4
2.3	Schematic of a setup with which an objective speckle pattern is measured. The limiting aperture is the illumination beam diameter.	9
2.4	Schematic of a setup with which a subjective speckle pattern is measured. The limiting aperture is given by the imaging system.	9
2.5	(a) raw CCD image of a section of a rat brain (b) the same section. The color in (b) is determined by the speckle contrast in regions of 5x5 pixels of the raw image, taken from [50].	11
3.1	Image of a typical DMD micromirror chip.	16
3.2	2D scanning mirror used by Microvision, taken from [82].	17
3.3	Application scenario for a mobile-phone-embedded pico-projector, taken from [82].	18
3.4	Prototype of an accessory pico-projector from Microvision, taken from [82].	18
3.5	CIExy chromaticity diagram. The colored area represents all colors a human observer can see with his eye.	21
3.6	Gamut of a typical CRT system	22
3.7	Color coordinates of different LEDs, taken from [101].	22
3.8	Color gamut achievable with a laser projection system.	23
3.9	Comparison of the sizes of recent projection lenses used by Mitsubishi in systems with (a) standard UHP lamps and (b) lasers, taken from [108]. .	25
3.10	Schematic of a color sequential lamp projection system using a color filter wheel, taken from [110].	25
3.11	Schematic of NECSEL based color sequential projection system, taken from [110].	26
3.12	Schematic of a three imager projection system using a lamp, taken from [110].	26
3.13	Schematic of a three imager system using NECSEL illumination of the imagers, taken from [110].	26
3.14	Simulated speckle images with (a) C=100% and (b) C=4%.	28

4.1	Classification of methods for speckle reduction according to whether the statistically independent speckle patterns are created instantaneously or time-sequentially and according to how these speckle patterns are mutually decorrelated.	32
4.2	Wavevectors for the illumination of a rough surface and observation in reflection.	33
4.3	Resulting speckle contrast for broadband illumination of a surface with roughness σ_t in reflection where the source has an 1/e-bandwidth $\delta\lambda$ and a mean wavelength $\bar{\lambda}$	36
4.4	Schematic of a single microlens array beam homogenizer, taken from [121].	38
4.5	The illuminating light spot is scanned in circular motion over the microlens beam homogenizer. This results in a continuous change of the screen illumination angle.	39
4.6	An observer resolves the individual coherence areas on the screen and perceives a high speckle contrast in (a). In (b) a reduced speckle contrast will be perceived because of spatial integration.	41
4.7	Schematic of (a) coherence areas incident onto a volume scattering target, (b) backscattered or transmitted coherence areas with regions of overlap because of diffuse scattering, (c) reduced speckle contrast in the regions of overlap.	41
4.8	Schematic of (a) linearly scanned spot, (b) nonlinearly scanned spot with increased speckle contrast reduction.	42
5.1	Schematic of the investigated free space propagation setup.	53
5.2	(a) 3D plot of the simulated degree of coherence regarding the centre of the detector plane for the free space propagation setup. (b) Cut along the x-axis of the plot in (a). The solid line indicates the theoretical description using the van Cittert-Zernike theorem.	54
5.3	Schematic of the investigated single lens system setup.	55
5.4	(a) 3D plot of the simulated degree of coherence regarding the centre of the detector plane for the single lens setup. (b) Cut along the x-axis of the plot in (a). The solid line indicates the theoretical description using ABCD-matrix formalism.	56
5.5	Schematic of the investigated two-tandemarray microlens beam homogenizer setup.	57
5.6	Schematic of the two-tandemarray microlens beam homogenizer.	57
5.7	3D plot of the degree of coherence regarding the centre of the fully coherent illumination spot on the first tandemarray of the beam homogenizer.	58
5.8	3D plot of the simulated degree of coherence regarding the centre of the detector plane for the two-tandemarray microlens beam homogenizer for fully coherent, quasi-parallel illumination.	59
5.9	3D plot of the intensity distribution for fully coherent illumination of the beam homogenizer. A grid like interference pattern is clearly visible.	59
5.10	Degree of coherence (red line) in the homogenized plane of a single monoarray microlens beam homogenizer as depicted in Fig. 4.4 under fully coherent illumination, taken from [121].	60

5.11	3D plot of the degree of coherence regarding the centre of the spatially partially coherent illumination spot on the first tandemarray of the beam homogenizer.	61
5.12	3D plot of the simulated degree of coherence regarding the centre of the detector plane for the two-tandemarray microlens beam homogenizer for spatially partially coherent, quasi-parallel illumination.	62
5.13	3D plot of the intensity distribution for partially coherent illumination of the beam homogenizer. The interference pattern is no longer visible.	62
6.1	Schematic of a typical volume scattering path of a backscattered photon which was incident under normal direction. In case (a) it propagates mainly in air, in case (b) it propagates in a screen material with refractive index $n > 1$	67
6.2	Schematic setup for measurement of the path length distribution via intensity crosscorrelation.	69
6.3	Schematic of the streak camera setup.	70
6.4	Plot of a typical measurement of unscattered Ti:Sa pulses and its approximation by a Gaussian fit.	71
6.5	Plot of a typical measurement of Ti:Sa pulses backscattered from the OP.DI.MA screen and its approximation by a Gaussian fit.	73
6.6	Plot of the modeled speckle contrast which results for illumination of the investigated screens with spatially fully coherent 808 nm light of different bandwidths.	75
7.1	Setup to measure the speckle contrast (lens inserted) and the $1/e^2$ -radius of the laser beam after passage through the screen (lens removed). The camera images the screen which is filled with the colloidal dispersions. The thickness of the screen can be varied from approximately 0.1 to 5 mm.	78
7.2	Measured speckle contrasts and $1/e^2$ -radii of the laser beam after passage through the screen filled with colloidal dispersion 1 (diluted skimmed milk). The speckle contrast measurements were done for 20 and 40 ms camera integration time. The lines are to guide the eye.	81
7.3	Measured speckle contrasts and simulated and measured $1/e^2$ -radii of the laser beam after passage through the screen filled with colloidal dispersion 2 (diluted whole milk). The camera integration time was 40 ms. The lines are to guide the eye.	82
7.4	Measured speckle contrasts and $1/e^2$ -radii of the laser beam after passage through the screen filled with colloidal dispersion 3 (whole milk). The lines are to guide the eye.	83
8.1	Schematic of an edge emitter (a) and a VCSEL (b), taken from [180]. . .	90
8.2	(a) Projection with a lens (D) of the VCSEL's (V) nearfield onto the screen (T), CCD-camera (C) imaging the paper screen. (b) Measured speckle contrasts.	94
8.3	(a) Projection with a lens (D) of the VCSEL's (V) nearfield onto the screen (T), CCD-camera (C) placed in the farfield of the paper screen. (b) Measured speckle contrasts.	95

8.4	(a) Projection of VCSEL's (V) farfield onto the screen (T), CCD-camera (C) imaging the paper screen. (b) Measured speckle contrasts.	96
8.5	(a) Projection of VCSEL's (V) farfield onto the screen (T), CCD-camera (C) placed in the farfield of the paper screen. (b) Measured speckle contrasts.	97
8.6	Schematics of (a) the VCSEL's nearfield incident onto the screen for the nonmodal emission regime. The nearfield consists of about 318 coherence islands (red spots). (b) the VCSEL's nearfield backscattered from the volume scattering screen. Light from the beamlets is diffusely scattered and the backscattered beamlets overlap.	102
8.7	Schematic of the illumination and measurement setup.	107
8.8	Measured and modeled speckle contrast values for illumination of the beam homogenizer with a 5.2 mm diameter nearfield spot.	109
8.9	Measured and modeled speckle contrast values for illumination of the beam homogenizer with a 9 mm diameter nearfield spot.	109
8.10	Measured and modeled speckle contrast values for illumination of the beam homogenizer with an 18 mm diameter nearfield spot.	110
8.11	Schematic of a section of the illuminated beam homogenizer. The microlenses of the beam homogenizer are indicated by the rectangular grid: (a) for a 5.2 mm nearfield spot with coherence islands of 145 μm radius, (b) for a 9 mm nearfield spot the coherence islands have a radius of approximately 250 μm and their size is comparable to the size of a homogenizer lens, (c) for an 18 mm nearfield spot with coherence islands of 500 μm radius.	112
8.12	Radially resolved measurement of the intensity distribution in the VCSEL's aperture in the nonmodal emission regime.	114
8.13	Schematic of the illumination and measurement setup.	117
8.14	Speckle pattern for a distance of 9 mm (upper row) and 59 mm (lower row) between VCSEL and homogenizer: (a) and (c) in cw operation at 16 mA, (b) and (d) in pulsed operation at 240 mA.	118
8.15	Evolution of the speckle contrast as a function of the distance VCSEL - homogenizer for the cw currents of 16 mA (black diamonds) and 70 mA (gray squares), and pulses of 157 mA amplitude (black circles) and 240 mA amplitude (gray triangles). Also shown is the modeled speckle contrast for 157 mA pulses (black line) and 240 mA pulses (gray line).	119

List of Tables

6.1	Determined coefficients of polarization P after scattering in the screens and resulting speckle contrast reduction factors as calculated according to Eq. (6.1)	72
6.2	Determined standard deviations σ_τ of the scattering path time distributions $p(\tau)$ of the investigated screens	72
6.3	Measured and expected speckle contrast values (as calculated according to Eq. (6.5) for illumination of the screens with 20 nm bandwidth Ti:Sa pulses with 808 nm mean wavelength.	74
7.1	Optical properties of the investigated colloidal dispersions.	80
8.1	Driving parameters of the VCSEL in cw and pulsed operation.	93
8.2	Shift of the emission wavelength of the VCSEL induced by Joule heating for different pulses. Furthermore, the estimated speckle contrast reduction factor as calculated according to Eq. (8.1) is given taking into account quasi-broadband illumination of the paper screen.	100
8.3	Comparison between the measured and estimated speckle contrast for the setup in Fig. 8.2(a).	102
8.4	Comparison between the measured and estimated speckle contrast for the setup in Fig. 8.3(a).	103
8.5	Comparison between the measured and estimated speckle contrast for the setup in Fig. 8.4(a).	104
8.6	Comparison between the measured and estimated speckle contrast for the setup in Fig. 8.5(a).	105
8.7	Shift of the emission wavelength of the VCSEL for different pulse parameters and resulting speckle contrast reduction factor for the used paper screen	111

Symbols and Abbreviations

Symbol	Explanation
1D, 2D, 3D	one-, two- and three-dimensional
BA-VCSEL	Broad-area vertical-cavity surface-emitting laser
BPM	Beam Propagation Methods
CIE	Commission Internationale de l'Éclairage
CONV	convolution tool for MCML
CRT	cathode ray tube
DLS	Dynamic Light Scattering
DMD	Digital Micromirror Device
DWS	Diffusing Wave Spectroscopy
ESPI	Electronic Speckle Pattern Interferometry
FDTD	Finite Difference Time Domain
FWHM	full width at half maximum
GLV	Grating Light Valve
GEMS	Kodak Grating Electromechanical System
HID lamp	High Intensity Discharge lamp
LASCA	Laser Speckle Contrast Analysis
LC	liquid crystal
LCoS	liquid crystal on silicon
LED	light emitting diode
LSI	Laser Speckle Imaging
MCML	simulation tool “Monte Carlo for Multi-Layered media”
MTF	modulation transfer function
NECSEL	Novalux extended cavity surface emitting laser
OCT	Optical coherence tomography
OP.DI.MA	Optical Diffuse Material

OPS	Optical Programming System
QELS	Quasi Elastic Light Scattering
SHG crystal	second harmonic generation crystal
Teflon	product name from DuPont for polytetrafluorethylen
Ti:Sa laser	Titanium:Sapphire laser
UHP lamp	Ultra High Performance lamp
VCSEL	vertical-cavity surface-emitting laser
c	speed of light in vacuum
C	speckle contrast
D	diffusion coefficient of scattering globules in a colloidal dispersion
g	scattering asymmetry parameter, scattering unisotropy parameter
L	screen or slab thickness
n	refractive index
$N.A.$	numerical aperture
P	degree of polarization
T	integration time
A_{cov}	area corresponding to the normalized covariance function of the intensity distribution in a speckle pattern
A_j	amplitude of the optical field of point source j
A_j^l	amplitude contribution of point source j to detector pixel l
\overline{A}_j^l	ensemble mean value of the amplitude contribution point source j to detector pixel l
a_n	length of phasor n in a random phasor sum
A_{obs}	field in an observation point
$c_I(\Delta x, \Delta y)$	normalized covariance function of the intensity distribution in a speckle pattern
$d_{speckle}$	diameter of a single speckle spot in a speckle pattern
δ_{jk}	Kronecker delta
η	viscosity
$f/\#$	f-number
$g_1(\tau)$	field autocorrelation function
$\Gamma(\mathbf{x}_1; \mathbf{x}_2; \tau)$	mutual coherence function between the positions \mathbf{x}_1 and \mathbf{x}_2 at times t_1 and $t_2 = t_1 + \tau$ in a stationary optical field
$\gamma(\mathbf{x}_1; \mathbf{x}_2; \tau)$	complex degree of mutual coherence between the positions \mathbf{x}_1 and \mathbf{x}_2 at times t_1 and $t_2 = t_1 + \tau$ in a stationary optical field

$ \gamma(\mathbf{x}_1; \mathbf{x}_2; \tau) $	degree of coherence
γ_{lm}	complex degree of mutual coherence between detector pixels l and m
$\Gamma_A(x_1, y_1; x_2, y_2)$	field autocorrelation function of a speckle field or field crosscorrelation function of two speckle fields
$I(\mathbf{x})$	intensity in point \mathbf{x}
\vec{k}	wavevector
k_B	Boltzmann constant
$K_{\hat{G}}(\Delta\nu)$	autocorrelation function of a source's normalized power spectrum where $\Delta\nu$ is a frequency shift
l^*	transport mean free path length
l_p	depolarization length
$l_{speckle}$	length of a single speckle
λ	wavelength
$\delta\lambda$	1/e-width of the wavelength spectrum of a source
$\Delta\lambda$	wavelength shift or wavelength separation
$\bar{\lambda}$	mean value of the wavelengths emitted by a source
$\mu_A(\vec{q}_1, \vec{q}_2)$	normalized field crosscorrelation of two speckle fields with scattering vectors \vec{q}_1 and \vec{q}_2
μ_a	absorption coefficient
μ_s	scattering coefficient
$M_l(\Delta q_z)$	characteristic function corresponding to the path length distribution $p(l)$. Δq_z is the magnitude of the normal component of the scattering vector difference $\vec{q}_1 - \vec{q}_2$
N_A	Avogadro constant
$\delta\nu$	1/e spectral width of a source with Gaussian frequency spectrum
opl_j^l	mean value of the optical path lengths of all rays from the point source j in the detector pixel l
$p_I(I)$	probability density function of the intensity distribution in a speckle pattern
$p(l) = p(s)$	distribution of the scattering path lengths s or l
$p(s n)$	probability density of a photon travelling a path of length s and participating on n scattering events along this path
$p(\tau)$	distribution of the scattering path times τ
ϕ_j	start phase of the optical field of point source j
φ_n	phase of phasor n in a random phasor sum
\vec{q}	scattering vector

q_z	z-component of a scattering vector \vec{q}
$\Delta\vec{q}_t$	component of a scattering vector difference which is transverse to the scattering surface
Δq_z	component of a scattering vector difference which is normal to the scattering surface
r_{coh}	coherence radius
$\rho_{n,m}$	normalized intensity correlation coefficient of two independent speckle patterns
σ_{opl}	standard deviation of the optical path lengths of the rays from a point source in a detector pixel
$\bar{\sigma}_{opl}$	mean value of the standard deviations of the optical path lengths of the rays per point source in each detector pixel
$\sigma_{opl,max}$	maximum value of the optical path lengths of the rays from a point source in a detector pixel
T_{abs}	absolute temperature in Kelvin
τ_0	characteristic diffusion time of scattering globules in a colloidal dispersion
Θ_{coh}	half-width farfield coherence angle of the investigated BA-VCSEL
Θ_{ff}	half-width farfield divergence angle of the investigated BA-VCSEL
U^l	optical field in a detector pixel l
U_j	optical field of a point source j
U_j^l	field contribution of point source j to the optical field in detector pixel l
$\langle U_j^l \rangle$	ensemble average of the field contribution of point source j to the optical field in detector pixel l
$wt - \%$	weight percents
ζ	minimally required angular difference of the angles of incidence of two beamlets to produce fully uncorrelated speckle patterns

Acknowledgements

First of all, I want to thank Prof. Uli Lemmer for giving me the opportunity to conduct this work at the Light Technology Institute under his supervision. Uli, discussions with you were always very useful and brought me and my work a lot forward.

Second, I want to thank Prof. Hugo Thienpont for being co-examiner of my thesis.

I thank the Karlsruhe School of Optics and Photonics (KSOP) for the financial support, for the possibility to get in contact with many interesting people, and for the possibility to look outside the box of my research.

I want to thank Sony Deutschland GmbH for financial support within our industry project. Special thanks to Markus Kamm from the European Technology Center (EuTEC) in Stuttgart for his support.

I thank Fabian Dürr for his excellent work in his diploma thesis. Fabian, I wish you all the best for the success of your own Ph.D. work at the Department of Applied Physics and Photonics at the Vrije Universiteit Brussels.

I thank Prof. Georg Bastian for bringing me into contact with speckle. Georg, it was always a pleasure to work with you.

I thank the people from the Department of Applied Physics and Photonics from the Vrije Universiteit Brussels, especially Guy Verschaffelt, Youri Meuret, Gordon Craggs and the former members Ingo Fischer, Michael Peeters and Bart van Giel. Thanks for the nice time during our fruitful collaboration.

I thank all my co-authors (Uli Lemmer, Hugo Thienpont, Guy Verschaffelt, Youri Meuret, Gordon Craggs, Fabian Dürr, Felix Glöckler, Georg Bastian, Ingo Fischer, Udo Rohlffing, Bart van Giel and Michael Peeters) for their contribution. You all contributed a lot to my publications and also to the success of the whole Ph.D. project.

And of course I want to thank all my friends and colleagues at the Light Technology Institute. Thanks for the nice working atmosphere and all the fun we had together.

Index

- Étendue, 24
- ABCD-matrix formalism, 48, 55
- Absorption coefficient, 79
- Autocorrelation function of a source's normalized power spectrum, 35
- Avogadro constant, 85
- BA-VCSEL, 89
 - farfield divergence angle, 91
 - coherence radius, 91, 113, 119
 - farfield coherence angle, 101, 118
 - farfield divergence angle, 118
 - nonmodal emission regime, 89, 90
 - spatially incoherent emission regime, 89, 90
- Ballistic light, 86
- Beam homogenizer
 - single microlens array, 38, 58
 - two-tandemarray homogenizer, 57, 107, 116
- Blurring
 - acceptable blurring, 79
 - Monto Carlo simulation of blurring, 83
 - quantification, 79
- Boltzmann constant, 85
- BPM, 48
- Brownian movement, 77
- Characteristic function, 33, 67
- Chromaticity diagram, 20
- Coherence
 - simulation of a spatially partially coherent source, 49
 - coherence radius, 50, 61, 91, 113, 119
 - complex degree of mutual coherence, 48, 52
 - degree of coherence, 48
 - mutual coherence function, 3, 47
- simulation of a spatially fully coherent source, 49
- simulation of a spatially fully incoherent source, 49, 50, 53, 55
- Colloidal dispersion, 77
- Color
 - saturation, 20
 - triangle, 20
- Color filter wheel, 16
- Color gamut
 - CRT system, 21
 - laser system, 21
 - LED system, 21
- CONV, 83
- Correlation methods, 68
- CRT, 17
- Depolarization
 - depolarization length, 86
 - depolarizing scattering, 42, 43, 70, 92, 110, 118
- Dichroic mirror, 21, 25
- DLS, 84
- DMD, 16
- DWS, 84
- FDTD, 48
- Field autocorrelation function, 7
- Field crosscorrelation, 32
- Fill factor, 16
- Front projection screen
 - OP.DI.MA, 66
 - paper, 66, 92, 108, 116
 - Sample 1-3, 66
 - Teflon, 66
- Gaussian beam, 49
- Gaussian beam decomposition, 49
- GEMS, 17

- GLV, 17
 Green's function, 48
 Helmholtz equation, 49
 HID lamp, 19
 Human visual perception
 chromaticity diagram, 20
 contrast sensitivity, 27
 integration time, 79
 spatial resolution, 40
 speckle disturbance limit, 27
 visual acuity, 40
 Imager
 2D, 16
 fill factor, 16
 Intensity correlation, 34
 Intensity correlation coefficient, 6
 Laser price, 27
 Laser safety, 27
 Local continuity, 50
 Maxwell's equations, 48
 MCML, 83
 Mean ray, 50
 Milk, 79
 optical properties, 80
 size distribution of fat globules, 80
 size distribution of protein globules, 80
 Monte Carlo simulations, 83
 Normalized covariance function, 7
 Numerical aperture, 8, 108, 113, 120
 OP.DI.MA screen, 66
 OPS, 49
 Optical engine, 24
 Paper screen, 66, 92, 108, 116
 Polarization
 degree of polarization, 66, 70
 degree of polarization, 7
 methods for polarized LED output, 24
 recovery, 24
 Projection system
 color gamut of CRT system, 21
 color gamut of laser system, 21
 color gamut of LED system, 21
 consumer front and rear projectors, 15
 CRT projector, 17
 full frame, 16, 107
 large venue, high lumen output, 15
 line scanning, 17
 pico-projectors, 1, 15, 20
 pocket-projectors, 15, 20
 raster scanning, 17
 ultra portable projectors, 15
 Projection systems market
 current laser projection systems market, 18
 segmentation, 15
 volume, 1
 QELS, 84
 Raytracing, 49
 Rear projection TV, 1
 rear projection TV, 15, 19, 27
 Roughness
 surface roughness, 35, 67
 volume roughness, 87
 volume roughness, 67, 74
 Scattering
 anisotropy parameter, 79
 asymmetry parameter, 79
 diffusive scattering, 84
 forward peaked scattering, 80
 Mie scattering, 80
 Rayleigh scattering, 79
 scattering coefficient, 79
 scattering globules, 78–80
 scattering path time distribution, 68, 71
 scattering properties of milk, 80
 single scattering, 84
 volume scattering, 40, 65, 67, 87
 Scattering coefficient, 79
 Scattering path length distribution, 35, 67
 Scattering path time distribution, 68, 71
 SHG, 68
 Source
 quasi-homogeneous source, 49
 spatially fully incoherent source, 49
 electrode free lamp, 19

- ensemble of point sources, 49
Gaussian Schell-model source, 91
HID lamp, 19
point source, 49
quasi-homogeneous source, 91
spatially extended source, 49
spatially fully coherent source, 49
spatially fully incoherent source, 50, 58, 61
spatially partially coherent source, 49
warm-up time, 20
- Speckle**
applications of speckle
determination of MTF, 10
LASCA, 10
LSI, 10
speckle interferometry, 10
speckle photography, 10
stress/strain measurements, 10
study of displacements of diffuse objects, 10
study of vibrations of diffuse objects, 10
surface metrology, 10
testing of ophthalmic testing, 11
x-ray speckle, 11
- contrast reduction
by angular decorrelation, 37
by scrambling, 42
by scrambling of the polarization, 42, 43
by scrambling with a moving screen, 43
by scrambling with colloidal-dispersion-filled projection screens, 77
by scrambling with moving diffusors, 43
by scrambling with multimode optical fibers, 43
by spatial decorrelation, 39
by wavelength decorrelation, 34
classification of methods, 31
definition of speckle contrast, 5
disturbance limit, 28
emergence, 3
history of speckle research, 4
- length, 8
measurement of speckle, 8
objective speckle, 8
problems with speckles
fatigue, 12
in astronomy, 11
in bar code scanners, 12
in holography, 11
in laser Doppler vibrometry, 12
in laser projection applications, 12, 27
in laser triangulation, 12
in multimode optical fibers, 12
in OCT, 11
in radar, 12
in ultrasound applications, 12
size, 7, 8
statistical properties, 5
subjective speckle, 8
- Streak camera, 66
Surface scattering, 31, 34, 36
- Teflon screen, 66
Ti:Sa laser, 69, 99
Transmissive projection screen
colloidal-dispersion-filled, 77
Lumin 360°, 79
- Transport mean free path, 80
- van Cittert-Zernike theorem, 50, 53
- VCSEL, 89
farfield divergence angle, 91
coherence radius, 91, 113, 119
farfield coherence angle, 101, 118
farfield divergence angle, 118
nonmodal emission regime, 89, 90
spatially incoherent emission regime, 89, 90
- Viscosity, 85
- Wavelength chirp, 37, 98, 99, 110, 118
Wolf's equations, 48

The use of lasers as light sources in projection applications has been envisaged already since the 1960s. Laser sources can provide considerable advantages compared to standard projection lamps. These are, for example, a larger color gamut, a small étendue of the light source, emission of polarized light and a long lifetime. However, the appearance of an unwanted granular structure in projected images is observable when lasers are used as light sources. This so called “speckle pattern” is a quasi-random interference pattern which is formed because of the high coherence of the laser light. A typical laser produces a speckle pattern with large unwanted intensity fluctuations. These can severely degrade the image quality of projected images and speckle reduction is therefore a major issue.

This work investigates different practical methods and strategies for speckle reduction in laser projection applications.

ISBN: 978-3-86644-418-8

www.uvka.de

SBN 978-3-86644-418-8

